Recrystallisation and γ' precipitation during industrial open die forging of the nickel based superalloy AD730

Angus Coyne-Grell

Supervisors: Salaheddin Rahimi, Ioannis Violatos, Sébastien Nouveau, Christian Dumont, Jérôme Blaizot, Nathalie Bozzolo

A thesis submitted in fulfilment of the requirements for the degree of Doctor of Philosophy (PhD)



University of Strathclyde Glasgow

AUBERT&DUVAL

Advanced Forming Research Centre

Design, Manufacturing and Engineering Management

2023

Declaration

This thesis is the result of the author's original research. It has been composed by the author and has not been previously submitted for examination which has led to the award of a degree.

The copyright of this thesis belongs to the author under the terms of the United Kingdom Copyright Acts as qualified by University of Strathclyde Regulation 3.50. Due acknowledgment must always be made of the use of any material contained in, or derived from, this thesis.

Signed:



Dated: 11/07/2023

Previously published works

Parts of this thesis have appeared in the following peer reviewed publications:

- A. Coyne-Grell, J. Blaizot, S. Rahimi, I. Violatos, S. Nouveau, C. Dumont, A. Nicolaÿ, N. Bozzolo, "Recrystallization mechanisms and associated microstructure evolution during billet conversion of a gamma-gamma′nickel based superalloy", *Journal of Alloys and Compounds*, **916**, 2022

- A. Coyne-Grell, J. Blaizot, S. Rahimi, I. Violatos, S. Nouveau, C. Dumont, A. Nicolaÿ, N. Bozzolo, "Evolution of γ' Precipitation During the Early Stages of Industrial Forging of a Nickel-Based Superalloy", *Metallurgical and Materials Transactions A*, **54**, 2023

Abstract

Ni-based superalloys are used in very challenging operating conditions in jet turbine engines. In order to withstand these challenging operating conditions, and be used in safety critical parts such as turbine discs, the microstructure of such alloys must be well controlled. Much of this control is achieved during open die forging, where as-cast ingots are converted into billets. During this process the coarse as-cast structure is massively refined through recrystallisation.

To design an effective forging route, and produce the desired, refined, uniform microstructure, the microstructural evolutions happening during the open die forging must be investigated; that is the aim of this thesis. The Ni-based superalloy AD730, produced by Aubert&Duval is studied. The microstructure from different stages of the industrial forging process is analysed, and stages of this process are simulated on the lab scale to allow microstructural mechanisms to be investigated. The precipitate distribution which forms during first cooling through the solvus temperature is characterised, including with 3D observations. It is observed that this distribution is very inhomogeneous, comprising a mixture of continuous and discontinuous precipitates and some regions with no precipitation. The potential role of chemical segregation in producing the inhomogeneous precipitate distribution is investigated. It is found that the regions without precipitates have lower concentrations of the γ' forming elements. A key finding is that cooling through the γ' solvus temperature has a significant effect on grain size and morphology, with grain size decreasing and grain boundaries becoming more serrated.

The interaction of this inhomogeneous distribution with recrystallisation during compression is studied, and it is seen that regions with different precipitation show different mechanisms and kinetics of recrystallisation. A key finding is that regions with discontinuous precipitation are harder to recrystallise than those with continuous precipitation. Local crystallographic texture also influences the kinetics of recrystallisation during compression, grains with a $\langle 110 \rangle$ axis close to the macroscopic compression direction being harder to recrystallise than grains without. The role of annealing twin formation in assisting the nucleation and growth of recrystallised grains is discussed, and examples of its effect are shown. The effect of

forging parameters (cooling rate after forging, number of forging strokes used) is also investigated.

A detailed study is performed on the interaction between recrystallisation and precipitates during the final sub-solvus forging stage of the industrial forging process. It is observed that precipitates can interact in at least four different ways with recrystallisation. Suggestions are made for future work, and for ways to exploit the observations made in an industrial forging process.

Acknowledgements

The work in this thesis would not have been possible without the funding and support of Aubert&Duval. I would like to thank them for the provision of raw materials, for allowing me to visit their site at Les Ancizes, and for sharing with me some of their expertise.

In particular I want to thank: Jérôme Blaizot, for the careful feedback he provided throughout this thesis and guiding my visit to Les Ancizes; Sébastien Nouveau for welcoming me to the AFRC and giving very clear motivation to finish the thesis on time; Christian Dumont for his enthusiasm and warm encouragement throughout.

Thank you also to my academic supervisors: Ioannis Violatos, for his guidance on modelling and always impactful interventions; Salah and Nathalie for the motivation, guidance and constructive feedback throughout. This made the difficult tasks easier, and the easy ones more difficult. Thank you also to Nathalie for including me in training courses at the CEMEF, and online, throughout.

Thank you to the technicians at the AFRC who helped me massively in carrying out this thesis, particularly Ryan O'Neill, Kornelia Kondziolka, Jacqueline Schramm, Lee McGarry, Adam Robbins and Calum Boyle.

Thank you to the other PhD students at the AFRC, for their help and friendliness: David Connolly, John Catterson, Michail Dellepiane, Luis Reig Buades, Mauro Arcidiacono, Michael McPhillimy, Rory Brown-Kerr, Kyle 'shadow' Nelson, Matthew Ferguson, Arthur Paquette, Beatrice Crocco. Without you the PhD would have been far less enjoyable (but finished far sooner!). Thank you as well to the students and staff at (CEMEF) for welcoming me during my visit.

Thank you to Andrew, Anna, Stuart and Henry for being fantastic friends throughout. Thank you to mum and dad for the encouragement, and getting me here.

Thank you to Alexis Nicolaÿ for carrying out the FIB-SEM nanotomogaphy work at CEMEF, and to Paul Edawrds for carrying out the WDS work at Strathclyde's Technology & Innovation Centre

A special thank you to the other members of the AFRC Late club, for the snacks and motivation. I hope that with this submission I can be awarded a lifetime ban.

Acronyms

BD ..... Billet direction
BSE ..... Backscattered electron
CD ..... Compression direction
DIGM ..... Diffusion induced grain boundary migration
EBSD ..... Electron backscatter diffraction
EDS ..... Energy dispersive spectroscopy
EDM ..... Electrical discharge machining
EPMA ..... Electron probe microanalyzer
FE ..... Finite element
FSE ..... Forward scattered electron
FCC ..... Face centred cubic
FEG ..... Field emission gun
FIB ..... Focused ion beam
GAKAM ..... Grain average kernel average misorientation
GAM ..... Grain average misorientation
GOS ..... Grain orientation spread
GROD ..... Grain reference orientation deviation
HAGB ..... High angle grain boundary
HERX ..... Heteroepitaxial recrystallisation
IPF ..... Inverse pole figure
KAM ..... Kernel average misorientation
LAGB ..... Low angle grain boundary
MAGB ..... Medium angle grain boundary
MRD ..... Multiples of the random distribution
RD ..... Radial direction
SE ..... Secondary electron
SIBM ..... Strain induced boundary migration
SEM ..... Scanning electron microscope
TMP ..... Thermo-mechanical processing
WDS ..... Wavelength dispersive spectroscopy

Contents

1 Introduction **12**

1.1 The need for high temperature materials 12
1.2 Producing high temperature materials 12
1.3 Thesis structure 15

2 Literature review **17**

2.1 Introduction 17
2.2 Overview of the microstructure of AD730 21
2.3 Thermodynamics of γ' in AD730 24
2.4 Control of γ' in AD730 27
2.4.1 Precipitation 27
2.4.2 Size and morphology 30
2.4.3 Coarsening 33
2.4.4 Splitting 38
2.5 Control of γ in AD730 39
2.5.1 Large recrystallised grains and their precipitates 40
2.5.2 The formation of recovered grains 45
2.5.3 Comparison with other Ni-based superalloys 47
2.6 Forging process parameters 48
2.6.1 Strain rate and temperature 49
2.6.2 Strain 52
2.6.3 Initial microstructure 53
2.7 Conclusions and outlook 55

3 Methodology **58**

3.1 General strategy 58
3.2 Limitations 60
3.3 Microstructural characterisation techniques 61
3.3.1 Focused ion beam SEM tomography 61

3.3.2 Electron back scattered diffraction (EBSD) . . . 63
3.3.3 EBSD analysis . . . 64
3.4 Experimental details . . . 69
3.4.1 As-received material . . . 69
3.4.2 Experiments 1 and 2 - intermediate scale forging . . . 69
3.4.3 Additional precipitation heat treatments . . . 76
3.4.4 Experiment 3 -lab scale forging . . . 78

4 Characterisation of industrial microstructures 82
4.1 The industrial forging route . . . 82
4.2 Samples investigated . . . 84
4.3 Samples from the static recrystallisation step . . . 85
4.3.1 General microstructural overview . . . 85
4.3.2 Microstructures at different billet locations . . . 89
4.4 Samples from the final sub-solvus forging step . . . 93
4.4.1 General microstructural overview . . . 93
4.4.2 Microstructural observations along radial direction at the billet foot . . . 96
4.5 Microstructural evolution during sub-solvus forging . . . 98
4.6 Summary . . . 101

5 Precipitate evolution during the early stages of billet conversion 104
5.1 Microstructure after homogenisation . . . 105
5.2 Overview of microstructure after precipitation . . . 106
5.3 Discontinuous precipitates . . . 110
5.3.1 Classification and mechanisms . . . 110
5.3.2 Size and morphology . . . 112
5.4 Grain boundary motion during discontinuous precipitation . . . 117
5.4.1 Thermodynamic driving force . . . 117
5.4.2 Effect on grain structure . . . 118
5.4.3 Additional investigations into grain boundary motion . . . 122
5.5 Continuous precipitates . . . 129
5.5.1 Morphology . . . 129
5.5.2 Spatial distribution . . . 130
5.6 Summary . . . 133

6 Recrystallisation evolution during the early stages of billet conversion 135
6.1 Evolution of unrecrystallised grains . . . 135
6.1.1 Texture evolution . . . 135
6.1.2 Influence of texture on recrystallisation . . . 137
6.2 Precipitation in unrecrystallised grains . . . 140
6.2.1 Overview . . . 140
6.2.2 Origin of fine spherical precipitation . . . 140
6.2.3 Effect of fine spherical precipitates on recrystallisation . . . 146
6.2.4 Influence of precipitation on recrystallisation . . . 149
6.3 Formation of recrystallised grains . . . 151
6.3.1 Overview . . . 151
6.3.2 Recrystallisation around octodendrites . . . 151
6.3.3 The role of twinning in recrystallisation . . . 155
6.4 Summary . . . 156

7 Impact of forging parameters on microstructural evolution 158
7.1 Comparison of strain distribution in experiments 1 and 2 . . . 158
7.2 A method for estimating strain and recrystallisation level . . . 160
7.2.1 Uncertainty in local strain level . . . 161
7.2.2 Estimating recrystallisation level and uncertainty . . . 161
7.3 Influence of forging parameters on recrystallisation level and microstructural evolution . . . 164
7.3.1 Influence of strain level and cooling rate . . . 164
7.3.2 Influence of number of forging strokes . . . 165
7.3.3 Evolution of γ' precipitates . . . 168
7.4 Summary . . . 179

8 Recrystallisation in an inhomogeneous microstructure from an intermediate stage of billet conversion 180
8.1 Starting microstructure . . . 180
8.2 Overall microstructural evolution with strain . . . 185
8.3 Recrystallisation of the large initially statically recrystallised grains . . . 187
8.4 Recrystallisation in and around the initially unrecrystallised grains . . . 191

8.4.1 Necklace recrystallised grains . . . 193
8.4.2 Large recrystallised grains . . . 197
8.4.3 Recrystallised channels . . . 203
8.5 The effects of microstructural heterogeneity on recrystallisation . . . 205
8.6 The origin of primary γ' . . . 207
8.7 Summary . . . 208

9 Summary and conclusions **210**
9.1 Conclusions . . . 211
9.1.1 Precipitation during slow cooling . . . 211
9.1.2 Interaction between recrystallisation and precipitation . . . 213
9.1.3 Recrystallisation mechanisms . . . 214
9.2 Outlook and future work . . . 215
9.2.1 Discontinuous precipitation and its effect on grain structure . 215
9.2.2 The effect of minor differences in composition on precipitation and recrystallisation . . . 216
9.2.3 Exploiting the easy recrystallisation of the large intially statically recrystallised grains . . . 217
9.2.4 Precipitate free bands and the origin of fine and dense spherical precipitates . . . 218

1 Introduction

1.1 The need for high temperature materials

Increasing the turbine entry temperature of a jet engine makes the engine both more efficient and more economical, as it must use less fuel. As such, higher entry temperatures, and the materials which can withstand them, are desirable.

The jet turbine presents very demanding material operating conditions, with operating temperatures up to 1030 °C for the turbine blades, and around 650 °C for the rim of the turbine discs. The disc must resist centrifugal stresses, stresses due to the thermal gradient from bore to rim, be as lightweight as possible, and resist corrosion. Additionally, they face changing conditions of stress and temperature, so have to resist fatigue failure.

1.2 Producing high temperature materials

Ni-based alloys are a suitable choice for such applications. Nickel has an FCC crystal structure from room temperature up to its melting point, and so avoids allotropic phase transformations which can cause shape or volume changes. It has low intrinsic diffusivity, meaning creep rates are low, and the FCC structure also means it is ductile. Furthermore, it has a reasonable density and is not very expensive. Nickel also acts as a good solvent, allowing properties to be altered by a wide range of alloying elements.

Alloys based on nickel *can* display excellent high temperature mechanical properties and oxidation resistance. However, these high temperature mechanical properties are very dependent on microstructure and alloy composition.

AD730 is a recently developed Ni-based superalloy intended for use in turbine discs which offers an attractive combination of cost and high temperature properties (creep, tensile strength and microstructural stability) [1]. A comparison between selected mechanical properties of AD730 and other cast and wrought Ni-based superalloys is shown in Fig. 1.1. Achieving these properties consistently in industrial

scale manufacturing requires the microstructural evolution during open die forging to be understood and controlled.

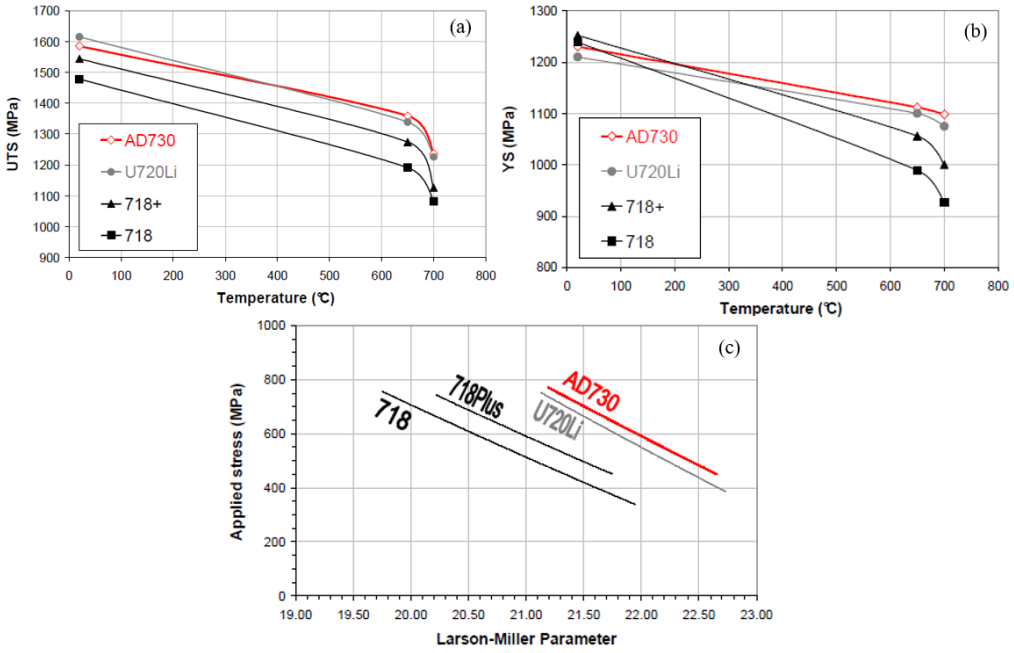


Figure 1.1: Selected mechanical properties of AD730 compared with other cast and wrought superalloys (ultimate tensile strength (a), yield strength (b) and Larson-Miller parameter (c)). Figure taken from [1].

The microstructure of AD730 comprises a γ matrix with a face centered cubic (FCC) crystal structure containing γ' precipitates which have a nominal composition of Ni_3(Al,Ti) and an ordered $L1_2$ crystal structure.

The size, stored energy level and texture of the γ grains and the size and distribution of strengthening precipitates (in AD730, there is just γ') affect mechanical properties, so they are controlled through a multistage process. An overview of this process is given in Fig. 1.2.

First, the raw alloying elements are melted together to form an ingot. This melting can comprise three stages: Vacuum induction melting (VIM), electro-slag remelting (ESR) and vacuum arc remelting (VAR). The ingot so produced will then be homogenised to further reduce remnant chemical segregation.

Then, open die forging is performed, which aims to break down the as-cast microstructure. The structure of the γ grains is massively changed during open die forging. As-cast grains which are on the order of millimeters in diameter should be broken down into equiaxed grains with diameters on the order of 20 µm during

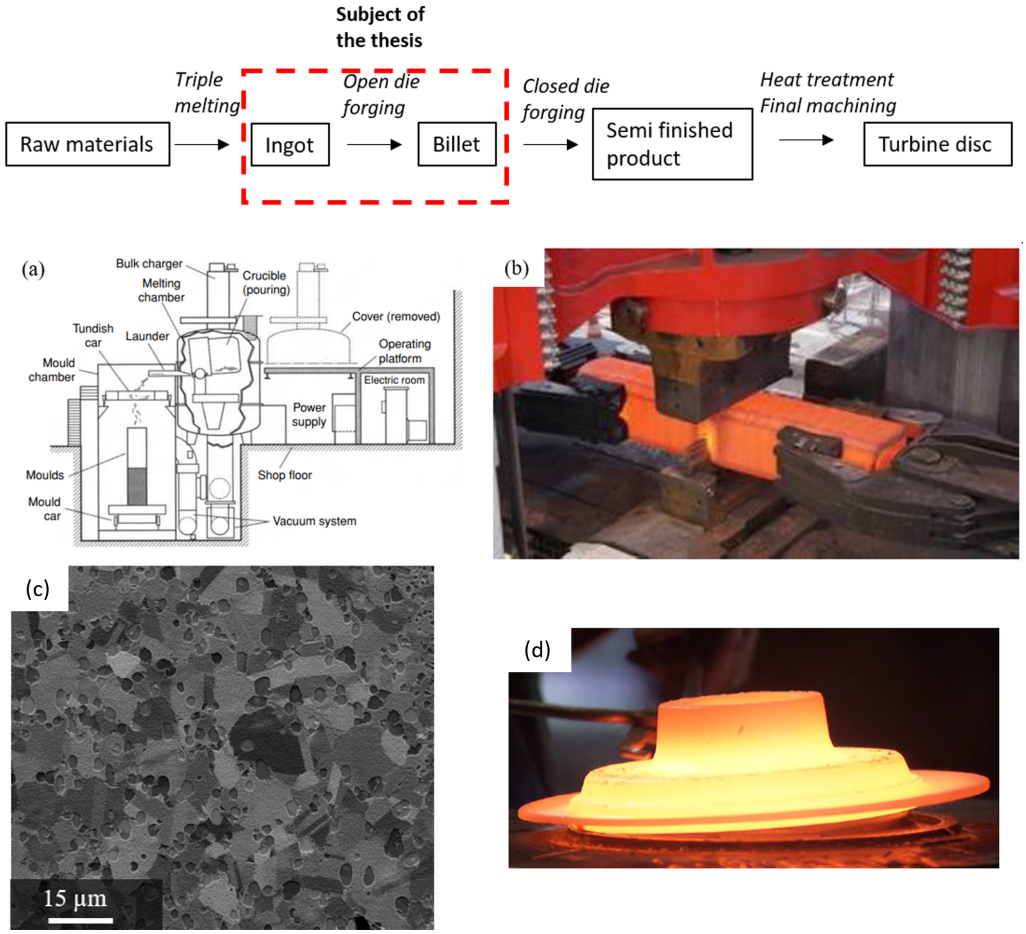


Figure 1.2: An overview of the manufacturing route for cast and wrought turbine discs. The open die forging stage of this process will be the focus of this thesis. A schematic of the vacuum induction melting (VIM) stage (a) from [2], a picture of hot working during open die forging (b), and a secondary electron image of a microstructure typical of the end of open die forging (c), and a nearly finished disc at the end of closed die forging (d).

the billet conversion process. This occurs through recrystallisation. Achieving this uniform, highly recrystallised structure eases the following processing steps and allows the correct mechanical properties to be achieved. Additionally, it improves the ultrasonic inspectability of the billets [3]. Open die forging is a complex, multi-stage operation which can involve super-solvus forging [2], controlled cooling at a slow rate through the solvus temperature, sub-solvus forging and static recrystallisation stages.

The shape of the billet is then controlled through closed die forging, after which

heat treatments may be performed to achieve a suitable distribution of strengthening precipitates. After this final heat treatment the disc is quenched, typically in oil to lock in the precipitate structure. Finally, the discs are machined to the required final shape.

During billet conversion, an ingot is converted into a billet through a series of heating and forging operations, the first of which are above the γ' solvus temperature, and the last below. During these latter stages, precipitates will influence recrystallisation. To understand microstructural evolution during open die forging, and optimise the forging route used, the formation of precipitates and their interaction with recrystallisation should be investigated.

Studying this process presents several challenges. It is not economically feasible to interrupt industrial forgings to take samples for characterisation, so trials must done at a smaller scale. The industrial conditions can not be directly replicated on the lab scale (heating and cooling rates are much slower than is typical for lab-scale experiments, and these rates vary through the radius of the ingot, as do strain and strain rates). Additionally, at the early stages of the forging process, the microstructure is very coarse, with as cast grains having sizes on the order of 10 mm [2]. Investigating such microstructures requires large samples to ensure a representative number of grains can be analysed. As such, microstructures and processing conditions typical of the ingot to billet conversion process are not much analysed in the scientific literature.

1.3 Thesis structure

In this thesis, the microstructural evolutions happening during the open die forging of AD730 will be investigated.

First a literature review focusing on the forging of AD730 is conducted, and some open questions are outlined.

Then, in Chapter 3, a methodology is set out describing experiments done to address these open questions, and the techniques used to extract and analyse the data produced.

Chapter 4 describes the microstructures typical of the latter stages of the industrial forging route, and shows that even at the end of the industrial forging process, the microstructure remains inhomogeneous, containing large unrecrystallised grains

with a relatively fine and dense distribution of γ', as is often observed in such heavily alloyed γ/γ' grades. This gives a basis and motivation for the following chapters.

Chapter 5 considers the microstructural evolution during the transition from super-solvus to sub-solvus forging. The precipitate distribution which forms during cooling through the solvus temperature, at a cooling rate representative of industrial forging conditions is investigated. Notably, 3D images of precipitates are acquired using FIB-SEM nanotomography.

Chapter 6 examines the interaction of this precipitate distribution with recrystallisation during forging, simulating the first sub-solvus forging operation. The ease of recrystallisation around different precipitate types is investigated, and used to explain which precipitates survive in the unrecrystallised grains.

Chapter 7 looks at the influence of different forging parameters during the first sub-solvus forging. Different numbers of forging strokes and cooling rates after forging are considered, their influence on recrystallisation level and precipitation is examined, and the role of remnant chemical segregation is considered.

Next, in Chapter 8, the microstructural evolution during the final sub-solvus forging stage is simulated with a lab scale trial, where the starting material is taken from the penultimate stage of the industrial process.

Finally, Chapter 9 emphasises the main conclusions from the thesis and makes suggestions for future work.

2 Literature review

2.1 Introduction

The history of Ni-based superalloys stretches back almost 100 years to 1926 when Merica discovered that adding small amounts of titanium and aluminium to the oxidation resistant "80-20" nickel-chromium alloy increased its creep strength dramatically, and patented this new alloy [4]. Following decades of improvement in alloy composition and processing techniques, a considerable number of different alloys and processing routes are available, as indicated in Table 2.1. Today, the most widely used Ni-based superalloy for compressor and turbine discs is Inconel 718 [5]. Inconel 718 is low cost due to its cast and wrought processing route and low quantities of expensive alloying additions, and has suitable high temperature mechanical properties. However, problems arise when it faces prolonged exposure to temperatures above 650 °C, due to transformation of the strengthening γ'' phase to the δ phase [1]. Far better high temperature mechanical properties can be achieved in alloys processed via the powder metallurgy route. This route confines segregation to the scale of the powder particles used, and finer grain and defect sizes can be achieved with this method. However, these come with increased processing costs [6, 7]. Thus, Inconel 718 and powder processed superalloys populate two extremes of the cost-performance map, with cast and wrought superalloys between them (shown in Fig. 2.1).

AD730 is a relatively new Ni-based superalloy, developed by the forging company Aubert & Duval. Its chemical composition comprises low amounts of expensive alloying elements such as Co, Nb, Mo, W as compared with other $\gamma/\ \gamma'$ superalloys (such as Waspaloy and Udimet 720 Li), which helps reduce its cost. At the same time, AD730 shows good mechanical properties at 700 °C, primarily better yield strength and creep resistance than Udimet 720Li and Inconel 718 [1]. As such, it has the potential to fill a vacant space in the cost-performance map (as indicated schematically in Fig. 2.1).

The range of compositions possible for AD730 are shown in Table 2.2. The choice of alloying elements is fairly standard for Ni-based superalloys, and can be briefly

explained as follows:

- Chromium is added as it is essential in forming a protective Cr_2O_3 oxide scale, allowing parts to be exposed to oxygen at high temperatures without being rapidly corroded [9].
- The refractory elements (Mo, Zr, Nb, W) and Fe provide solid solution strengthening.
- Cobalt is added (albeit in relatively small amounts to help reduce costs), as it reduces the stacking fault energy [10], which can improve creep performance. Co has been shown to increase the yield strength of alloys by lowering the stacking fault energy, changing the deformation mechanism from isolated faulting to micro twinning at temperatures above 650 °C [11].
- Ti and Al are necessary as the γ' forming elements.
- Boron and carbon promote the formation of grain boundary carbides and borides [12], which help pin the grain boundaries and prevent excessive grain growth during thermomechanical processing. The addition of boron also improves ductility particularly at low strain rates [13].

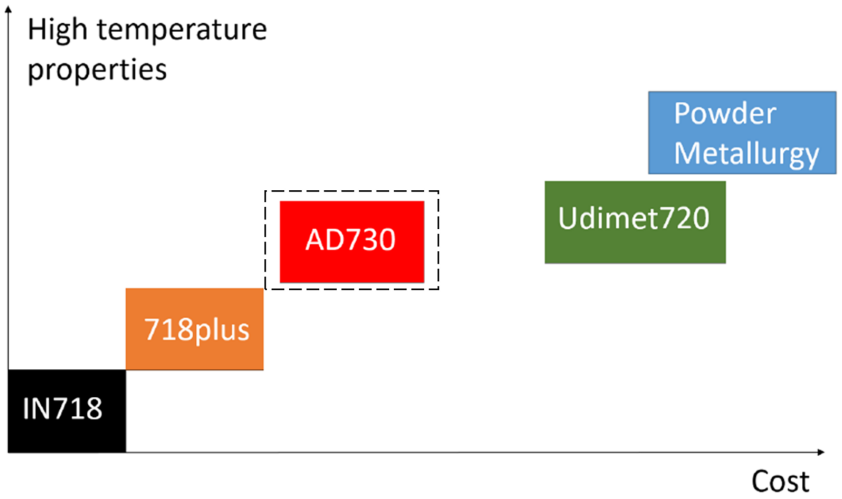


Figure 2.1: A schematic illustrating the gap in cost-performance space filled by AD730.

Table 2.1: The composition in Wt.% of different Ni-based superalloys. Table adapted from [6]. Composition of Rene 65 from [8]

Alloy	Cr	Co	Mo	W	Ta	Re	Nb	Al	Ti	Hf	C	B	Y	Zr	Other
Conventionally cast alloys															
Mar-M246	8.3	10	0.7	10.0	3.0	-	-	5.5	1.0	1.50	0.14	0.02	-	0.05	-
Rene 80	14.0	9.5	4.0	4.0	-	-	-	3.0	5.0	-	0.17	0.02	-	0.03	-
IN-713LC	12.0	-	4.5	-	-	-	2.0	5.9	0.6	-	0.05	0.01	-	0.10	-
C1023	15.5	10.0	8.5	-	-	-	-	4.2	3.6	-	0.16	0.01	-	-	-
Directionally solidified alloys															
IN792	12.6	9.0	1.9	4.3	4.3	-	-	5.0	1.5	-	-	-	-	-	-
GTD111	14.0	9.5	1.5	3.8	2.8	-	-	3.0	4.9	-	0.10	0.01	-	-	-
First-generation single-crystal alloys															
PWA 1480	10.0	5.0	-	4.0	12.0	-	-	5.0	1.5	-	-	-	-	-	-
Rene N4	9.8	7.5	1.5	6.0	4.8	-	0.5	4.2	3.5	0.15	0.05	0.00	-	-	-
CMSX-3	8.0	5.0	0.6	8.0	6.0	-	-	5.6	1.0	0.10	-	-	-	-	-
Second-generation single-crystal alloys															
PWA 1484	5.0	10.0	2.0	6.0	9.0	3.0	-	5.6	-	0.10	-	-	-	-	-
Rene N5	7.0	7.5	1.5	5.0	6.5	3.0	-	6.2	-	0.15	0.05	0.00	0.01	-	-
CMSX-4	6.5	9.0	0.6	6.0	6.5	3.0	-	5.6	1.0	0.10	-	-	-	-	-
Third-generation single-crystal alloys															
Rene N6	4.2	12.5	1.4	6.0	7.2	5.4	-	5.8	-	0.15	0.05	0.00	0.01	-	-
CMSX-10	2.0	3.0	0.4	5.0	8.0	6.0	0.1	5.7	0.2	0.03	-	-	-	-	-
Wrought superalloys															
IN 718	19.0	-	3.0	-	-	-	5.1	0.5	0.9	-	-	0.02	-	-	18.5 Fe
Rene 41	19.0	11.0	10.0	-	-	-	-	1.5	3.1	-	0.09	0.01	-	-	-
Rene 65	16.0	13.0	4.0	4.0	-	-	0.7	2.1	3.7	-	-	0.02	-	0.05	1.0 Fe
Nimonic 80A	19.5	-	-	-	-	-	-	1.4	2.4	-	0.06	0.003	-	0.06	-
Waspaloy	19.5	13.5	4.3	-	-	-	-	1.3	3.0	-	0.08	0.01	-	-	-
Udimet 720	17.9	14.7	3.0	1.3	-	-	-	2.5	5.0	-	0.03	0.03	-	0.03	-
Powder-processed superalloys															
Rene 95	13.0	8.0	3.5	3.5	-	-	3.5	3.5	2.5	-	0.07	0.01	-	0.05	-
Rene 88 DT	16.0	13.0	4.0	4.0	-	-	0.7	2.1	3.7	-	0.03	0.02	-	-	-
N18	11.2	15.6	6.5	-	-	-	-	4.4	4.4	0.5	0.02	0.02	-	0.03	-
IN100	12.4	18.4	3.2	-	-	-	-	4.9	4.3	-	0.07	0.02	-	0.07	-

- Zr strengthens grain boundaries by filling grain boundary vacancies, and influences the morphology of MC carbides, leading to formation of spheroidal carbides rather than script like carbides [14].

Table 2.2: Table showing range of alloying element compositions which define AD730.

	Composition in Wt. %										
	Cr	Co	Mo	W	Nb	Al	Ti	C	B	Zr	Fe
Min.	15	8	2.5	2	0.8	2.0	3.3	0	0.005	0.01	3.6
Max.	17	10	3.5	3	1.4	2.5	3.9	0.02	0.02	0.05	5.0

Research in AD730 specifically has branched out in several directions. Impressively thorough investigations into the thermodynamics and kinetics of the precipitation of the γ' phase [12, 15, 16], have been carried out. Alongside this, other prominent research themes have been; the mechanical properties of AD730 [17, 18, 19] and their control via ageing heat treatments [20, 21], γ' precipitation and its relation with recrystallisation [22, 23, 24], the forging of AD730 [25, 26] and welding of AD730 [27, 28, 29].

It was initially claimed that an advantage of AD730 was that it could be forged relatively easily above and below its γ' solvus [1]. However, subsequent investigations have shown that achieving a fully recrystallised microstructure in AD730 during ingot to billet conversion is not straightforward (as is the case in other Ni-based superalloys [8, 3, 30]), and large unrecrystallised grains persist in the final microstructure after forging [26]. These grains contain a fine and dense precipitation of primary γ', and have been dubbed 'recovered' grains [23], as they showed quite well defined recovery cells. AD730 is not the only Ni-based superalloy to show unrecrystallised grains with precipitation of this sort following billet conversion. They have also been seen in René 65 [8, 3, 30].

Increasing the degree of recrystallisation in AD730 during sub-solvus forging has been shown to require high strains, greater than are typically achievable under large scale industrial forging processes [25, 26]. In an industrial forging process, the final billet may be approximately 4 times longer than the initial ingot, with half the diameter, corresponding to a macroscopic true strain of $\epsilon \approx \ln(4) \approx 1.39$. In the lab-scale trails cited [25, 26] strains of up to 2 and 3 were investigated, and the samples still possessed non-recrystallised fractions of 10 - 20 percent %.

Forging in the super-solvus allows better recrystallisation kinetics (i.e., the level of recrystallisation achieved as a function of strain) owing to higher temperature. For example in one case super-solvus forging led to recrystallised fractions above 90 % with a strain of just 0.69 [22]. However, on industrial scale work-pieces, the achievable cooling rate through the solvus is limited by the large size of the work-

pieces, so grains will grow again following recrystallisation, necessitating further sub-solvus forging to control the grain size.

From an industrial standpoint, a major outstanding challenge is thus to provide an explanation for these unrecrystallised 'recovered' grains, and if possible propose an industrially viable means of generating a fully recrystallised microstructure with reasonably sized recrystallised grains (i.e. equivalent diameters on the order of 20 µm).

This review will be focused primarily around the forging of AD730, and assess works on and around this topic. Section 2 provides an overview of the microstructure of AD730 to inform the subsequent discussions. Sections 3 and 4 deal with the γ' phase in AD730. Section 5 turns to control of the γ matrix via thermomechanical treatments. Section 6 reviews what is known about the effect of forging process parameters on microstructural evolution during forging. Finally, section 7 provides conclusions and an outlook on useful work that could be carried out to address the questions raised in this review.

2.2 Overview of the microstructure of AD730

The microstructure of AD730 is made up of precipitates of the γ' phase, with a nominal composition of $Ni_3(Al,Ti)$ and an ordered $L1_2$ crystal structure, in a γ matrix solid solution with a face centered cubic (FCC) crystal structure. These unit cells are illustrated in Fig. 2.2. A low density of MC carbides and M_3B_2 borides [18] are also present, primarily at grain boundaries. The γ' precipitates in final part microstructures typically display a multi-modal size distribution. Larger so called "primary" precipitates with sizes on the order of 1 - 5 µm are found at grain boundaries, with smaller secondary precipitates (sizes around 100 nm) and tertiary precipitates (sizes around 50 nm) found intragranularly. The smaller precipitates strengthen the alloy by inhibiting the motion of dislocations through order strengthening [2], while the larger precipitates pin grain boundaries and limit grain growth during the final processing steps. This multi-modal size distribution arises due to multiple nucleation bursts at different temperatures on cooling [16], though very fast cooling (i.e. quenching) can lead to just a single burst, giving a microstructure consisting of very fine (10-30 nm diameter) γ' precipitates [22].

The γ matrix, while not primarily responsible for the in-service high tempera-

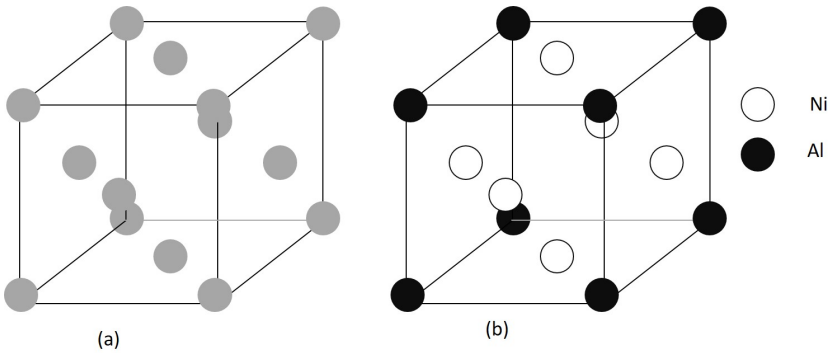


Figure 2.2: The FCC crystal structure of the γ phase (a) and the L12 crystal structure of the γ' phase (b). Other alloying elements may substitute for the Ni or Al atoms at the faces or corners of the γ' unit cell.

ture strength of AD730, can significantly affect its mechanical properties. The key properties of the γ matrix will be its grain size and recrystallisation level. A higher degree of recrystallisation is desirable as it means more small grains with low stored energy, though is not necessarily straightforward to achieve. The optimum grain size is variable, and application dependent. Smaller grains lead to higher strength and higher toughness due to the Hall-Petch effect and an increased grain boundary area, respectively. However, they have faster creep rates, due to larger grain boundary area. As such, microstructure gradients are proposed for turbines discs, with larger grains at the rim to resist high temperature creep, and smaller ones towards the bore to resist the higher stresses [31].

Previous investigations into the microstructure of AD730, and its evolution during thermomechanical treatments, identified different types of grain and precipitate arising during forging. The most notable of these are listed below and highlighted in Fig. 2.3:

- 'Recovered' grains. These are large, unrecrystallised grains with a fine and dense precipitation of γ', first identified (and named) in [23].

- Recrystallised grains. These are small grains with low dislocation densities, large intergranular (primary) γ' precipitates and much smaller (secondary and tertiary) intragranular precipitates populating their interiors [24].

- Large recrystallised grains. These grains were also first identified in [24]. These are grains which grow to far larger sizes than regular recrystallised grains. They also show distinctive precipitation, and are thought to form by a specific

mechanism during static recrystallisation, discussed further in section 2.5 [24, 32].

- T and C type γ' precipitates. These are seen inside the large recrystallised grains, and display a rectangular cross section in 2D micrographs [24]. The T type precipitates show a close to twin orientation relationship with the γ matrix. The C type precipitates are close to coherent with the matrix (coherent here meaning sharing the same crystallographic orientation) [24]. These are also discussed further in section 2.5.

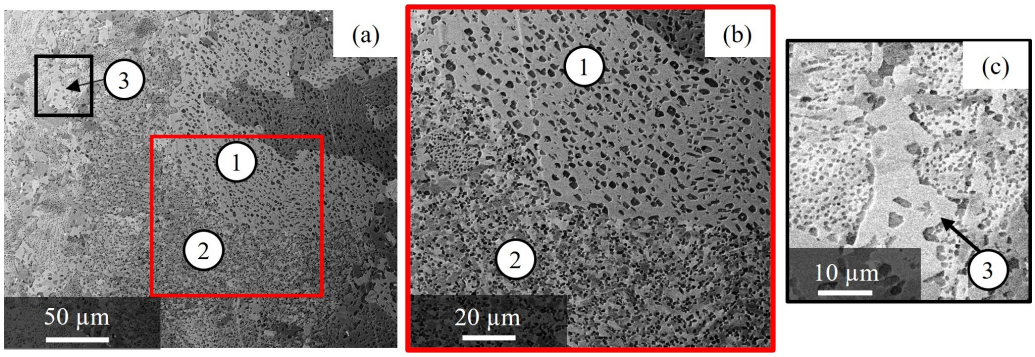


Figure 2.3: Overview of the microstructural features identified in AD730 at the intermediate stages of billet conversion (after a static recrystallisation treatment). Grain 1 is large, recrystallised and contains T type precipitates, whose rectangular cross sections are shown in (b). Grain 2 is a deformed grain, with a relatively fine and dense precipitation of primary γ'. Grain 3 is a small recrystallised grain, highlighted in (c).

Control of this microstructure is possible via suitable thermomechanical processing. Thermomechanical processing can be used to control the size and morphology of the γ' phase [12, 15] as well as the grain size and recrystallisation level of the surrounding γ matrix [25]. Thermomechanical processing can also partially control the coherency of the γ/γ' interface. This depends on the lattice parameters of the respective phases which is primarily determined by alloy composition [33]. However, precipitate size and the storage of dislocations at the γ/γ' interface can also affect coherency, and these can be influenced by thermomechanical treatments.

The following sections focus on attempts made to control AD730's microstructure, and theories suggested for the mechanisms underpinning microstructural changes. Firstly, however, there is a brief section on the thermodynamics of γ' in AD730, which is key in the design of thermomechanical treatments.

It is important to note, that the key aspects of the microstructure of AD730 which can be controlled through thermomechanical processing are not independent of one another. As an example, the effects of simultaneous γ' precipitation and recrystallisation have been investigated [22]. When γ' is sufficiently large it can pin the recrystallisation front, which proceeds by dissolving the precipitate, and reprecipitating it in its wake, i.e. on the recrystallised side. This reprecipitation has been shown to happen both continuously and discontinuously, highlighted in Fig. 2.4 [22].

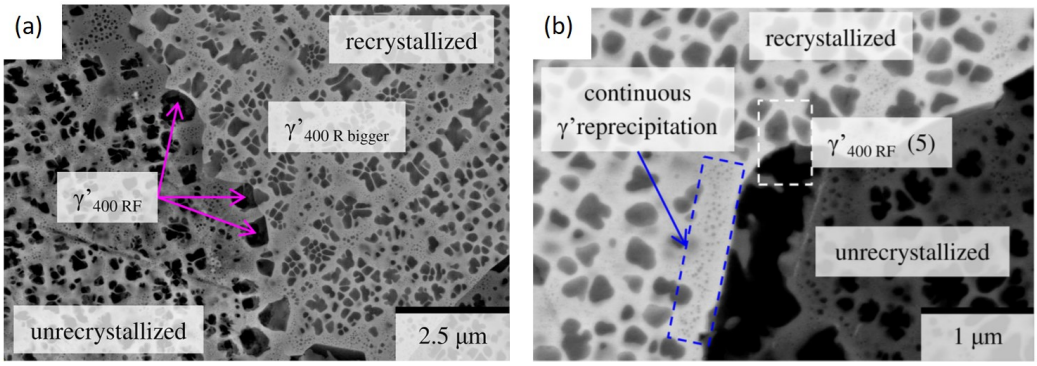


Figure 2.4: Both discontinuous (a) and continuous reprecipitation (b) are seen behind the advancing recrystallisation front in AD730. The precipitates labeled with the RF subscript are at the recrystallisation front. The subscript 400 indicates that these precipitates formed after slow cooling from super-solvus and quenching at 400 °C. The subscript R bigger refers to precipitates in a recrystallised grain which are larger than other precipitates in that grain. Figure adapted from [22].

2.3 Thermodynamics of γ' in AD730

As mentioned in Section 2.2, the γ' phase has an $L1_2$ crystal structure, with a nominal composition of $Ni_3(Al,Ti)$. This phase field is indicated in the Ni rich corner of the Ni-Al-Ti ternary phase diagram in Fig. 2.5. Of course, superalloys containing more than three alloying elements are used in reality, so the composition of the γ' phase depends on the overall composition of the alloy and the partitioning behaviour of the individual alloying elements. It has been shown that Cr, Co and Mo preferentially segregate to the γ phase, while Ti, Ni, Hf, Ta and Al segregate to the γ' phase [34].

For an alloy system with a large number of components such as AD730, it is not possible to easily visualise how the amount and composition of the phases present

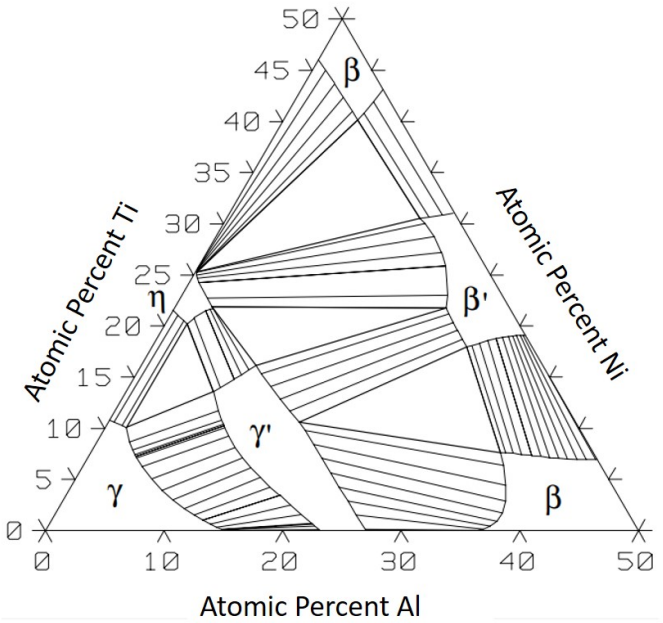


Figure 2.5: An isothermal section of the ternary Ni-Al-Ti phase diagram at 1000 °C, the dashed region between the γ and γ' phase fields indicates the compositional range over which these two phases co-exist. Figure adapted from [35].

varies as a function of temperature and alloy composition. However, some of the effects of alloying additions can be understood by considering simplified alloy systems, such as the Al-Ni-X system in Fig. 2.6. It shows that of the possible alloying elements in added to the Ni-Al system, some predominantly replace Ni atoms (e.g. Co), whereas others predominantly replace Al atoms (e.g. Ti, V, Ta).

A key parameter in understanding the microstructural evolution of AD730 during heat treatments is the γ' solvus temperature. However, there is considerable variation in reported values of the γ' solvus. The first paper published on AD730 stated that the γ' solvus was close to 1100 °C, though this value was not measured experimentally, and Thermo-Calc data provided in the work actually indicates a solvus temperatue around 1140 °C [1]. Masoumi *et al.* used Thermo-Calc to estimate the γ' solvus temperature, several years later, and obtained a much reduced value of 1090 °C. They also measured γ' solvus temperatures experimentally for 4 different heating rates [16]. The slowest heating rate employed of 10 °C/s gave a solvus temperature of 1080 °C. Faster heating, a rate of 120 °C/s, gave rise to a higher solvus temperature of 1120 °C. However, earlier work by some of the same authors gave a solvus temperature of 1099 °C at a heating rate of 2 °C/s, which would suggest the value of 1080 °C

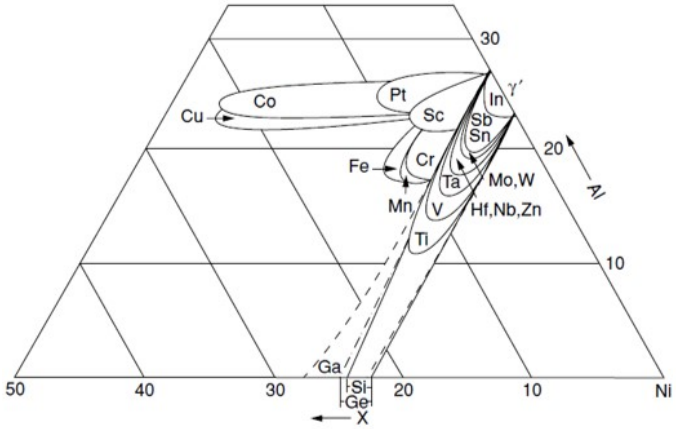


Figure 2.6: The ternary phase diagram for the Al-Ni-X system for different alloying additions X. The alloying additions which generate a phase field parallel to the Ni-X axis replace Ni atoms, whereas those that generate a phase field parallel to the Al-X axis replace Al atoms. Figure taken from [2].

at 10 °C/s is an underestimate [12]. Slower cooling rates suggest the true value of the equilibrium solvus temperature is closer to 1100 °C, with a cooling rate of 1 °C/s yielding a value of 1107 °C [12]. Alvarado *et al.* used both Thermo-calc modelling and measurement of precipitate volume fraction after 4h holds at near solvus temperatures to calculate a solvus temperature of 1108 °C [36].

The consensus seems to be to treat the solvus as being around 1100 to 1110 °C [23, 24, 37, 38]. The value of 1107 °C, which was measured at the slowest cooling rate of all reported values, seems to be the most accurate value available.

To some extent, variability in reported solvus temperatures is inevitable. Precipitate size and morphology as well as heating and cooling rates are known to influence the measured solvus temperature [39]. Additionally, the onset of precipitation is delayed with respect to dissolution, due to barriers to nucleation (i.e. interfacial energy, misfit strain energy) [39]. However, as the values quoted in Table 2.3 show, the solvus temperature for γ' in AD730 has been reported at relatively fast cooling/heating rates. For the forging of large scale billets, heating/cooling rates in the vicinity of the solvus temperature are likely to be on the order of tens of °C per hour, rather than several °C per second.

As such, work dedicated to highlighting the effect of heating/cooling rates, and γ' size and morphology on solvus temperatures may be instructive for the design of thermomechanical treatments.

Table 2.3: Table showing the range of quoted γ' solvus temperatures in AD730.

Solvus temperature / °C	Comment	Reference
1140	Thermo-Calc simulation (2012)	[1]
1099	Measured at a heating rate of 2 °C/s	[15]
1080	Measured at a heating rate of 10 °C/s	[16]
1090	Thermo-Calc simulation (2016)	[12]
1107	Measured at a heating rate of 1 °C/s	[12]
1108	Thermo-Calc simulation and isothermal heat treatments for 4hr	[36].

2.4 Control of γ' in AD730

While the composition of γ' is fairly fixed in AD730, the size distribution and morphology of γ' precipitates can be manipulated through processing parameters. This section will review what is known about the precipitation, coarsening and dissolution of γ' in AD730.

2.4.1 Precipitation

A thorough examination of the reprecipitation of γ' on cooling from sub- and supersolvus temperatures in AD730 has been conducted by Masoumi *et al.* [16]. As had been observed in other investigations, there were multiple bursts of γ' precipitation on cooling giving rise to multimodal size distributions [22]. A relatively monomodal dispersion can be achieved by employing very rapid cooling rates (e.g. through water quenching), which results in small, between 10-30 nm diameter, spherical precipitates [22]. There are no reported instances of the precipitation of γ' being suppressed via rapid cooling in AD730, and it has been estimated that the cooling rate needed to achieve this would be 5.95×10^4 °C/s [15].

Here, the classical terminology of primary, secondary and tertiary γ' is commonly used. These precipitates are highlighted schematically in Fig. 2.7. Primary γ' refers to precipitates which are large and found at grain boundaries. These typically have

rounded shapes, and sizes in the range of 1 - 5 µm. These precipitates are too large to contribute significantly to the static strength of alloys, but they can be useful in pinning grain boundaries [2]. This can also be achieved by grain boundary MC carbides and M_2B_3 borides which form at the grain boundaries, though the volume fraction of these phases is typically low. The primary γ' are only removed by extended super-solvus holds. Alvarado *et al.* showed that multiple hours at 1110 °C were required to fully remove γ' precipitates in AD730 [36]. Additionally, Seret *et al.* showed that a 2 hour and 25 minute super-solvus hold at 1125 °C didn't fully remove primary γ' in AD730 (private communication, [22]).

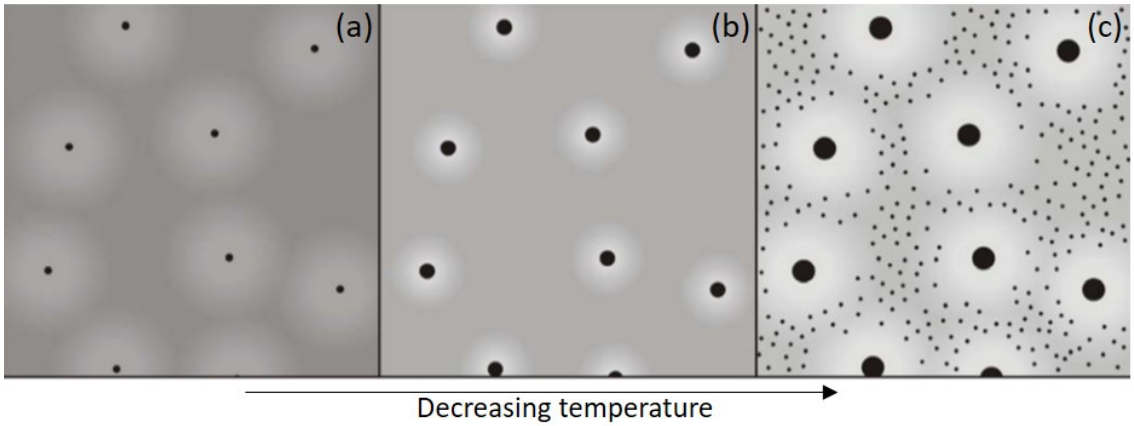


Figure 2.7: Schematic sketches illustrating the formation of a multimodal size distribution of γ' precipitates on cooling. In (a), the first population of γ' has just formed, (b) shows these precipitates after they have grown, and supersaturation has built up in the matrix, and (c) shows the second nucleation burst, leading to the formation of the second population of γ' precipitates. Figure adapted from [40].

On cooling further below the γ' solvus temperature, secondary γ' form. These are intragranular, and typically smaller than the primary γ' with sizes in the range 100 - 400 nm [41] (though precipitate size depends heavily on cooling rate). Further cooling leads to another burst of nucleation, and formation of the tertiary γ'. These are typically smaller again, with sizes in the range 5 - 50 nm. It is possible for more than three distinct bursts of nucleation to occur on cooling from super-solvus temperatures, leading to 'quaternary' precipitates. Indeed, such a population has been theoretically predicted in a Ni-based superalloy, albeit with an equivalent diameter of less than 10 nm [40].

The final distribution of γ' precipitates obtained can be rationalised by consid-

ering a balance between thermodynamic and kinetic factors. Solute supersaturation in the γ matrix is the driving force for the nucleation of new precipitates; once this is sufficiently large to overcome the surface energy associated with the formation of new precipitates, nucleation can occur. Once nucleation has occurred, further supersaturation is consumed by diffusional growth of these precipitates. The growth rate of precipitates thus depends on both supersaturation and diffusion. This can be modelled as equation 2.1 [42]:

$$\frac{dx}{dt} = \frac{S\sqrt{D}}{2\sqrt{t}} \tag{2.1}$$

Where:

$$\begin{aligned} t &= \text{time } (s) \\ x &= \text{precipitate radius } (m) \\ S &= \text{matrix supersaturation} \\ D &= \text{diffusivity of the rate limiting species } (m^2 s^{-1}) \end{aligned}$$

When temperatures become sufficiently low that atomic motion by diffusion is too slow to allow for continued precipitate growth at a rate matching the increase in equilibrium volume fraction, matrix supersaturation again begins to creep up, and eventually becomes sufficiently high to drive another nucleation burst, forming a new population of precipitates. Since these form at lower temperatures than their predecessors, atomic mobility is lower, and their growth limited by slow diffusion.

These arguments are laid out by Masoumi *et al.* in [16], and the same arguments had been made previously by Radis *et al.* when investigating the influence of cooling rate on γ' precipitation in Udimet 720 Li [40]. Radis *et al.* also observed a multimodal size distribution of γ' precipitates, and attributed this to "nucleation waves", caused by the simultaneous increase of supersaturation and decrease of diffusivity on cooling. Radis *et al.* went further and were able to model these "nucleation waves" using the MatCalc software. This simulation is noteworthy, as it predicts four nucleation bursts on cooling from a super-solvus temperature (1180 °C) to low temperatures (400 °C) at a relatively high cooling rate of 78 °C/s. However, in the experimental work by

Radis *et al.*, as in the work by Masoumi *et al.*, only three precipitate populations were observed by scanning electron microscopy. This is due to two factors; the fourth population of precipitate is only predicted to occur at cooling rates $> 10^4$ K/s, and these precipitates are predicted to be very small, i.e. approximately 1 nm radius at a cooling rate of 10^5 K/s [40].

2.4.2 Size and morphology

Given the time dependence of diffusional growth of precipitates, cooling rate will clearly be an important factor in determining precipitate size. Masoumi *et al.* provide an empirically derived formula to estimate the average diameter of the first population of γ' precipitates forming from the γ matrix in AD730 during cooling from 1200 °C down to room temperature as a function of cooling rate [16]:

$$D_{\gamma'} = 521 \times \psi^{-0.44} \tag{2.2}$$

Where:

$$D_{\gamma'} = \text{precipitate diameter } (nm)$$
$$\psi = \text{cooling rate } (^{\circ}C/s)$$

While this is a useful tool, it is based on data from only 4 cooling rates, the slowest of which is 10 °C/min, which is still fast compared to the cooling rates at the centre of a large billet in industrial forging processes.

Regarding precipitate morphology, Mullins and Sekerka analysis allows an estimate to be made of a critical radius, above which precipitates become morphologically unstable and deviate from a spherical shape. A Mullins and Sekera analysis predicts whether a spherical precipitate will deviate from its original shape by considering a balance between solute gradients, which favor the growth of perturbations (an example of the 'point effect of diffusion'), and capillarity (or surface energy), which favours a spherical morphology [43]. Using such an analysis Masoumi *et al.* estimate this critical radius for a cooling rate of 10 °C/min. They obtain a result of 78 nm, which is close to the measured size at which instabilities occur (89 nm) [16].

Mullins and Sekerka analysis may be suitable for analysing small precipitates, but it only considers surface energy and solute gradients, and not the impact of

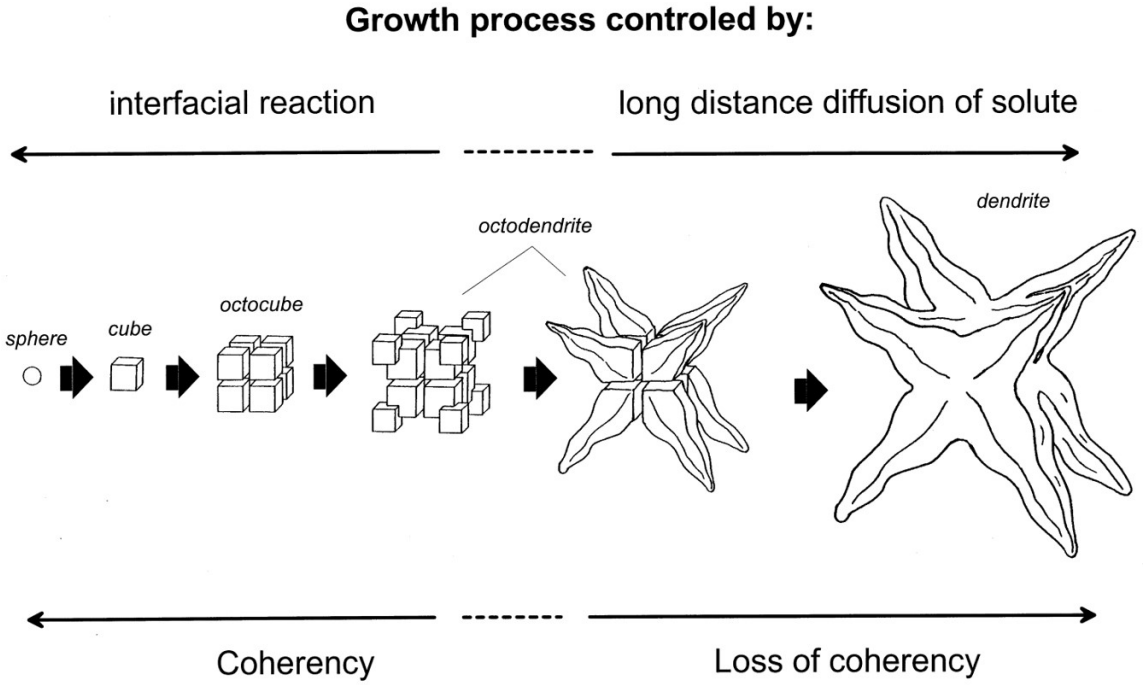


Figure 2.8: The morphological changes of γ' precipitates as they grow. Figure taken from [44].

interfacial strains, which will be important for coherent γ' precipitates, and become increasingly important with precipitate size. Ricks *et al.* were the first to identify the morphological evolution of continuous γ' precipitation, which follows the sequence spheres/cubes/octocubes/octodendrites [45]. They identified this sequence in six different alloy compositions, and it has also been described subsequently [44]. This sequence is illustrated in Fig. 2.8 and can now be well explained:

Precipitates initially form as spheres, to minimise their interfacial energy with the matrix. As they grow, since they are coherent with the matrix, strain energy builds up in the matrix and the precipitate. Since this strain scales with precipitate volume, and the interfacial energy only scales with precipitate area, the strain energy will dominate the interfacial energy beyond a critical precipitate size. As Grosdidier *et al.* point out, there are three ways this strain can be relaxed, either by local changes in composition of the two phases, with a corresponding change in lattice parameter. Or by precipitate shape changes, with growth favoured along the elastically softest directions. Finally, precipitates may lose coherency to relax the strain energy at the interface. Thus, the sphere to cube shape transition is driven by the need to reduce strain energy, and this is achieved by spherical precipitates becoming cubic.

The cubes have their edges along $\langle 100 \rangle$ directions, which are the elastically softest directions in both the matrix and precipitate phases.

The next transition is from cube to octocube, and this involves a single cube splitting to form eight smaller cubes. Clearly, such a transition increases the surface area of the precipitate(s). Cha *et al.* have modeled precipitate coarsening in 2D, accounting for interfacial energy, strain energy and solute fields, and shown that the splitting of cuboidal precipitates is driven by elastic strain energy reduction [46]. Cuboidal precipitate tend to coarsen along the $\langle 111 \rangle$ directions, which creates a concavity in the centre of the $\{100\}$ faces, where strain energy builds up, and drives the dissolution of the particle parallel to a $\langle 100 \rangle$ direction. This dissolution turns a cubic precipitate into an octocube.

Cha *et al.* point out that coarsening along the $\langle 111 \rangle$ directions is due to the greater rate of solute supply to these exposed points [46]. This has been referred to as the 'point effect of diffusion' [47, 48].

The octocube can then coarsen along the $\langle 111 \rangle$ directions, to form an octodendritic shape. Initially, the protrusions along $\langle 111 \rangle$ directions can form cubic shapes, but as coherency is lost smoother, less cuboidal surfaces form.

The above explanation of the evolution schematised in Fig. 2.8 considers continuous precipitation evolving in a matrix, with no influence of any other microstructural factors, e.g. any possible effect due to dislocation densities, or grain boundary motion during recrystallisation. Such effects will be relevant during industrial forging operations. For example, it has been shown that γ' forming across the moving recrystallisation front may develop with a particular orientation to the surrounding γ matrix in recrystallised grains in AD730 [23, 24]. Such precipitates show rectangular cross sections in 2D micrographs, and are facetted by the $\{111\}$ planes.

While the analysis of Masoumi *et al.* addresses the onset of morphological instability well, it is of limited relevance to open-die forging operations, as it doesn't address the significant morphological evolution of precipitates with prolonged thermal treatment. In an industrial forging process the precipitates will grow during sub-solvus forging operations, and the Mullins and Sekerka analysis doesn't account for several factors which will be important during this growth. For example, it does not consider the possible effects of growth along preferred crystallographic directions, either due to enhanced diffusion rates or the influence of coherency strains generated during cooling.

It is noteworthy that there is only one set of published data on lattice parameters

for γ and γ' in AD730 [49]. From the data in [49], the room temperature lattice misfit in AD730 is 0.031 %, with the γ and γ' phases having lattice parameters of 3.590 Å and 3.592 Å, respectively. This can be compared with other superalloys of similar compositions. Rene 65 has a very similar composition to AD730, and can be used to give a rough indication of the lattice parameters in AD730. The lattice parameter of the γ matrix in Rene 65 has been estimated as 3.552 Å, and the lattice parameter of primary γ' in Rene 65 has been estimated as 3.566 Å [50]. These estimates were made using the MAP_NICKEL_LATTICE program [51].

2.4.3 Coarsening

Another aspect of the development of γ' during heat treatment is its coarsening behavior. This is relevant to industrial forging processes, as small γ' precipitates strongly impede the motion of dislocations, hindering recrystallisation. The dependence of γ' strengthening on precipitate size is shown in Fig. 2.9. There are two different regimes. This is due to the fact that dislocations pass through the precipitates in pairs. At lower radii the spacing of dislocations is larger than the precipitate size, so only one of the two dislocations intersects a precipitate at a time. This is referred to as weak coupling. At larger precipitate sizes both dislocations can intersect the same precipitate. This is referred to as strong coupling. The strengthening provided by precipitates in each of these regimes is derived in [2]. The resulting equations are presented below, and plotted in Fig. 2.9.

$$\tau_{weak} = \frac{\gamma_{APB}}{2b}\left[\sqrt{(\frac{6\gamma_{APB}fr}{\pi T})} - f\right] \tag{2.3}$$

$$\tau_{strong} = \sqrt{\frac{3f}{2}}\left(\frac{Gb}{r\pi^{\frac{3}{2}}}\right)\sqrt{\left(\frac{2\pi r\gamma_{APB}}{Gb^2} - 1\right)} \tag{2.4}$$

Where:

τ = Shear stress needed for a dislocation to bypass precipitate (GPa)

γ_{APB} = Antiphase boundary energy (J/m^2)

b = Magnitude of Burgers vector (m)

f = Volume fraction of precipitates

r = Precipitate radius (m)

G = Shear modulus (GPa)

T = Dislocation line tension (J/m)

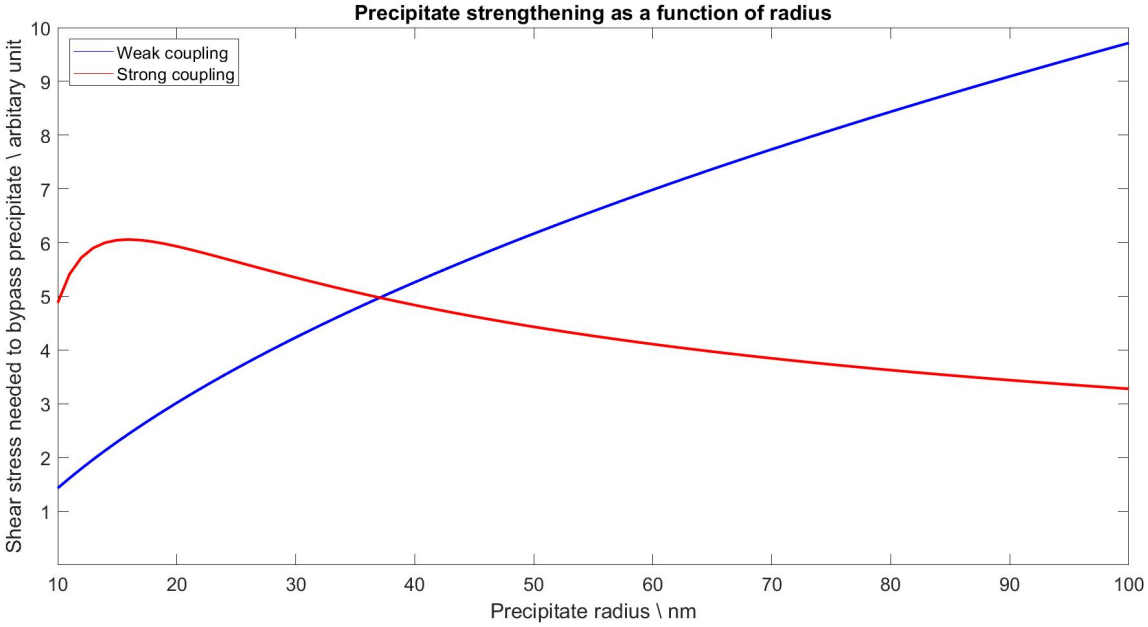


Figure 2.9: The increase in shear stress due to γ' precipitates as a function of precipitate radius. The strengthening that would be caused by both strong and weak coupling is shown, but only the lower of these is active. This means peak strengthening is achieved at the intersection of the two curves. The following values were used to generate this plot: G =80 GPa, b = 0.25 nm, γ_{APB} = 0.1 J/m^2, f = 0.3, and T= 0.5 Gb^2.

The optimum size of γ' to maximally impede dislocations is alloy dependent (for example it is in the range 26-30 nm for PE16 and in the range 55-85 nm for Nimonic 105 [2]), but corresponds to very small sizes, in the 10's of nanometers. Controlling

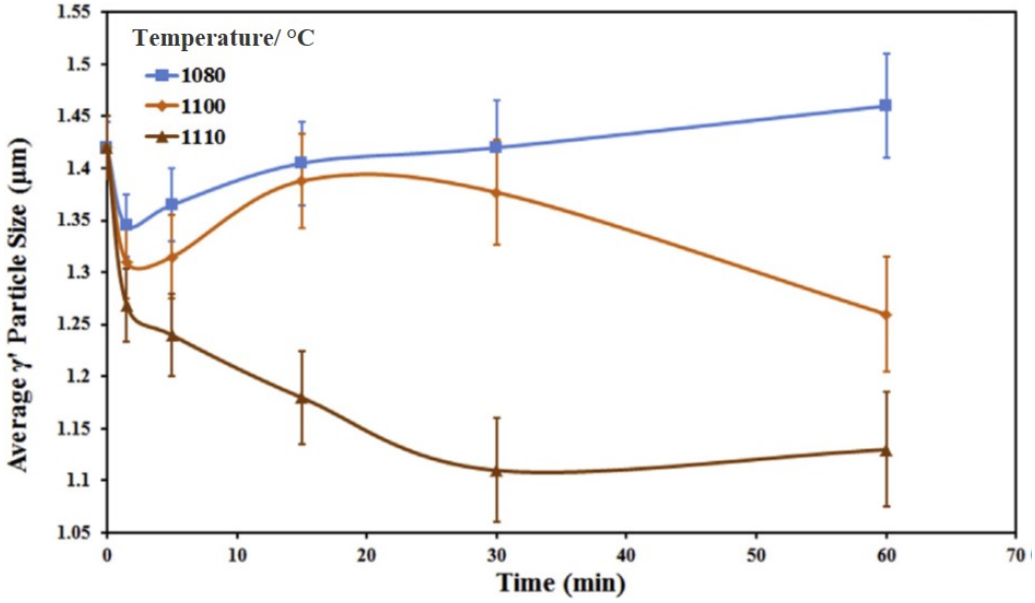


Figure 2.10: Plots of the evolution of primary γ' precipitate size over one hour of coarsening for three different coarsening temperatures. It is striking that small changes in coarsening temperature can have a dramatic effect on coarsening behavior. Figure adapted from [12].

the coarsening of γ' to achieve higher precipitate sizes increases forgeability.

The coarsening and dissolution behavior of γ' around its solvus temperature in AD730 has been studied comprehensively by Masoumi *et al.* in 2015 [12]. This revealed that the dissolution behaviors of primary, secondary and tertiary γ' were dramatically different, as the solvus temperatures for these precipitates were found to be roughly 1100 °C, 800 °C and 600 °C, respectively. The primary precipitates had an average radius of 1.4 µm, the secondary 30 nm and the tertiary 8 nm. This suggests that control of the secondary and tertiary precipitates could be achieved by relatively low temperature heat treatments. The large gaps between solvus temperatures for the different precipitates mean that heat treatments and forging operations performed around the solvus temperature of the primary γ' rapidly dissolve all the secondary and tertiary precipitates.

It was shown that extended holds around the primary γ' solvus temperature (1100 °C), following rapid (20 °C/s) heating from room temperature, can lead to either an increase or a decrease in the average size of γ' precipitates, depending on the exact temperature and duration of the hold. For example, 1 hour at 1080 °C led to an increase in γ' precipitate size, whereas 1 hour at 1100 °C caused a decrease

in γ' precipitate size [12], both occurring while the overall volume fraction of γ' fell. This behavior is illustrated in Fig. 2.10

This large change in behavior due to relatively small changes in temperature may at first seem surprising, but it can be rationalized by considering the competing effects of dissolution and coarsening. The former tends to remove and shrink precipitates, while the latter leads to an increase in the size of precipitates. It is worth noting that coarsening can occur via either Ostwald ripening [52] or agglomeration, though it has been shown in AD730 that agglomeration is by far the dominant mechanism. A separate investigation by Masoumi *et al.* found that 97 % of particle growth was due to agglomeration, and only 3 % accounted for by Ostwald ripening [12]. At higher temperatures (1100 °C), dissolution is dramatically accelerated compared with agglomeration, and so dominates, leading to an overall reduction in precipitate size. This dramatic dependence of dissolution rate on temperature has been noted in other Ni-based superalloys. Semiatin *et al.* showed that a 27 °C increase in dissolution temperature, from 1177 °C to 1204 °C, increased the dissolution rate by a factor of 4 in a study on the superalloy LSHR (which stands for low solvus high refractory). This was rationalized by pointing out that both diffusivity and the driving force for dissolution are being increased as temperature increases [53]. These results suggest that quite accurate temperature control is needed to control the γ' size distribution in AD730, and that temperature variation across a large part could lead to different microstructures in different regions. This would especially be the case during the first stages of open die forging, when temperatures are close to the solvus temperature.

Given this interplay between dissolution and coarsening, it would have been more useful for precipitate size distributions to be presented, rather than just mean precipitate radius to be shown in [12]. This could have shown simultaneously to what extent the change in mean radius was due to larger precipitates growing (through agglomeration and coarsening) and to what extent it was due to smaller precipitates dissolving. Additionally, it would have allowed the variance in precipitate size to be assessed.

As well as being very temperature sensitive in the near solvus region, the coarsening and dissolution of γ' in Ni-based superalloys can also be significantly affected by prior deformation. While the study by Masoumi *et al.* provides detailed and quantitative insights into the coarsening and dissolution of γ' precipitates in grains with low stored energy, it doesn't indicate how these processes differ in deformed (i.e.

unrecrystallised) regions. This is of course important information when designing thermomechanical treatments. Semiatin *et al.* illustrated that an anneal to remove dislocation sub-structure from an as-received sample of LSHR led to a significant reduction in the dissolution rate of γ' during a subsequent super-solvus hold. This was attributed to enhanced diffusion through the dislocation sub-structure. This is a well-supported explanation, since a mechanism by which dislocation build up around a γ' precipitate can cause enhanced diffusion of chromium and cobalt has been provided by Kontis *et al.* [54]. Chromium has been identified as the solute limiting the rate of dissolution of γ' [53].

The effects of dislocation sub-structure on the coarsening behavior of γ' in AD730 were also noted by Seret *et al.*, when investigating the microstructural evolution of AD730 following dynamic recrystallisation [22]. γ' precipitates were formed on cooling after a super-solvus dynamic recrystallisation hot compression test [22]. Horizontal bands of γ' precipitates with larger than average sizes were observed. Their morphology in the micrographs presented by Seret *et al.* indicates that they may have grown via agglomeration (see Fig. 2.11), and it is suggested that their large sizes are due to enhanced diffusion enabled by retained dislocation substructure from the prior deformation. This is in line with the observations of Masoumi *et al.* that coarsening primarily occurs via agglomeration [12], and those of Kontis *et al.*, that dislocations can enhance the rate of rafting/agglomeration in Ni-based superalloys. However, while this explanation has theoretical support, it was not possible to show that the density of geometrically necessary dislocations in these horizontal bands

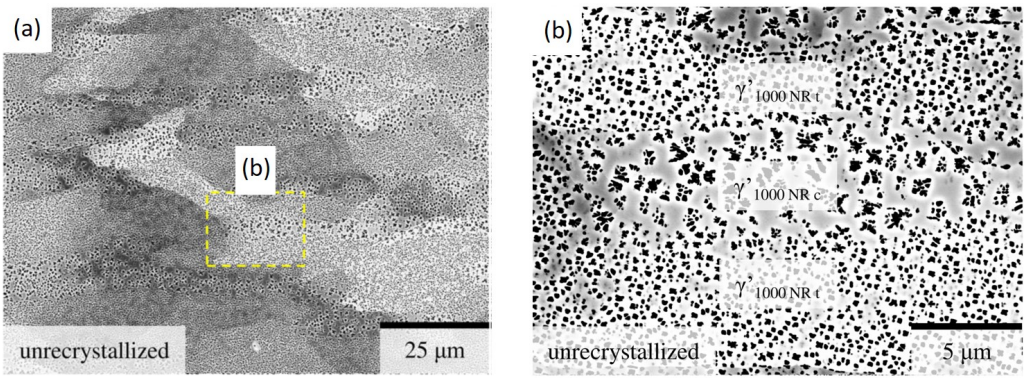


Figure 2.11: Micrographs adapted from [22] showing the horizontal bands of coarse precipitates whose formation was attributed to higher local dislocation densities (a), and a higher magnification image (b) indicates that these may have grown by agglomeration.

was higher than elsewhere in [22].

2.4.4 Splitting

As well as the extensive work done on the coarsening and dissolution of γ', discussed above, there have also been investigations into the splitting up of γ' precipitates (i.e. the reverse of agglomeration) in Ni-based superalloys [55, 56]. This effect can occur via the precipitation of γ particles within pre-existing γ' on cooling.

This may be observed for one of two reasons. Firstly, it is possible that splitting one γ' particle into two smaller particles is energetically favorable due to an elastic interaction between the two particles formed by splitting (if the precipitates are coherent with the matrix). This explanation is possible in the case when the volume fraction of γ' is low, and precipitates are widely spaced [55]. However, in the case where there is a high volume fraction of γ', this splitting is explained simply by the need to attain the equilibrium volume fraction of the γ phase. Usually this occurs when heating to the γ' solvus temperature, where the equilibrium volume fraction of γ grows. Here, the nucleation of γ within the existing γ' help increase the volume fraction of γ towards the equilibrium value.

In alloys with an abnormal γ' solvus, i.e. one such that the volume fraction of the γ phase increases on cooling, within a certain temperature range below the γ' solvus, splitting of γ' occurs on cooling rather than heating, giving a hierarchical microstructure containing small γ precipitates within the γ' precipitates at room temperature. The controlled formation of hierarchical microstructures in Ni-based superalloys is being investigated as a way of controlling the coarsening of γ' [56].

While AD730 does not display the abnormal solvus behavior, significant amounts of splitting have been observed during dissolution [12]. An example is shown in Fig. 2.12. Alongside dissolution and coarsening, this splitting behavior is a third effect which influences the size distribution of γ' precipitates obtained during prolonged holds at elevated temperatures, and further shows why there can be significant differences in the size evolution of precipitates during holds at similar sub-solvus temperatures, as shown in Fig. 2.10.

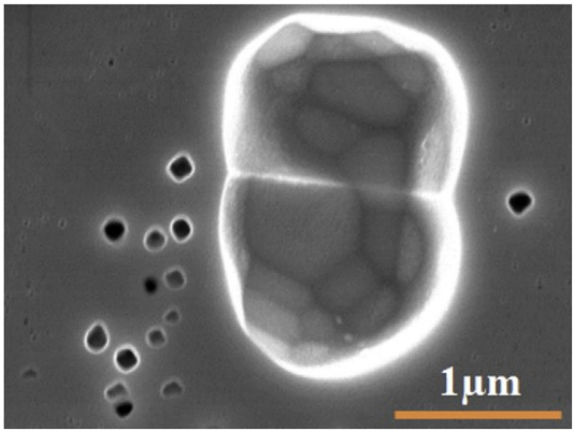


Figure 2.12: Splitting of a γ' precipitate in AD730. Figure taken from [12].

2.5 Control of γ in AD730

Alongside the work done to understand the behavior of γ' in AD730, attention has also been paid to controlling the γ matrix, in terms of recrystallisation level and grain size achieved via forging. Here, the aim is to achieve a uniform, relatively small grain size (with radii on the order of 20 µm for a billet, and around 10 µm for a turbine disc), in a fully recrystallised microstructure. The thermomechanical treatment performed to attempt to achieve this during open-die forging consists of several steps, as mentioned in Chapter 1, section 1.2. In practice, unrecrystallised grains persist after open-die forging [26].

The unrecrystallised grains present in AD730 after an industrial forging have been shown to be large, and contain a fine and dense precipitation of primary γ' [23, 24, 26]. An example microstructure showing these large unrecrystallised grains is shown in Fig. 2.13. The unrecrystallised grains are elongated in the vertical direction of the micrograph, which is parallel to the billet direction, with lengths on the order of 100 µm and widths on the order of 40 µm. These have been dubbed 'recovered' grains. They present a serious problem; turbine disk manufacturers require uniform microstructures in billet material. The final microstructure in disks must be homogeneous, and there is limited scope to achieve this after the billet has been produced.

Having serious inhomogeneity in the grain size distribution presents difficulties during ultrasonic testing. Ultrasonic testing is a non-destructive testing method that can be used to detect small internal flaws in alloys. Grain size, relative to the

wavelength of the ultrasonic signal, affects the nature of attenuation [57].

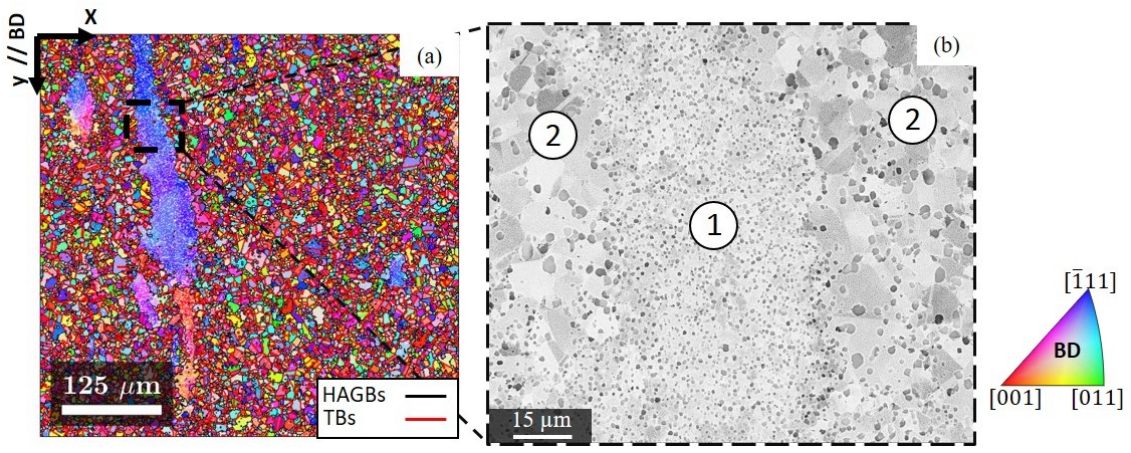


Figure 2.13: An IPF map coloured along the billet direction (BD) (a) and a corresponding BSE image (b) of AD730 billet material. The unrecrystallised/recovered grains in (a) can be identified by their internal misorientations. The overall size of the unrecrystallised/recovered grains relative to the recrystallised grains is evident in (a), and the different precipitation in the two types of grain is highlighted in (b). In (b) the large unrecrystallised grains are labeled as 1 and the regions of smaller recrystallised grains are labeled as 2.

2.5.1 Large recrystallised grains and their precipitates

While the formation mechanism of the recovered grains is as yet unknown, their interaction with recrystallised grains growing during laboratory scale forging has been studied [24, 32]. It was shown that certain recrystallised grains were able to grow into and consume neighboring recovered grains during static recrystallisation. Interestingly, recrystallised grains which shared a $\langle 111 \rangle$ axis with the neighbouring recovered grain grew into the recovered grain to a significant extent, despite the dense γ' precipitation present [24]. This effect is highlighted in Fig. 2.14. These recrystallised grains become far larger than other recrystallised grains. They will henceforth be referred to as "large recrystallised grains".

It was suggested that this orientation relationship (a shared $\langle 111 \rangle$ axis between the recovered grain and the growing recrystallised grain) led to large recrystallised grains due to possibility of γ' dissolution and reprecipitation by the recrystallisation front. Vernier *et al.* [24] pointed out that recrystallised grains growing with no

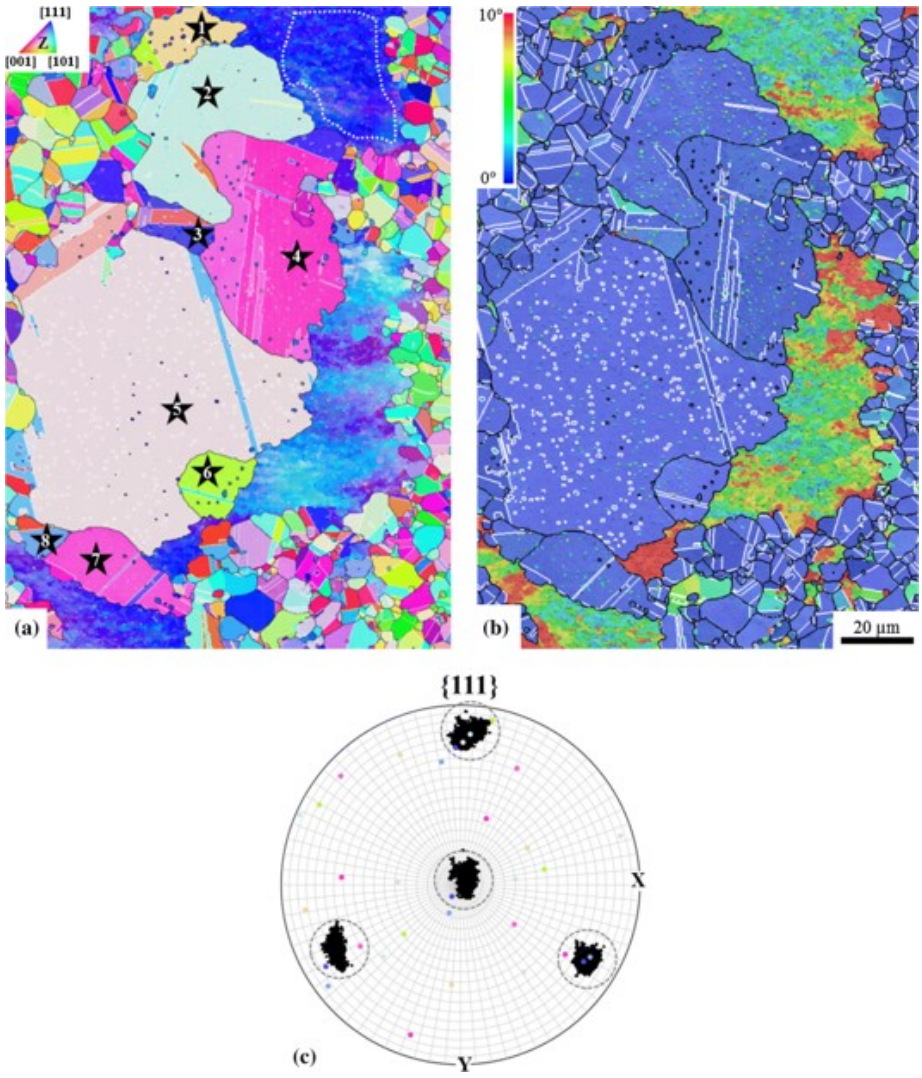


Figure 2.14: Recrystallised grains sharing a ⟨111⟩ axis with the nearby deformed grain it grows into have been shown to grow to much larger sizes than other recrystallised grains. The orientation map (a) shows eight recrystallised grains. The map in (b) shows the misorientation of each pixel with respect to the mean orientation of the grain containing it, allowing deformed grains to be identified. The {111} pole figure from the area inside the white dotted line in the deformed grain in the top right of maps (a) and (b) is shown by the black dots in (c), along with the {111} poles from the numbered grains in (a), which are shown in the same colour as the colour the grains have in (a). It can be seen that the 8 numbered grains have a ⟨111⟩ axis close to that of the deformed grain (with the exception of grain 1). Figure taken from [24].

particular orientation relationship to the recovered grain which they consume do not grow to large sizes, and end up with γ' precipitates at their grain boundaries. Such

grains are shown in Fig. 2.15 (a).

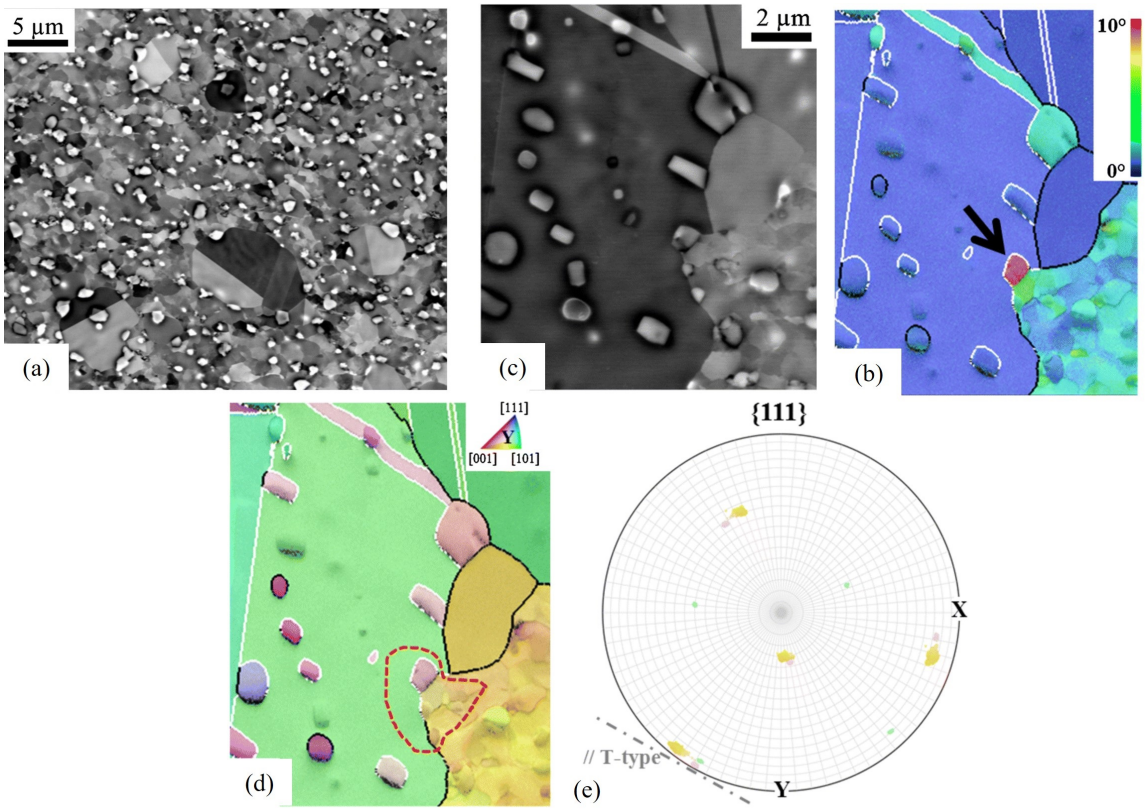


Figure 2.15: Two of the important microstructural behaviors of AD730 observed in [24]. (a) Shows many small recrystallised grains, which have not grown large, and have γ' precipitates pinning their boundaries. The next four images, (b) – (e) show a γ' precipitate forming across the recrystallisation front. The misorientation to mean map (c) shows the grain on the right side of the boundary to be highly deformed, while the grain on the left of the boundary is not. The $\{111\}$ pole figure (e) shows the precipitate shares a single $\langle 111 \rangle$ axis with both the deformed and non-deformed grain, making it a T type precipitate. Figure adapted from [24].

It is suggested in [24] that this occurs as follows: A recrystallised grain nucleates and begins to grow into a neighbouring deformed grain (reducing stored energy). As it grows, its boundary encounters γ' precipitates which it dissolves. As the concentration of γ' forming elements in the boundary increases, the boundary is slowed by solute drag. Eventually, the boundary, supersaturated with γ' forming elements, encounters precipitates which it can't dissolve, and is pinned. Aided by accelerated diffusion along the recrystallisation front, the γ' forming elements stored in the recrystallisation front feed these pinning particles, giving rise to a small recrystallised

grain with relatively large precipitates at its boundary, as is observed.

However, when the recrystallised and recovered grains do share a $\langle 111 \rangle$ axis, a different observation is made. Here, γ' precipitates are seen to form at the recovered/recrystallised boundary (see Fig. 2.15 (b)-(d)), and the recrystallised grain keeps growing, so that it does show intragranular precipitation in the final microstructure, unlike the small recrystallised grains. These intragranular precipitates are either a few degrees away from having a twin orientation with the recrystallised grain in which they form, or a few degrees away from sharing the orientation of the grain in which they form. These two types of precipitate have been dubbed T and C type, respectively. The key properties of these precipitates can be summarized as follows:

- T and C type precipitates form in recrystallised grains which share at least one $\langle 111 \rangle$ axis with the recovered grain which they consume as they grow.
- T type precipitates have an orientation a few degrees away from a twin orientation with the recrystallised grain they appear in, whereas C type precipitates have an orientation a few degrees away from matching that of the recrystallised grain in which they appear.
- Both T and C type precipitates are facetted by the $\{111\}$ planes, and show rectangular cross sections in 2D electron microscope images, with their long sides parallel to the $\{111\}$ planes (the morphology of these precipitates will be detailed further in Chapter 8).
- Both T and C type precipitates have been observed to form at the interface between recrystallised and recovered grains, sharing a $\langle 111 \rangle$ axis with each.

Vernier *et al.* suggest that it is interfacial energy which controls the precipitation of the T/C type precipitates. Since they are large and incoherent, misfit dislocations must form at the interface, relaxing the elastic strain, meaning elastic strain energy is not an important consideration in their formation, and interfacial energy takes over as the main barrier to precipitation. Since $\langle 111 \rangle$ twist boundaries are low energy interfaces in FCC materials, precipitation occurring across the recrystallised/recovered interface can be energetically favorable, if the precipitate can (approximately) share a $\{111\}$ axis with both grains. The energy of $\langle 111 \rangle$ twist boundaries as a function of misorientation angle has minima at 0° and 60°, corresponding to C and T type precipitates respectively [24].

The arguments set out by Vernier *et al.* explain two of the key experimental observations they make regarding the formation of large recrystallised grains and T/C type precipitates. Firstly, the shared {111} axis between large recrystallised grains and nearby recovered grains (shown in Fig. 2.14), and secondly the observation that T/C type precipitates form at the interface between large recrystallised grains and recovered grains (shown in Fig. 2.15). However, there are still some unanswered questions. As the authors point out [24], it is surprising that we don't see precipitation occurring behind the moving recrystallisation front, as this is what is expected when the moving boundary dissolves the encountered precipitates [58]. Indeed, matters are confused further by the fact that both continuous and discontinues precipitation behind the moving recrystallisation front were reported in [22] (see Fig. 2.4).

It is unclear why reprecipitation sometimes occurs at the interface between recovered and recrystallised grains, leading to the formation of T/C type precipitates shown in Fig. 2.15 [24], sometimes occurs behind the recrystallisation front (as shown in Fig. 2.4 [22]) and in other cases does not occur at all (as was argued to explain the small recrystallised grains with precipitates at their boundary shown in Fig. 2.15 [24]).

Regarding the first of these three different modes of reprecipitation, it is clear that a necessary condition for the formation of T/C type precipitates is a shared $\langle 111 \rangle$ axis between the growing recrystallised grain and the recovered grain it is consuming. So this shared $\langle 111 \rangle$ axis will be a necessary condition for C/T type precipitation to occur at the interface between recovered and recrystallised grains. When this condition is not fulfilled, it isn't clear what factors determine whether reprecipitation will happen behind the moving front or not.

Recrystallised grains sharing a $\langle 111 \rangle$ axis with the recovered grain which they consume could have nucleated via continuous recrystallisation or heteroepitaxial recrystallisation (HERX), as these both give rise to sub-grains with an initial orientation close to that of the recovered grain in which they form. HERX has been relatively recently discovered as a recrystallisation mechanism in Rene 65 [59]. This mechanism has subsequently been shown to operate in other low mismatch Ni-based superalloys [60].

Discontinuous recrystallisation, on the other hand, involves distinct nucleation and growth stages. Nucleation has been shown to occur at grain boundaries during discontinuous recrystallisation, with the nucleated grains having a high misorienta-

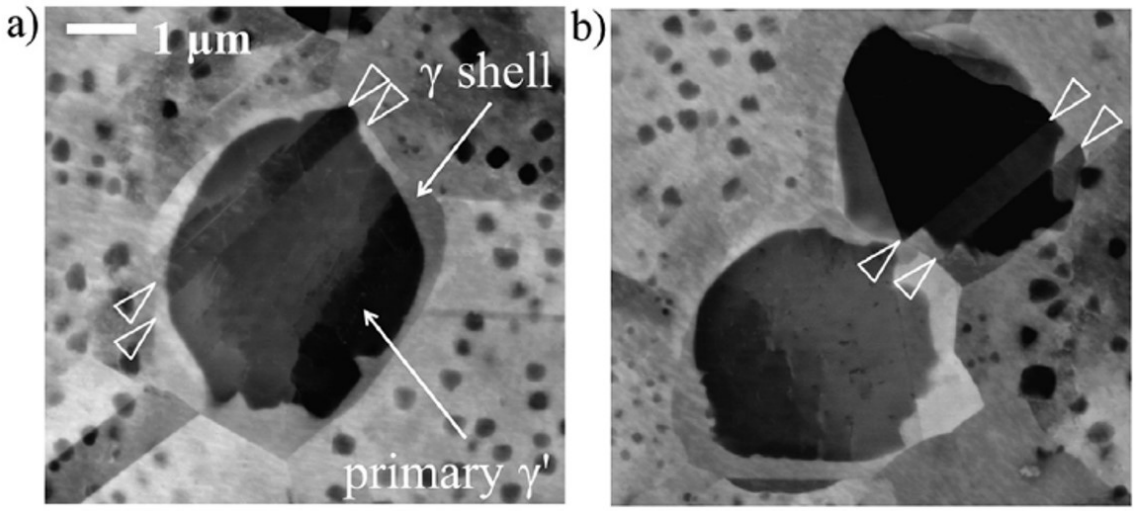


Figure 2.16: Illustration of the onset of the HERX mechanism. A coherent shell of γ forms round the edge of a γ' precipitate (a). (b) Illustrates that twin boundaries are continuous across the interface between precipitate and γ shell, highlighting their coherency. Figure taken from [59].

tion angle with respect to the grain whose boundary they nucleate upon [61], i.e. not giving recrystallised grains with an orientation close to that of surrounding grains. This gives rise to a characteristic "necklace" microstructure. Continuous recrystallisation differs in that it occurs continuously, i.e. not involving distinct nucleation and growth stages. Various mechanisms have been proposed for continuous recrystallisation, but in all cases misorientation develops gradually, so that at least initially, the new grain has an orientation close to that of the deformed grain in which it forms [62]. The same principle is true for HERX, where a recrystallised grain forms on the rim of a precipitate, in a region enriched in γ forming elements, and depleted of γ' forming elements. This γ shell has the same orientation as the γ' precipitate round which it forms. It is noteworthy that the terms continuous and discontinuous refer 'only to the spatial and temporal heterogeneity of microstructural evolution, and [imply] no specific mechanism of recrystallisation' [63], although continuous and discontinuous recrystallisation are often referred to as mechanisms.

2.5.2 The formation of recovered grains

While there is a relatively well detailed explanation for the formation of large recrystallised grains, which can grow into and consume the recovered grains (i.e. large un-

recrystallised grains) under certain conditions, the formation of the recovered grains is less understood. It is worthwhile to investigate the cause of these recovered grains, with a view to finding a thermomechanical route to avoid their formation. The formation of these grains is both an academically and industrially relevant question, as there are no suggestions in the literature as to how they form. As discussed previously, large unrecrystallised grains should not be present in billet material, as this material is required to have a homogeneous microstructure and they complicate ultrasonic inspection. As such, the presence of such grains in billet material could limit the industrial usage of AD730. An understanding of the origin of the recovered grains is needed in order to prevent their formation.

Despite the lack of dedicated research on the cause of these unrecrystallised grains, it is possible to suggest three potential mechanisms by which these large, unrecrystallised grains with dense and relatively fine precipitation (compared to primary precipitates found anywhere else in the microstructure) might appear in the billet microstructure:

1. super-solvus forging may not be creating a fully recrystallised microstructure. As such, some large grains will be inherited from super-solvus forging. A high dislocation density in these large grains would affect the precipitation of γ'. The start temperature of precipitation would be higher, due to elastic relaxation as precipitation occurs [22], there would also be a higher density of nucleation sites, giving rise to the higher density of precipitates seen in these grains. The growth of precipitates may be accelerated due to pipe diffusion through dislocation cores, though no evidence was found for this in the thesis of Anthony Seret [64]. Once precipitation has occurred, it is very difficult to recrystallise these grains during sub-solvus forging, due to the high density of precipitates hindering dislocation and subgrain boundary motion.

2. The formation of such grains may be linked to chemical segregation inherited from solidification of the alloys. This segregation would have to have survived homogenisation. The composition of recrystallised and unrecrystallised grains has been measured in AD730 (using EDS) following sub-solvus forging to three different strain levels, and no consistent difference was found [25]. In the thesis of Suzanne Vernier, a large billet was forged (with a diameter of 640 mm, rather the 500 mm diameter which is typical in the industrial forging process). This did show some segregation between dendritic and inter-dendritic regions,

with the interdendritic regions having a slightly higher concentration of the γ' forming elements. However, the degree of segregation was quite small (at most 0.6 %) as compared with the precision of the EDS technique used to measure it [32]. It is thus worthwhile to examine the possible role of remnant chemical segregation in affecting precipitation and subsequently recrystallisation during open die forging.

3. Large recrystallised grains growing during sub-solvus forging containing T/C type precipitates (i.e. the large recrystallised grains) may become the recovered grains. These grains would grow and precipitate γ' in the way described by Vernier *et al.* in [24] during static recrystallisation. The large recrystallised grains have low stored energies as they form statically, rather than dynamically, which may mean large unrecrystallised grains recrystallise faster (i.e. at lower strain levels) during subsequent forging.

All 3 hypotheses involve 'special' precipitation occurring in relatively large grains. Under hypothesis 1, dense precipitation occurs in deformed grains, assisted by their high dislocation density. Under hypothesis 2, precipitation heterogeneity would be related to chemical segregation. Under hypothesis 3, T/C type precipitates form in recrystallised grains which share a $\langle 111 \rangle$ axis with the recovered grain they consume.

2.5.3 Comparison with other Ni-based superalloys

While the mechanisms discussed regarding the formation of large recrystallised grains and 'recovered' grains in this section have been looked at in the context of AD730, similar processes can happen in other low lattice mismatch Ni-based superalloys.

The formation of large recrystallised grains which share a $\langle 111 \rangle$ axis with a nearby recovered grain, containing C/T type precipitates, was also shown to happen in PER 72 and Rene 65 [24]. However, these large recrystallised grains with C/T type precipitates have not yet been observed in any other Ni-based superalloys.

Regarding the recovered grains, given that their formation mechanism is unknown, it is not possible to know under what conditions we should expect to find them in other alloys.

A couple of studies have indicated that super-solvus forging doesn't necessarily lead to full recrystallisation, and that the unrecrystallised grains have an elongated shape similar to the 'recovered' grains in AD730, reflecting the overall change in

billet shape. For example Lin *et al.* forged a 'typical' Ni-based superalloy (based on the composition given for this alloy, it was very likely Inconel 718), and elongated, unrecrystallised grains were seen under certain forging conditions [65]. Such grains were more common at lower forging temperatures (920 °C) than at higher forging temperatures (980 °C), and also more common when deformation was done at higher strain rates ($0.1\ s^{-1}$) than when it was done at lower strain rates ($0.001\ s^{-1}$).

This second observation, that lower strain rates give higher dynamically recrystallised fractions during super-solvus forging, has also been made by Xie *et al.* [66]. By subjecting the superalloy 718Plus to various different super-solvus forging conditions, they showed that full dynamic recrystallisation could be obtained (even with a relatively low strain level 0.69), provided strain rates of $0.01\ s^{-1}$ or less were used. When a higher strain rate of $0.1\ s^{-1}$ was used, dynamic recrystallisation was incomplete, and large unrecrystallised grains were present in the microstructure. These had an elongated shape similar to that shown by the 'recovered' grains in AD730. The exact effect of strain rate on recrystallisation level will be discussed in more detail in section 2.6.1.

The observations from both of these studies are inline with the predictions of hypothesis 1, as they show that super-solvus forging is not creating a fully recrystallised microstructure, and elongated unrecrystallised grains which could go on to become the 'recovered' grains during subsequent forging, are present. These grains are shown in Fig. 2.17. However, the studies mentioned above did not look at how precipitation evolved in the recrystallised and unrecrystallised grains, nor how the microstructure evolved further due to sub-solvus forging. Both of these would have to be explored to see if these unrecrystallised grains go on to become similar to the 'recovered' grains in AD730.

In order to reach the goal of avoiding the formation of recovered grains, the influence of forging process parameters (strain, strain rate, temperature) on microstructure should be well understood. The next section of this review will focus on how these process parameters are known to influence the outcome of forging operations.

2.6 Forging process parameters

Forging process parameters determine the microstructure achieved in the billet at the end of forging. The parameters discussed here (strain rate and temperature, strain,

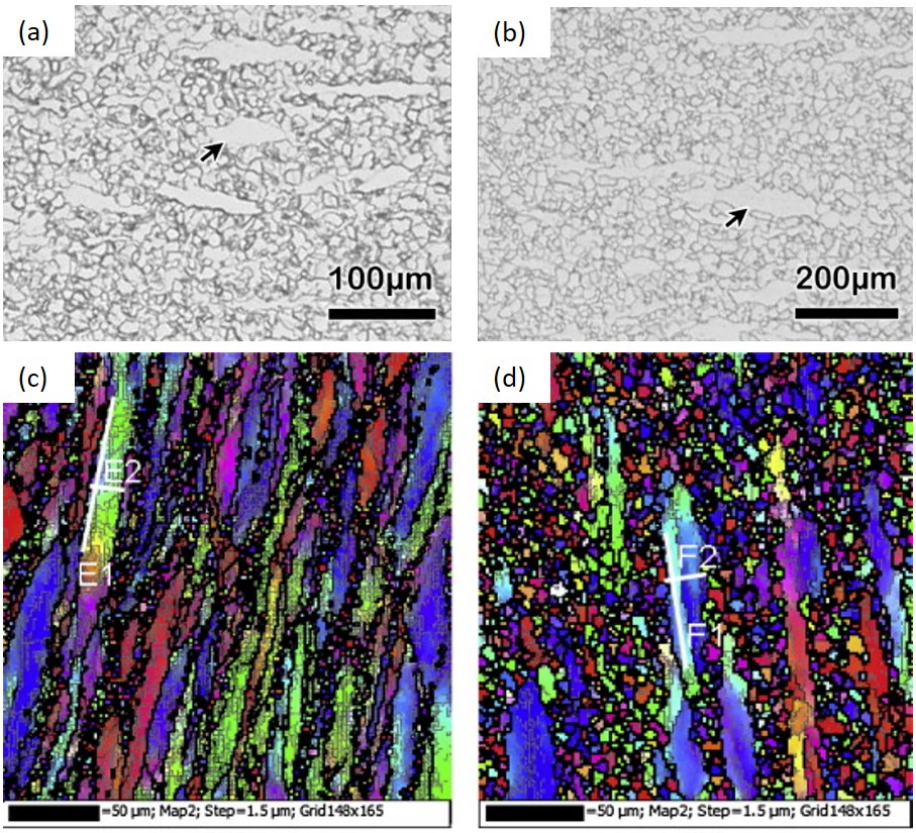


Figure 2.17: Microstructures showing incomplete dynamic recrystallisation after super-solvus forging. (a) and (b) show optical micrographs of IN718 forged at 1100 °C and 1140 °C respectively, with the unrecrystallised grains indicated by the arrows (figures taken from [65]). (c) and (d) show IPF maps of 718Plus forged at 920 °C and 980 °C respectively (figures taken from [66]).

and initial microstructure) are all mutually inter-dependent, as the effect of varying one depends on the other two. They are all also dependent on temperature, through its effect on microstructure, and its providing the energy for thermally activated processes.

2.6.1 Strain rate and temperature

In determining the rate of dynamic recrystallisation, it's clear that both strain rate and temperature are important. When deforming to a fixed strain, the strain rate determines how long dynamic processes have to occur, and temperature controls how fast they occur (provided they are thermally activated). Temperature, heating rates and holding times also affect recrystallisation through their effect on grain

size, precipitate size and precipitate volume fraction. Such microstructural effects will be discussed in section 2.6.3. Strain rate does not just influence the rate of recrystallisation, as will be discussed, it also controls the nature of recrystallisation. Notably, strain rate affects the level of dislocation density introduced during forging to a particular strain level, and thus the energetic driving force for recrystallisation.

The effect of strain rate during forging, rather than just total strain level has not been considered in AD730 specifically. However, strain rate has recently been shown to affect the type (i.e. dynamic or post-dynamic) and extent of recrystallisation occurring in the Ni-based superalloy Inconel 718 [67].

After hot deformation the total recrystallised volume is made up of dynamically and post-dynamically recrystallised grains (strictly, the post-dynamically recrystallised grains are not present immediately after deformation, but can form within seconds after). Dynamically recrystallised grains form dynamically, i.e. during forging. Post dynamically recrystallised grains form after forging, e.g. in the experimental delay between forging and water quenching a lab scale sample. Post-dynamically recrystallised grains have slightly lower dislocation contents than dynamically recrystallised grains; this slight difference in dislocation contents can be used to distinguish between the two types of grain in EBSD data [68].

The amount of each type of recrystallised grain can vary depending on strain rate. While it had previously been thought that there existed a "critical strain rate", above which increasing strain rate gave higher amounts of dynamic recrystallisation, and below which increasing strain rate gave lower amounts of dynamic recrystallisation (for example [69, 70]. In [67] it was shown that the extent of *dynamic* recrystallisation decreases monotonically with strain rate (in the range [0.001:1] s^{-1} for Inconel 718 forged to a strain of 0.7 at 980 °C). This is simply due to there being less time in which dynamic recrystallisation can occur, if deformation is performed to a given strain. Post-dynamic recrystallisation, on the other hand, can be accelerated by higher strain rates. There are two reasons for this; firstly, an increase in adiabatic heating with increasing strain rate, and secondly an increase in stored energy due to increased dislocation densities being generated by deformation at higher strain rates. The effect of strain rate on the relative amounts of dynamic and post-dynamic recrystallisation is shown in Fig. 2.18.

The adiabatic heating caused by higher strain rates was argued to be the main driver of the increased amounts of post dynamic recrystallisation occurring with increasing strain rates in [67], as opposed to the increased dislocation density caused

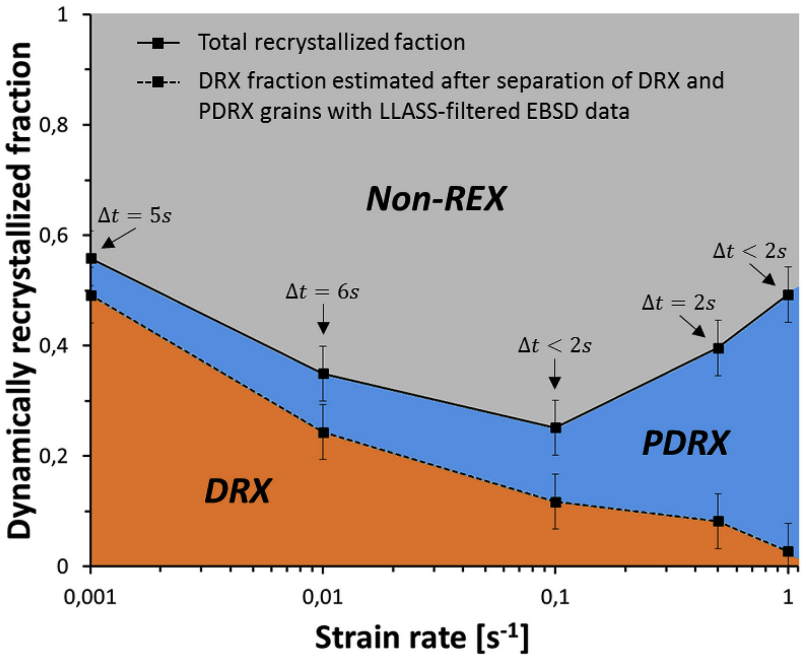


Figure 2.18: Graph showing the influence of strain rate on the extent of PDRX and DRX in the alloy IN718, forged at 980 °C to a strain of 0.7. The various values of Δt indicate the experimental delay between forging and quenching for each data point. Figure taken from [67].

by higher strain rates. A reason for this is that adiabatic heating leads to accelerated recovery, which in turn lessens the increase in dislocation density caused by the forging operations studied. This adiabatic heating could potentially also affect any precipitates present, particularly during sub-solvus forging close to the solvus temperature, where adiabatic heating could push the sample over the solvus temperature, leading to dissolution of precipitates. Indeed, dissolution of the δ phase in Inconel 718 due to this adiabatic heating was observed in [67].

Overall, the results from [67] seem to indicate that a low strain rate (≈ 0.001 s^{-1}) offers two important advantages. Firstly, it led to the highest total recrystallised fraction, working to a defined strain of 0.7. Secondly, it presents the lowest amount of adiabatic heating, allowing more exact control of the sample's temperature and hence precipitate distribution during deformation.

The effect of strain rate on dynamic recrystallisation was also considered in a recent investigation involving a γ- γ' powder metallurgy Ni-based superalloy [71]. This investigation also showed that low strain rates lead to higher levels of recrystallisation, after comparing strain rates of 0.001, 0.01, 0.1 and 1 s^{-1} at sub-solvus

temperatures. This was again attributed to the extra time available for dynamic recrystallisation at lower strain rates, in agreement with [67].

The results in [67] are quite important, in that they shed light on the real effect of strain rate on dynamic and post-dynamic recrystallisation, and underline that strain, strain rate and temperature can't be considered in isolation.

2.6.2 Strain

The effect of strain magnitude on the recrystallisation level achieved through forging and the size of the recrystallised grains has been explored in AD730 [25, 26].

It has been clearly shown that applying higher strains during sub-solvus forging can lead to higher levels of recrystallisation in AD730 [25, 26]. In [25], increasing the magnitude of the applied strain during forging from 0.5 to 3 led to an increase in the recrystallised fraction from 62 % to 88 % when forging at 1080 °C under a nominal strain rate of 0.067 $^{-1}$. The fact that some grains did not recrystallise, even at such high strain levels, was attributed to local strains in those locations being lower than the threshold needed to trigger recrystallisation. This would be a relatively simple explanation for the presence of unrecrystallised grains in AD730, simply that the strain applied is insufficient for the stored energy to reach a critical level needed for recrystallisation. However, this cannot be a full explanation, as the particular precipitation found in unrecrystallised grains shows that this also plays a role, so the interaction between recrystallisation and precipitates must be considered as well.

Very high strains may not be achievable in practice, particularly on large billets. Moreover, strain as high as 2 did not remove the recovered grains shown in [26] when forging at a nominal strain rate of 0.15 s^{-1} and a sub-solvus temperature of 1080 °C.

In terms of grain size, [25] showed larger recrystallised grain sizes following higher strains, with the average recrystallised grain size increasing from 3.8 µm at a strain of 0.5 to 5.4 µm at a strain of 3. This was explained as higher strains providing the energy needed for grain growth after recrystallisation. This observation is different from the conclusion made during constant strain rate deformation of IN718, where the size of recrystallised grains did not vary much with strain level, except for at the very start of recrystallisation (i.e. at relatively low strain levels), where recrystallised grain sizes were slightly higher than their constant value maintained at higher strains [72]. A constant grain size as a function of strain during dynamic recrystallisation is the expected behavior (e.g., chapter 13 of [**?**].

An important factor accounting for this difference between [72] and [25], the influence of which was not considered in [25], is the difference in the time spent forging and the strain rates experienced by different samples forged to different strain levels. In [25], deformation was applied via a constant die speed of 5 mm/s on a cylinder with a height of 75 mm, the sample strained to 3 was deformed for longer than the sample strained to 0.5 (14.3 s rather than 5.9 s) and it was exposed to much higher strain rates (a maximum strain rate of 1.34 s^{-1} rather than 0.11 s^{-1}). This higher strain rate will lead to faster post-dynamic recrystallisation [67], and greater amounts of adiabatic heating, which additionally leads to longer times at high temperatures during which post dynamic recrystallisation can occur. Thus, it is possible that the larger recrystallised grains seen after higher strain levels are predominantly post-dynamically recrystallised grains, whereas those seen after the lower strain levels (and therefore under lower strain rates) are predominantly dynamically recrystallised. The larger grain size would be explained by post-dynamically recrystallised grains consuming dynamically recrystallised grains (and unrecrystallised grains) after deformation. This is feasible, since post-dynamically recrystallised grains have slightly lower dislocation contents than dynamically recrystallised grains, and so their growth at the expense of dynamically recrystallised grains is energetically favourable. Indeed, this slight difference in dislocation contents is exploited to distinguish between the two types of grain in EBSD data [68] (this allowed the work in [67] to be done).

Table 2.4 uses results from [25] and [67] to show that the effects of strain and strain rate on the total recrystallised fraction are both significant, and of similar magnitudes. This underlines the fact that both must be considered when interpreting the results of a forging experiment.

2.6.3 Initial microstructure

The effect of initial microstructure has not been studied in AD730 specifically, though it has been studied in Nimonic 80a, a γ' strengthened Ni-based superalloy which has high Ni content [73], and some general principles apply.

For example, the larger the starting grain size before forging, the fewer nucleation sites are available for discontinuous dynamic recrystallisation, which can occur initially via the bulging of grain boundaries [63]. Additionally, the presence of precipitates, whether they be carbides or γ', can hinder the migration of both dislocations

Table 2.4: The impact of both strain and strain rate on recrystallised fraction in Ni-based superalloys. The first three rows use data collected on AD730, and show the effect of varying levels of total strain [25]. The last five rows use data collected from Inconel 718, and show the effect of strain rate [67]. Note that data for the first three rows were collected during a forging experiment which involved deformation using a constant die speed, resulting in a varying strain rate. The range of strain rates experienced by the samples are provided.

Alloy	Strain	Strain rate $/s^{-1}$	Forging temperature / °C	Recrystallised fraction / %	Reference
AD730	0.5	0.067 - 0.110	1070	62	[25]
AD730	0.9	0.067 - 0.164	1070	72	[25]
AD730	3	0.067 - 1.34	1070	88	[25]
IN718	0.7	0.001	980	56	[67]
IN718	0.7	0.01	980	35	[67]
IN718	0.7	0.1	980	26	[67]
IN718	0.7	0.5	980	40	[67]
IN718	0.7	1	980	50	[67]

and grain boundaries, limiting the growth of recrystallised grains, and hence the final size of recrystallised grains and recrystallised fraction. Indeed, the pinning effect of the precipitates has been suggested as a factor hindering complete recrystallisation in AD730 [26]. Both of these effects were seen in the investigation in Nimonic 80a [73], where a pre-forging soaking heat treatment for one hour was carried out at three different temperatures, in order to investigate the effect of initial microstructure on subsequent forging.

A soaking temperature about 200 °C above the solvus led to relatively large recrystallised grains after forging, due to the large grains present prior to forging (i.e. lower grain boundary area, and fewer nucleation sites). A soaking treatment around the solvus temperature ($\approx$ 950 °C) led to very low levels of recrystallisation ($\leq$ 10 %), likely due to incomplete dissolution of precipitates. A pre-forging soaking treatment of 100 °C above the solvus temperature proved most successful, as it dissolved precipitates better than the treatment at the solvus temperature, and led to less grain growth than the treatment 200 °C above the solvus temperature. This treatment led to a fully recrystallised structure, provided suitable levels of strain were applied. These results are summarised in Fig. 2.19.

The investigation into Nimonic 80a also looked at the effect of strain, strain rate

and temperature on forging, as well as the pre-forging heat treatment [73]. However, the simultaneous variation of all these parameters meant it was difficult to attribute any particular microstructural development to just one of them.

In AD730, the state of the initial microstructure when commencing sub-solvus forging is particularly interesting, and there are several open questions:

- Different γ' populations have been identified in recrystallised and unrecrystallised grains. How do they affect the kinetics and mechanisms of recrystallisation?
- How can heat treatments designed to control the size and volume fraction of γ' (e.g. those explored in [12]) be used to enhance forgeability?
- Are the large recrystallised grains more difficult to recrystallise during sub-solvus forging than deformed grains, due to their lower stored energy and unique γ' precipitates?

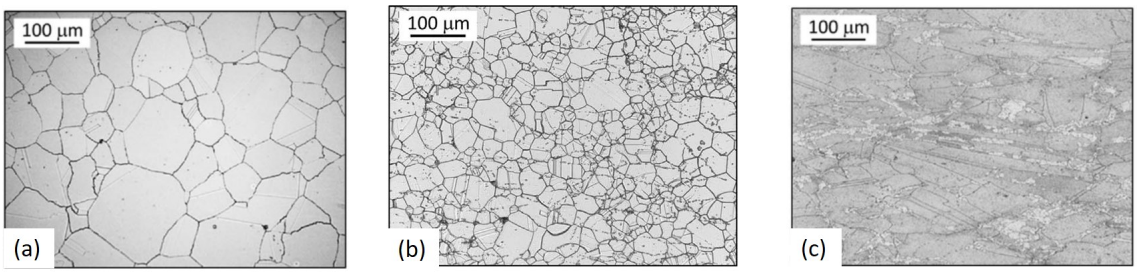


Figure 2.19: Different initial microstructures lead to different microstructures after forging. Sample (a) was soaked at 200 °C above the solvus temperature before forging, sample (b) was soaked 100 °C above the solvus temperature (c) was soaked at a sub-solvus temperature. Sample (b) shows the most desirable final microstructure, giving a large recrystallised fraction and a small final grain size. Figure adapted from [73].

2.7 Conclusions and outlook

This review focused on two main areas. Firstly, it provided an overview of γ' precipitation as well as microstructural features of γ grains in AD730. Secondly, it explored the influence of forging parameters (strain, strain rate, microstructure and temperature) on the microstructural evolution of AD730 and other γ/γ' alloys.

Regarding the first area of investigation, certain aspects of the microstructural evolution of AD730 have been thoroughly investigated and are now well understood. The works by Masoumi *et al.* into the precipitation and coarsening of γ' in AD730 are particularly impressive, and provide a detailed understanding of the relationship between cooling rate and the temperature at which γ' precipitation occurs, the size and morphology of these precipitates, and how they evolve with near solvus annealing treatments.

However, this work aimed at understanding precipitate development during the heat treatments applied after closed-die forging, so only considered cooling rates far quicker than those applied to large scale billets during industrial open-die forging. Additionally, this understanding does not extend to the precipitation in the so-called recovered grains, which is of critical importance from the viewpoint of forging. The primary precipitation seen in recovered grains is finer and denser compared with primary precipitation in recrystallised grains [24, 26] (primary here meaning the largest precipitates in the grains of interest). The reasons behind the differences in precipitate evolution were briefly commented on in [22], where it was suggested that some grains retained higher dislocation densities from the super-solvus forging and developed a more fine and dense precipitation subsequently. It is unclear how the size/volume fraction of precipitates in recovered grains can be controlled by thermal treatments; this is a critical point since the dense precipitation in these grains is very likely to cause their resistance to recrystallisation.

Regarding the influence of forging parameters, there is again a mixture of clear results and open questions.

Applying very high strains (up to 3) during sub-solvus forging does lead to high levels of recrystallisation [25], though such an approach is not feasible for large scale forging. Additionally, this strain was achieved with a constant die speed, generating a macroscopic average strain rate of 1.34 s^{-1} and associated adiabatic heating. Recent advancements point to low strain rates as best for achieving both the highest levels of recrystallisation and close control of temperature through minimising adiabatic heating [67]. However, the effect of strain rate on microstructural evolution in AD730 is yet to be explored.

On the basis of the above findings, the following areas are suggested as profitable avenues for future work:

- The formation of recovered grains. This has been speculated on here, though

experimental evidence is needed to validate the proposed mechanisms. In particular, the suggestions that recovered grains originate from the large recrystallised grains or from deformed grains inherited from super-solvus forging need experimental validation.

- Clarity around reprecipitation (or lack thereof) behind the moving recrystallisation front. In [24] when the growing recrystallised grain shared a $\langle 111 \rangle$ axis with the 'recovered' grain it was consuming precipitation occurred at the front, though no precipitation was seen behind the moving front. This contrasts with the behaviour observed in [22], where precipitation did occur behind the moving front. An explanation for this difference is lacking.

- The difficulty of recrystallising 'recovered' grains. It has been suggested here that the fine and dense primary precipitation in these grains impedes their recrystallisation. However, the extent of this effect is unclear. It may be that an unfavourable orientation, which leads to a low resolved shear stress in the recovered grains, is needed in addition to this fine and dense primary precipitation to prevent them from recrystallising. To this end, investigations showing the effective of precipitates and texture on recrystallisation may be instructive.

- Control of precipitates during open die forging. While the coarsening and dissolution of γ' precipitates in undeformed grains has been well-characterised [12], this work only considered small, approximately spherical precipitates which form during relatively quick cooling through the solvus temperature. Precipitates which form at slow cooling rate more representative of industrial forging conditions should be investigated.

- The possible role of chemical segregation in influencing precipitation and thereby recrystallisation. There is some evidence that remnant chemical segregation still exist in billet material, inherited from former dendritic and inter-dendritic regions [32]. This possibility should be checker further to inspect whether or not there is a difference in composition between regions with different precipitate distributions.

3 Methodology

This chapter details the materials used and methodologies implemented in the experiments carried out during the course of this thesis, as well as the methods used to analyse their results.

There are three major experiments described in this thesis. Experiments 1 and 2 involve intermediate scale forging; they examine the precipitate distribution which forms during slow cooling from the super-solvus, and how this interacts with recrystallisation under different forging conditions, respectively. Experiment 3 analyzes the microstructural evolution during sub-solvus forging of a microstructure from an intermediate stage of the billet conversion process.

3.1 General strategy

Thermo-mechanical processing is used to control the microstructures (and hence properties) of a wide range of metallic materials. Thermo-mechanical treatments consist of a series of sequential heatings and coolings, combined with hot working (i.e. deformation). In an industrial setting, these treatments are carried out on large billets weighing several tonnes.

A schematic forging route for the billet conversion process of a Ni-based superalloy is shown in Fig. 3.1. In general, such a forging route can involve super-solvus and sub-solvus forging stages, and static recrystallisation stages. Super-solvus forging experiments are not carried out in this thesis, so this step has been omitted on the schematic. The aim of such a forging route would be to generate a fully recrystallised microstructure, made up of small, equiaxed and deformation free γ grains (with diameters on the order of 20 µm) with a uniform distribution of γ' precipitates.

The *goals* of the individual steps are summarised below, note that in practice achieving these goals may not be straightforward:

1. Homogenisation, to eliminate any remnant chemical segregation.

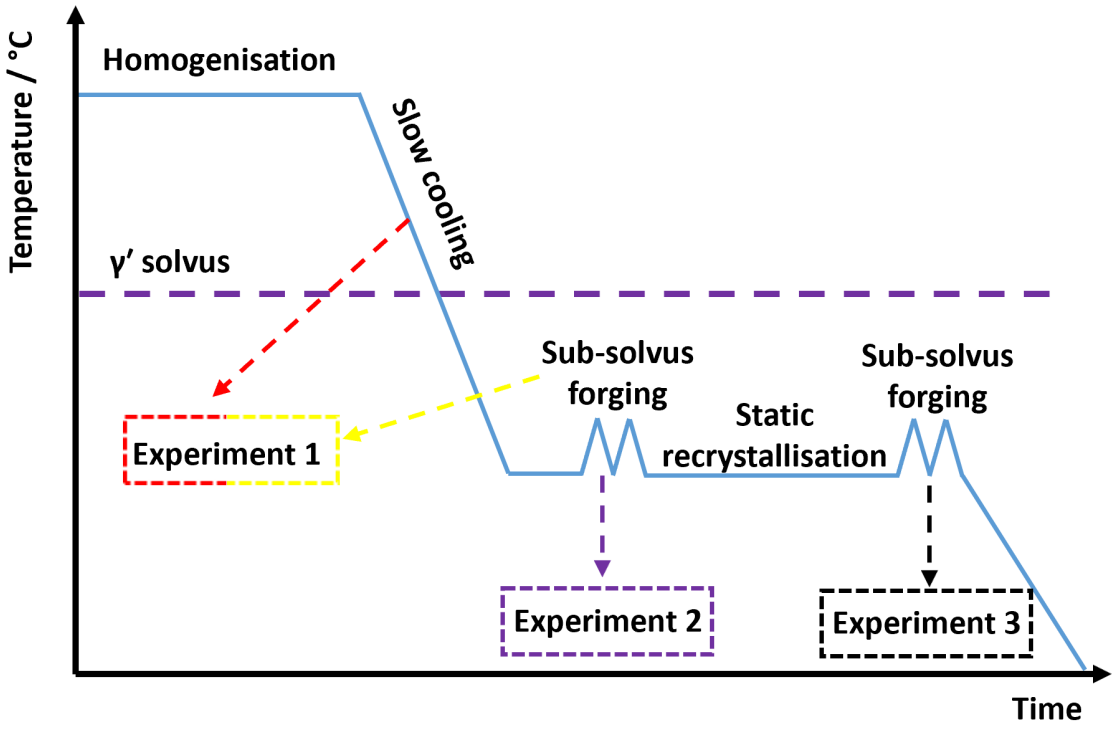


Figure 3.1: A schematic plot of an ingot to billet conversion process. The portions of the route to which the three major experiments in this thesis are related are indicated.

2. Super-solvus forging may be performed, with the aim of refining the large and textured as-cast grain structure.

3. Controlled furnace cooling through the γ' solvus (at a rate on the order of 10 °C/s), which leads to precipitation.

4. Sub-solvus forging, to further refine grain size by forming small recrystallised grains.

5. A static recrystallisation to increase the recrystallisation level.

6. A final sub-solvus forging to reduce the billet to its final dimensions (typically a diameter on the order of 250 mm) and refine any large statically recrystallised grains.

This thesis aims to characterise the microstructural evolution occurring during the industrial open die forging of AD730. Each chapter relates to a separate part of the

forging process.

Chapter 4 presents the results of microstructural characterisation s carried out on samples taken from the final two stages of an industrial forging process (i.e. after static recrystallisation and after a final sub-solvus forging). Subsequent chapters attempt to rationalise, using lab scale experiments, how such microstructures arose. The progress of recrystallisation and precipitation will be the main focus of each chapter. The aim of the lab scale trials is not to mimic the industrial process as closely as possible, but to be sufficiently similar that the key microstructural evolution mechanisms at each stage can be detected.

Chapter 5 investigates the precipitation state which develops during slow cooling through the γ' solvus. Here, a very slow cooling rate (10 °C / hour) was used, to match the slow cooling rates experienced by large industrial billets undergoing controlled cooling. The precipitate state developed will have an influence on subsequent recrystallisation behavior. This chapter discusses results from experiment 1.

Chapter 6 starts with the microstructure developed by slow cooling through the solvus in Chapter 5, and studies how this evolves during sub-solvus forging. In particular, the interaction of recrystallisation with different populations of precipitate is investigated. This chapter discusses results from experiment 1. Chapter 7 looks at the effect of forging parameters on recrystallisation during the sub-solvus forging of Chapter 6. This chapter discusses results from experiments 1 and 2.

Chapter 8 takes a microstructure from the penultimate stage of the industrial forging (i.e. after the static recrystallisation step), which is forged at a sub-solvus temperature to mirror the final sub-solvus forging stage. This chapter discusses results from experiment 3.

3.2 Limitations

The approach outlined in the preceding section has the following limitation, relating to experiments 1 and 2. The starting material used in these investigations does not come directly from ingot material, but rather from either the end of the industrial open die forging process, or near to the end of this process. As such, the samples investigated will not have the very large grain sizes ($\approx$ several cm) typical of ingot material (although this size may be reduced by super-solvus forging operations). Using material from the ingot would require very large samples to be used in forging

trials, to have a representative number of grains in a cross section, and using such large sections is impractical. This is not considered a serious limitation, since the microstructural mechanisms observed in experiments 1 and 2 are not expected to be strongly affected by this.

3.3 Microstructural characterisation techniques

Microstructural analysis was done using standard techniques in the SEM, i.e. backscattered electron (BSE) and secondary electron (SE) imaging, energy dispersive X-ray spectroscopy (EDS) and electron back scatter diffraction (EBSD).

In this work, the majority of SEM analysis was done using a FEI Quanta 250 field-emission gun (FEG)-SEM equipped with an Oxford instruments Nordlys electron backscatter diffraction (EBSD) camera, and an Oxford instruments energy dispersive x-ray spectroscopy (EDS) system. The Aztech software was used to collect EBSD and EDS data. EBSD and EDS data were all collected using an accelerating voltage of 20 kV, with EBSD data being collected at a sample tilt of 70 °.

Wavelength dispersive spectroscopy (WDS) was done using a JEOL hyperprobe JXA-8530F field emission electron probe micro-analyser (EPMA) operating at 20 kV. The microscope was operated by Paul Edwards at the university of Strathclyde's Technology and Innovation centre.

3.3.1 Focused ion beam SEM tomography

Serial sectioning with a focused ion beam (FIB) can be used to take a stack of 2D BSE images, which can be reconstructed to gain a 3D view of microstructure.

FIB –SEM tomography was performed in order to show the actual 3D shape of γ' precipitates at various stages of open die forging. This was done using a Tescan Fera 3 microscope equipped with a plasma technology ion column using Xe+ ions at the CEMEF in France. The microscope was operated by Alexis Nicolaÿ.

A region of interest was found and delimited by milling small markers using the FIB. To align the sample to be perpendicular to the ion beam, the sample was tilted to 55° during milling. To allow serial sectioning and imaging a cross section had to be milled away to give the electron beam access to the plane perpendicular to the region of interest. This was done using a relatively high ion beam current (2 µA).

After this, the plane perpendicular to the region of interest was polished with the ion beam using progressively lower currents to produce a flat cross section with minimal "curtaining". To do this a current of 1 µA was first used, followed by fine polishing with a current of 100 nA. At this point the cross section was prepared, and serial sectioning followed by BSE imaging could begin. A slice thickness of 100 nm was removed at each step. During all milling stages fluorine gas was introduced into the SEM chamber, with aim of minimising the curtaining effect. A schematic overview of this process is shown in Fig. 3.3.

The images produced were passed through a frequency filter in Fiji to remove the curtaining effect [74] and were then segmented using the Pixel classification workflow of ilastik [75]. In the pixel classification workflow the user labels a sub-set of pixels in an image to assign them to one of two classes (in this case identifying whether they belong to the γ or γ' phase). Every pixel has a set of features (related to the pixel intensity, and edge and texture properties), and based on the labels assigned by the user all pixels in an image are assigned to one of the classes. The labels thus act as training data, instructing the classifier what properties (relating to intensity, edge and texture) pixels in each class have. Fig. 3.2 shows the process of labelling and segmenting an image in the pixel classification workflow of ilastik.

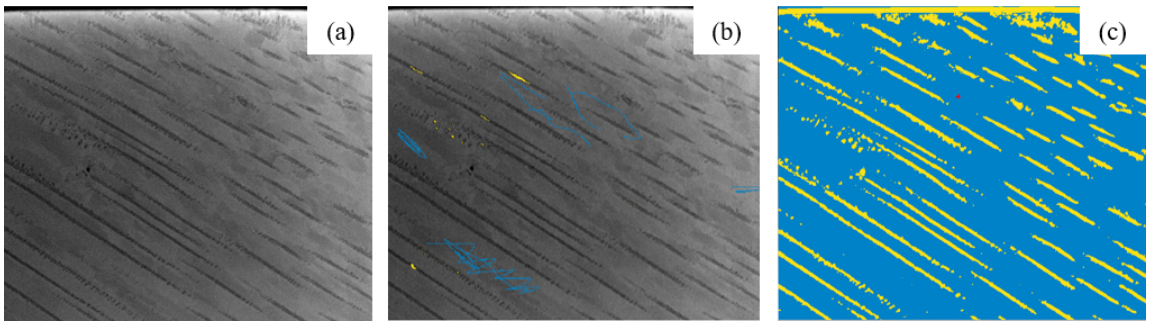


Figure 3.2: An example of segmentation in ilastik. The image (a) is labelled, with some pixels labelled as belonging to the γ' phase (marked yellow) and some to γ (marked blue) (b). From these labels the segmentation of the whole image is predicted(c). The user can accept this segmentation, or add additional labels to try and improve it.

For the analysis of the micrographs collected by FIB-SEM nanotomography, a few images from the stack of images were partially labelled, and the remaining images were segmented using these labels as training data. The segmented images were visually inspected to check the quality of the segmentation. Segmentation errors

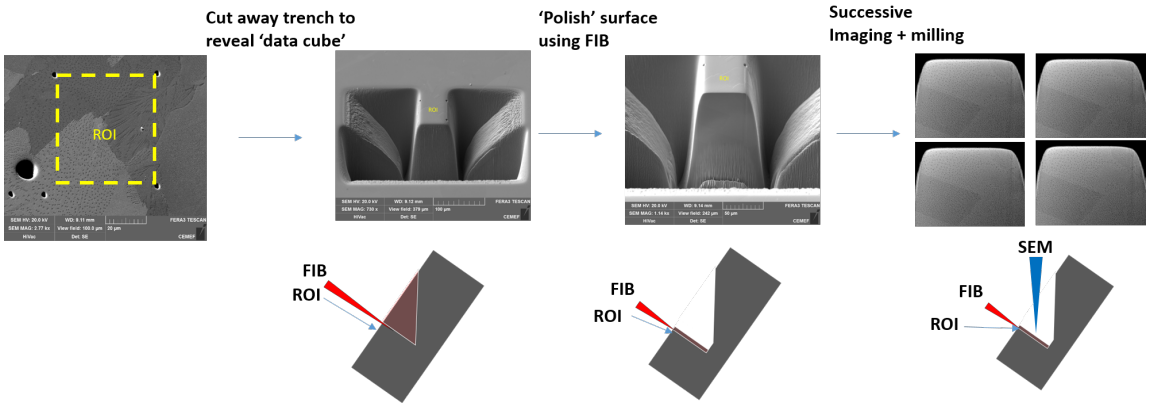


Figure 3.3: An overview of the stages involved in the FIB SEM tomography process.

could be corrected by adding labels to incorrectly segmented pixels, and in this way the whole stack could be segmented accurately (such that there no obvious errors by visual inspection of the images) with relatively little labelling (a total of about 5 images were partially labelled). Additional information on pixel classification and other workflows in ilastik can be found here [75].

The stack of segmented images were reconstructed in Fiji to produce a 3D view of precipitation. From this 3D view, the length of precipitates which are connected in 3D can be measured. Additionally, orthogonal 2D projections were produced, showing how the same precipitates can look different when viewed from different planes in 2D images. Based on these 2D projections, the equivalent area circle diameter and aspect ratio which would be measured for the same precipitates viewed from different planes were calculated.

3.3.2 Electron back scattered diffraction (EBSD)

EBSD was done using a FEI Quanta 250 field-emission gun (FEG)-SEM equipped with an Oxford instruments Nordlys electron backscatter diffraction (EBSD) camera, and an Oxford instruments energy dispersive x-ray spectroscopy (EDS) system. The Aztech software was used to collect EBSD data.

EBSD is not capable of distinguishing between the γ and γ' phases. The two phases have very similar crystal structures, and produce very similar electron diffraction patterns, which cannot be readily distinguished [76]. As such, the size, shape, and texture of the precipitates cannot be measured from EBSD data. Instead, the precipitates can be identified in BSE and FSE images, where their increased concen-

tration of Ti and Al makes them appear darker than the surrounding matrix. As EBSD and FSE data can be collected under the same conditions (i.e. both at 70° tilt), the EBSD derived data (e.g. an IPF map) can be overlaid onto the FSE image, and the locations of precipitates identified.

3.3.3 EBSD analysis

The EBSD data were analysed using the MTEX toolbox [77] developed in MATLAB. High angle grain boundaries (HAGBs) were defined according to a misorientation angle of at least 10° between neigbouring pixels, and twin boundaries (TBs) were defined as those with a 60° misorientation angle about a ⟨111⟩ axis, allowing an 8.66° tolerance, following the Brandon criterion. Low angle grain boundaries (LAGBs) were defined as boundaries with misorientation angles between 3° and 5°, and medium angle grain boundaries (MAGBs) were defined as boundaries with misorientation angles between 5° and 10°. Where possible, Inverse pole figure (IPF) maps were plotted with respect to a physically relevant macroscopic direction, e.g. the compression direction (CD) of samples which were compressed, or along the billet direction (BD) or radial direction (RD) of billet material. The standard colour key for FCC materials was used and is the same for all IPF maps. In IPF maps, grain boundaries were plotted as black lines, and twin boundaries as red lines

Texture

Crystallographic texture will be represented in pole figures. This are shown as contour plots, where the values of the contours represent the texture strength in multiples of the random distribution (MRD).

Grain size measurement

EBSD data allows the area of each individual grain to be measured. For the EBSD data presented here, a grain was defined as group of at least 3 neighbouring pixels bounded by a HAGB.

Twin boundaries were defined as boundaries with a misorientation corresponding to a 60 ° rotation about a ⟨111⟩ axis, along an 8.66 ° tolerance.

Twin boundaries were counted as grain boundaries, unless otherwise specified. It can be useful to discount twin boundaries when looking at grain boundary morphol-

ogy, as the twin boundaries are usually very flat. When discounting twin boundaries, the resulting grains are referred to as 'merged grains".

The total length of twin boundary in a micrograph can be measured, and the fraction of boundary which is twin boundary can be calculated. This fraction (the twin boundary %) is defined as the total length of twin boundaries divided by the total length of grain boundary.

There are different ways that the size of an individual grain may be reported, including: Grain area, equivalent area circle radius, equivalent area circle diameter, equivalent area square side length. An average value across all measured grains can be calculated based on either number weighting or area weighting.

In this thesis, when referring to grain size, a number weighted average equivalent area circle diameter is being referred to, unless otherwise specified. Area weighted average equivalent area circle diameters will also be used in this thesis. In EBSD data where there are a very large number of very small grains, these control the number weighted average - but not the area weighted average. Grain sizes are reported as mean ± one standard deviation.

The definition of number weighted average equivalent area circle diameter is given in equation 3.1, where N is the total number of grains and d_j is the equivalent area circle diameter of the j^{th} grain.

$$\bar{d}_{num} = \frac{1}{N} \cdot \sum_{j=1}^{N} d_j \tag{3.1}$$

The definition of area weighted average equivalent area circle diameter is given in equation 3.2, where N is the total number of grains, A_j is the area of the j^{th} grain and d_j is the equivalent area circle diameter of the j^{th} grain.

$$\bar{d}_{area} = \frac{1}{\sum_{j=1}^{N} A_j} \cdot \sum_{j=1}^{N} A_j \cdot d_j \tag{3.2}$$

Grain reference orientation deviation

Grain reference orientation deviation (GROD) is a value defined at each measurement point which shows the misorientation angle of that point to the average orientation of the grain that contains it. It is helpful in showing where orientation changes are

occurring, and is used for that purpose in this thesis. The GROD value of pixel j having an orientation g_j in a grain with mean orientation $\bar{g}$ is given in equation 3.3.

$$GROD_j = \omega(g_j, \bar{g}) \tag{3.3}$$

Where ω denotes the misorientation between g_j and $\bar{g}$. In MTEX, orientations are defined as coordinate transformations from the crystal reference frame into the specimen reference frame, and inverse orientations ($inv(g_j)$) are therefore coordinate transformations from the specimen reference frame into the crystal reference frame. The rotation matrix describing the misorientation between two orientations is given by equation 3.4.

$$\omega(g_j, \bar{g}) = inv(g_j) * \bar{g} \tag{3.4}$$

From this matrix ($\omega(g_j, \bar{g})$) the rotation angle between the two orientations can be calculated as $\arccos(tr(\omega) - 1)/2))$.

Grain orientation spread

Grain orientation spread (GOS) is the GROD value averaged over all measurement points in a grain, defined in equation 3.5. It is a measure of the average misorientation angle of all n points in a grain to the average orientation of that grain ($\bar{g}$).

$$GOS = \frac{1}{n} \cdot \sum_{j=1}^{n} \omega(g_j, \bar{g}) \tag{3.5}$$

This gives a value which can be used to assess the overall level of stored energy within a grain. It will be used to discriminate recrystallised from non recrystallised grains in this thesis. Two potential artefacts arising from this measure are that it will tend to give larger grains higher values (since a given orientation gradient extended over a large distance has a higher average misorientation from the mean) and that grains containing sub-grain boundaries can be given very high GOS values, even if the two sub-grains have uniform orientations.

Kernel average misorientation

Kernel average misorientation (KAM) gives a local measure of orientation gradients at each measurement point. A kernel of specified size centred around a measure-

ment point is considered, and the average misorientation angle of all measurement points in the kernel to the central point is measured. In this calculation the neighbours belonging to another grain are discounted, thus KAM is used as a measure of intragranular misorientation. The kernel size is defined by the number of nearest neighbours considered; an example of a 4th order kernel is shown in Fig. 3.4. Here, the 4th orer KAM value would be the average misorientation angle between the central point (marked 0) and all 20 neighbours shown.

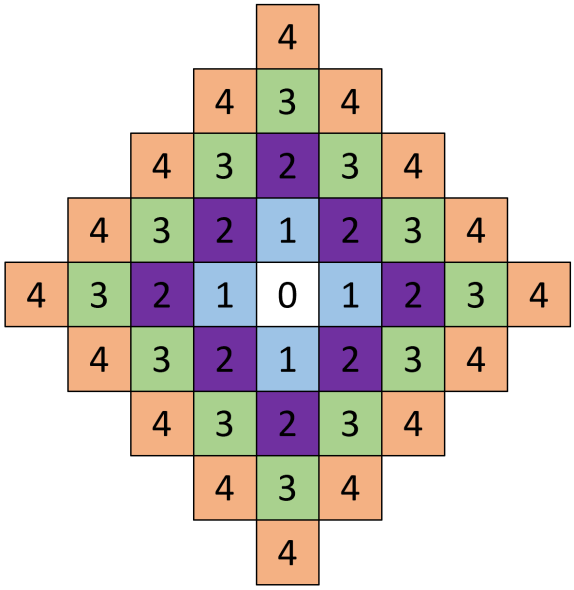


Figure 3.4: A kernel showing upto and including 4^{th} order nearest neighbours. All pixels shown would be used in calculating the 4^{th} order KAM value.

In a square EBSD grid there will be 4n n^{th} order nearest neighbours, so the total number of neighbours considered in an n^{th} order kernel is $4(1+2+...+n) = 2n(n+1)$. The definition for the n^{th} order KAM value at point i is given in equation 3.6.

$$KAM_n^i = \frac{1}{2n(n+1)} \cdot \sum_{j=1}^{j=2n(n+1)} \omega(g_i, g_j) \tag{3.6}$$

KAM will also be used to give a measure of *long-range* orientation gradients in this thesis. These are an important microstructural parameter for recrystallisation, since they are required for the formation of high angle boundaries between differently oriented regions (see chapter 2 of [63]). Despite their importance, there does not seem to be a standard way of quantifying the magnitude of long range orientation

gradients. A line profile can show the orientation gradients along a particular line, but this does not assess the whole grain, and differently drawn lines will produce different gradients.

Using KAM as defined in equation 3.6, the misorientation angle between a point and *exclusively* its nth order neighbours can be measured (i.e., using *just* the points on the rim of the nth order kernel). As described above, KAM measures all points within the kernel, but the average misorientation angle between a point and *just* its nth order neighbours can be calculated by considering both the (n-1)th and nth KAM kernel. The KAM value due *exclusively* to a point i's nth order neighbours (denoted by KAM_{n*}), ignoring all others in the kernel, is given by equation 3.7. This value, KAM_{n*}, can be used as a quantitative measure of long range orientation gradients at each pixel of an EBSD map.

Given that the distance between a pixel and its nth order neighbours is dependant on step size, KAM values for any given kernel size will be step size dependant, thus comparisons in nth order KAM values can not be made directly between maps taken using different step sizes.

$$KAM^i_{n*} = \frac{n+1}{2} \cdot \left(KAM^i_n - \frac{n-1}{n+1} \cdot KAM^i_{n-1} \right) \tag{3.7}$$

Grain average misorientation / grain average kernel average misorientation

Grain average misorientation (GAM) and grain average kernel average misorientation (GAKAM) both refer to the grain averaged value of KAM. This is similar to GOS in being a grain averaged property, but since it uses local averaging it does not suffer the potential artefacts associated with the GOS metric mentioned previously. The definition for GAKAM in grain i with N measurement points is given in equation 3.8. This metric will be used a measure of the grain averaged long range orientation gradients.

$$GAKAM_i = \frac{1}{N} \cdot \sum_{k=1}^{k=N} \frac{1}{2n(n+1)} \sum_{j=1}^{j=2n(n+1)} \omega(g_i, g_j) \tag{3.8}$$

Table 3.1: Nominal chemical composition of AD730 in Wt. %

Composition in Wt. %											
Ni	Fe	Cr	Co	Mo	W	Al	Ti	Nb	C	B	Zr
Balance	4.0	15.7	8.5	3.1	2.7	2.25	3.4	1.1	0.02	0.01	0.03

3.4 Experimental details

3.4.1 As-received material

The material used in this thesis was AD730 supplied by Aubert&Duval. The nominal composition of this material is given in Table 3.1.

For the intermediate scale forging trials discussed in section 3.4.2 (experiments 1 and 2) the as-received material had been triple melted (i.e., vacuum induction melted, electro-slag re-melted, and vacuum arc re-melted) and had undergone the entire billet conversion process. This material was in the form of cylinders with diameters of 50 mm and lengths of 75 mm. The long axis of these cylinders was parallel to a long axis of the billet from which they had been extracted.

For the additional heat treatments described in section 3.4.3 and the lab scale forging experiments described in section 3.4.4 (experiment 3) the as-received material had been triple melted (i.e., vacuum induction melted, electro-slag re-melted, and vacuum arc re-melted) and had undergone the billet conversion process up to and including the static recrystallisation stage. This material was in the form of cylinders with diameters of 10 mm and lengths of 15 mm. The long axis of these cylinders was parallel to a radial axis of the partially forged billet from which they had been extracted.

3.4.2 Experiments 1 and 2 - intermediate scale forging

The experimental work detailed in Chapters 5 - 7 is based on a series of thermo-mechanical treatments carried out on AD730 billet material.

In total nine different thermo-mechanical treatments were applied to these cylinders to investigate the precipitation and recrystallisation behavior during the early stages of billet conversion of AD730. Results from the first five of these treatments (collectively termed experiment 1) are discussed in Chapters 5 and 6. The thermo-

mechanical path for experiment 1 is shown in Fig. 3.5 and is summarised as follows:

Heat treatments were carried out in two furnaces. Samples were first held for 40 mins at 1160 °C in a Carbolite RHF 1400 furnace, and were then quickly transferred using tongs to a Carbolite GPC furnace at 1125 °C, which was programmed to cool at a rate of 10 °C/h down to 1080 °C, at which temperature the samples were held for 1 hr. Sample A was water quenched right at the end of the first holding at 1160 °C. Sample B was quenched as soon as it reached 1080 °C at the end of the controlled cooling, and sample C after one hour at 1080 °C. The fourth sample (D) followed the same thermal path as sample C and was then transferred to a 500 T hydraulic press with flat dies, which had been pre-heated to 450 °C and lubricated using graphite. The sample was placed on the lower die and compressed by the upper die, which moved down at a constant speed of 3 mm/s. The sample was compressed for 9 s, corresponding to a height reduction of 27 mm and a macroscopic average true strain of 0.45 (macroscopic average engineering strain of 0.36). After compression, sample D was removed from the dies and quenched in water. Sample E followed the same thermal path as sample D, but after forging it was removed from the press and cooled in air, rather than being water quenched.

The whole compression process was filmed, allowing accurate determination of dwell time on the lower die before compression, and the delay time between the end of compression and quenching.

These five paths are shown schematically in Fig. 3.5. These five samples are referred to as 1A, 1B, 1C, 1D and 1E henceforth.

A similar thermo-mechanical treatment, with forging being done in two steps rather than one, was applied to an additional four samples. This treatment is referred to as experiment 2, and is summarised as follows:

Heat treatments were carried out in two furnaces. Samples were first held for 40 mins at 1160 °C in a Carbolite RHF 1400 furnace, and were then quickly transferred to a Carbolite GPC furnace at 1125 °C, which was programmed to cool at a rate of 10 °C/h down to 1080 °C, at which temperature the samples were held for 1 hr. Samples were then transferred to a 500 T hydraulic press with flat dies, which had been pre-heated to 450 °C and lubricated using graphite. Following the initial heat treatments, sample 2A was placed on the lower die and compressed by the upper die, which moved down at a constant speed of 3 mm/s. The sample was compressed for 4.5 s, corresponding to a height reduction of 13.5 mm and a macroscopic average true strain of 0.28. After compression, sample 2A was removed from

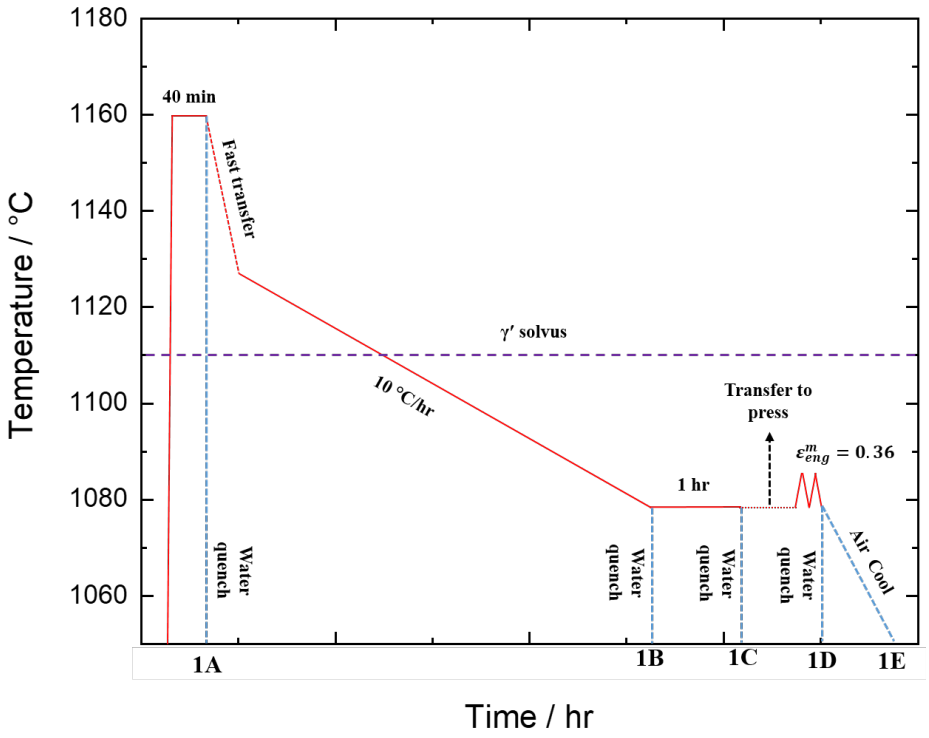


Figure 3.5: A schematic plot of the thermo-mechanical path applied to the cylindrical samples in experiment 1 aimed at studying the early stages of billet conversion. The macroscopic engineering strain applied ($\epsilon^{\mathrm{m}}{}_{\mathrm{eng}}$) in the forging step is indicated.

the dies and quenched in water. Sample 2B followed the same path as sample A, but after forging it was returned to the Carbolite GPC furnace (still at 1080 °C) for 10 minutes, then quenched in water. Sample 2C followed the same path as sample 2B, but after the 10 minutes re-heating at 1080 °C it was returned to the press and forged again where the dies had been pre-heated to 450 °C and lubricated using graphite. The sample was compressed by the upper die, at a constant speed of 3 mm/s. The sample was compressed for 4.5 s, corresponding to a height reduction of 13.5 mm and an additional macroscopic average true strain of 0.17, producing a total macroscopic average true strain of 0.45 (i.e. macroscopically equivalent to the deformation applied in experiment 1). After forging sample 2C was quenched in water. Sample 2D followed the same thermo-mechanical path as sample 2C, but it was cooled in air after the second forging step, rather than being water quenched. The

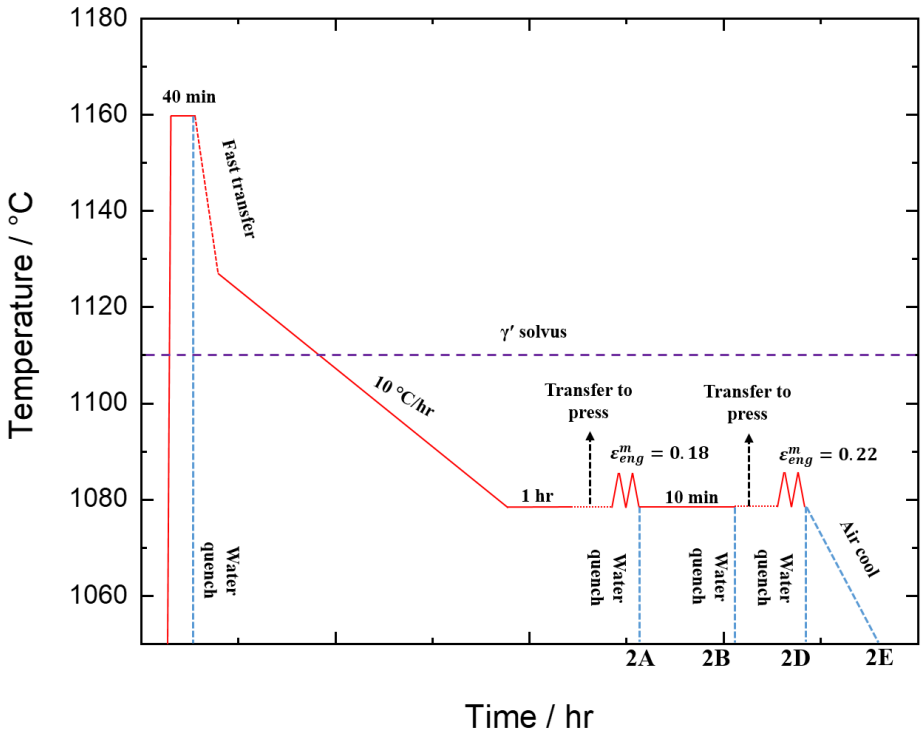


Figure 3.6: A schematic plot of the thermo-mechanical path applied to the cylindrical samples in experiment 2 aimed at studying the early stages of billet conversion. The macroscopic engineering strain applied ($\epsilon^{\mathrm{m}}{}_{\mathrm{eng}}$) in each of the two forging steps is indicated.

thermo-mechanical paths followed by these four samples are shown schematically in Fig. 3.6.

Finite element (FE) analysis of experiments 1 and 2

To obtain an estimate of the strain distribution in the deformed samples from experiments 1 and 2, the DEFORM software was used to perform a 2D axisymmetric FE simulation of the compression tests conducted on the samples compressed in one or two strokes (i.e., samples 1D and 1E forged in one stroke in experiment 1, 2A and 2B forged in one stroke in experiment 2, and 2C and 2D forged in two strokes in experiment 2). Material data for AD730 in the temperature range 300 -1200 °C was supplied by Aubert & Duval. A heat transfer coefficient of 11 mW/m^{2}K and a

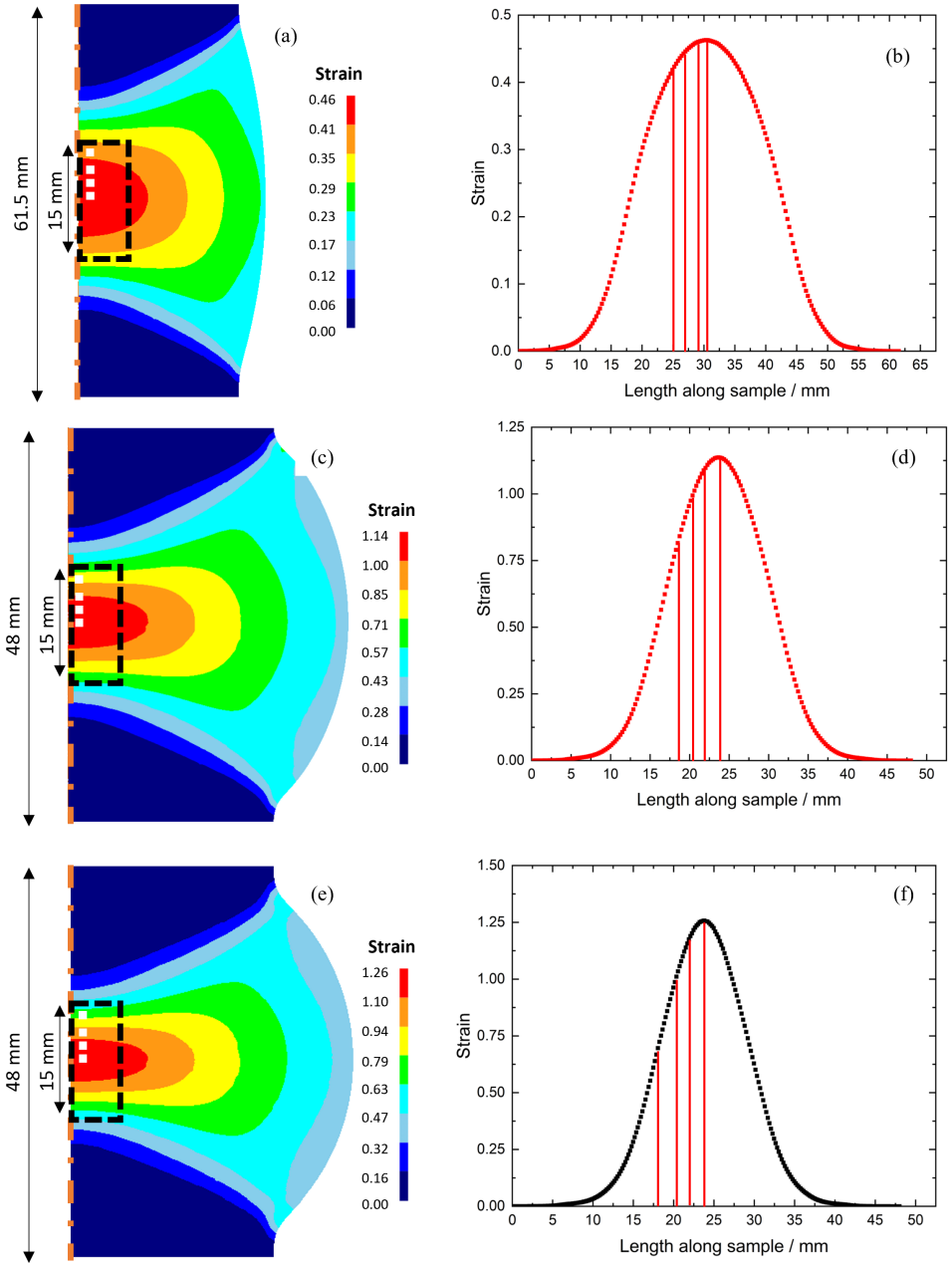


Figure 3.7: Strain distributions predicted by DEFORM FE simulations for samples 2A/2B, which underwent 1/2 forging strokes in experiment 2 (a-b), samples 2D/2E, which underwent 2/2 forging strokes in experiment 2 (c-d), and samples 1D/1E, forged in 1 stroke in experiment 1, (e-f). Black rectangles show extracted areas from deformed samples. White squares indicate approximate regions for EBSD maps. Red lines in (b), (d), and (e) mark strain levels at map locations.

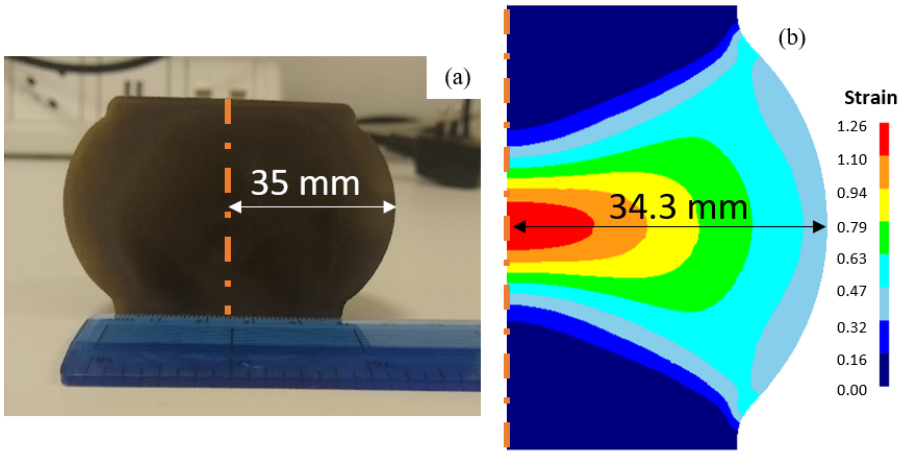


Figure 3.8: A comparison of the maximum diameters of sample 1D (a) and the FE simulation done to model its forging (b).

friction coefficient of 0.3 between the dies and the sample were implemented, as per the software's suggested values for lubricated hot forging. A Taylor-Quinny factor of 0.9 was used, which is a typical approximation for the fraction of mechanical work converted into heat during deformation [78]. The workpiece was meshed into 3143 quadrilateral elements. The actual forging trials were filmed, and this allowed the duration of different stages of the trials to be estimated. It was found that transferring samples between the furnace and the press typically took 3.0 s, that samples would typically rest on the lower die for 7.0 s before being contacted by the moving upper die, and that transferring from the press back to the furnace typically took 3.0 s. The strain distributions predicted for samples 2A/2B, 2D/2E and 1D/1E are shown in Figs. 3.7 (a),(c) and (e), respectively.

The shape of sample 1D after deformation was measured and compared with the shape predicted by the FE simulation. This comparison is shown in Fig. 3.8. The sample's maximum diameter (due to barreling) was measured to be 70 mm, compared with 68.7 mm predicted by the FE model. The close match suggests that the chosen values of friction and heat transfer coefficient were reasonably good.

Microstructural analysis in experiments 1 and 2

The samples produced in experiments 1 and 2 were analysed using the electron microscope. To do this, the 9 samples were first sectioned using wire electrical discharge machining (EDM). A 12 x 15 mm plate was cut out from the centre of

each sample using EDM. In experiment 1, large area (5 mm x 5 mm) EBSD maps were collected from samples 1A and 1C using a 5 µm step size to assess the size and shape of the relatively large grains present. These achieved indexing rates of 99.6 % and 97.0%, respectively.

In sample 1C an additional EBSD map of 1 mm x 1mm was taken using a 1 µm step size, with a FSE image being recorded simultaneously, to show the precipitate distribution in this sample. This map was produced by merging together 20 smaller individual maps.

Sample 1B was used to examine the 3D shape of precipitates, FIB-SEM tomography was used as described in section 3.3.1. Data was captured from a data cube with dimensions of 53.0 µm x 68.2 µm x 52.5 µm. From this volume, a sub-volume with dimensions of 48.4 µm x 45.4 µm x 35.0 µm which displayed minimal curtaining effect was extracted and analysed. The analysis was done as described in section 3.3.1.

From samples 1D and 1E which underwent hot compression, a 12 x 15 mm plate was cut out from the centre of each sample using wire electrical discharge machining (EDM). The location of these plates is indicated by the dotted black line in Fig. 3.7(e). 1 x 1 mm large EBSD maps were acquired from four different regions on this plate, indicated by the white squares in 3.7(e). These locations were the centre of this plate (i.e. the centre of the compressed samples), and three other spots centered distances of 1.8 mm, 3.75 mm and 6 mm vertically away from the centre. The strain magnitudes in these regions were $\epsilon \approx 1.26$, $\epsilon \approx 1.19$, $\epsilon \approx 0.99$ and $\epsilon \approx 0.69$, respectively, as shown by the vertical red lines in Fig.3.7 (f). For each sample, these regions will be referred to as regions 1,2,3 and 4, with region 1 being the lowest strain, and region 4 the highest.

These four maps were each acquired with a step size of 1 µm. FSE images were recorded simultaneously, to show the precipitate distributions in these samples. The maps were made by merging together 20 smaller individual maps

From samples 2D and 2E in experiment 2, EBSD maps were taken in the same four locations as for samples 1D and 1E, i.e. at the centre of the sample and at distances of 1.8 mm, 3.75 mm and 6 mm vertically away from the centre. Note that due to the slightly different thermal histories in the two experiments, samples 2D and 2E do not have the same strain distribution as samples 1D and 1E, so the four strain levels in these two samples were $\epsilon \approx 1.13$, $\epsilon \approx 1.10$, $\epsilon \approx 0.99$ and $\epsilon \approx 0.76$, as shown in Fig. 3.7 (d). These maps had dimensions of 1 mm x 1mm, used a 1 µm

step size, and were made by merging together 20 smaller individual maps.

From samples 2A and 2B in experiment 2, four EBSD maps were collected from each sample. These EBSD maps were taken in the same four locations as for samples 1D and 1E, i.e. at the centre of the sample and at distances of 1.8 mm, 3.75 mm and 6 mm vertically away from the centre. The strain magnitudes in these regions were $\epsilon \approx 0.46$, $\epsilon \approx 0.44$, $\epsilon \approx 0.42$ and $\epsilon \approx 0.39$, respectively, as shown in Figs. 3.7 (c) and (d). These maps had dimensions of 1 mm x 1 mm and used a 1 µm step size, and were made by merging together 20 smaller individual maps.

3.4.3 Additional precipitation heat treatments

In addition to Experiments 1 and 2, a further set of 10 heat treatments were performed to sequentially follow the development of precipitation and the associated microstructural changes during slow cooling through the γ' solvus.

Of the 10 heat treatments, 8 involved first a 1 hour super-solvus hold (at either 1160 °C or 1200 °C) followed by quick cooling down to 1125 °C (achieved by changing the furnace set temperature, this cooling took around 10 minutes in practice) then slow cooling at 10 °C / hour down to either 1100 °C, 1090 °C or 1070 °C before quenching in water. The aim of these was to produce different amounts of γ' precipitation. The idealised thermal paths, and sample names, are summarised in Figs. 3.9 (a) and (b) and Table 3.2. The two different temperatures for the initial heat treatment will produce different initial grain sizes.

In addition to these 8, a further 2 heat treatments were carried out. These samples (1200 E and 1200 F) were initially held for 4 hours at 1200 °C before cooling. However the very large grain sizes produced in these samples meant it was not possible to make representative measurements of grain size and shape in EBSD maps, so they are not considered further.

10 x 15 mm cylindrical samples of AD730 from after the static recrystallisation stage of the industrial forging route were used for these aditional heat treatments. The samples were heated in a Carbolite RHF 1400 furnace. To have an accurate measure of the temperature experienced by the part being heat treated, the following in-furnace set up was used:

A porous brick had two holes drilled into it, into one of which the sample being treated was placed and into the other an identical dummy sample. The brick was left in a consistent position in the furnace for all tests. The dummy sample had a ≈ 1.5

Table 3.2: Intended thermal paths for additional investigations into grain boundary motion associated with discontinuous precipitation.

Sample	Super-solvus holding time + temperature	Cooling rate from 1125 °C / °C /hr	Quenching temperature / °C
1160 A	1 hr, 1160 °C	-	1160
1160 B	1 hr, 1160 °C	10	1100
1160 C	1 hr, 1160 °C	10	1090
1160 D	1 hr, 1160 °C	10	1070
1200 A	1 hr, 1200 °C	-	1200
1200 B	1 hr, 1200 °C	10	1100
1200 C	1 hr, 1200 °C	10	1090
1200 D	1 hr, 1200 °C	10	1070

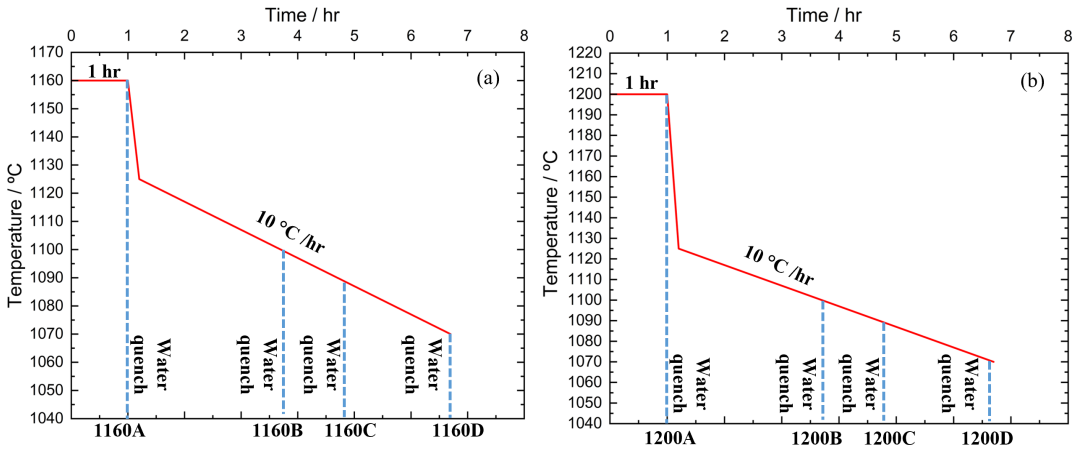


Figure 3.9: Idealised thermal paths for the additional heat treatments carried out to investigate precipitation during slow cooling.

mm diameter hole drilled into it, into which a K type thermocouple was placed for the duration of the heat treatment. Thus the temperature close to the centre of the dummy sample was measured, and this was taken to be the same as the temperature of the actual sample.

Once the empty furnace reached the starting temperature (either 1160 °C or 1200 °C) both the samples were placed into the holes in the brick (first the dummy sample, then the actual sample). At the end of each test the furnace door was opened and the actual sample was quenched in water. The temperature history recorded by the K type thermocouple in the dummy sample was logged.

Microstructural analysis of additional precipitation heat treatments

After heat treatments, the 8 samples produced (1160 A-D and 1200 A-D) were sectioned along their length and prepared for microscopy. From close to the centre of each sample a large area ($\approx$ 6.9 mm x 6.0 mm) EBSD map was taken from which grain sizes were measured. These maps were taken with a large (7.5 µm) step size, due to the coarse grains being investigated.

Samples 1160D and 1200D were further analysed using WDS. In these samples, the local composition was measured along lines of defocused spots with diameters of 6 µm around features of interest. The results from these additional heat treatments are described in Chapter 5.

3.4.4 Experiment 3 -lab scale forging

The experimental work detailed in Chapter 8 is based on a thermo-mechanical treatment carried out at the CEMEF under isothermal conditions using a hot-compression machine equipped with a furnace.

Compression testing was done in an MTS 250 machine equipped with a furnace. The sample was placed in the furnace at 1080 °C and soaked for 5 minutes to allow temperature homogenisation (a heat transfer simulation in DEFORM predicts that the centre of the sample will reach temperature within 200 s). The sample was then deformed in compression to a 50 % reduction in height, corresponding to a macroscopic true strain ϵ_m of 0.7, under a nominal constant strain rate of 0.1 s^{-1} ($\dot{\epsilon}_m$). Graphite foils were placed at the tool/sample interfaces for lubrication. As quickly as possible after deformation, the furnace was lifted out and the sample was removed and quenched in water. Water quenching was recorded on video, and in practice the delay between the end of deformation and the sample being quenched was 3.0 s. This thermo-mechanical path is referred to as experiment 3 henceforth. A schematic plot of the thermo-mechanical procedure for experiment 3 is shown in Fig.3.10.

FE analysis for experiment 3

A 2D axisymmetric FE simulation of the compression test carried out in experiment 3, including the initial heating and soaking stages, was performed using the DEFORM software to predict the strain distribution at different locations along the

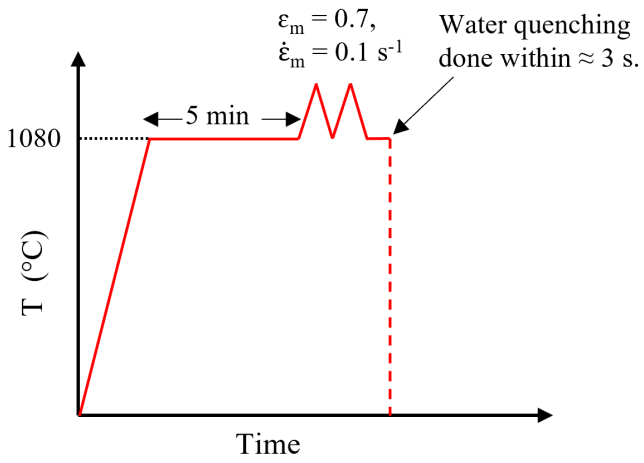


Figure 3.10: A schematic plot of the thermo-mechanical path applied in experiment 3.

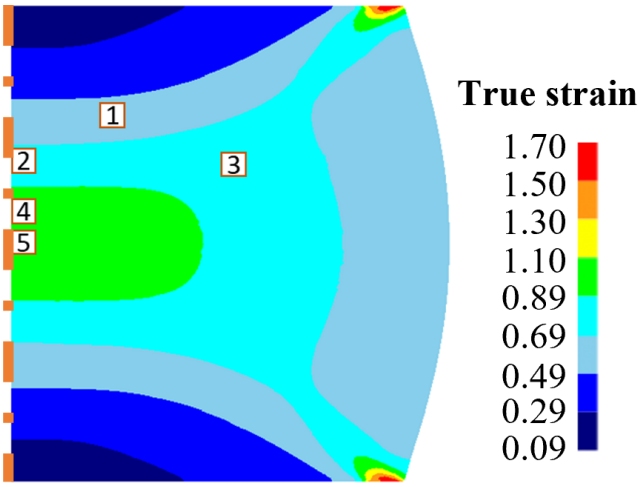


Figure 3.11: The strain distributions predicted by DEFORM FE simulations for the sample compressed in experiment 3. The locations of 5 regions from which EBSD data was collected are indicated.

sample. The strain distribution produced is shown in Fig. 3.11. The same material data and values of heat transfer coefficient, friction coefficient and Taylor-Quinny used for modelling experiment 1 and 2 were used again here.

The workpiece was meshed into 5102 quadrilateral elements. The upper die's movement speed during the compression test was recorded, and this was used as an input for the FE simulation. The sample dimensions predicted by the model were compared with the actual dimensions of the deformed cylinder after compression.

Table 3.3: Map properties for five regions investigated with EBSD in Chapter 8.

Region number	Local strain	Map area (µm^2)	Step size	Indexing rate (%)
1	0.53	231.6 x 202.4	0.20	91.0
2	0.72	148.2 x 111.1	0.20	98.5
3	0.76	122.3 x 107.0	0.15	94.0
4	1.00	98.6 x 74.0	0.20	98.5
5	1.04	86.5 x 45.5	0.50	96.2

The model was set up to match the height of the deformed cylinder (7.83 mm), and it predicted a maximum diameter of 14.54 mm, which was within 3 % of the measured diameter of 14.13 mm. This validates the chosen values of heat transfer coefficient and friction coefficient, and suggests that the predicted strain distribution is reasonably accurate.

Microstructural analysis for experiment 3

The 3D shape of precipitates in the starting microstrucutre of this experiment were captured using FIB-SEM tomography as described in section 3.3.1. Data was captured from a data cube with dimensions of 59.3 µm x 18.2 µm x 14.9 µm was analysed. From this volume, a sub-volume with dimensions of 35.9 µm x 10.0 µm x 14.9 µm which displayed minimal curtaining effect was extracted and analysed. The analysis was done as described in section 3.3.1.

Four large area EBSD maps were taken at different strain levels to assess the overall progress of recrystallisation as a function of strain. These four EBSD maps came from four different regions along the axis of the compressed sample, and had areas of approximately 1.24 mm^2. They were taken using a step size in the range 2.5 to 4 µm. In these low magnification maps, at least 80 % of the points were indexed in all cases.

To investigate the local interaction between recrystallisation and precipitates, five additional EBSD maps were collected in selected regions of interest. The locations of these are shown schematically in, and the details of the five maps are given in Table 3.3.

Immediately before and after these five EBSD scans, FSE images were also captured from the same area using a FSD attached to the EBSD camera. Data from the two can be compared and overlaid (e.g., grain boundaries from the EBSD data

overlaid onto the FSE images).

4 Characterisation of industrial microstructures

Samples extracted from semi-converted ingots from the latter stages of industrial forging were made available for microstructural characterisation. Samples were extracted from different physical locations on the billet.

For samples from such large scale billets (with diameters around 200 mm at the end of open die forging), being produced under industrial conditions, the exact forging parameters used (i.e. time, temperature, strain and strain rate) are not readily available, and can vary significantly between different locations. Despite this, different grain and precipitate populations can be identified, and their micro-scale formation mechanisms can be explored. This will provide a useful introduction to the typical microstructure of AD730 during the latter stages of industrial billet forging.

4.1 The industrial forging route

Fig. 4.1 shows a schematic of an ingot to billet conversion process. The *goals* of the individual steps have been outlined in Chapter 3. However, achieving these goals in practice is not straightforward, and there are several considerations at each step:

1. Homogenisation is carried out at high temperatures, whilst avoiding incipient melting (limited to about 1200 °C [12]). Note that an excessive duration of homogenisation becomes too expensive and is not economically viable.

2. There is very little information available about the grain size and level of recrystallisation achieved after super-solvus forging. On the basis of a single super-solvus forging test done on AD730 in the literature it is unlikely that the as-cast structure is fully broken up dynamically, especially given the large starting grain size which will be present after homogenisation [22]. A mix of

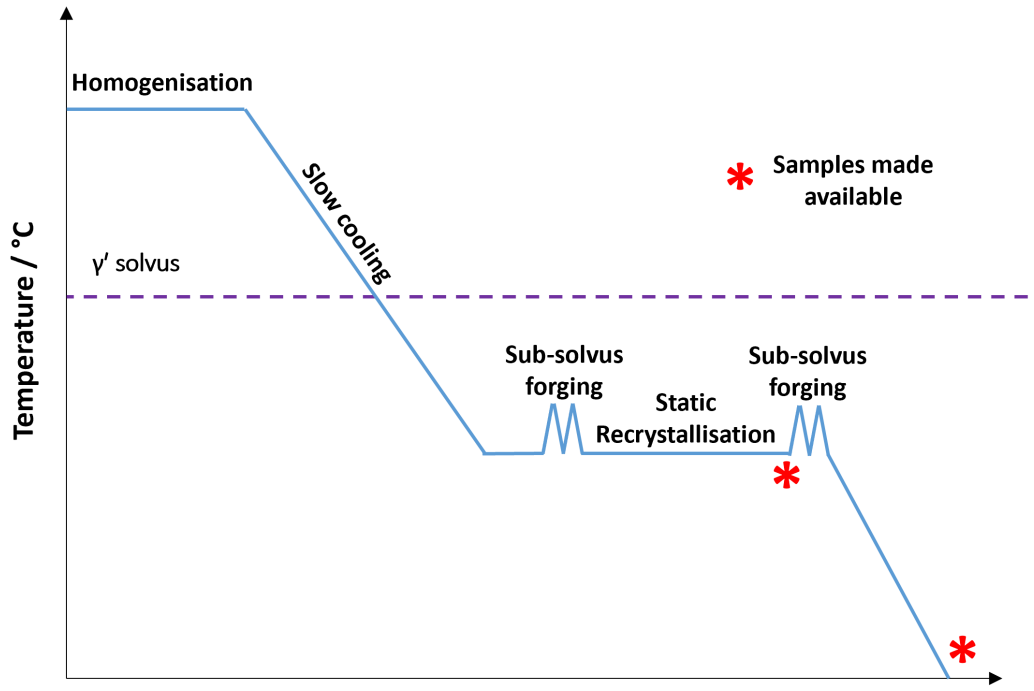


Figure 4.1: Schematic of an ingot to billet forging route. The stages of this process from which samples were made available are indicated by the red asterisks.

smaller recrystallised grains and much larger, deformed unrecrystallised grains are likely to persist in the billets being processed after super-solvus forging.

3. Cooling rate through the solvus will affect the temperature at which precipitation first occurs, the size precipitates grow to, and their morphology [15]. On industrial scale billets, cooling rates under controlled conditions in a furnace will be on the order of 10 °C/hr. Such slow cooling rates are not considered in lab scale trials, where slow cooling is, at slowest, 0.1 °C / s, i.e. 36 times faster than on the industrial scale [79]. Additionally, the temperature at which precipitation commences, and the kinetics of precipitation growth may be different in recrystallised and unrecrystallised grains due to their different dislocation densities [22], although this effect may be lessened by recovery.

4. The level of recrystallisation achieved during sub-solvusolvus forging has been shown to depend heavily on the applied strain, but even in lab scale samples compression to a macroscopic strain of 3 only generated a structure which was 88 % recrystallised [25]. Such high strains are not feasible in an industrial scale

process. Generally, in billet conversion the length of the ingot is increased by a factor of 4, and the diameter is halved, i.e. a macroscopic strain of 1.39.

5. Static recrystallisation can be very effective in consuming unrecrystallised grains remaining after sub-solvus forging. Certain recrystallised grains with favourable orientation relationships to the unrecrystallised grains can grow rapidly, and overcome the fine and dense precipitation in the unrecrystallised grains [23]. This could, however, bring the risk of overgrowing the recrystallised grains, such that their sizes fall outwith acceptable limits and cannot be reduced sufficiently in the final sub-solvus forging. This treatment may also affect the size of the γ' precipitates; as discussed in Chapter 2 (section 2.4.3), the evolution of precipitate size is very sensitive to temperature, and becomes faster and faster on approaching the solvus [12].

6. As will be shown in section 4.4, large unrecrystallised grains remain, even after the final sub-solvusolvus forging. These could result from either unrecrystallised grains which resist static recrystallisation, or from large recrystallised grains formed by static recrystallisation, which are then deformed in the final sub-solvus forging, but do not fully recrystallise.

In this chapter, samples taken from the end of the static recrystallisation step and the end of the final sub-solvus forging were analysed by means of BSE and SE imaging, and using EBSD data. These data allow for different phases to be identified, precipitates to be assessed in terms of size and morphology, and grain size and recrystallisation level to be calculated. This information allows suggestions to be made regarding the mechanisms underpinning the microstructural changes.

4.2 Samples investigated

Samples were available from two different stages of the industrial forging route; after static recrystallisation and after the final sub-solvus forging stage. These stages are indicated in Fig. 4.1. For each case, samples were also provided from different physical locations on the billet. The location of each sample on the billet is described by its axial position (i.e. at the head (H) or foot (F) of the billet) and its radial position (i.e. at the centre (C), mid-radius (M) or the edge (E) of the billet).

Six samples were provided from after the after static recrystallisation stage. Their locations with respect to the billet are indicated in Fig. 4.2. Only three samples were provided from after the final sub-solvus forging, from locations FE, FM and FC on Fig. 4.2, i.e., from the centre, mid-radius and edge at the foot of the billet. In both cases, the samples provided came from the so called 'Dead zone' of the billet. These zones correspond to the axial extremities of the billet, which are removed at the end of open die forging, as the levels of strain applied here are lower than elsewhere on the billet.

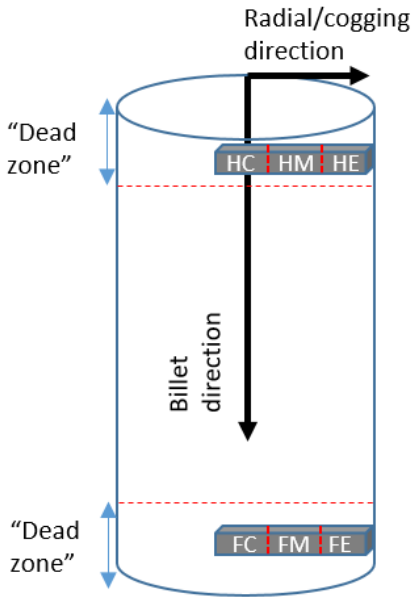


Figure 4.2: A schematic of a billet indicating the different locations from which samples were provided. H and F refer to axial position on the billet, being head and foot, respectively. The second letters C, M and E refer to radial position, being centre, mid-radius and edge, respectively.

4.3 Samples from the static recrystallisation step

4.3.1 General microstructural overview

This sub-section will give an overview of the microstructure after the static recrystallisation stage of the industrial forging process, and comment on the statically recrystallised grains whose formation Vernier *et al.* have described previously [23].

Fig. 4.3 shows a sample from the static recrystallisation step of the industrial forging route, from location HE. Note that the IPF map in (c) is not colored with respect to any particular billet direction. Three types of grain population are present at this stage of the forging process. A summary of these is given below:

1. Statically recrystallised grains. These are recrystallised grains which have grown during the static recrystallisation stage to large sizes. Such grains have been observed and described previously by Vernier *et al.* [23, 24]. These grains are observed to approximately share a $\langle 111 \rangle$ axis with a neighbouring unrecrystallised grain, which they rapidly consume. Vernier *et al.* also observed that these grains contain precipitates which appeared rectangular in 2D sections, and had either a close to twin or close to coherent orientation relationship with their host grain (coherent here meaning they share the same crystallographic orientation). Such precipitation is also seen here, highlighted in Fig. 4.3 (e).

2. Unrecrystallised grains. These are large grains (equivalent circle diameters on the order of 200 µm) with higher dislocation densities than the other grain populations. These higher dislocation densities can be seen through their varying contrast in IPF maps, and the higher KAM values in these grains. They contain a more fine and dense distribution of precipitates than the other grain populations. By segmenting the image in Fig. 4.3 (d) and measuring 1016 of the precipitates in the unrecrystallised grains, their average equivalent circle diameter was estimated at 1.2 ± 0.5 µm.

3. Small recrystallised grains. These are found at the boundaries between large unrecrystallised grains. They contain a mix of intergranular and intragranular precipitates. The intragranular precipitates share the orientation of their host grain sufficiently closely that the two can not be well distinguished in EBSD data. The size and locations of these grains indicate that they have formed dynamically/post-dynamically during sub-solvus forging, but not grown significantly during the static recrystallisation treatment.

The formation mechanism of the large statically recrystallised grains has been covered in section 2.5.1 Chapter 2. Fig. 4.4 shows a special case of a statically recrystallised grain which allows an additional observation to be made regarding the growth of these grains. In Fig. 4.4 (a),(c),and (e), the beige statically recrystallised grain has partially consumed its neighbouring purple unrecrystallised grain. The

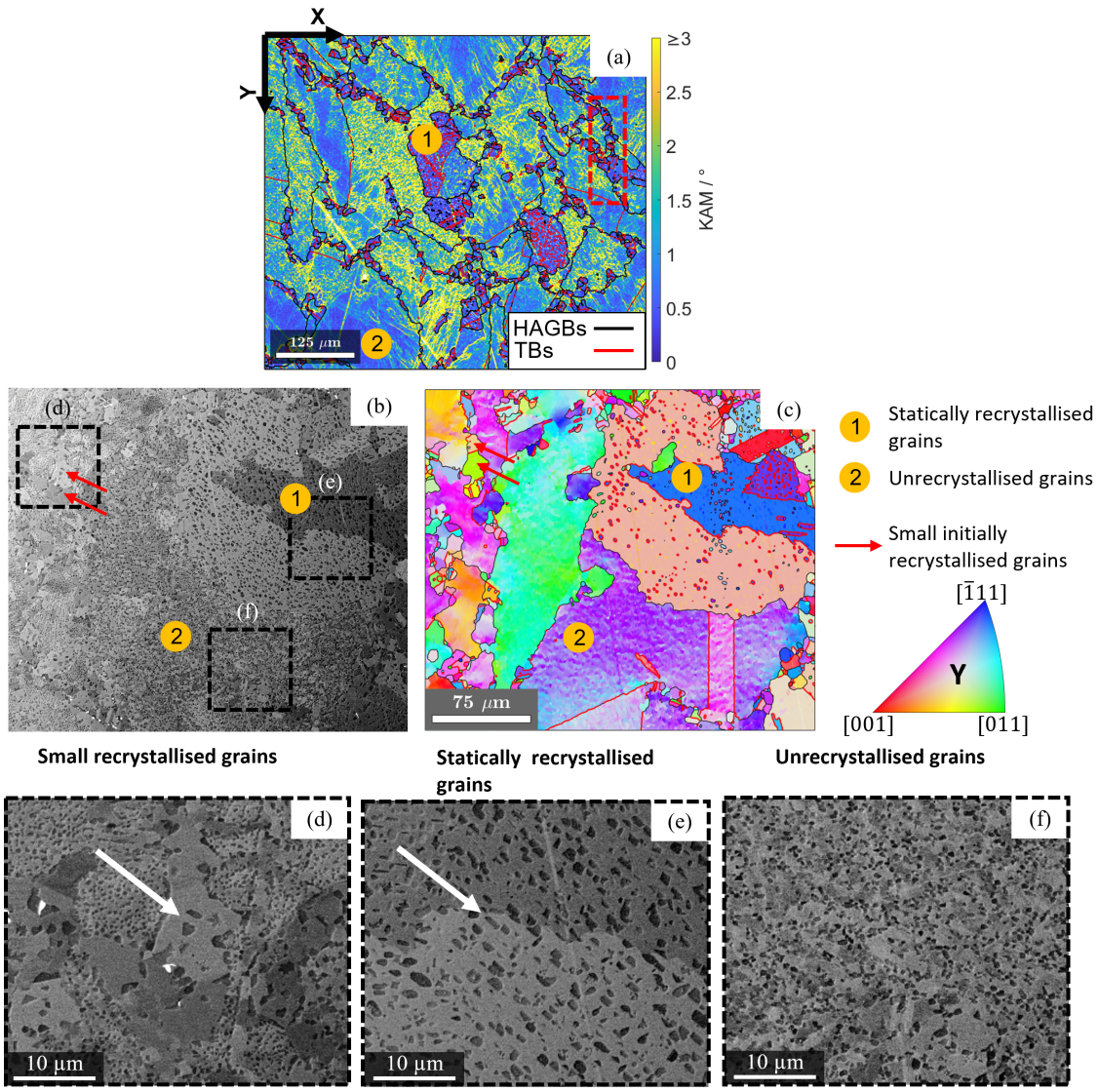


Figure 4.3: Overview of the microstructure after the static recrystallisation step of the industrial forging process, from a sample from location HE. (a) A wide field KAM map with a kernel radius of 5 µm (first order neighbours), values limited to 3 °, where three distinct populations are indicated, (b) a BSE micrograph and (c) the corresponding IPF map of another area. (d),(e) And (f) show higher magnification views of the precipitate states in the three grain populations. The white arrows in (d) and (e) indicate some typical precipitates for the small recrystallised grains and statically recrystallised grains.

two approximately share a ⟨111⟩ axis, as is shown by the pole figure in Fig. 4.4 (b), where the shared ⟨111⟩ axis is enclosed by the red circle. This purple grain contains a twin, with a pink contrast, and this twinned region does not share a ⟨111⟩ axis with

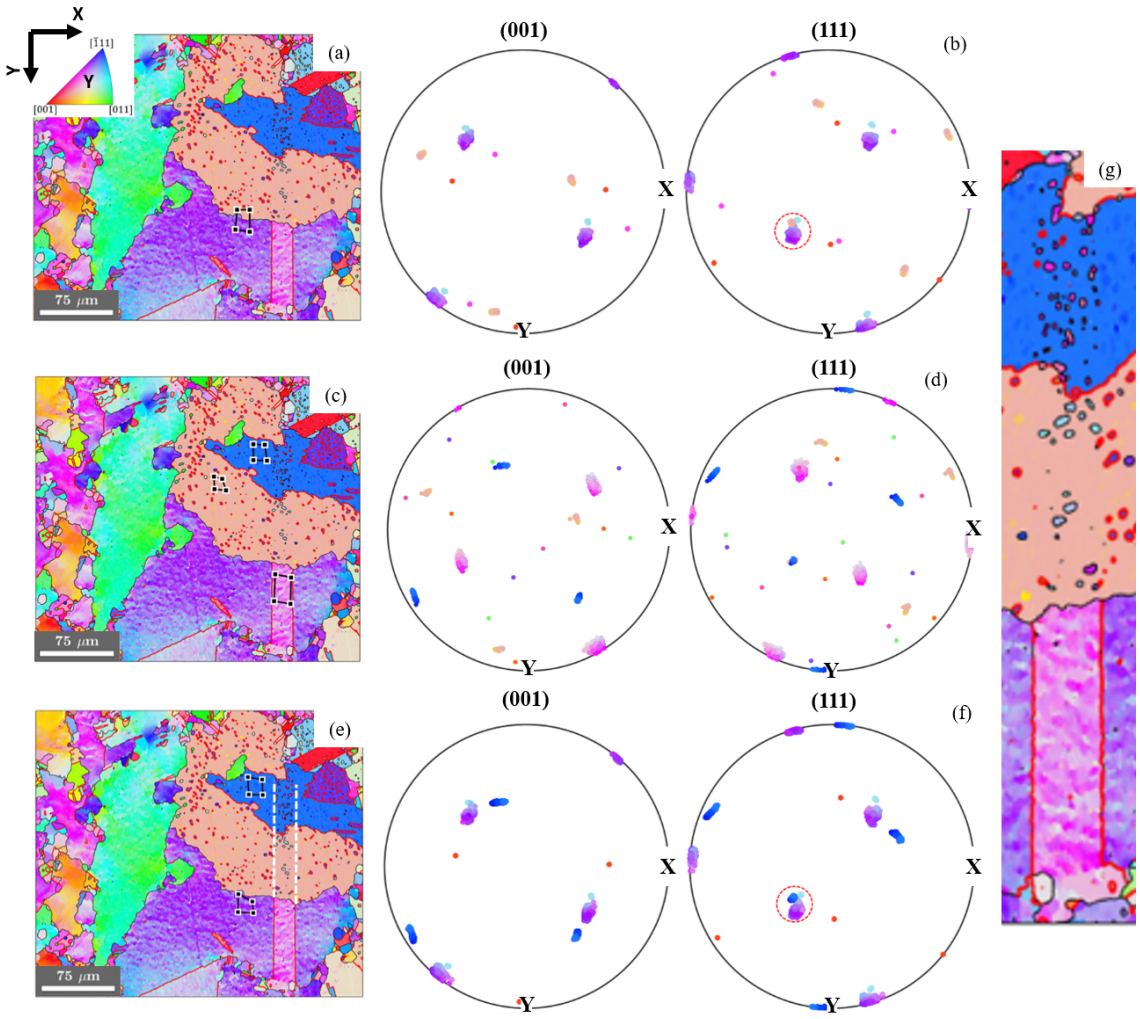


Figure 4.4: The effect of a twin in a deformed grain on the growth of statically recrystallised grains; taken from a sample from location HE. The first column ((a),(c),(e)) shows an IPF Y map from which (001) and (111) pole figures have been plotted from the indicated areas. The second column ((b),(d),(f)) shows the (001) and (111) pole figures for the areas highlighted in the first column. A region of interest is indicated with the white dashed lines in (e) is enlarged in (g) for clarity. The same orientation color coding defined in the insert in (a) is used to plot the pole figures.

the beige grain, which is shown in the pole figure in Fig. 4.4 (d). It does, however, share a ⟨111⟩ axis with its purple parent grain (the twin boundary misorientation axis is the ⟨111⟩ axis lying closest to the x direction). Despite this, the beige grain still consumes the twinned region with which it does not share a ⟨111⟩ axis.

The twinned region of the recrystallised grain has also had an influence on the

orientation of the precipitates forming in the blue and the beige statically recrystallised grains. Along the length of the twin in the unrecrystallised grain which has been consumed (shown by the white dotted lines in Fig. 4.4 (e), and enlarged in (g)), the precipitates in the statically recrystallised grains have different orientations to elsewhere in those grains. In the portion of the beige grain which has consumed the twin, the precipitates are not twin related to the beige grain, although they are elsewhere in that grain. In the portion of the blue grain which has consumed the twin, the precipitates are not close to coherent with the blue grain, although they are elsewhere in that grain. In terms of morphology, the precipitates in the twinned region show similar rectangular facets to the other precipitates in the statically recrystallised grains, although these are not aligned in the same direction as the other precipitates.

This unrecrystallised grain containing a twin provides an example of a special case where two atypical features can be noted. These only arise in the special case where the deformed grain being consumed contains a twin, which is not twinned about the $\langle 111 \rangle$ axis it shares with the statically recrystallised grain:

1. A statically recrystallised grain can grow to large sizes by consuming a deformed region with which it does not locally share a $\langle 111 \rangle$ axis.

2. As a consequence, the precipitates formed in a statically recrystallised grain can show an orientation which is neither close to twin related or close to coherent with the grain which houses them.

4.3.2 Microstructures at different billet locations

Microstructural observations along radial direction at the billet head

The first column of Fig. 4.5 shows low magnification IPF maps for samples from locations HE, HM, and HC of the billet from the static recrystallisation stage of the industrial forging process. These show that grain size is very large, diameters on the order of 500 µm, and that the area fraction of small recrystallised grains at the boundaries of the larger unrecrystallised grains is low. The second column shows corresponding GOS maps, from which the statically recrystallised grains, which are large and have GOS values $\leq 2°$, can be distinguished from the unrecrystallised grains, which are large but have GOS values $\geq 2°$. Some twin γ/γ' interphase

boundaries can be found in large grains with low GOS values in Fig. 4.5 (b), which likely correspond to the T type precipitates. The large step size used to collect these maps (5 µm) means few such precipitates can be distinguished in this way.

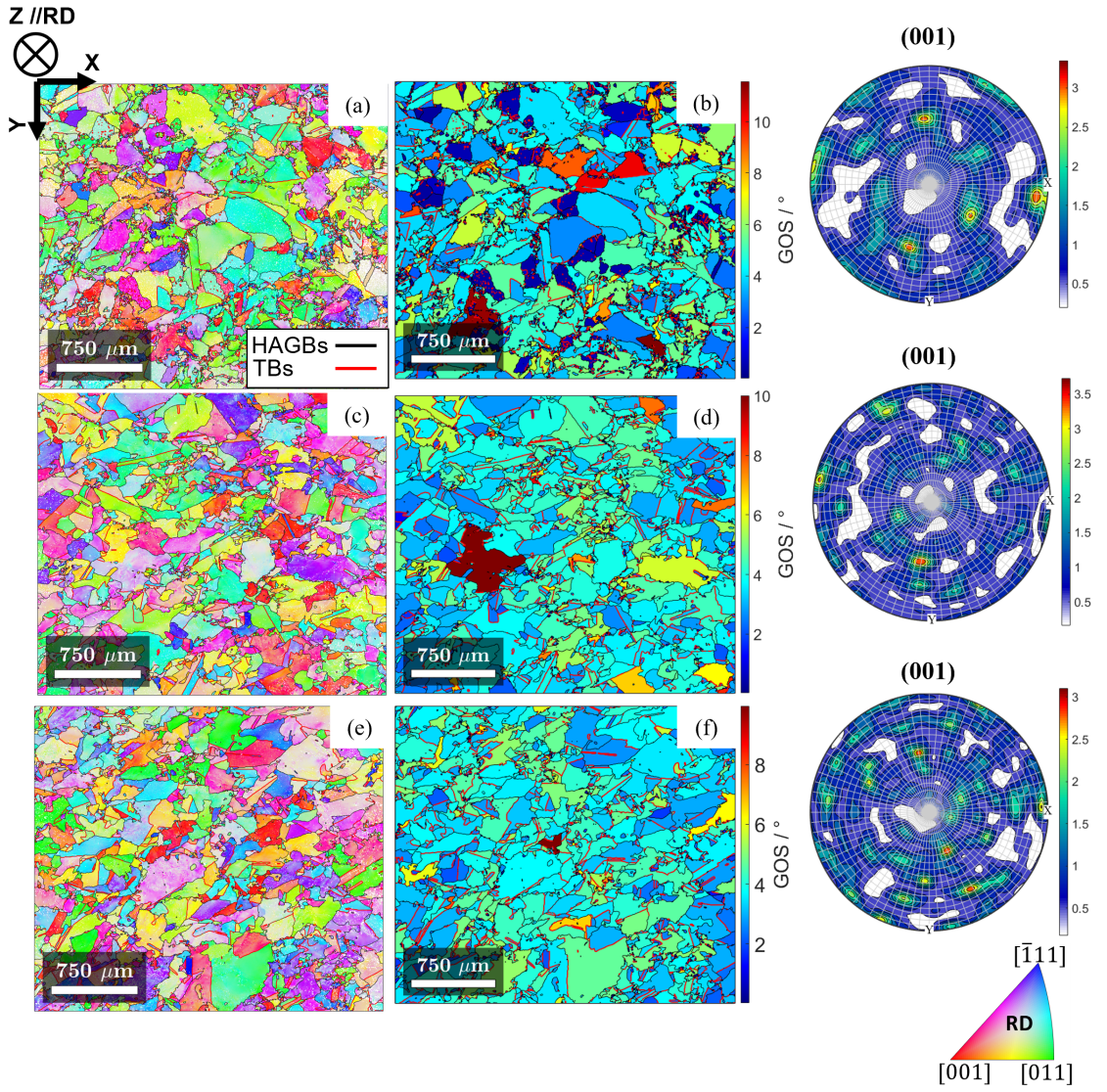


Figure 4.5: IPF maps, coloured with respect to a radial direction (RD) of the billet, of samples taken from the end of the static recrystallisation stage of the industrial forging route. The first column ((a),(c) and (e)) show IPF Y maps for samples from locations HE, HM and HC, respectively, while the second column ((b), (d), and (f)) shows the corresponding GOS maps. (001) Pole figures show that there is not a very strong texture at this stage of processing.

Microstructural data extracted from Fig. 4.5 have been summarised in Fig. 4.6,

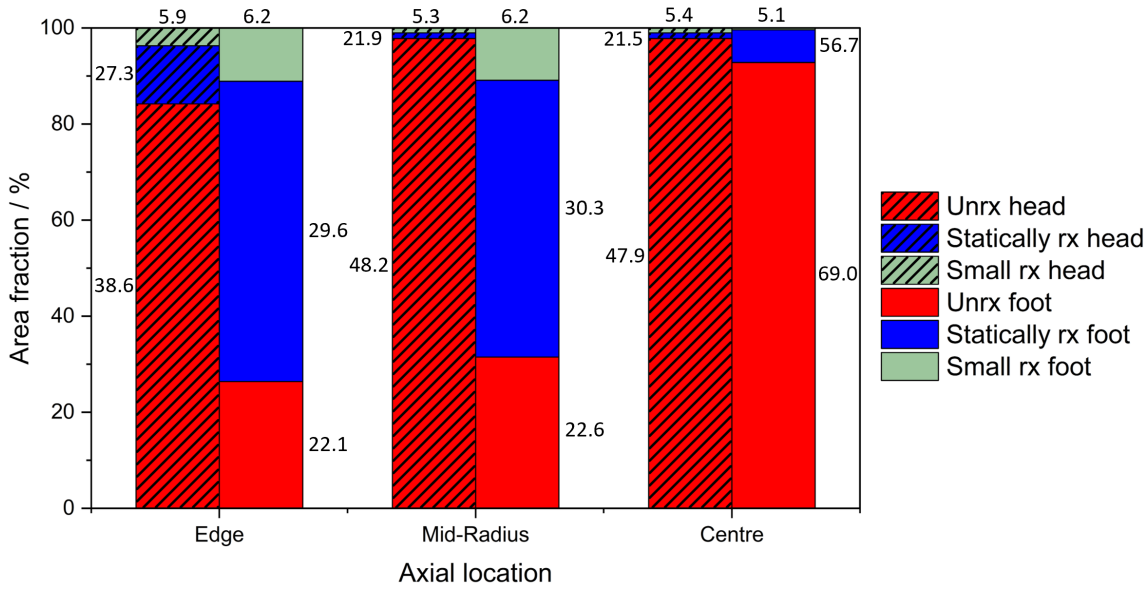


Figure 4.6: Area fractions of different grain populations at the head and foot of the billet (solid and dashed bars, respectively). The numbers indicate the average grain size for each population in micrometers.

and are shown in the solid bars. The area fraction of small recrystallised grains (i.e. grains which have equivalent circle diameters less than 15 µm and GOS values ≤ 2 °) is shown, as is the area fraction of statically recrystallised grains (i.e. grains which have equivalent circle diameters greater than 15 µm and GOS values ≤ 2 °). The area fraction of unrecrystallised grans (i.e. grains which have GOS values ≥ 2 °) is also shown.

The data in Figs. 4.5 and 4.6 show some of the differences in microstructure with radial position in the billet. The overall recrystallisation level is larger towards the edge of the billet and lower towards the centre. This difference is due to the presence of the large statically recrystallised grains, which are found at the edge of the billet but not at the centre or mid-radius positions.

Due to the lack of large statically recrystallised grains, C/T type precipitates are not found in samples from the mid-radius and centre of the billet.

Microstructural observations along radial direction at the billet foot

Similar data to those in Fig. 4.5 obtained from the billet head are shown for the samples from along the radius of the foot of the billet in Fig. 4.7. Microstructural

data extracted from Fig. 4.7 have been summarised in Fig. 4.6, and are shown in the dashed bars. The trends are similar to the ones identified at the head of the billet. Again, the fraction of large statically recrystallised grains containing C/T type precipitates is higher at the edge, and decreases towards the center. In this case, however, such grains can be identified at the mid-radius position, which was not the case at the head of the billet. The area fraction of small recrystallised grains also decreases towards the centre, as was the case at the head of the billet. Here however, the overall fraction of such grains is much higher at the edge of the billet (11.1 %) than it was at the head (1.0 %). For both the head and foot of the billet, whenever the large statically recrystallised grains have formed they cover a significant area fraction, well in excess of that covered by the small recrystallised grains.

Although there is a significant difference in terms of overall recrystallisation level between head and foot of the billet, the same trend is seen on moving from the edge to the core in each region.

Without further information on the thermo-mechanical path experienced by the billet, the following can be suggested to explain this observation:

The lower area fraction of large statically recrystallised grains at the core, may be due to a non-uniform temperature distribution across the billet during the static recrystallisation step (shown schematically in Fig. 4.1). Here, the periphery of the billet will reach temperature quicker than the core, and will be held at the target static recrystallisation temperature for longer, giving more time at temperature for the statically recrystallised grains to grow. These different thermal histories will may also cause different precipitate states across the billet radius, though this was not investigated in detail.

An additional factor is the distribution of stored energy across the radius of the billet. The first sub-solvus forging step may impart more stored energy towards the edges of the billet (hence the slightly higher fractions of small recrystallised grains towards the edges of the billet) and this provides a larger driving force for the static growth of recrystallised grains.

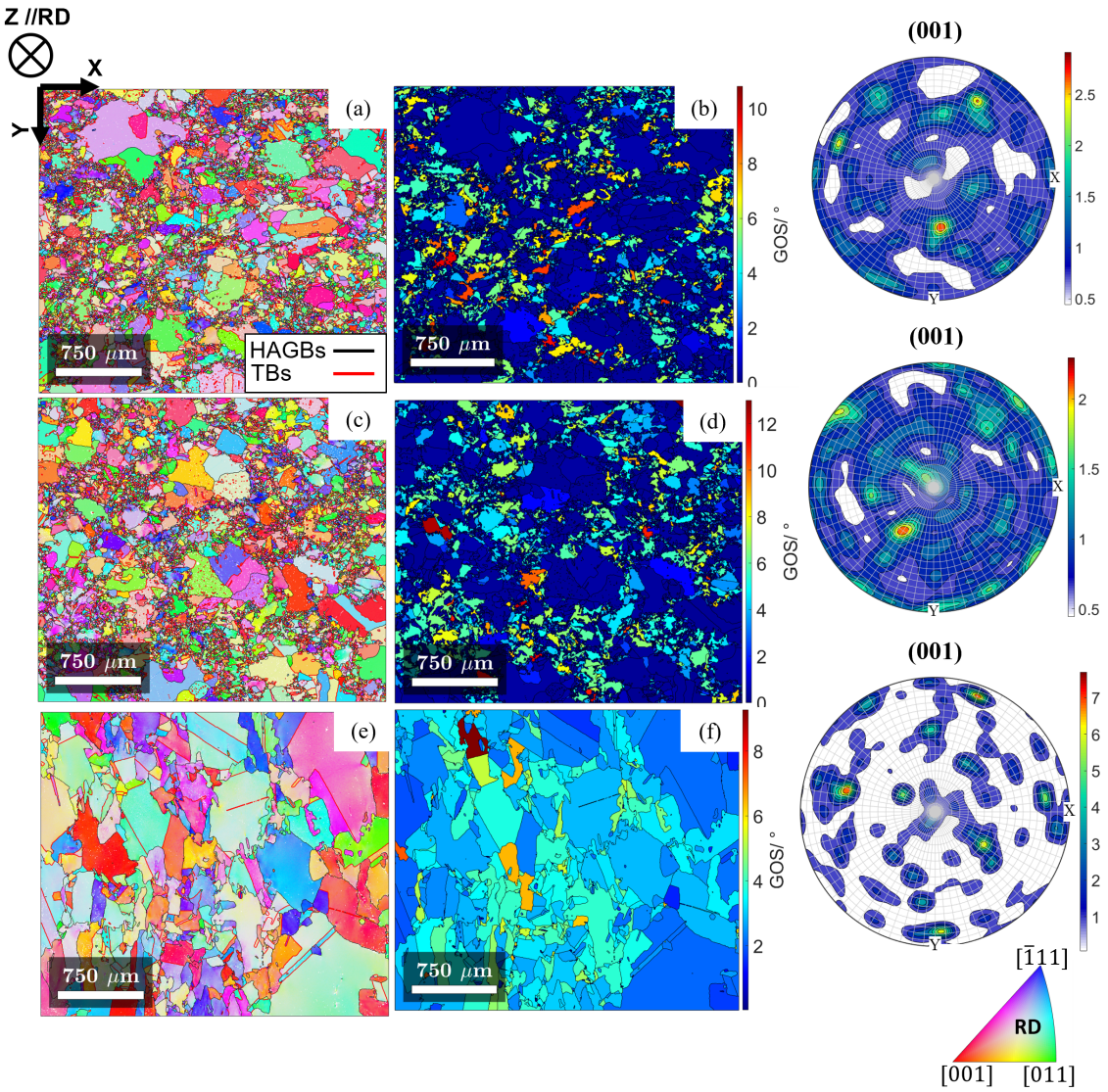


Figure 4.7: IPF maps, coloured with respect to a radial direction (RD) of the billet, of samples from the static recrystallisation stage of the industrial forging route. The first column ((a),(c) and (e)) show IPF Y maps for samples from locations FE, FM and FC, respectively, while the second column ((b), (d), and (f)) shows the corresponding GOS maps. (001) Pole figures that there is not a very strong texture at this stage of processing. The higher mrd values in location FC are due to the larger grains there, meaning fewer orientations are sampled.

4.4 Samples from the final sub-solvus forging step

4.4.1 General microstructural overview

Three samples were investigated from the end of the industrial forging process, i.e. from the final billet material. These all came from the foot of the billet, i.e. locations

FE, FM and FC (see Fig. 4.2.

An overview of the microstructure in location FE at this stage is given in Fig. 4.8. Here two distinct grain populations can be identified (as opposed to the three grain populations found after the static recrystallisation stage). There are (i) large unrecrystallised grains, and (ii) small recrystallised grains. In Fig. 4.9 the precipitates found in these two grain populations are shown in more detail, and their crystallographic orientations with respect to their host grains are shown. From these two figures the following observations can be made:

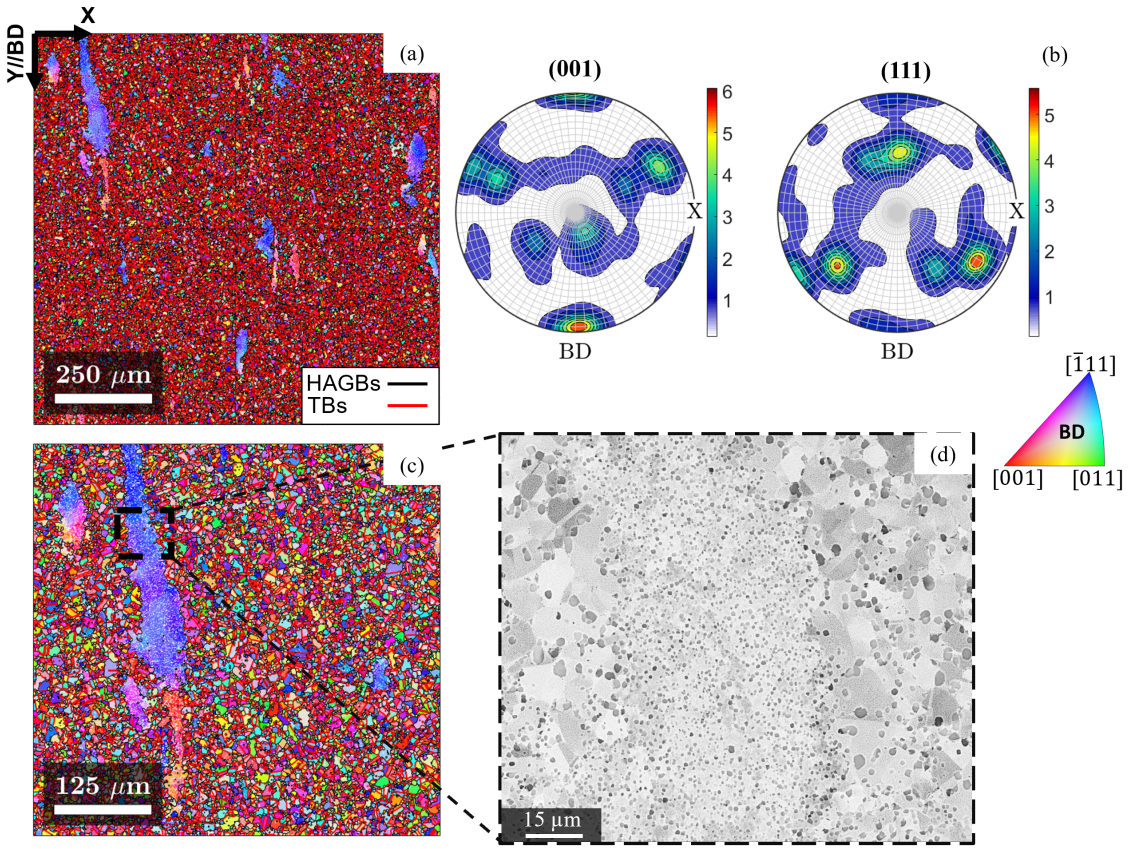


Figure 4.8: An overview of the microstructure in location FE at the end of the industrial forging route. An IPF map coloured with respect to the billet direction (a) with (111) and (100) pole figures for the large unrecrystallised grains (b). A higher magnification view of the top left corner of (a) and an associated BSE image (d) showing the different precipitation states in small grained recrystallised areas and in unrecrystallised grains.

1. The small recrystallised grains are equiaxed, with an average area weighted

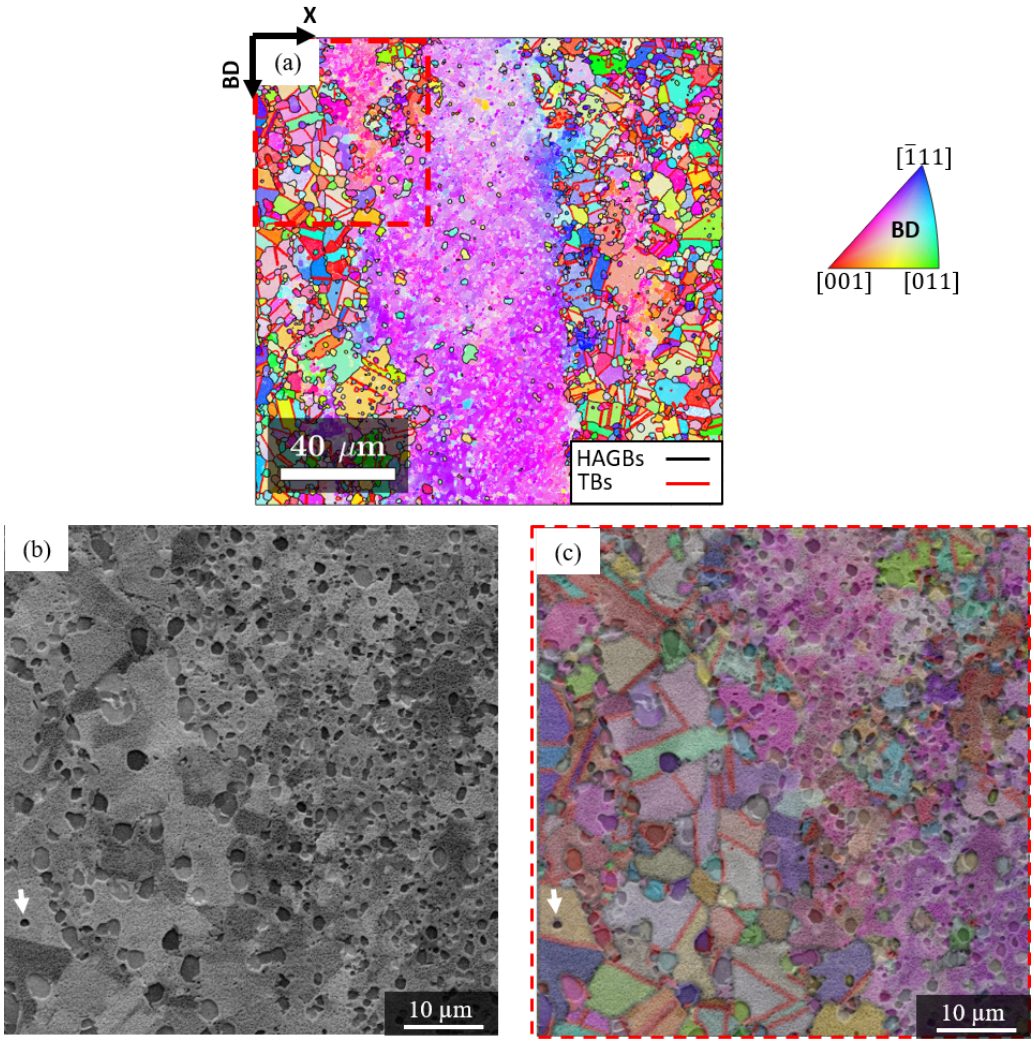


Figure 4.9: An IPF map coloured with respect to the billet direction from location FM at the end of the industrial forging route, showing small recrystallised grains and a large unrecrystallised grain (a). A BSE image from a selected region of interest, showing the precipitation state (b). Overlaying the IPF map onto this image shows the crystallographic orientations of the precipitates compared with their host grains (c). The white arrow indicates an example of a precipitate which appears intragranular and shows no special orientation relationship to its host grain.

equivalent circle diameters on the order of 6.6 µm. They have primary γ' precipitates with equivalent circle diameters on the order of 2.2 µm located predominately at their boundaries, which do not show any special orientation relationship to the grains whose boundaries they intersect. There are some precipitates which appear intragranular in these 2D micrographs, which also

do not show any special orientation relationship to their host grains. They also contain smaller intragranular secondary γ', which can just be made out in Fig. 4.9 (b). The orientations of these secondary precipitates could not be well measured due to the limited resolution of EBSD. These will have formed on cooling after forging.

2. The large unrecrystallised grains are elongated parallel to the billet direction. Their geometry reflects the overall shape change of the billet during the conversion process, which becomes elongated along the billet direction, and compressed along the radial directions. These grains show a crystallographic texture, which in this case is a $\langle 111 \rangle$ axis along the billet direction, shown in the pole figures in Fig. 4.8 (b). In this pole figure the unrecrystallised grains were identified as those with equivalent diameters above 15 µm and GOS values above 2 °. It will be shown in section 4.4.2 that the unrecrystallised grains may also show a $\langle 100 \rangle$ axis along the billet direction. These grains contain intragranular primary precipitates which approximately share the crystallographic orientation of their host grain, indicated in Fig. 4.9 (c). These precipitates have equivalent diameters on the order of 1.3 µm; these are smaller than in the surrounding recrystallised regions, where precipitates have equivalent diameters on the order of 2.2 µm. Note that this value of 1.3 µm is almost identical to the size of precipitates in the unrecrystallised grains after the static recrystallisation step, which was estimated at 1.2 µm based on precipitates measured in Fig. 4.3 (b). The large unrecrystallised grains also contain small secondary precipitates.

4.4.2 Microstructural observations along radial direction at the billet foot

Fig. 4.10 shows large area (8 mm^2) IPF maps for the samples taken from locations FE, FM, and FC from the end of the industrial forging process, along with $\langle 111 \rangle$ and $\langle 100 \rangle$ pole figures for the unrecrystallised grains (unrecrystallised grains were classed as those with equivalent circle diameters above 15 µm and GOS values $>$ 2 °). These EBSD data were taken with a step size of 3 µm, which allows the large unrecrystallised grains to be investigated, but with limited details of the small recrystallised grains.

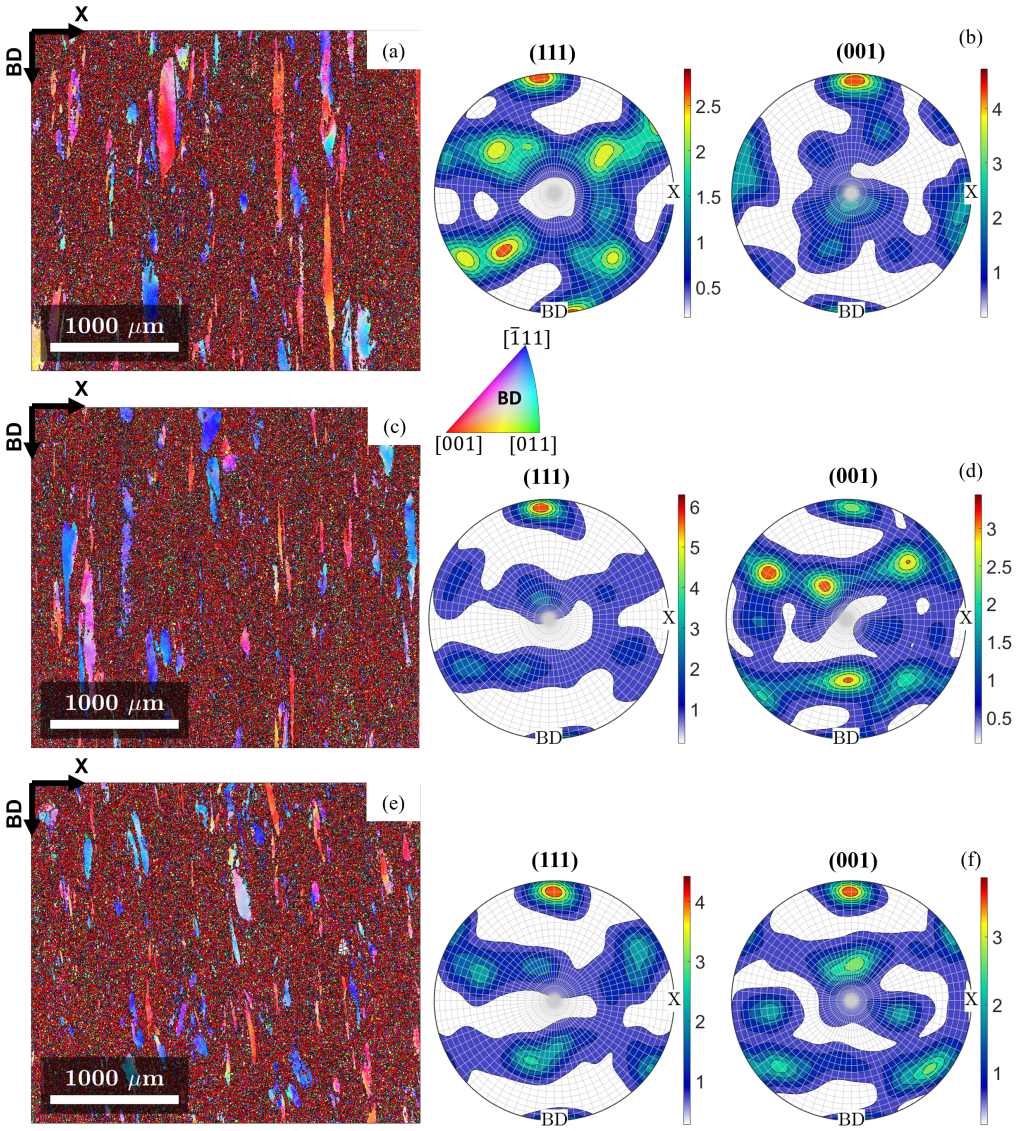


Figure 4.10: An overview of the microstructure at different locations at the foot of the billet at the end of the industrial forging route. The first column ((a),(c) and (e)) shows IPF maps coloured along the billet direction (BD). The second column ((b),(d) and (f)) shows corresponding $\langle 111 \rangle$ and $\langle 100 \rangle$ pole figures for the unrecrystallised grains. The first row (a-b) shows data from location FE, the second row (c-d) shows data from location FM, and the third row (e-f) shows data from location FC.

These show that the microstructure is consistent along the radial direction after the final sub-solvus forging than after the static recrystallisation stage (see Figs.4.7 and 4.5). The overall level of recrystallisation is quite similar in all three positions,

although there are a greater number of smaller unrecrystallised grains on moving from the edge of the billet (FE) to the centre (FC). In all three locations the unrecrystallised grains tend to show either a ⟨111⟩ or a ⟨100⟩ axis parallel to the billet direction. This is reflected in the pole figures in Fig. 4.10, and the tendency of the unrecrystallised grains to show blue or red colors in the IPF maps in Figs. 4.10 (a), (c) and (e). Some microstructural parameters extracted from the IPF maps are shown in Table 4.1. Notably this shows that the unrecrystallised grains are about 3 times smaller at the centre than at the periphery.

Table 4.1: Microstructural characteristics for samples FE, FM and FC taken from the foot of the billet at end of the industrial forging route.

Sample	Twin fraction (%)	Area weighted unrecrystallised grain size (µm)	Area fraction unrecrystallised grains (%)
FE	16.6	174 ± 123	19.4
FM	16.7	130 ± 101	16.1
FC	18.3	57 ± 86	16.7

4.5 Microstructural evolution during sub-solvus forging

Comparing the microstructures present after the static recrystallisation step and at the end of the final sub-solvus forging shows that the following are the major changes occurring during the final sub-solvus forging:

1. The large, statically recrystallised grains, and their characteristic C/T type precipitation are no longer present after the final sub-solvus forging.

2. The area fraction of small recrystallised grains increases significantly in all locations, such that the microstructure becomes more uniform with respect to radial position.

The loss of the large statically recrystallised grains suggests that the large increase in the area fraction of small recrystallised grains between at the foot of the billet

is primarily due to the consumption of the large statically recrystallised grains by recrystallised grains formed during the final sub-solvus forging. This would suggest that the unrecrystallised grains still present at the end of the industrial forging do not originate from the statically recrystallised grains. This hypothesis is based on examining the microstructure before and after this step, and will be investigated in more detail in Chapter 8, where samples from the static recrystallisation stage are forged on the lab-scale and recrystallisation mechanisms are studied in detail.

After the static recrystallisation step of the industrial forging process, the overall level of recrystallisation is determined almost exclusively by the large, statically recrystallised grains, as very few small recrystallised grains are present. Small recrystallised grains were observed to account for, at most, 11.1 % of the area fraction after the static recrystallisation step. This was in sample FE, shown in Figs. 4.7 (a) and (b). This suggests that the initial sub-solvus forging (i.e., that prior to the static recrystallisation stage shown in Fig. 4.1) does not produce a high level of dynamic recrystallisation. It is *possible* that small recrystallised grains had formed, but were consumed by the large statically recrystallised grains during the static recrystallisation treatment; however this is unlikely for two reasons:

1. The particular morphology and orientation of the C/T type precipitation found in the statically recrystallised grains is the result of a growth mechanism which is possible when the growing grain shares a $\langle 111 \rangle$ axis with the grain(s) which it is consuming. This condition would not be fulfilled for all the (differently orientated) recrystallised grains encountered by a growing statically recrystallised grain.

2. The thermodynamic driving force for consumption of the small recrystallised grains would be low, since these have low levels of internal stored energy.

As such, while the first sub-solvus forging treatment does not seem to be very effective at producing recrystallised grains, the subsequent static recrystallisation treatment can be very effective (producing recrystallisation levels up to 70 %). This is driven by the stored energy in the unrecrystallised grains which was introduced during the first sub-solvus forging.

Regarding the unrecrystallised grains, after the static recrystallisation they show relatively weak texture compared with after the final sub-solvus forging (compare the pole figures in Figs. 4.5 and 4.7 with those in Fig. 4.10). After the final sub-

solvus forging the remaining unrecrystallised grains show either a ⟨111⟩ or a ⟨100⟩ axis along the billet direction.

The precipitation in the unrecrystallised grains is not changed significantly during the final sub-solvus forging. Both after the static recrystallisation stage and at the end of the industrial forging route, the precipitates in the unrecrystallised grains are smaller than elsewhere and have a spherical morphology. The size of the precipitates in the unrecrystallised grains is similar after the static recrystallisation step and at the end of the industrial forging route (1.3 µm and 1.2 µm, respectively).

Fig. 4.11. shows a few examples of in unrecrystallised grains where the precipitates align and show a morphology typical for a discontinuous precipitation process. Examples of this were only found at the core of the billet. Examples are shown from after the static recrystallisation step and at the end of the industrial forging process.

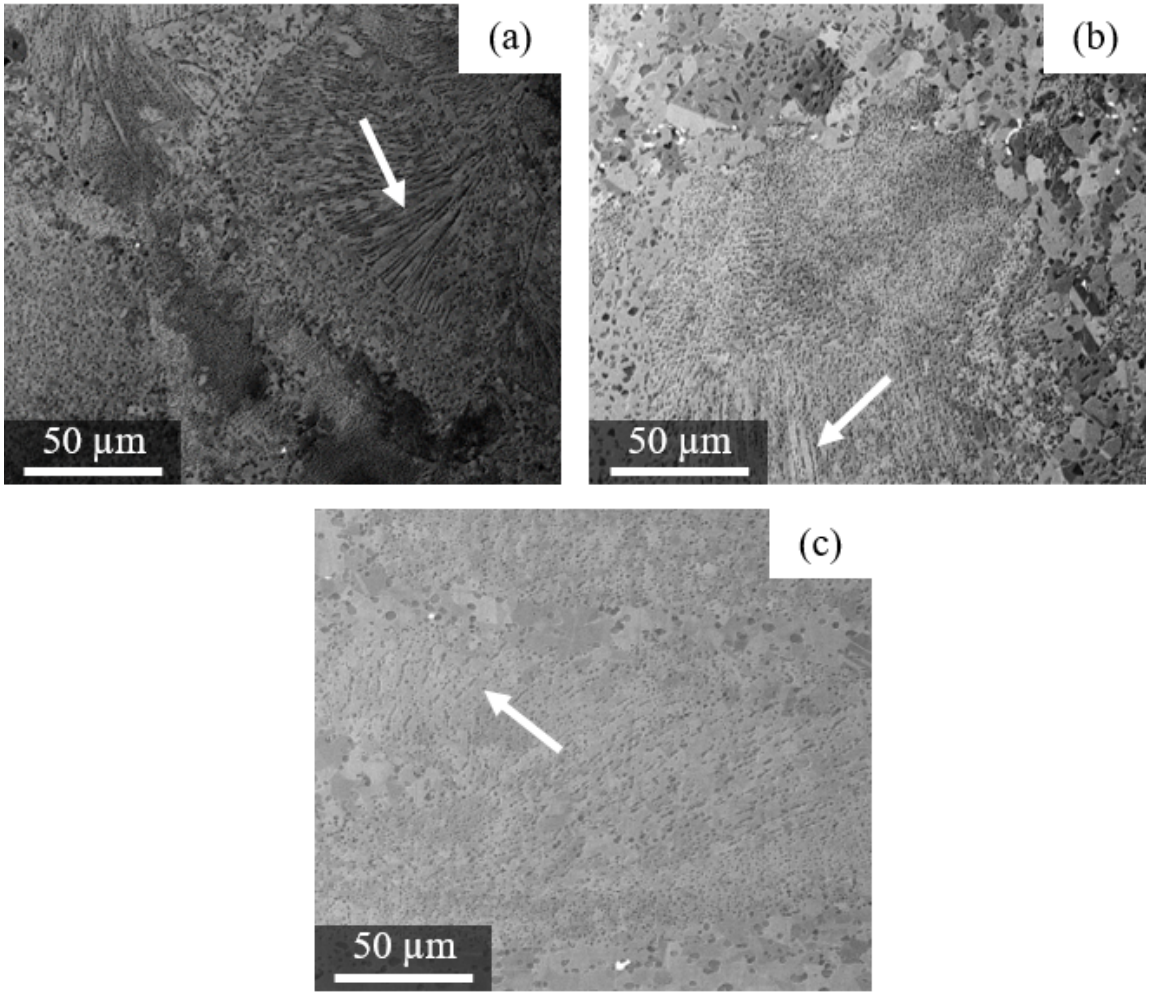


Figure 4.11: Examples of discontinuous precipitates after the static recrystallisation stage at the centre of the head of the billet (a) and at the centre of the foot of the billet (b). A discontinuous morphology can also be observed at the end of the industrial forging, at the centre of the foot of the billet (c). The white arrows indicate the regions where precipitates show a discontinuous morphology. The white particles in (a), (b) and (c) are likely to be MC carbides.

4.6 Summary

This chapter has described the microstructures typical of the latter stages of the industrial forging route. A fully recrystallised microstructure is not achieved at the end of this forging, and large unrecrystallised grains with a fine and dense distribution of spherical precipitates remain. The main conclusions are:

1. After the static recrystallisation step of the industrial forging route, three dis-

tinct populations of grain are present: (i) Large statically recrystallised grains, (ii) unrecrystallised grains and (iii) small recrystallised grains. At this stage, the area fraction of small recrystallised grains is higher towards the billets core than the edges, but quite low in all billet regions investigated ($\leq$ 11.1 %), implying that the first sub-solvus forging does not lead to significant dynamic recrystallisation. The area fractions of the other two grain types varies with billet location.

2. The area fraction of the statically recrystallised grains changes along the radial direction both at the head and foot of the billet. The static recrystallisation step is more effective at growing large statically recrystallised grains at the edges of the billet than at the core, perhaps because these regions spend longer at the intended temperature than the core of the billet, which is slower to heat up. A secondary reason for this radial dependence could be that the first sub-solvus forging step imparts more stored energy towards the edges of the billet, also resulting in the slightly higher fractions of small recrystallised grains there. Additionally, there may be a different precipitate distribution in the unrecrystallised grains along the radius of the billet, although this was not investigated in detail. Where effective, very large areas can be consumed by the statically recrystallised grains (area fractions in excess of 70 %).

3. There were some differences in microstructure along the axial direction of the billet. In the mid-radius and edge locations, the area fractions of both the small (likely dynamically) recrystallised grains and large statically recrystallised grains were higher at the billet foot than at its head, though the reason for this is not clear.

4. A case of a statically recrystallised grain which has grown by consuming an unrecrystallised grain containing a twin was observed, and this gave rise to an unusual case of precipitates in a statically recrystallised grain which were neither close to twin related (i.e. T type) nor close to coherent (i.e. C type) with it. However, these precipitates still showed the rectangular shape (in 2D micrographs) typical of precipitates in such grains.

5. After the final sub-solvus forging, only two distinct populations of grain were present; small recrystallised ones and large unrecrystallised ones. The large statically recrystallised grains and their distinctive precipitation could no longer

be identified. At this stage the microstructure was less sensitive to position within the billet than after the static recrystallisation step. From billet edge to centre, the recrystallisation level increased only slightly, although the average size of the unrecrystallised grains decreased significantly.

5 Precipitate evolution during the early stages of billet conversion

The early stages of the ingot to billet conversion process typically comprise a homogenisation heat treatment at high temperatures (limited to 1200 °C due to incipient melting) followed by super-solvus forging, cooling through the solvus temperature, then a sequence of sub-solvus forging and heating stages, as schematised in Fig. 3.1. This chapter will examine the microstructural changes happening during the early stages of this process, i.e. during the solvus transition. The precipitation state developed during *slow* cooling through the solvus will be characterised, with the role of remnant segregation being considered. The experimental protocol carried out was detailed in section 3.4.2 of Chapter 3, and a schematic of the relevant trials is given in Fig. 5.1 as a reminder. The starting material used in these trials was billet material, i.e. material from the end of the billet conversion process.

The cooling rate applied through the solvus temperature strongly affects the precipitate distribution which forms. Discontinuous precipitation in the form of fan type precipitates is favoured by slow cooling through the solvus [80], due to the higher grain boundary mobility. For continuous precipitation, slower cooling promotes a lower density of larger precipitates, and fast cooling promotes a higher density of smaller precipitates [16].

The slow cooling rate through the solvus applied here (10 °C/hr) is not typical of lab-scale trials on γ' precipitation, where the slowest cooling rates considered are not below 0.1 °C [79]. These rates are chosen to investigate the hardening precipitates forming during heat treatments which are carried out after forging. The slow rates investigated here are instead representative of the rates experienced by large billets during controlled cooling during industrial forging.

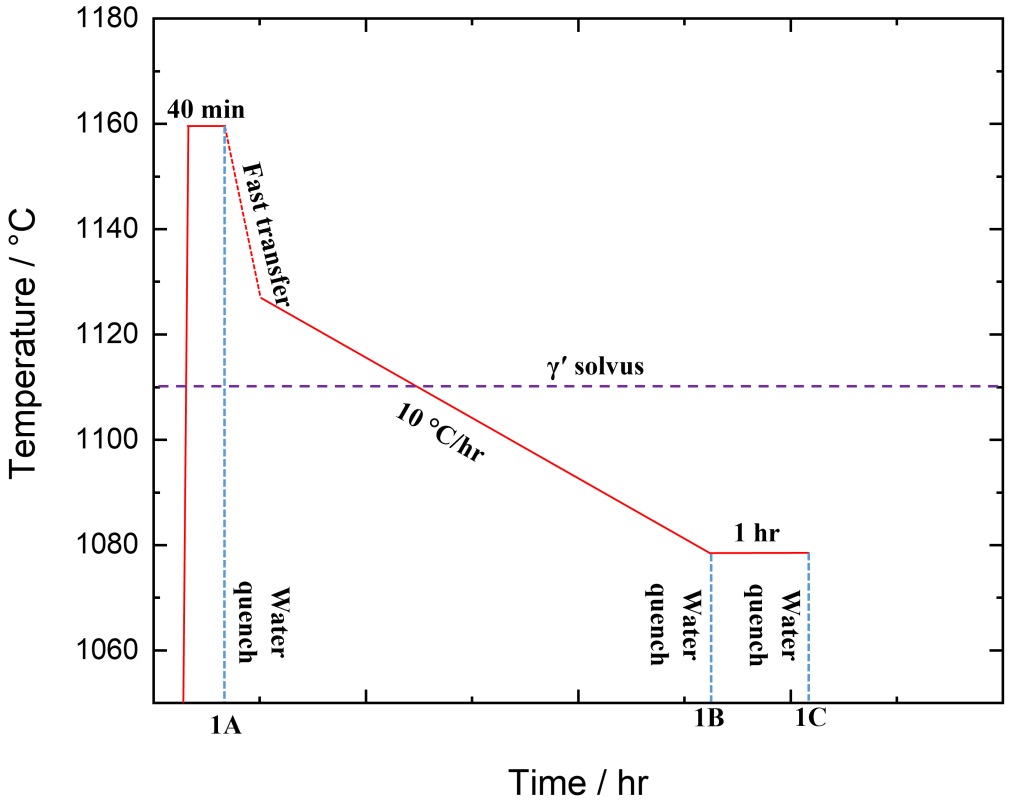


Figure 5.1: An overview of the experiments done to investigate precipitation during the early stages of industrial forging.

5.1 Microstructure after homogenisation

Fig.5.2 (a) shows a low magnification IPF Y color-coded map for sample A, which was held at 1160 °C for 40 minutes then water quenched. Discounting twin boundaries, the average equivalent circle diameter of the grains in this micrograph is 268 ± 215 µm. Figs. 5.2 (b-d) show sample A at a higher magnification, where there is evidence of pockets of remnant stored energy, predominantly near the grain boundaries and triple junctions. Regions can indeed be found where the γ matrix within a single grain shows contrast in BSE images, e.g., Fig. 5.2 (c). This is likely due to small orientation gradients, which can be an indication of stored energy.

These gradients are sufficiently small that they are not apparent in the IPF color-coded map (Fig. 5.2 (b)). A grain reference orientation deviation (GROD) plot, which shows the misorientation angle between each pixel in a grain and the average orientation of that grain, is shown in Fig. 5.2 (d). This shows that these orientation

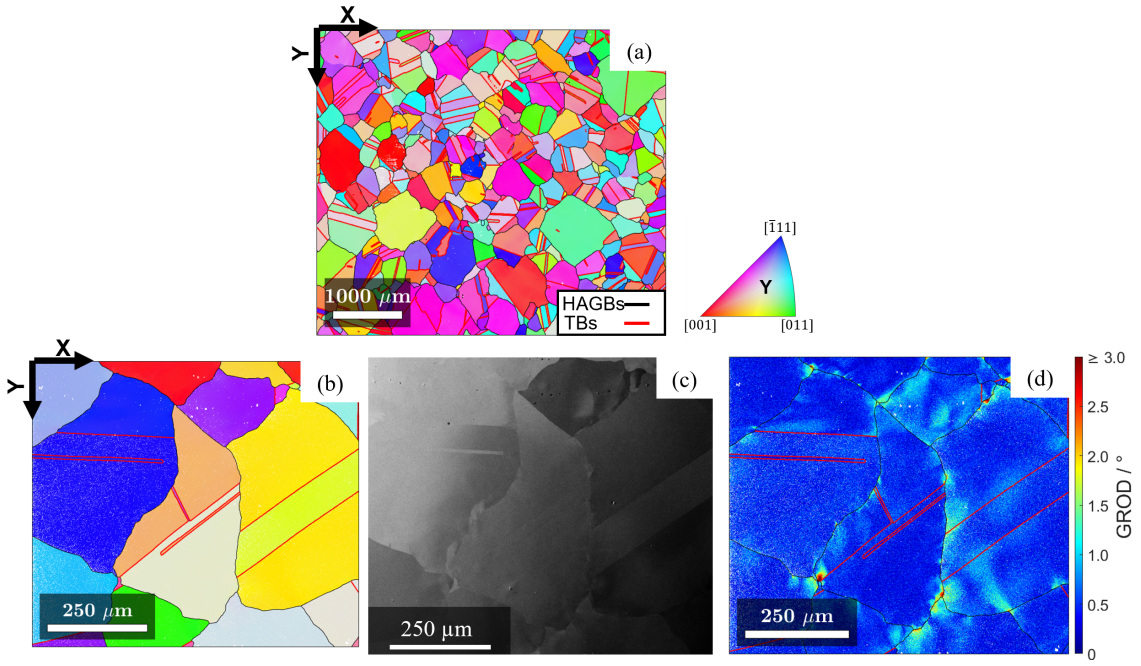


Figure 5.2: Overview of the microstructure of sample 1A, which was water quenched immediately after super-solvus holding. (a) A low magnification IPF Y map showing large, approximately equiaxed grains, (b - d) higher magnification micrographs of a region in sample A where the γ matrix shows intragranular contrast variations in BSE images (c), which correspond to low misorientations, indicated by the low values in the GROD map in (d). The Y direction is parallel to the sample's cylindrical axis.

gradients are indeed rather small, with few points exceeding a GROD of 1°, and these are concentrated around grain boundaries. However, since BSE contrast can be very sensitive to crystal orientation, these gradients are detected in the BSE image [81]. Such orientation gradients could be due to dislocations which form during water quenching; the formation of such dislocations has been shown in Inconel 718 [82], and is due to plastic flow under thermal stresses. Only γ' precipitates which formed during the water quenching are present, and these were too fine to be resolved at these magnifications. γ' Precipitates forming during water quenching from above the solvus temperature will have diameters on the order of 10 - 30 nm [22].

5.2 Overview of microstructure after precipitation

The 1 hour holding at the sub-solvus temperature (1080 °C) after slow cooling did not induce any significant microstructural changes; samples 1B and 1C (see Fig.5.2)

showed similar microstructures and will be discussed together.

Fig. 5.3 provides an overview of the microstructure in sample 1C, which shows the same key features as sample 1B. In both cases, a mixture of discontinuous and continuous precipitates have formed, producing a very heterogeneous precipitate distribution. All the precipitates formed have the same crystallographic orientation as their host grain (at least, the orientations are sufficiently similar that they cannot be distinguished based on EBSD data). The overall area fraction of precipitates was measured to be 12.6 % (based on the segmented FSE image, shown later in Fig. 5.19 (c)). All together, three different precipitate categories can be identified:

1. Discontinuous precipitates. These are most easily identified based on their morphology as alternating bands or branches of precipitates and matrix. Such a morphology is similar to the one produced by the eutectoid transformation. It should be borne in mind that depending on how these 3D branches intersect the 2D imaged surface, different apparent morphologies are possible in a 2D micrograph. Using the classifications of Williams and Butler, both type 1 and type 2 discontinuous precipitation reactions are observed [83]. In type 1, the reaction happens as a grain boundary moves through a super-saturated matrix with no precipitates, and type 2 when a boundary moves through a region with precipitates. An example of the type 1 reaction is shown in Fig. 5.3 (c).

2. Continuous precipitates. These are most easily identified in the form of ocotodendrites, which is a shape known to be the result of the growth of initially spherical continuous precipitates [44, 47]. Fig. 5.3 (b) shows this type of continuous precipitate. There are also more regularly shaped precipitates which show a spherical morphology in the micrograph in Fig. 5.3 (c), though these could be an end on view of discontinuous precipitates.

3. Grain boundary precipitates. There are two separate categories of grain boundary precipitate which can be observed after slow cooling through the solvus; those which are at the discontinuous reaction front (Fig. 5.3 (c)) and those which are not (Fig. 5.3 (b)). Zhang *et al.* have shown that in the γ-γ'' superalloy alloy945X, precipitation happens preferentially at twin boundaries, and this could be explained based on a local phase transformation to the equilibrium δ phase [84]. Fig. 5.4 shows precipitation along selected twin boundaries in sample 1C; the precipitation shows no preference for, or aversion to, the

twin boundaries.

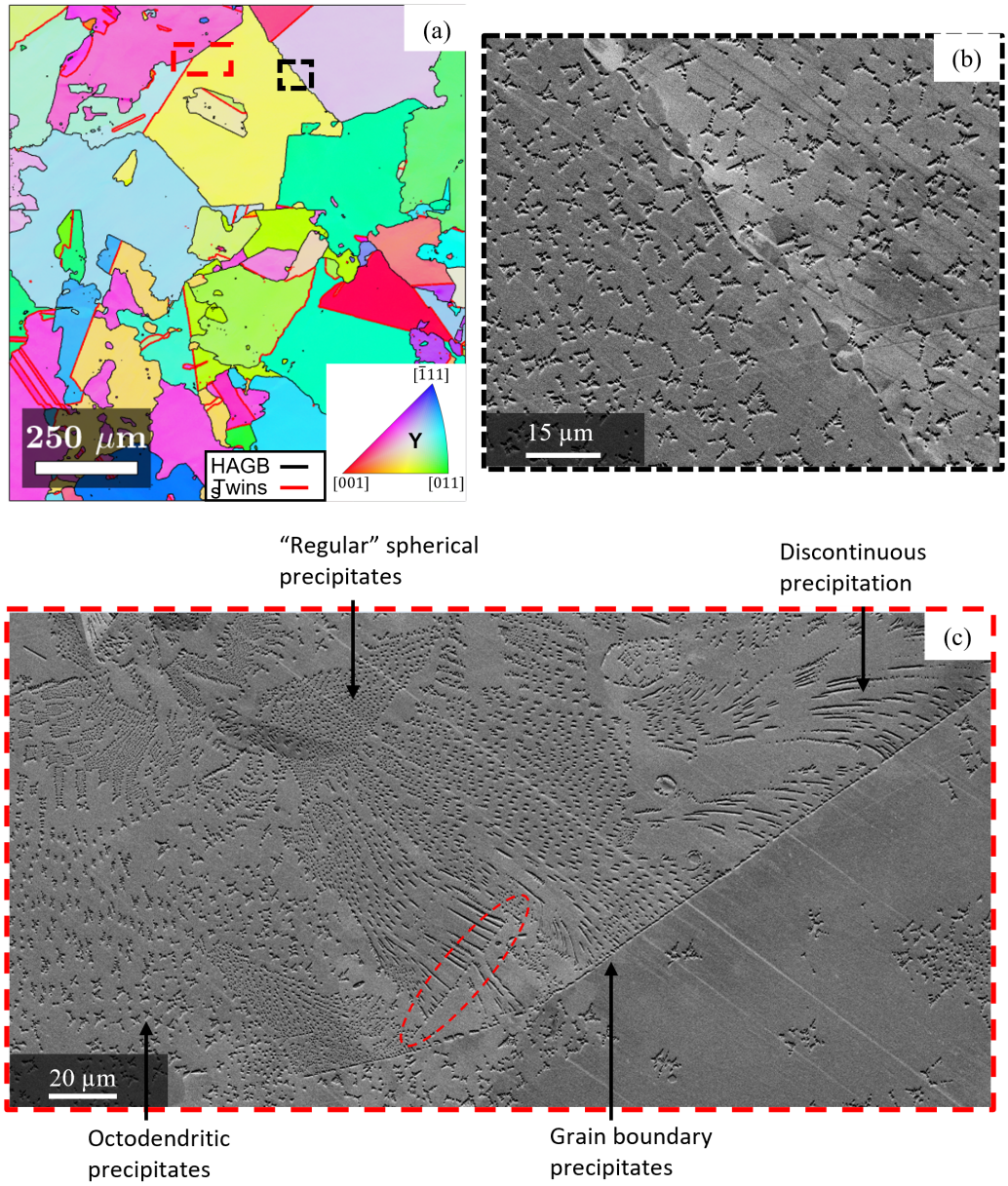


Figure 5.3: (a) A 1 mm^2 IPF Y map of sample 1C, with (b-c) corresponding FSE images from selected areas which highlight the different precipitate morphologies. Precipitation along a grain boundary is highlighted in (b) and four different morphologies can be identified from the 2D micrograph in (c); both the ocotodendritic precipitates and the regular spherical precipitates belong to the category of continuous precipitates.

In sample 1C (water quenched after slow cooling through the solvus), a number

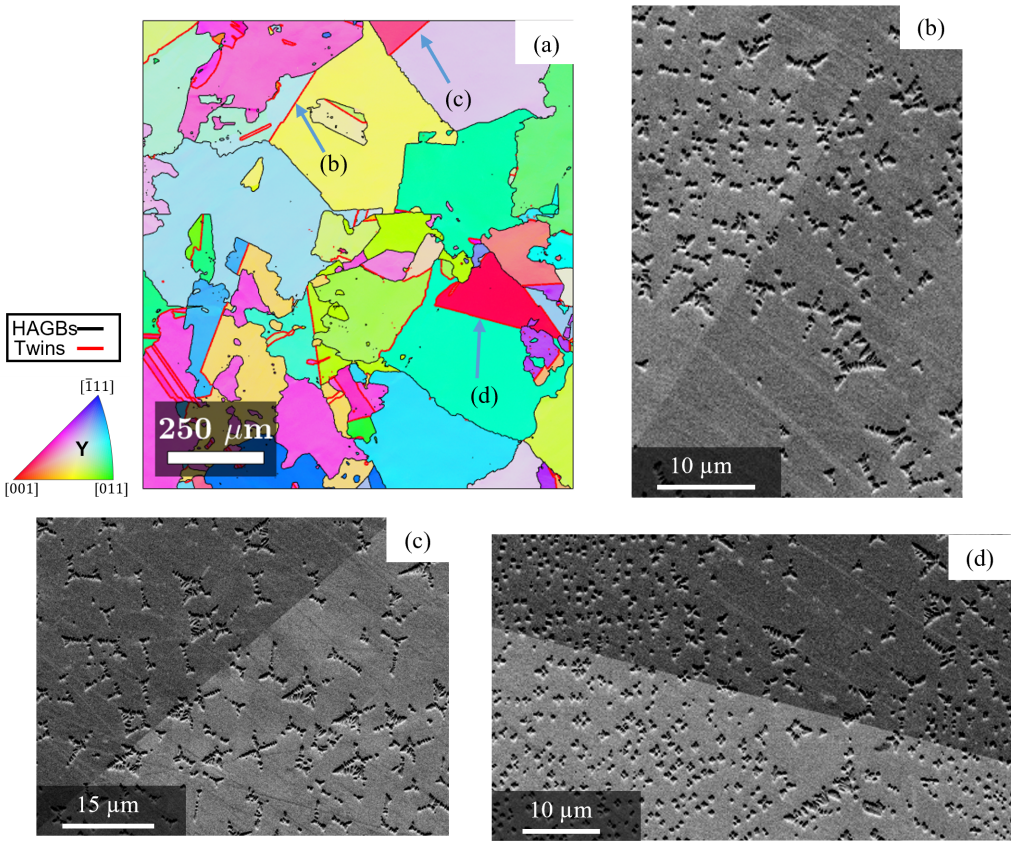


Figure 5.4: An IPF map of sample C (a) with the corresponding FSE micrographs from the indicated (arrows) twin boundaries (b-d) showing the precipitation along these boundaries.

of very flat grain boundaries which are not twins can be identified; these correspond to the discontinuous precipitation reaction interface. One example of such a boundary is shown in Fig. 5.3 (c). Specifically, these flat boundaries appear to be boundaries which separate regions with discontinuous precipitation from regions free from precipitation (i.e. a type 1 discontinuous precipitation reaction). The discontinuous precipitation reaction interface does not always correspond to a very flat grain boundary, and in the cases where this interface is serrated, the grain containing the discontinuous precipitation appears to be consuming a region containing continuous precipitation (i.e. type 2 discontinuous precipitation). One example of this is shown in Fig. 5.5 (b), indicated by the black arrow. Since islands of the grain containing continuous precipitation (pink contrast in Fig. 5.5 (a)) are left behind in the grain with discontinuous precipitation (beige contrast in Fig. 5.5 (a)), it appears that the grain with

discontinuous precipitation is consuming the one with continuous precipitation.

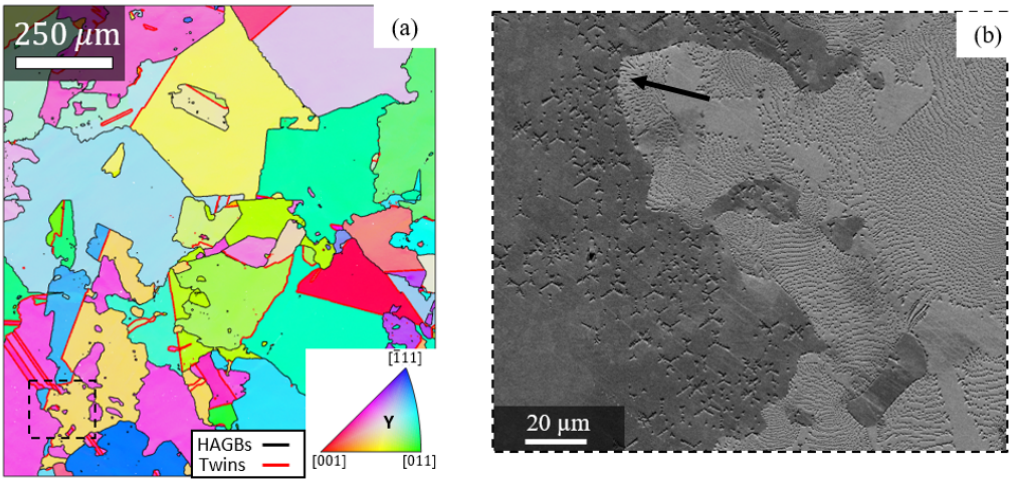


Figure 5.5: (a) A 1 mm ^{2} IPF Y map of sample 1C, with (b) corresponding FSE image showing an example of a type 2 discontinuous precipitation reaction. The boundary at which the reaction is occurring is shown by the black arrow, and this boundary moves in the direction of the arrow.

5.3 Discontinuous precipitates

5.3.1 Classification and mechanisms

Williams and Butler identified three types of grain boundary discontinuous precipitation reactions in their review on the subject [83]. In this case both type 1 and type 2 reactions have been identified. Type 1 reactions ($\gamma^* \rightarrow \gamma + \gamma'$) involve decomposition of a single phase super saturated matrix (γ^*) behind a moving grain boundary. An example of this type of reaction can be found in Fig.5.3 (c); the grain boundary ahead of the labeled discontinuous precipitation separates the discontinuous precipitates from a grain with a relatively low area fraction of precipitates, i.e. one where the γ matrix may be supersaturated. In type 2 reactions ($\gamma^* + \gamma' \rightarrow \gamma + \gamma'$), the matrix ($\gamma$) ahead of the advancing boundary already contains precipitates (γ'), which are dissolved and redistributed into the discontinuous precipitation behind the moving boundary. An example of this type of reaction is shown in Fig. 5.5 (b). In this second case, the discontinuous precipitates are replacing continuous precipitates.

Different nucleation mechanisms for discontinuous precipitation have been suggested. One set of mechanisms involves precipitation as a consequence of grain boundary motion, the other involves grain boundary motion as a consequence of precipitation.

Tu and Turnbull in 1967 proposed a mechanism for cellular precipitation (which is used interchangeably with discontinuous precipitation [85]) in Pb-Sn alloys, in which precipitation causes the grain boundary to be displaced [86] . This is referred to as a "pucker" mechanism by Williams and Butler in their review on discontinuous precipitation [83]. In this mechanism, precipitation occurs at the grain boundary, and the precipitate assume a "special" orientation in order to be coherent with its host grain. However, this causes it to be incoherent with the neighbouring grain, across the boundary. The grain boundary migrates to have the precipitate completely embedded in the grain with which it is coherent. This "replacive" motion of the boundary is driven by a reduction in the interfacial energy of the precipitate.

Fournelle and Clark proposed a different mechanism for the nucleation of cellular precipitation, in which grain boundary motion is instead thermodynamically driven by the reduction in free energy achieved by precipitation in the supersaturated matrix [87]. Here, precipitation occurs along the moving grain boundary, locally pinning it, and causing it to bow out between precipitates. The moving boundary absorbs solute and deposits it onto the branches of discontinuous precipitation, which move along with the boundary. This alternative mechanism was suggested to occur for precipitates which do not show a strict orientation relationship between precipitate and matrix. Fournelle and Clark show micrographs where the boundary is clearly bowed, but it can be seen in Fig. 5.3 (c) that discontinuous precipitation is found along a very flat boundary, with no bowing.

These two distinct nucleation mechanisms of discontinuous precipitation at least have in common that the grain boundary acts as a reaction interface and fast diffusion pathway. However, Ferguson *et al.* recently investigated continuous and discontinuous precipitation of an $L1_2$ phase in a Cu-Ni-Al alloy, and found an example of the discontinuous reaction front being ahead of the associated grain boundary [88]. There was evidence that precipitation was occurring ahead of the initiating grain boundary, and matrix reorientation occurred subsequently. The mechanism by which this occurs could not be characterised, but clearly does not rely on the grain boundary to act as a diffusion pathway, since precipitation is occurring away from the boundary.

In the present case, Fig. 5.3 (c) shows a discontinuous reaction front which does not coincide with a grain boundary, highlighted by the red dashed ellipse. The precipitation in the red ellipse appears to be an example of a region where the grain boundary could have broken away from the discontinuous reaction front, leaving the precipitation behind unable to advance further. This produces a striking straight line of precipitation, not associated with a grain boundary. This observation is similar to the observation in [88], insofar as the initiating grain boundary and reaction front have separated, but in this case the boundary appears to have moved on leaving the precipitation behind, rather than the precipitation advancing ahead of the boundary.

The mechanism(s) by which discontinuous precipitation is occurring in this case is unknown, though a mechanism similar to the pucker mechanisms is possible. In general the mechanisms producing discontinuous precipitation seem to be much less well understood than those for continuous precipitation.

5.3.2 Size and morphology

To characterise the morphology of the discontinuous precipitates in more detail, FIB-SEM tomography was performed on a region of interest in sample 1B at the CEMEF (see section 3.4.2). These data, shown in Fig. 5.6, show the 3D morphology of the discontinuous precipitates. The following observations can be made:

1. From Fig.5.6 (a), we can see different apparent morphologies in 2D, which come from precipitates which in fact have the same morphologies when viewed in 3D. Both the precipitates which appear to have a cellular morphology and those which appear more regular in (a) are found to have a "spaghetti" shape in 3D. As such the "regular", approximately cuboidal, precipitates identified in Fig. 5.3 (c) should be treated with caution, as they could either be an end on view of discontinuous precipitates or small continuous precipitates.

2. A striking straight line of precipitation, indicated by the red arrow. This is similar to the straight line of precipitation in the red ellipse in Fig. 5.3 (c).

3. A few octodendritic precipitates were detected, one indicated by the black arrow in Fig. 5.6 (c). These are found in regions where there is a low nucleation density of precipitates, which have not been swept through by the discontinuous precipitation.

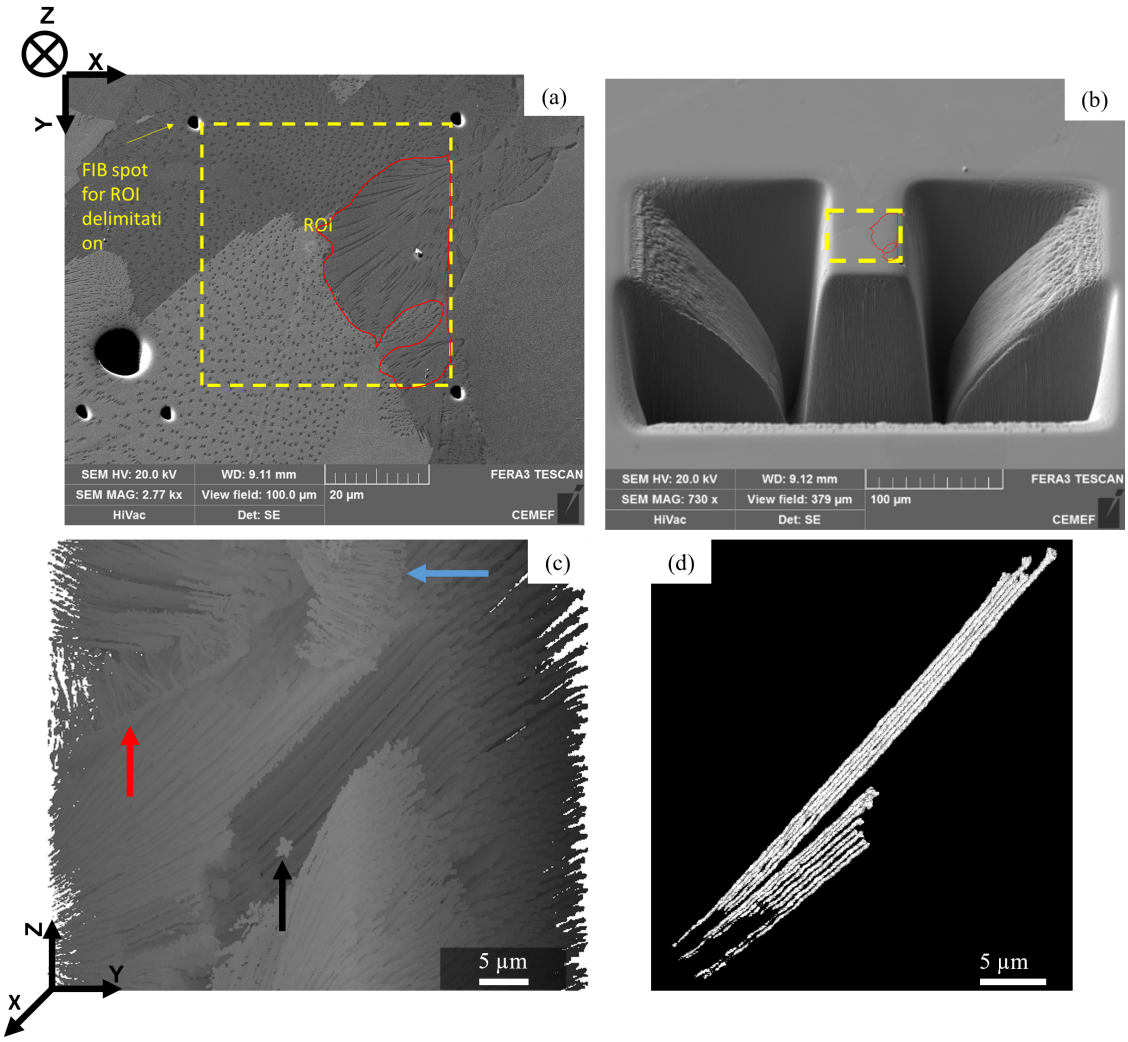


Figure 5.6: FIB-SEM tomography to reveal the 3D shape of discontinuous precipitates. (a) A region of interest from sample 1B, which appears to contain a mixture of approximately cuboidal and discontinuous precipitates, when viewed in this in 2D section. (b) The same region after FIB milling to prepare for serial sectioning. (c) The 3D data set produced by serial sectioning and image segmentation showing that the region of interest contains almost exclusively discontinuous precipitation with a "spaghetti" morphology, and (d) a selection of discontinuous precipitates, some of which extend throughout the whole length of the investigated volume.

4. An example of a "Fan-type" precipitate is found, indicated by the blue arrow.

In terms of their morphology, and forming behind a moving boundary, the discontinuous γ' precipitates are similar to the fan-type structures (FTS) which have been reported to form in a number of Ni-based superalloys. An early example of the

use of the term FTS was by Danflou *et al.* in 1996, where the growth kinetics of the fans was studied and used to confirm that they form discontinuously [89]. A similar morphology had been identified by Henry *et al.* in 1993, though the term fan was not used to describe it [90]. Subsequently, the name has been used in 1999 by Furrer *et al.*, who observed the formation of fan-type γ' precipitates during "slow" cooling of Udimet 720 (at a cooing rate of 0.12 °C/s) [91]. The effects of cooling rate on the size and spacing of fan type γ' precipitates have been investigated by Mitchell *et al.* [79] and Hu *et al.* [92], who looked at cooling rates in the range 10.8 °C/s to 0.1 °C/s. Both found that slower cooling rates lead to larger FTS, with larger spacing between the fans, i.e. between the branches of γ'. Most recently, Atrazhev *et al.* have given a detailed model for the formation of fan type γ' precipitates, and shown that grain boundary migration rate is the key factor favouring their formation [80]. When grain boundary migration rate is high, the formation of FTS behind moving boundaries is favoured. When it is lower, grain boundary γ' precipitates form and can cause grain boundary serrations to develop. As a consequence, slow cooling rates in the vicinity of the solvus temperature favour the formation of FTS, and discontinuous precipitation in general. This is because a long time is spent at high temperatures, where grain boundary mobility is high, and so grain grain boundary migration rates are high, for a given driving pressure.

Although an example of a FTS is highlighted in Fig. 5.6 (c), the majority of the discontinuous γ' precipitation observed in Fig. 5.6 (c) is not considered to be FTS. While similar in terms of forming discontinuously behind a moving boundary and presenting alternating branches of γ and γ' in 2D micrographs, it is different in that the majority of the discontinuous γ' precipitation here does not appear to originate from a single grain boundary precipitate (acting as a nucleation site). Additionally, most of the discontinuous precipitation was not found behind curved grain boundaries as is typical for FTS, but can be found behind very flat boundary sections (e.g. in Fig. 5.3 (c)).

The very elongated shapes of the discontinuous precipitates means that their shape cannot be well characterised based on 2D micrographs, and even the precipitate type (discontinuous or continuous) can be misidentified. The difficulty of measuring precipitate size and shape is clear from Fig. 5.6 (c), and is further exemplified in Fig. 5.7.

A sub-volume was selected from Fig. 5.6 (a), and a particular point in this sub-volume (indicated by the intersection of the black lines) is viewed from three

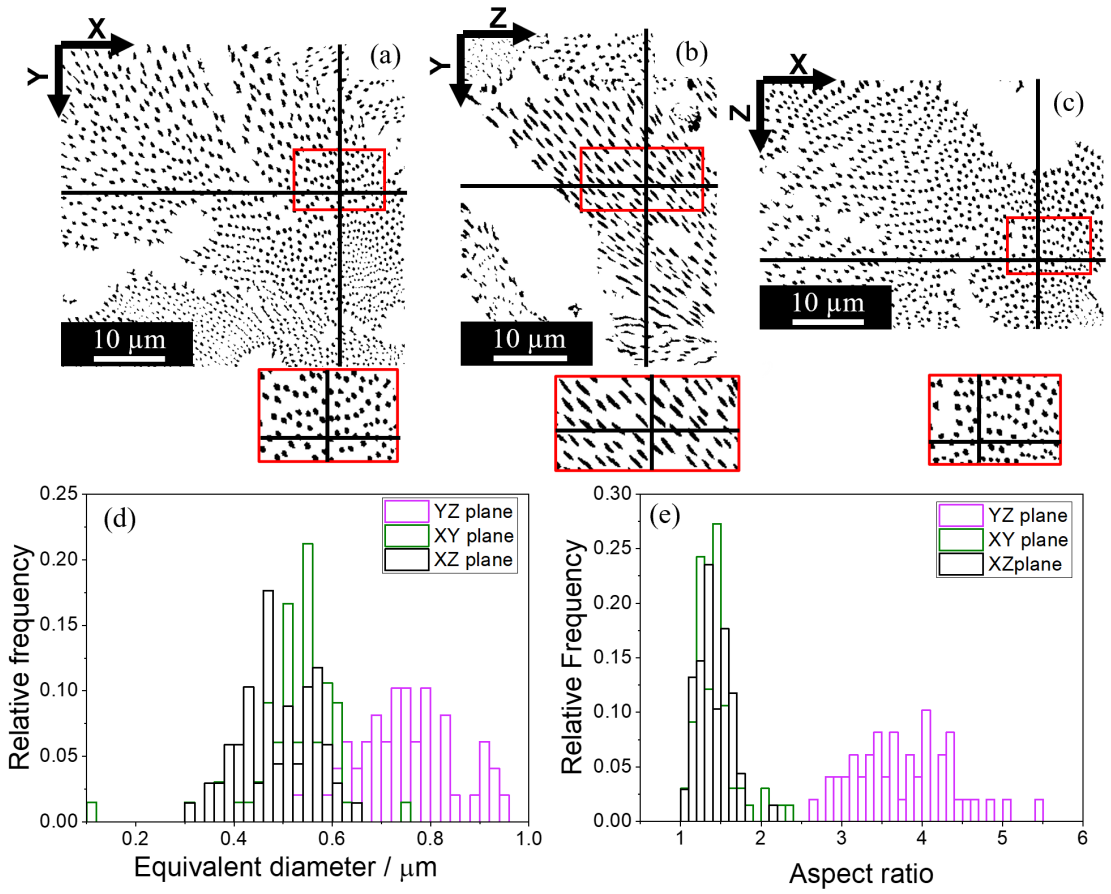


Figure 5.7: The distribution of equivalent diameter and aspect ratio of the same precipitates viewed from different planes. (a) - (c) A single point in a 3D dataset, indicated by the intersection of the black lines, viewed from XY, YZ and XZ planes, respectively, (d) and (e) the size and aspect ratio distributions of ≈ 50 precipitates, indicated in the red rectangles in (a) - (c).

perpendicular planes. The size and aspect ratio of approximately 50 precipitates surrounding this point (highlighted by the red rectangles) were measured. While these were quite similar in the XY and XZ planes, with equivalent circle diameters ≈ 0.49 µm and aspect ratios ≈ 1.42, the equivalent diameter shown in the YZ plane is 50 % higher at 0.75 µm, and the aspect ratio more than twice as much at 3.76. From this analysis it is clear, and one should keep in mind, that the analysis of precipitate size and shape must be done with great care in the case of such anisotropic systems. Observations made in 2D sections can indeed be very misleading when dealing with such very elongated precipitate shapes.

An example can be found in the literature where such precipitate shapes *may*

have led to a misleading estimate of precipitate size. Wu *et al.* proposed equations to predict the strength of nickel based superalloys [93]. This required the size distribution of γ' precipitates to be measured, and some BSE images showing the precipitate distribution were included. One of these showed precipitates which had a "disc" shape (as seen in the 2D micrograph). This shape is shown in Fig. 5.8 (b), and is very similar to those shown in Fig. 5.7 (b). Their shape was attributed to residual stress in the casting which restricted growth to certain directions, but this was not verified. The comparisons in Fig. 5.7 show that the measurement of the equivalent circle diameter of the precipitates in Fig. 5.8 (b) made by Wu *et al.* cannot be considered reliable, if these are indeed discontinuous precipitates. Fig. 5.8 shows that, morphological, the precipitates seen by Wu *et al.* are indeed very similar to discontinuous ones with a "spaghetti' shape in 3D.

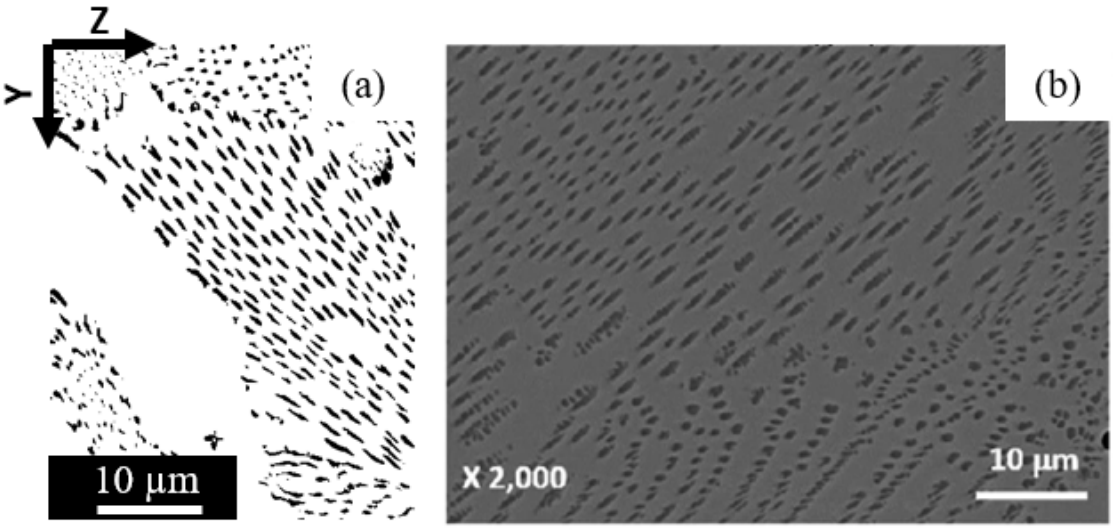


Figure 5.8: Comparison of the "spaghetti" shaped discontinuous precipitates found in this study (a) and the "disc" shaped precipitates found by Wu *et al.* in [93](b).

5.4 Grain boundary motion during discontinuous precipitation

5.4.1 Thermodynamic driving force

As discussed previously, there is not a clear single mechanism responsible for discontinuous precipitation, so there is not a clear mechanism causing the grain boundary motion associated with discontinuous precipitation. The thermodynamic driving force for the grain boundary motion which is associated with precipitation could either be due to:

1. Consumption of remnant stored energy
2. Reduction of grain boundary energy
3. Attaining the equilibrium volume fraction of γ' through grain boundary motion. The possibility that this acts as the driving force for discontinuous precipitation was first suggested by Cahn [94].

The first two explanations are unlikely. Fig.5.2 (d) suggests that stored energy is low prior to cooling through the solvus and Fig.5.2 (a) shows that very large equiaxed grains have formed prior to cooling through the γ' solvus. Thus the overall grain boundary energy is rather low, due to the low density of GBs. As such, it is likely that the thermodynamic driving force for the grain boundary motion associated with precipitation is due to the free energy decrease due to achieving the equilibrium volume fraction of γ'. However, this would not explain the type 2 discontinuous precipitation observed, where precipitation has already occurred ahead of the advancing discontinuous precipitation reaction front, unless precipitaion is incomplete, and the progression of the grain boundary is associated with an increase in the volume fraction of precipitates.

This precipitation induced grain boundary motion is similar to diffusion induced grain boundary migration (DIGM). DIGM was first observed by Den Broedert in 1972, in a Cr-W diffusion couple [95]. There, it was observed that initially flat grain boundaries became serrated during inter-diffusion, and this was explained due to an inter-diffusion mechanism between two phases with different atomic mobilities. This was noted to be similar to discontinuous decomposition.

More recently Kaur *et al.* have used molecular dynamics simulations to show that DIGM can occur in a binary alloy of Al with up to 5 at.% Ni [96]. Kaur *et al.* demonstrate that the strain energy associated with the solute Ni atoms in the Al matrix is likely to provide the driving force for boundary migration in DIGM, unlike in discontinuous precipitation where the driving force is due to achieving the equilibrium volume fraction of precipitate. In Kaur *et al.*'s simulations, the boundary would move in the direction of highest *local* solute concentration, and this varies along the length of the boundary, such that adjacent portions move in opposite directions. Importantly, DIGM should be possible prior to the onset of precipitation, but the grain boundary motion due to discontinuous precipitation seen here occurs only once precipitation has started. So, the strain energy due to solute atoms which can cause DIGM is unlikely to cause discontinuous precipitation.

5.4.2 Effect on grain structure

Comparing the grain structure of sample 1A (quenched from the super-solvus) with that of 1C (quenched after slow cooling from the super-solvus) reveals that grain size has **decreased** on cooling through the γ' solvus; this contradicts the possibility that a reduction of grain boundary energy provides the driving force for discontinuous precipitation. Fig. 5.9 highlights this; (a) is an IPF map of sample 1A and (b) an IPF map of sample C, both at low magnification. Some of the microstructural parameters from Figs. 5.9 (a) and (b) are extracted and shown in histograms in Figs. 5.9 (c) and (d). From the grain size distributions shown in Fig. 5.9 (c), we see that sample C has a higher fraction of smaller grains, and a smaller grain size than sample A. Fig. 5.9 (d) gives a measure of the grain boundary morphology. For grains of different sizes but a constant shape, the ratio of grain area to grain perimeter should be directly proportional to grain size. The slope of a plot of the ratio of grain area to grain perimeter against grain diameter depends on grain shape; it will be 0.25 for circular grains (i.e. perfectly equiaxed), and lower for grains with more torturous boundaries. The lower slope for sample C in Fig. 5.9 (d) confirms the grain boundaries are more wavy/torturous in sample C than sample A.

Table 5.1 shows that grain size is lower whether considering the number or area weighted grain size. The twin boundary fraction in Table 5.1 is the length of twin boundary which is twinned, divided by the total grain boundary length.

The difference in grain size is due to grain boundary motion, which is associated

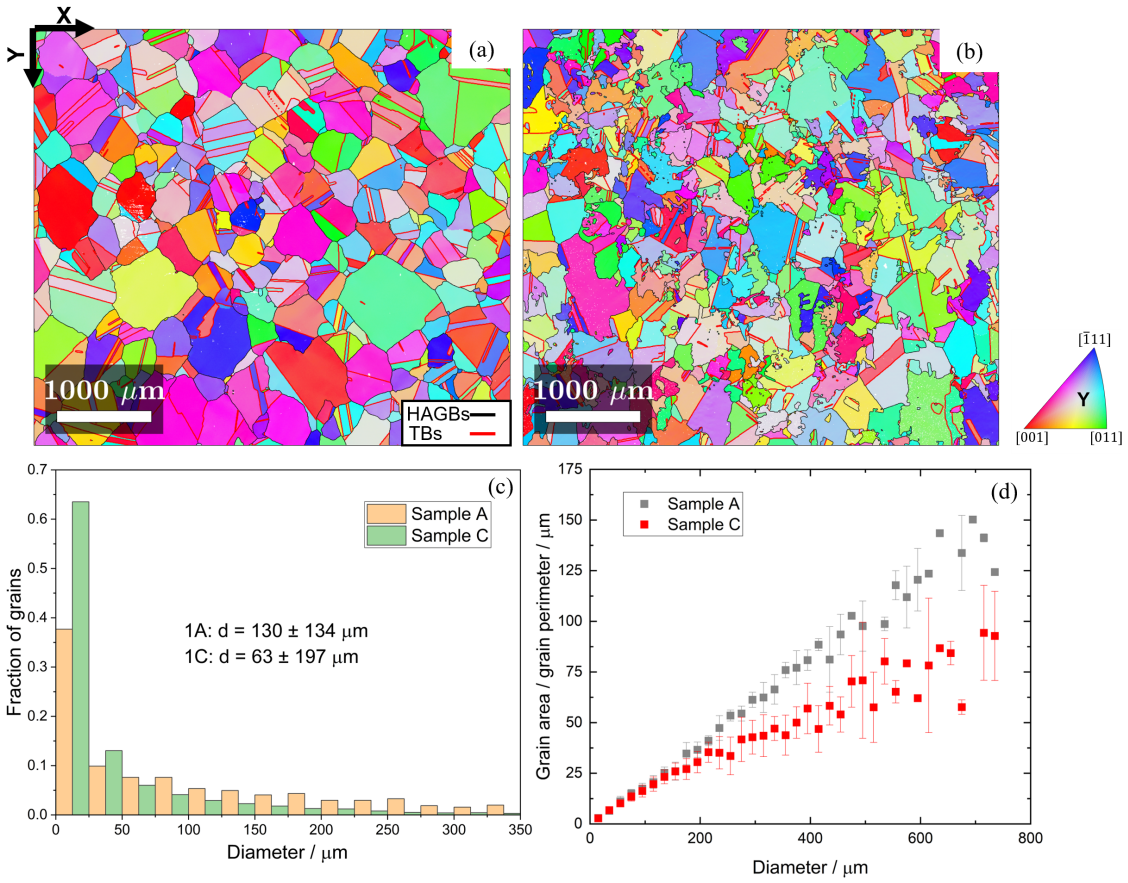


Figure 5.9: Low magnification IPF maps from samples 1A (a) and 1C (b). A relative frequency histogram with 25 μm wide bins showing the distribution of grain sizes, with the number weighted average grain diameter indicated (c). The ratio of grain area to grain boundary perimeter with the grains in 20 μm wide bins, error bars indicate one standard deviation (d).

with discontinuous precipitation. Grains with discontinuous precipitation appear to be growing and consuming grains with continuous precipitation, leading to these grains shrinking and becoming fragmented. This fragmentation strongly reduces the number weighted grain size, as it produces a high number of small grains. A clear example of this fragmentation is shown in Fig. 5.10 where multiple fragments of one grain with continuous precipitation are found within another grain having discontinuous precipitation.

As well as a change in grain size, a change in grain morphology can be observed in the two micrographs in Fig. 5.9. The boundaries in sample C are more serrated than in sample A. This can be demonstrated quantitatively by considering the ratio

Table 5.1: Comparison of selected microstructural parameters from Fig. 5.9. Values are in the format mean ± standard deviation. Grain sizes refer to equivalent circle diameters.

	Sample	
Property	1A	1C
Number weighted grain size /μm	134 ± 130	63 ± 197
Area weighted grain size / μm	365 ± 197	302 ± 164
Twin boundary length per unit area /mm^{-1}	9.8	9.8
Twin boundary fraction / %	46.6	27.9

of grain area to grain boundary length, as shown in Fig. 5.9 (d). Since this ratio tends to increase with grain size, the grain sizes calculated from the IPF maps in Fig. 5.9 (a) and (b) are put into 20 μm wide bins, and the average value of this ratio for all grains in that bin is plotted, along with error bars showing the standard deviation for all the grains in that bin. This was done using the merged grain size (i.e. discounting twin boundaries). This ratio is lower in sample C than sample A, due to its more serrated grain boundaries. This serration can result from type 2 discontinuous precipitation, as shown in Fig. 5.5. This highlights that grain boundary serration during slow cooling through the solvus can be due to grain boundary precipitation, as highlighted many times [79, 89], or due to the grain boundary motion associated with discontinuous precipitation, which has not been mentioned previously.

Table 5.1 also shows that the twin boundary length per unit area is almost identical between samples 1A and 1C, suggesting that the rates of twin boundary formation and consumption during precipitation and associated grain boundary motion are approximately equal - this could be due to the twin boundaries being unaffected by the grain boundary motion associated with discontinuous precipitation and neither being created nor consumed to a significant extent. At the same time as the total length of twin boundary is almost constant, the total length of grain boundary measured (in a 2D micrograph) increases, meaning the fraction of boundary which is twinned decreases.

To investigate the evolution of the twin boundaries during discontinuous precipitation further, the distribution of twin boundary lengths in samples A and C is shown in Fig. 5.11. This shows that in sample C there are a higher number of shorter twin boundaries than in sample A. Therefore, twin boundaries are in fact affected

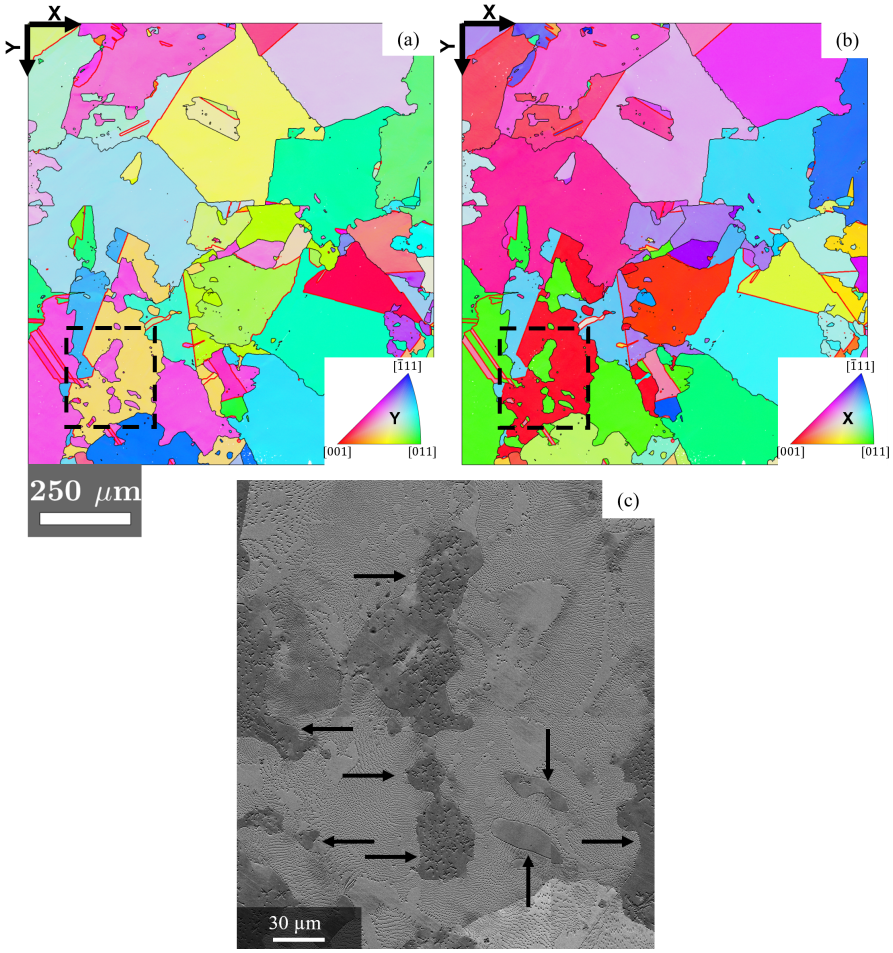


Figure 5.10: Example of a grain with discontinuous precipitation consuming a grain with continuous precipitation. IPF Y (a) and IPF X (b) maps show there are fragments of one grain, which is purple in (a) and green in (b), which has been consumed by another, which is beige in (a) and red in (b). The FSE image of the indicated region (c) shows the partially consumed fragments, indicated by the black arrows, have continuous precipitation.

by the grain boundary motion associated with discontinuous precipitation; existing boundaries are consumed and new ones are produced during the grain boundary motion associated with discontinuous precipitation. A smaller number of larger twin boundaries are replaced by a larger number of shorter twin boundaries.

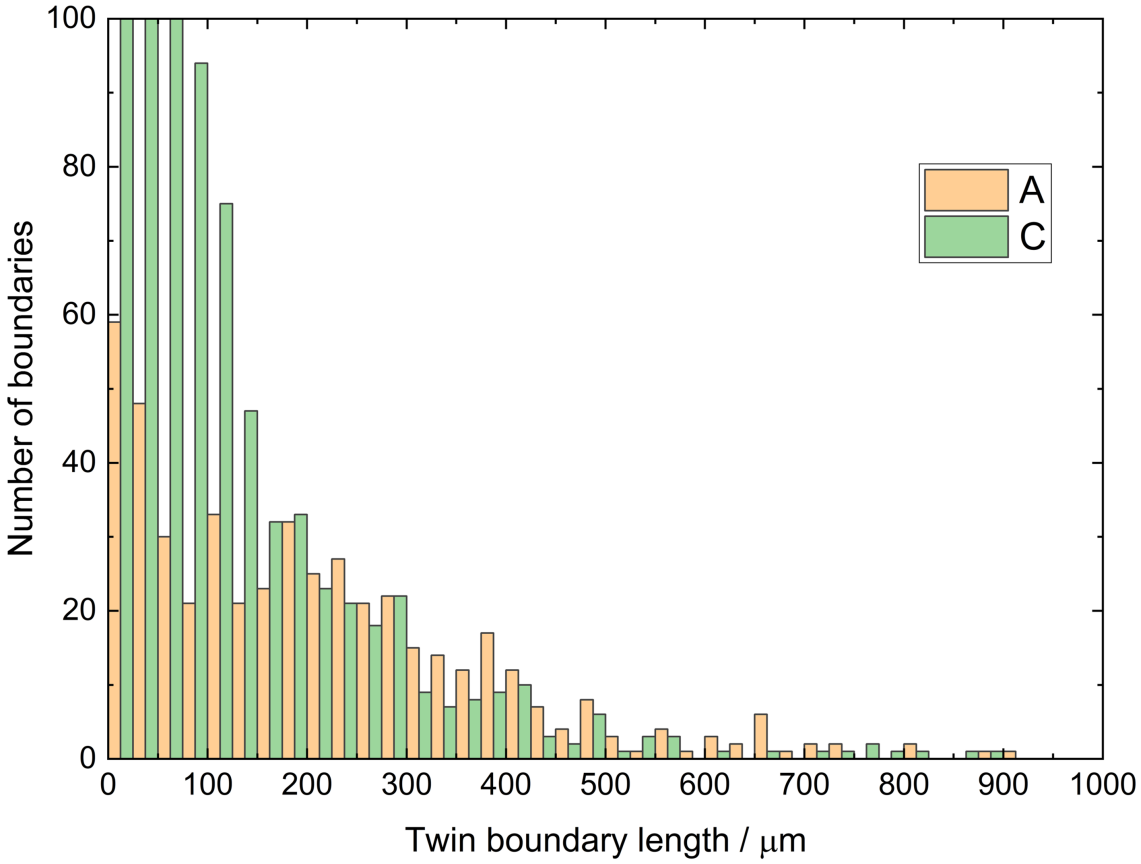


Figure 5.11: A low magnification map from sample A where twin boundaries are colourised according to their length (a). From this a histogram of twin boundary length can be plotted. Such a histogram comparing samples A and C is shown in (b).

5.4.3 Additional investigations into grain boundary motion

To confirm the effects of grain boundary motion associated with discontinuous precipitation shown in the previous sub-section (5.4.2), an additional 10 heat treatments were performed to sequentially follow the development of precipitation and the associated microstructural changes during slow cooling through the γ' solvus. These heat treatments were described in section 3.4.3.

Samples initially held at 1160 °C

IPF maps for the samples held for one hour at 1160 °C prior to cooling are shown in Fig.5.13, and corresponding grain size data is given in the table in 5.13.

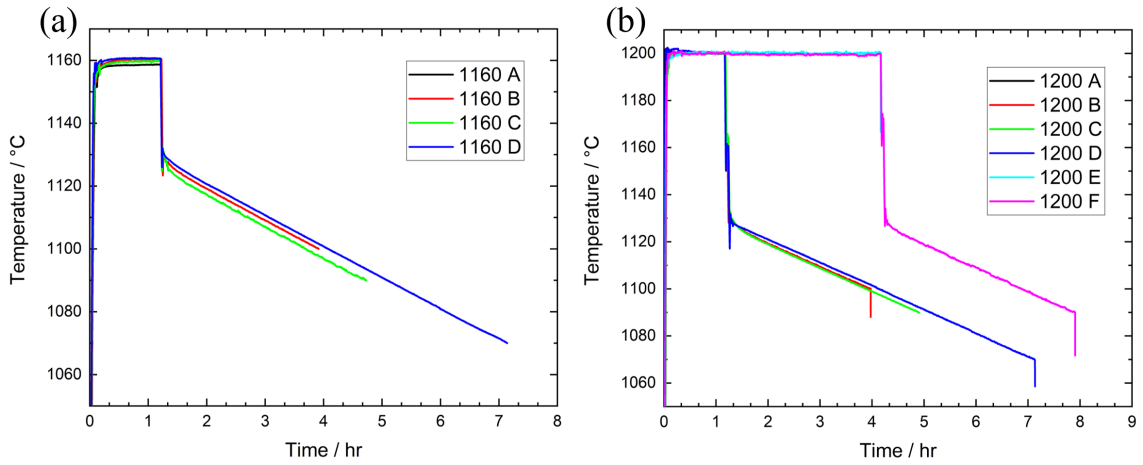


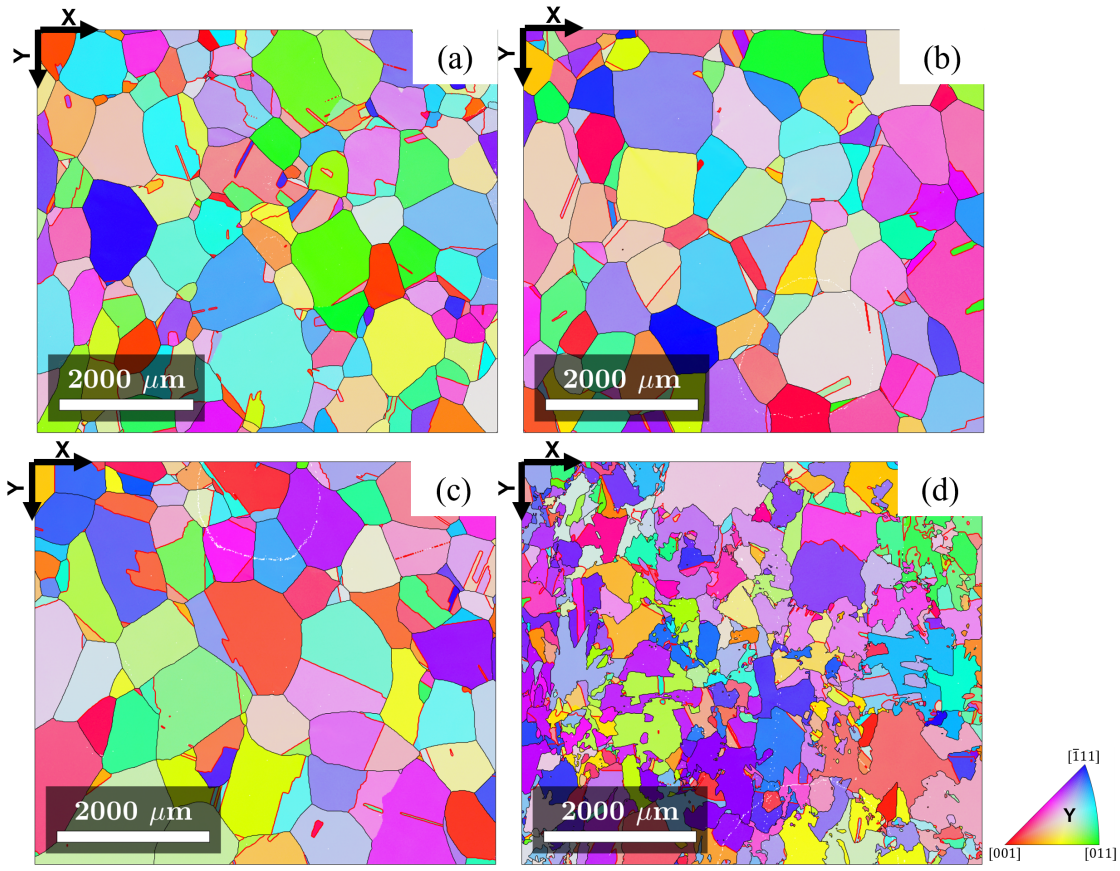
Figure 5.12: Recorded temperature data for samples which were subject to the additional heat treatments. Samples initially held at 1160 °C (a) and initially samples held at 1200 °C (b).

These show that a grain size of ≈ 320 µm is achieved during the super-solvus holding, and this does not change much after slow cooling to either 1110 °C or 1090 °C. However, the sample cooled to 1070 °C has a notably smaller average grain size. Fig. 5.13 (d) also shows that this sample has more serrated grain boundaries than the others. As observed previously, the fraction of twin boundaries has decreased.

These dramatic changes in grain size and morphology are due to discontinuous precipitation, which surprisingly has not started in the samples cooled to 1100 °C and 1090 °C, despite the slow cooling rate (10 °C/hr). Indeed, these samples (quenched at 1100 °C and 1090 °C) contain no precipitates. This is thought to occur due to the precipitation of γ' being kinetically hindered, occurring at an under-cooling $\geq$ 20 °C (the solvus temperature is around 1110 °C, see section 2.3 of Chapter 2). This assumption of retarded nucleation (rather than a lower than expected solvus temperature) is supported by the precipitate state which was found in sample 1C (quenched from 1080 °C), where the area fraction of precipitates is around 12.5 %; such a fraction is not consistent with this temperature being $\leq$ 10 °C below the solvus.

Samples initially held at 1200 °C

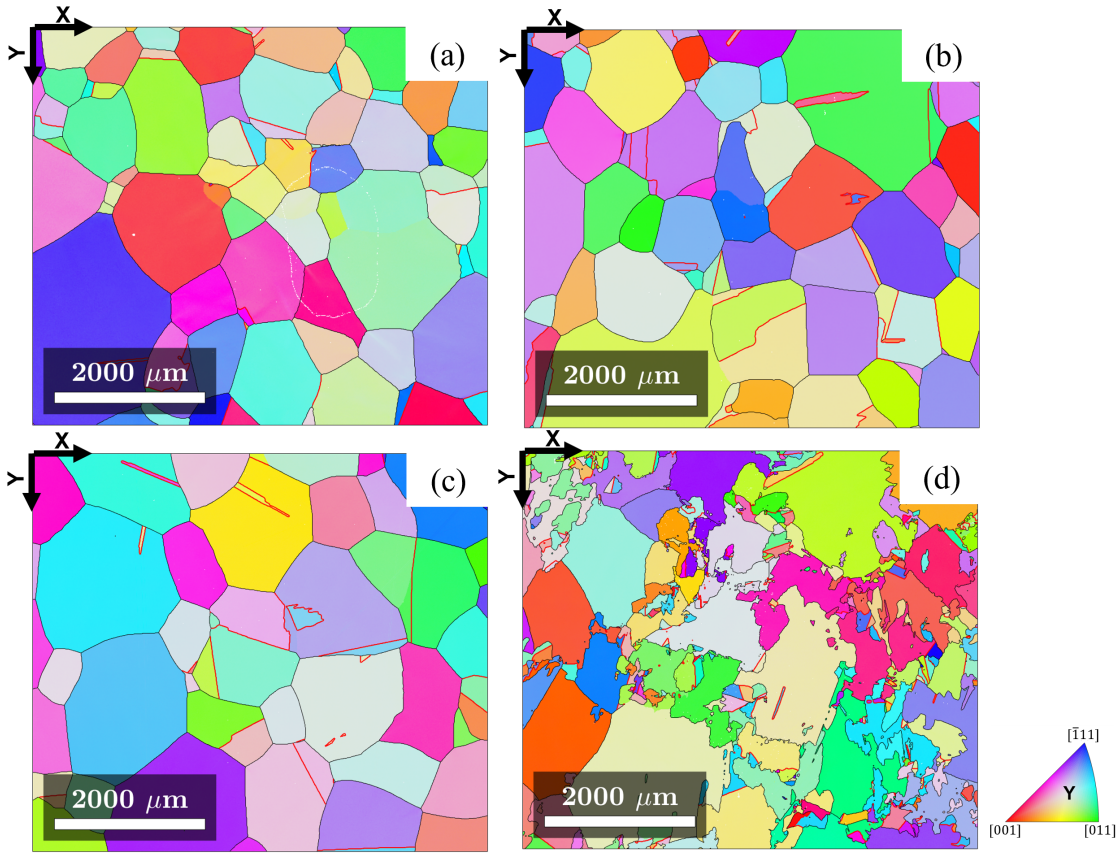
IPF maps for the samples held at 1200 °C prior to cooling are shown in Fig. 5.14, and corresponding grain size data is given in the table in Fig. 5.14.



	Sample			
Property	1160A	1160B	1160C	1160D
Number weighted grain size /μm	286 ± 295	348 ± 307	319 ± 329	96 ± 139
Area weighted grain size / μm	801 ± 360	786 ± 307	852 ± 312	523 ± 300
Twin boundary length per unit area /mm^{-1}	1.62	0.99	1.25	1.97
Twin boundary fraction / %	30.2	36.2	34.3	18.4

Figure 5.13: IPF Y maps of (a) a sample quenched after 1h at 1160 °C, (b-d) samples held for 1h at 1160 °C, then quickly cooled to 1125 °C, then cooled at 10 °C/hr and quenched at (b) 1100°C,) (c) 1090°C, (d) 1070 °C. The table shows selected microstructural properties for the four samples.

These show that a grain size of ≈ 540 µm is achieved during the one hour super-solvus hold at 1200 °C, and this does not change much after slow cooling to either 1110 °C or 1090 °C. However, the sample cooled to 1070 °C has a notably smaller



	Sample			
Property	1200A	1200B	1200C	1200D
Number weighted grain size /μm	489 ± 432	498 ± 438	624 ± 379	93 ± 185
Area weighted grain size / μm	1168 ± 563	1194 ± 572	1200 ± 431	939 ± 524
Twin boundary length per unit area /mm^{-1}	0.38	0.65	0.54	1.03
Twin boundary fraction / %	15.2	24.6	23.9	13.6

Figure 5.14: IPF Y maps of (a) a sample quenched after 1h at 1200 °C, (b-d) samples held for 1h at 1200 °C, then quickly cooled to 1125 °C, then cooled at 10 °C/hr and quenched at (b) 1100°C,) (c) 1090°C, (d) 1070 °C.

average grain size. Fig. 5.14 (d) also shows that this sample has more serrated grain boundaries than the others. These observations are the same as those made for the samples which were initially held at 1160 °C.

Grain size distributions for the samples initially held at 1160 °C and 1200 °C are

shown in Fig.5.15 (a) and (b), respectively. These show that in the samples where precipitation has commenced (1160D and 1200D), the grain size distributions shifts to have a higher fraction of smaller grains, resulting in a smaller average grain size.

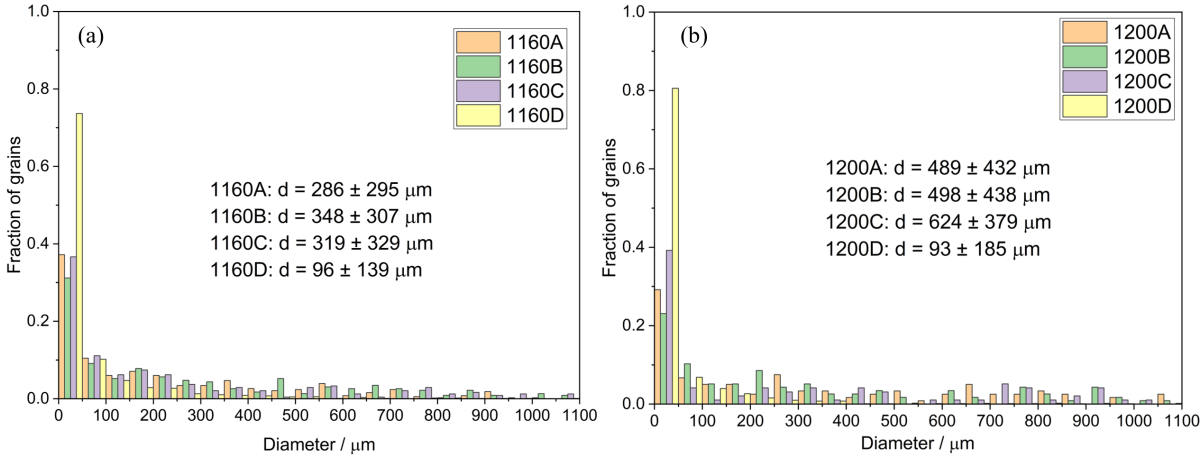


Figure 5.15: Grain size distributions with 50 µm wide bins for the samples initially held at 1160 °C (a) and 1200 °C (b) before slow cooling through the solvus temperature. Precipitates were only found samples 1160D and 1200D. The micrographs on which these distributions are based are shown in Figs. 5.13 and 5.14, respectively.

Role of chemical segregation

In section 5.2 it was noted that the discontinuous precipitation reaction front can present strikingly flat interfaces which are not along grain boundaries. These were again observed in these additional investigations, and an example is highlighted by taking a combined EBSD map and FSE image from the centre of the map in Fig. 5.13 (d). The IPF Y map from this region is shown in Fig. 5.16 (a), and an overlay of this map onto the corresponding FSE image from the region in the red rectangle is shown in (b). It is again seen that these flat interfaces do not coincide with grain boundaries.

The chemical composition behind and ahead of these flat lines of precipitation was investigated using WDS. This was done to investigate the possibility that these lines occur when a grain boundary, behind which discontinuous precipitation is occurring, encounters a region depleted in the γ' forming elements. In this scenario, it is possible that discontinuous precipitation would stop, but the boundary would continue migrating, leaving behind a flat interface.

This showed there could be slight differences in composition ahead of and behind these lines, but these did not show a consistent trend. In some cases the γ' forming elements are concentrated behind the line, in other cases they were concentrated in the precipitate free zone ahead of the line and in other cases still there was no clear difference on either side of the line. Three examples from sample 1160 D are shown are in Fig. 5.17, and two from sample 1200 D are shown in Fig. 5.18. These two figures also highlight the length of the discontinuous precipitates well; lines of precipitation on the order of 30 µm long can be seen in Figs. 5.18 (c) and (d). This is a remarkably large dimension for γ' precipitates.

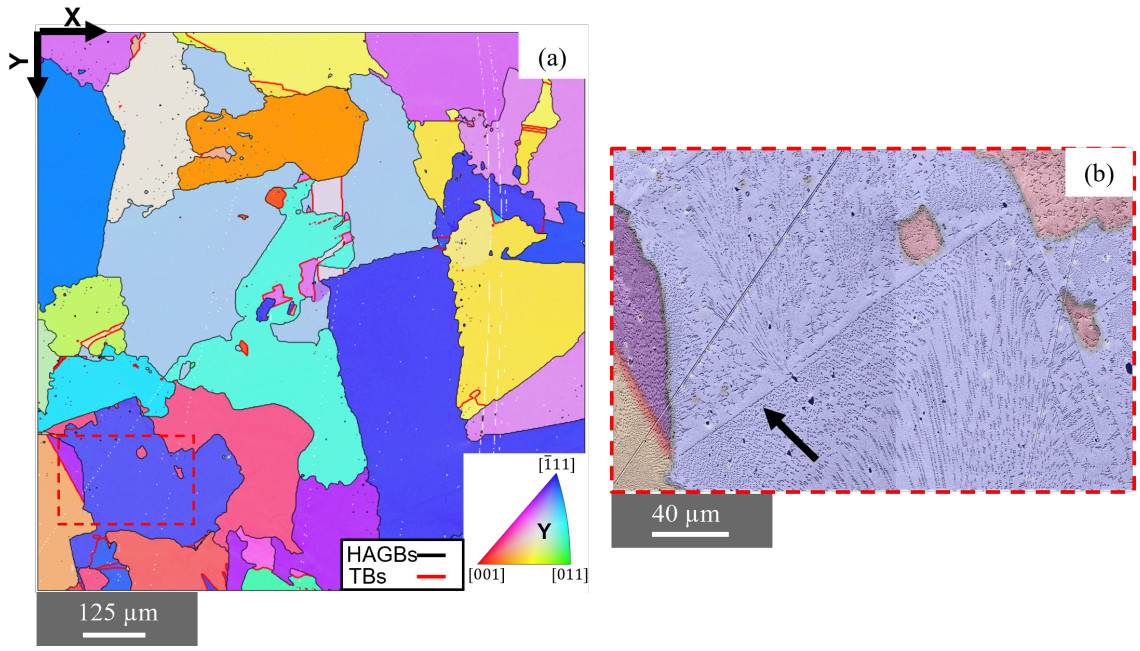


Figure 5.16: IPF Y maps taken from sample 1160 D (a), with a corresponding FSE image for the region in the red box (b). This region shows one of the striking straight lines of discontinuous precipitation, indicated with the arrow.

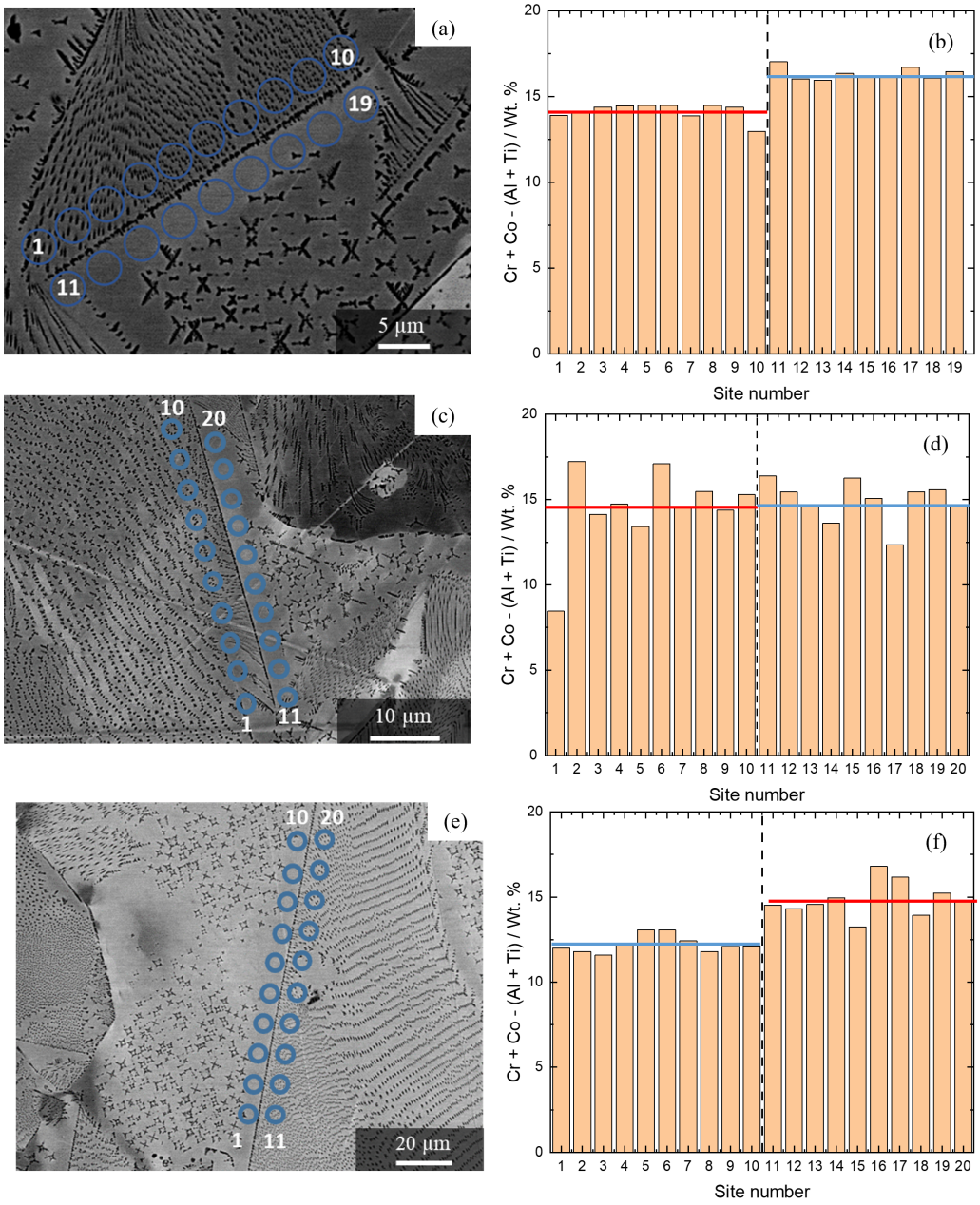


Figure 5.17: WDS data and BSE images from sample 1160 D. The first column ((a),(c),(e)) shows areas where the discontinuous precipitation reaction front is separated from a grain boundary. The local composition was measured in a line of 6 µm diameter circles on either side of this front. The measured difference in the Wt. % of strong γ forming elements (Cr and Co) and strong γ' forming elements (Al and Ti) is shown in the bar charts in (b), (d) and (f). The red and blue lines show the average values in the regions with and without precipitates, respectively.

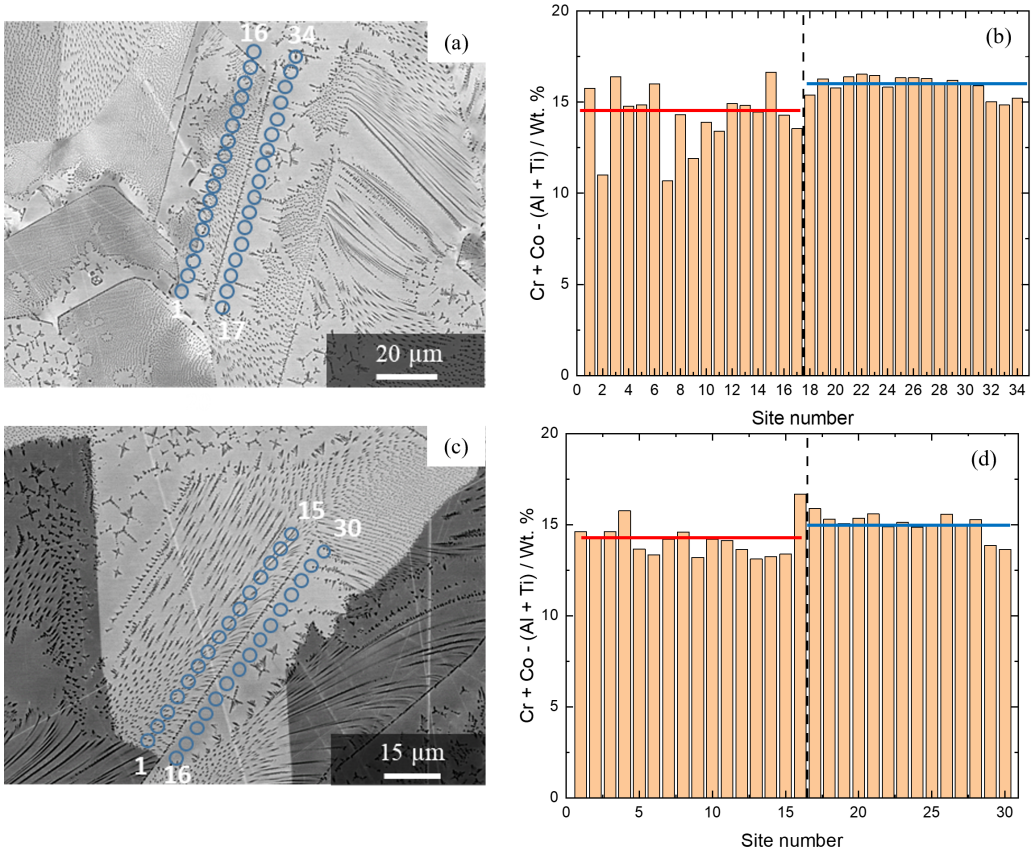


Figure 5.18: WDS data and BSE images from sample 1200 D. The first column ((a),(c)) shows areas where the discontinuous precipitation reaction front is separated from a grain boundary. The local composition was measured in a line of 6 µm diameter circles on either side of this front. The measured difference in the Wt. % of strong γ forming elements (Cr and Co) and strong γ' forming elements (Al and Ti) is shown in the bar charts in (b) and (d)). The red and blue lines show the average values in the regions with and without precipitates, respectively.

5.5 Continuous precipitates

5.5.1 Morphology

The shape changes which initially coherent precipitates undergo during their growth has been described by Ricks *et al.* and Grosdidier *et al.* [47, 44].This sequence involves a shape evolution from spherical to cuboidal to an octo-cube to octodendritic, and has been described in Chapter 2, section 2.4.2.

5.5.2 Spatial distribution

In sample 1B (held for one hour at 1160 °C, quickly cooled to 1125 °C, then cooled at 10 °C/hr down to 1080 °C) and sample 1C (same treatment as 1B, with an additional 1 hour hold at 1080 °C) different morphologies of continuous precipitates were found along the sphere to octodendrite progression. In both samples there was a very spatially inhomogeneous distribution of continuous precipitates. Within individual grains there were areas containing no precipitates, areas with a few large octodendrites spaced by several microns, and areas with a high density of approximately spherical precipitates. An example of this is shown in Fig. 5.19, where a FSE image from the region in (a) has been segmented to produce (b), which shows large precipitate free regions, and vertical bands with varying densities of precipitates. A region of interest magnified in (c) shows this variation in precipitate density within a single grain. An inhomogeneous nucleation density of precipitates can be identified in the turquoise grain which covers this area. Regions separated by roughly 100 µm can show either no precipitates, or a high density of spherical precipitates. The black arrow in (c) indicates an example of type 1 discontinuous precipitation, which is magnified in (d). In type 1 discontinuous precipitation, discontinuous precipitates form behind a grain boundary moving through a region super-saturated in the precipitate forming elements, i.e. the region in the turquoise grain with no precipitates. Fig. 5.19 (d) is thus an example of discontinuous precipitation consuming part of a precipitate free band, and shows how the inhomogeneous spatial distribution of precipitates can create conditions suitable for type 1 discontinuous precipitation.

One possible explanation for this inhomogeneity is remnant chemical segregation leading to some areas having higher concentrations of the γ' forming elements (Ti and Al), and some having higher concentrations of the γ forming elements (Cr and Co). Areas with higher concentrations of the γ' forming elements would correspond to inter-dendritic regions, and higher concentrations of the γ forming elements would correspond to dendritic regions [97].

To test this explanation, EDS was used to investigate the chemical composition in regions with different precipitate densities in sample 1C. The four regions (R1 - R4) used are shown in Fig. 5.20; the average composition of the whole area is given along with the compositions measured in the regions of interest indicated. There is evidence of a *slight* difference in chemical composition between the different regions, and these differences can be correlated with the different sizes of precipitates by

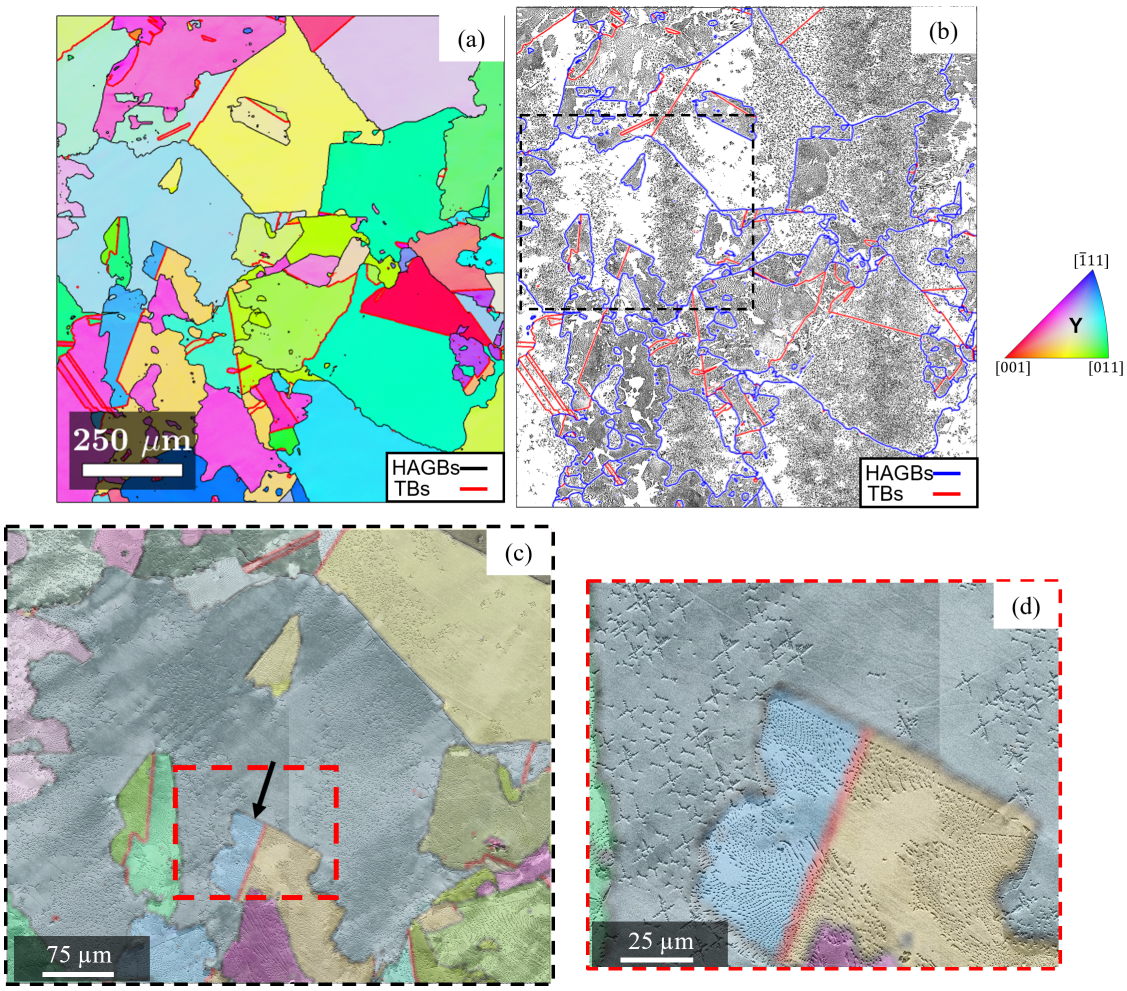
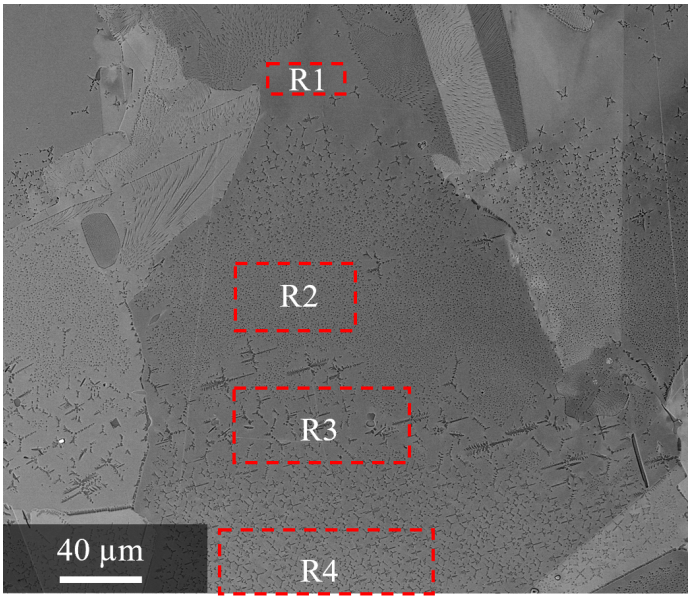


Figure 5.19: Example of the non-uniform distribution of continuous precipitates in sample 1C. An IPF Y map of sample 1C (a). The corresponding FSE image was segmented using ilastik, and the result is shown in (b) (where black pixels represent γ' precipitates), with grain boundaries overlaid. A region of interest showing the variation in precipitate density within a single grains is highlighted in (c), where a transparent copy of the IPF map is overlaid onto an FSE image. A sub-region where discontinuous precipitates are consuming one of the precipitate free bands in highlighted in (d).

considering the difference between the concentrations of γ and γ' forming elements (i.e. Wt. % (Cr + Co) - Wt. % (Ti + Al)) in the different regions. This difference (Wt. % (Cr + Co) - Wt. % (Ti + Al)) will be referred to as the segregation coefficient.

Region 1 in Fig. 5.20 has no γ' precipitates, and the highest value of the segregation coefficient, i.e. the highest relative concentration of γ forming elements. Region



		Composition in Wt. %										
Region	Comment	Ni	Cr	Co	Fe	Ti	W	Mo	Al	Nb	Zr	Segregation coefficient
Whole area		57.4	16.2	8.6	4.3	3.7	3.2	2.9	2.2	1.0	0.2	18.9
R1	No γ'	57.1	16.5	8.7	4.4	3.5	3.6	2.9	2.2	1.0	0.2	19.5
R2	Fine γ'	57.3	16.4	8.6	4.3	3.7	3.2	3.0	2.2	1.0	0.2	19.1
R3	Very coarse γ'	57.8	16.0	8.5	4.2	4.0	3.1	3.0	2.3	1.1	0.1	18.3
R4	Coarse γ'	58.0	16.0	8.5	4.2	4.0	3.0	2.9	2.3	1.1	0.1	18.3

Figure 5.20: Four regions with different distributions of continuous precipitates in sample 1C from which the local chemical composition was measured. The results are shown in the table.

2 has the smallest precipitates (here the precipitates have diameters $\approx 0.57 \pm 0.19$ µm), and the next highest value of the segregation coefficient. Regions 4 and 3 have coarser precipitates and the third highest and highest values of the segregation coefficient, respectively.

However, the volume fraction of precipitates in regions 2-4 is very similar. Considering both observations (i.e. the different precipitate sizes, but similar overall volume fractions), it is hypothesised that the remnant chemical segregation may be affecting the ease of precipitate nucleation more than the equilibrium volume fraction. Where the segregation coefficient is highest, nucleation is retarded, and a more coarse and sparse distribution of precipitates is formed.

The potential role of chemical segregation on precipitate distribution is investigated further in Chapter 7.

In this section, two effects influencing the evolution of precipitates during slow cooling have been identified. Firstly, there is the effect of remnant chemical segregation, which leads to a non-uniform spatial distribution of continuous precipitates; this is thought to be due to retarded nucleation. Secondly, there is discontinuous precipitation. As highlighted in Fig. 5.19 (d), discontinuous precipitation can consume the precipitate free bands. This is an example of type 1 discontinuous precipitation, where the discontinuous precipitation reaction occurs at a boundary advancing into a supersaturated matrix containing no precipitates.

5.6 Summary

In this chapter the precipitate distribution forming during slow cooling through the γ' solvus temperature was investigated. This precipitate distribution is very inhomogeneous. A mix of continuous, discontinuous and grain boundary precipitates are present. The continuous precipitates appear either as a fine and dense distribution of spherical precipitates or octodendrites, although the former could be an end on view of discontinuous precipitates. Discontinuous precipitation is observed to occur behind grain boundaries migrating into regions with and without precipitates ahead of the migrating interface, i.e. both type 1 and type 2 discontinuous precipitation as define by Butler and Williams in [83]. The main conclusions are that:

1. The discontinuous precipitates have the shape of "spaghetti" in 3D as shown by 3D FIB tomography in section 5.3.2, and this can lead to individual 2D micrographs giving misleading impressions of the shape and size of such precipitates. It has been demonstrated that measurements of precipitate size and aspect ratio based just on 2D micrographs can be significantly affected by which plane the precipitates are viewed from. Discontinuous precipitates may be misidentified as continuous ones, based on 2D micrographs.

2. Grain boundary motion happens with discontinuous precipitation, and has a significant impact on grain size and morphology. It is shown that the number weighted grain size can be reduced by over 50% (from 134 µm to 63 µm) and the area weighted grain size can be reduced by $\approx$ 35% (from 365 µm to 302

µm) just due to the grain boundary motion associated with discontinuous precipitation. This suggests that thermal cycling through the solvus temperature could be a means of reducing grain size at the start of sub-solvus forging without additional super-solvus forging. Additionally, the length fraction of twin boundaries is reduced due to this grain boundary motion, although the total length of twin boundary may increase or remain the same.

3. Grain boundary morphology is also affected by discontinuous precipitation. As precipitation occurs during cooling the ratio of grain area to grain perimeter decreases, indicating that grain boundaries become more serrated. This is partially due to the discontinuous precipitation reaction front encountering continuous precipitates and being locally pinned, as shown in Fig. 5.5. Notably, precipitation was observed to commence only at temperatures below 1090 °C, even at a cooling rate of 10 °C/ hr, i.e. more than 20 °C below the theoretical solvus temperature.

4. The continuous precipitates are very inhomogeneously distributed; within a single grain regions with no precipitates are within roughly 100 µm of regions with a fine and dense distribution of spherical precipitates. These differences could not be clearly explained based on remnant chemical segregation.

The early processing stages considered in this chapter are not generally considered in the scientific literature, and some novel observations have been made. Namely, the "spaghetti" like shape of discontinuous precipitates in 3D, their very long lengths (at least tens of µm) and the change in grain size associated with discontinuous precipitation.

The mechanisms underlying these novel observations are left as open questions; in the following chapters the evolution of the complex microstructures introduced here during forging will be investigated.

6 Recrystallisation evolution during the early stages of billet conversion

The early stages of the ingot to billet conversion process typically comprise a homogenisation heat treatment at high temperatures (1200 °C) followed by super-solvus forging, cooling through the solvus temperature, then a sequence of sub-solvus forging and heating stages. This chapter evaluates the microstructural changes happening during the first sub-solvus forging, where the precipitate distribution present has been examined in the previous chapter (Chapter 5). The interaction of the precipitate state developed during slow cooling through the solvus temperature with recrystallisation is examined.

The thermo-mechanical paths applied to samples discussed in this chapter are shown in Fig.3.5 in Chapter 3. These will be referred to as experiment 1A, 1B, 1C 1D and 1E. In experiment 1, 5 samples were generated by quenching at different points along the path, as indicated. The first three samples (1A,1B,1C) show the microstructure generated during slow cooling through the solvus temperature and were analysed in Chapter 5. Sample 1D was quenched immediately after forging and shows how this microstructure evolves during sub-solvus forging. Sample 1E, which was air cooled, shows if cooling rate has any significant influence.

The thermo-mechanical paths applied to samples discussed in this chapter are shown in Fig. 6.1.

6.1 Evolution of unrecrystallised grains

6.1.1 Texture evolution

Sample 1D allows the interaction of the precipitate distribution which has formed in sample 1C with recrystallisation to be studied. A series of low magnification IPF maps (coloured along the compression direction) from sample 1D are shown in Fig. 6.2. These come from four different locations, with four different strain levels, and

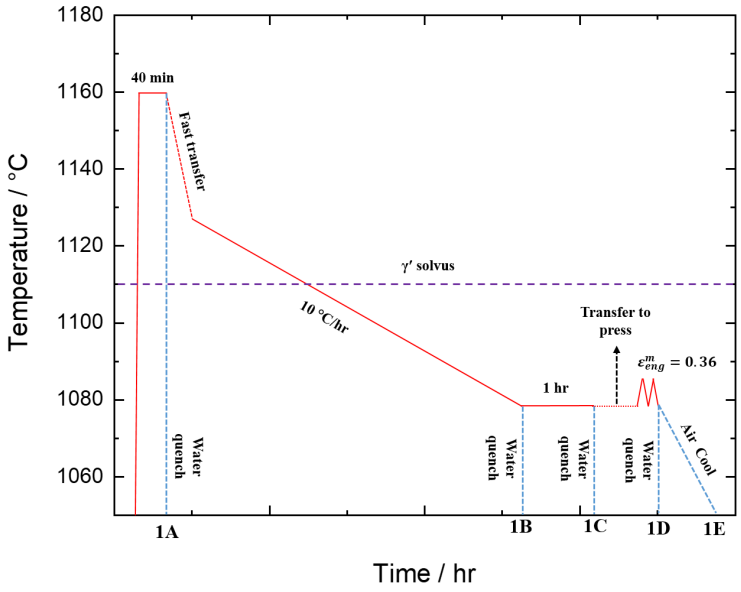


Figure 6.1: An overview of the experiments done to investigate recrystallisation during the early stages of industrial forging. The total macroscopic engineering strain applied during compression is indicated.

give a general overview of the progress of recrystallisation. These were taken using a step size of 1 µm and cover areas of approximately 1 mm^2.

The IPF maps in Fig. 6.2 (a) - (d) show that a typical necklace structure of recrystallised grains has developed around the unrecrystallised ones. The tendency for the unrecrystallised grains to appear green in these maps reflects the ⟨110⟩ fibre texture (parallel to the compression direction) which has developed in the unrecrystallised grains during forging. This is further highlighted in the (110) pole figures included in Fig.6.2 (e). These show the texture strength for the unrecrystallised grains in multiples of the uniform distribution; here unrecrystallised grains were classed as those grains having equivalent circle diameters above 10 µm.

Such a texture is expected in FCC materials during compression [98]. It should be noted that the ⟨110⟩ axis aligning with the compression direction is not the ⟨110⟩ axis of the active slip system; in fact slip systems involving this ⟨110⟩ axis will have low Schmidt factors, as the slip plane normal will be almost perpendicular to the compression direction. The highest Schmidt factor slip systems will have its ⟨110⟩ axis approximately 45 ° from the compression direction, and four small peaks

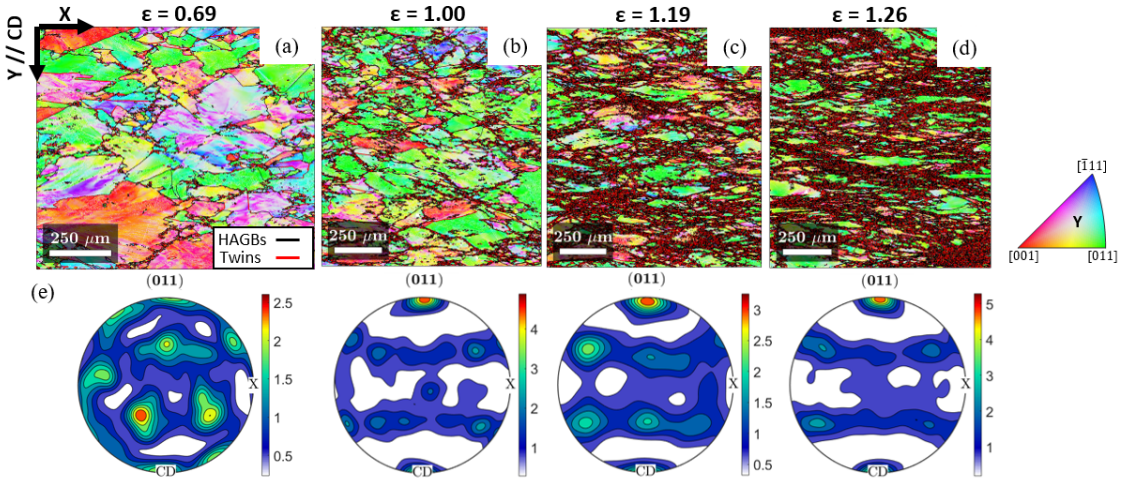


Figure 6.2: Large area IPF maps showing microstructure evolution as a function of strain in sample D (a) - (d). (110) pole density figures for the unrecrystallised grains, corresponding to each strain zone, which show the development of a ⟨110⟩ fibre texture in the unrecrystallised grains during forging (e). Note that in (a-d) the recrystallised grains cannot be well seen due to their small size, and their boundaries (coloured red or black) obscure them.

corresponding to this can be seen in the ⟨110⟩ highest strain pole figure in Fig. 6.2 (e).

6.1.2 Influence of texture on recrystallisation

The texture found in the unrecrystallised grains raises the question of whether such a texture may hinder recrystallisation; grains which, by chance, have a ⟨110⟩ axis along the upsetting direction at the onset of deformation may develop lower long-range orientation gradients as a result of upsetting, and be less likely to recrystallise during upsetting. Such an orientation could thus be considered "stable" with respect to upsetting; grains which have it undergo less rotation during deformation than grains which do not.

A similar effect of texture on recrystallisation has been characterised in Maric's PhD thesis [99]. There, in hexagonal titanium, it was found that certain grain orientations are stable during deformation (i.e. the orientation does not change much during deformation) and that these grains undergo less dynamic recrystallisation than grains whose orientations are not stable during deformation.

Here, this effect can be tested using the EBSD datasets shown in Fig. 6.2. This

was done in the following way:

1. Identify the unrecrystallised grains (here they were classed as grains with a GOS above 2 ° and an equivalent circle diameter of more than 20 µm).

2. Record the minimum angle between a ⟨110⟩ direction and the macroscopic compression direction for each unrecrystallised grain (using their average orientations).

3. Plot grains' internal misorientation (quantified with the GAKAM parameter) as a function of this angle (plots shown in Fig. 6.3.

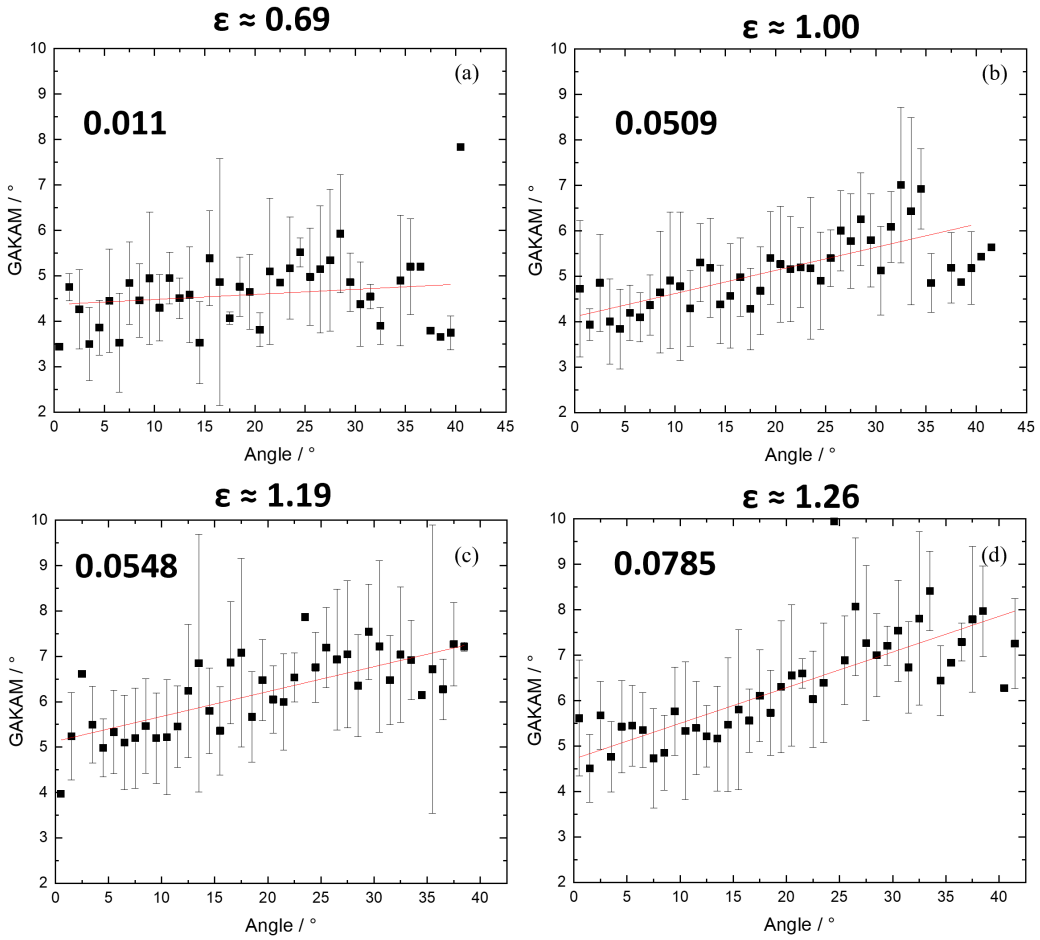


Figure 6.3: Dependence of 5th order GAKAM values on grain orientation. The angle plotted on the abscissa is the minimum angle between a ⟨110⟩ axis of a deformed grain and the macroscopic compression direction.

The angle between the ⟨110⟩ axis and the compression direction is here being used as a proxy measure of how close a given grain was to having the "stable" texture at the *start* of compression; which cannot be directly measured with the post test data available here. The assumption that this angle gives a measure of how close a grain was to having a "stable" orientation at the start of deformation is important in this analysis.

These data are plotted in Fig. 6.3. They show that there is a correlation between the proximity of a ⟨110⟩ axis of a particular grain to the compression direction at the start of deformation, and grain stability. Fig. 6.3 shows data for four different strain levels, indicated in the titles of the graphs (a-d). Here, the angles between the ⟨110⟩ axes of the deformed grains and the compression direction (plotted on the abscissa) have been put into 1 ° wide bins, and the 5^{th} order GAKAM for all grains in that bin has been calculated. 5^{th} order values were used so that orientation gradients on a reasonable length scale could be assessed; the 5^{th} order kernel has a width of 10 µm. These GAKAM values were averaged for each bin, and these average values are plotted as the ordinate. The error bars are from the standard deviation of the GAKAM values in each bin. The very large error bars arise when there are only 2 grains in a given bin.

Lines of best fit have been included in these graphs as a guide to the eye, and the gradient of these lines is positive for each graph. The positive slope of these lines shows that grains with a ⟨110⟩ axis closer to the compression direction become less misoriented during deformation, i.e. this is evidence that these grains develop lower long-range orientation gradients. This is very relevant to the onset of recrystallisation, since orientation gradients are precursors to the formation of recrystallised grains [63].

The slopes of these lines become more positive at higher strain levels, indicating that the orientation gradients in grains which don't have a "stable" texture increases more rapidly at higher strain levels, and these grains thus become increasingly likely to undergo recrystallisation. Therefore, the data in Fig. 6.3 shows that grains with a ⟨110⟩ fibre texture along the upsetting axis at the onset of upsetting are less likely to recrystallise than other grains, and the stability of these grains as well as the rotation of other grains during forging contributes to the observed texture.

6.2 Precipitation in unrecrystallised grains

6.2.1 Overview

Alongside the EBSD data which allows the texture of the unrecrystallised grains to be investigated, a series of FSE images were collected from the region at the centre of sample 1D, shown in Fig. 6.2, with a local strain level of $\epsilon \approx 1.26$. These allow precipitation in the unrecrystallised grains to be investigated. Fig.6.4 shows an IPF Y map from the centre of sample 1D, and selected magnifications from the FSE image. The selected images exemplify the fact that the remaining unrecrystallised grains rarely if ever contain octodendritic precipitation.

Indeed, in the region shown in Fig. 6.4, only one of the large unrecrystallised grains was found to contain octodendritic precipitation (by investigation of the FSE images). This grain is highlighted in Fig. 6.5.

Bearing in mind the previous discussion on the "stable" texture of the unrecrystallised grains, it can be noted that this single grain containing octodendrites is very closely aligned to the "stable" fibre texture. This grain has a [-0.03,-2.62,2.42] crystal direction parallel to the macroscopic compression direction, i.e. it has a $\langle 110 \rangle$ axis within 2.3° of the compression direction. This suggests that when octodendrites survive in unrecrystallised grains up to high strains, it is because the grain has developed low internal orientation gradients during forging, due to a "stable" orientation at the start of forging.

Instead the unrecrystallised grains contain predominantly discontinuous precipitation, or occasionally a very fine and dense spherical precipitation, as highlighted in the BSE image in Fig. 6.4 (d). Further examples of regions containing this fine and dense distribution of spherical precipitates are given in Fig. 6.6. The KAM maps in (a) and (c) and corresponding FSE images in (b) and (d) show that the regions containing the fine and dense spherical precipitates have very low local misorientation levels.

6.2.2 Origin of fine spherical precipitation

While the discontinuous precipitation found in unrecrystallised regions has persisted from the start of forging, the fine and dense spherical precipitation was not identified

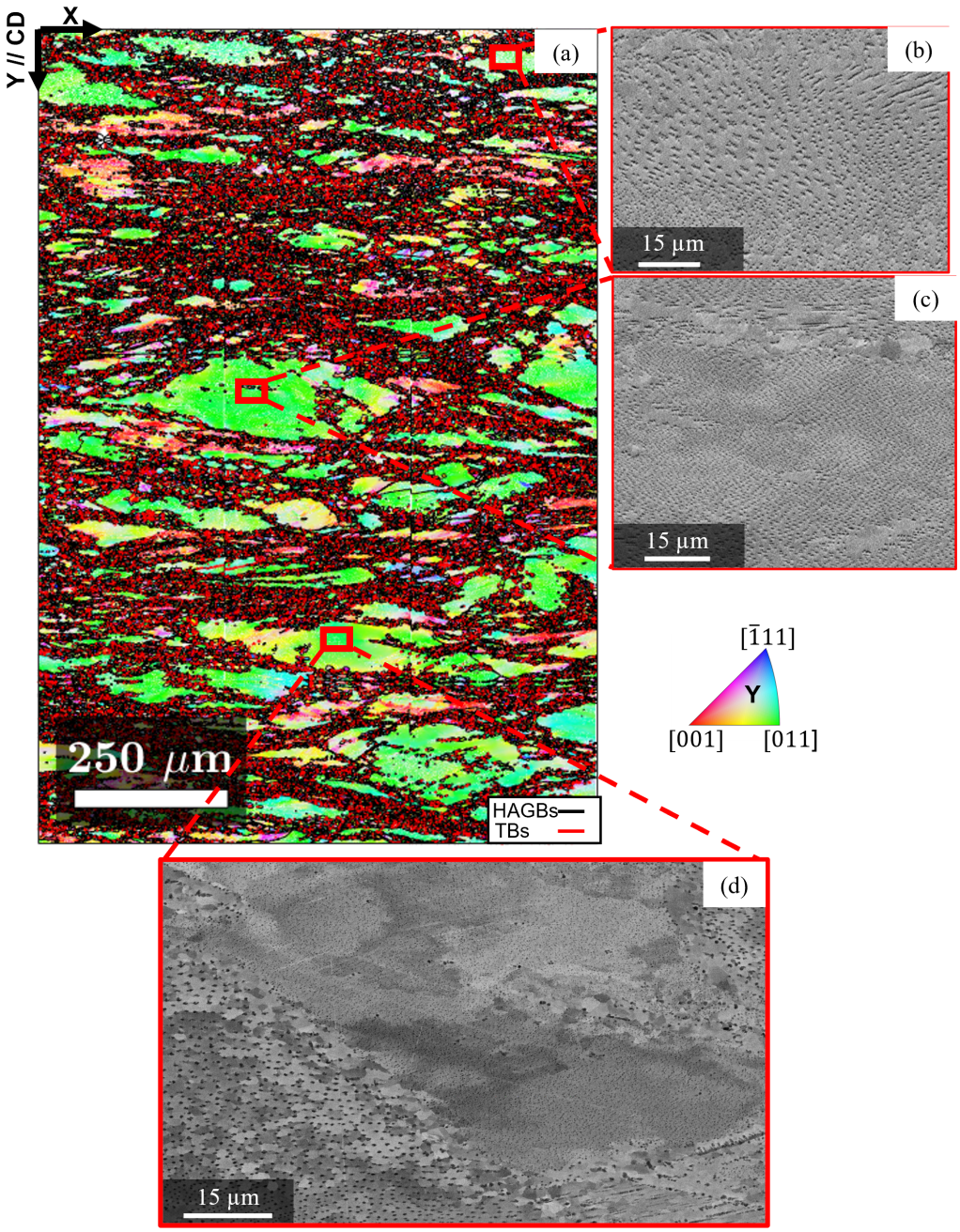


Figure 6.4: (a) IPF Y map of a large area from a region of sample 1D where $\epsilon \approx 1.26$, (b) - (c) magnified FSE images of the precipitation in selected unrecrystallised grains highlighted in (a). (d) A BSE image of a region with very fine spherical precipitates.

in samples 1B and 1C after slow cooling through the solvus temperature in Chapter 5. These fine and dense spherical precipitates have formed in the regions which were free from precipitation after slow cooling through the γ' solvus. Such regions were

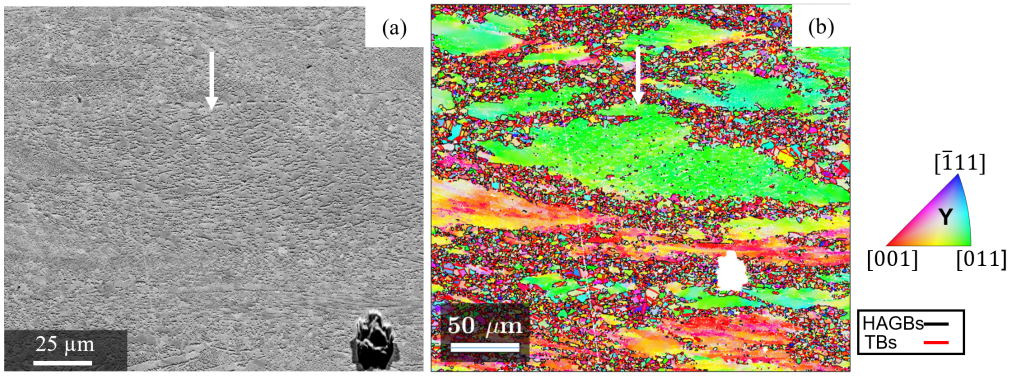


Figure 6.5: (a) An FSE image and (b) corresponding IPF Y map of an unrecrystallised grain which contains octodendritic precipitation. This grain can also be found towards the top left of Fig. 6.4 (a).

identified in Chapter 5, and EDS data suggested they had slightly lower concentrations of the γ' forming elements that elsewhere. There are three possible origins for this fine and dense spherical precipitation:

1. These could be an end on view of the discontinuous precipitates. As mentioned previously, these "spaghetti" shaped precipitates can look very different in different 2D sections.

2. They could be continuous precipitates, which formed during cooling through the solvus, in a region of high nucleation density, where little growth has occurred and the spherical to cuboidal shape transition has not happened.

3. These precipitates could have formed dynamically, i.e. during deformation.

Each of these possibilities will be considered. The first of these possibilities was investigated using FIB-SEM tomography to create a 3D view of these precipitates. A suitable example of these spherical precipitates in sample 1D from a region with a local strain level $\epsilon \approx 0.95$ is shown in Fig. 6.7. As in the previous example, these precipitates are found in a grain alongside other precipitate types; in this case both octodendrites and discontinuous precipitates are also present. The 3D data confirmed that these precipitates are indeed (approximately) spherical in shape, so the first possibility listed above is eliminated.

The second possibility can be assessed by comparing the size of spherical precipitates found prior to deformation and subsequent to it. Taking an example of

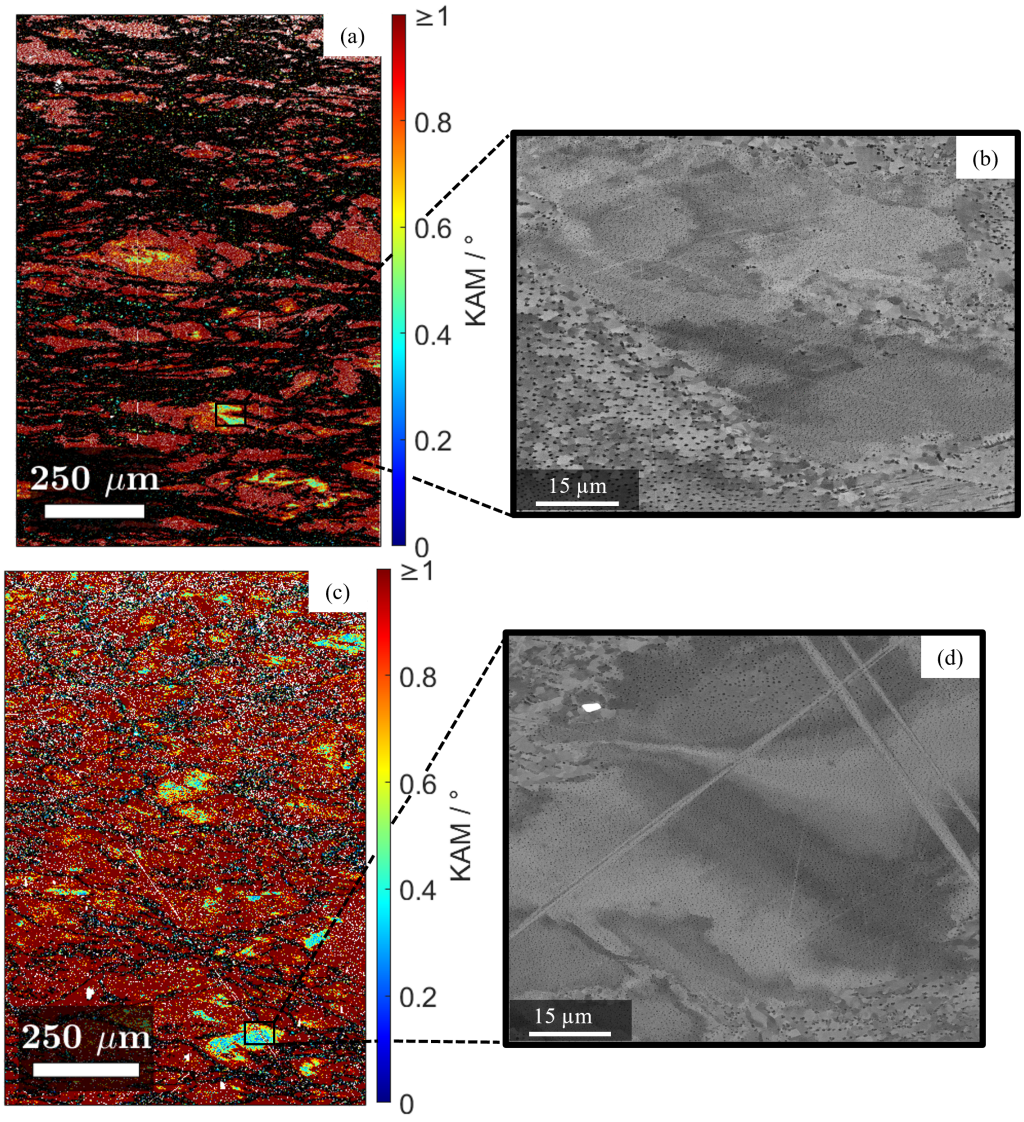


Figure 6.6: (a) KAM map of a large area from a region of sample 1D where $\epsilon \approx 1.26$, (b) a BSE image showing the precipitate state in a very low KAM area. (c) KAM map of a large area from a region of sample 1D where $\epsilon \approx 1.00$, (d) a BSE image showing the precipitate state in a very low KAM area.

the fine and dense precipitates from a region with a local strain level of $\epsilon \approx 1.00$ after forging, a mean equivalent diameter of 0.18 ± 0.08 µm is found from measuring 677 precipitates. The spherical continuous precipitates present prior to forging are considerably larger than those found after forging (measured to have equivalent diameters $\approx 0.57 \pm 0.19$ µm) which counts against the second possibility above, and suggests these precipitates were not present prior to compression.

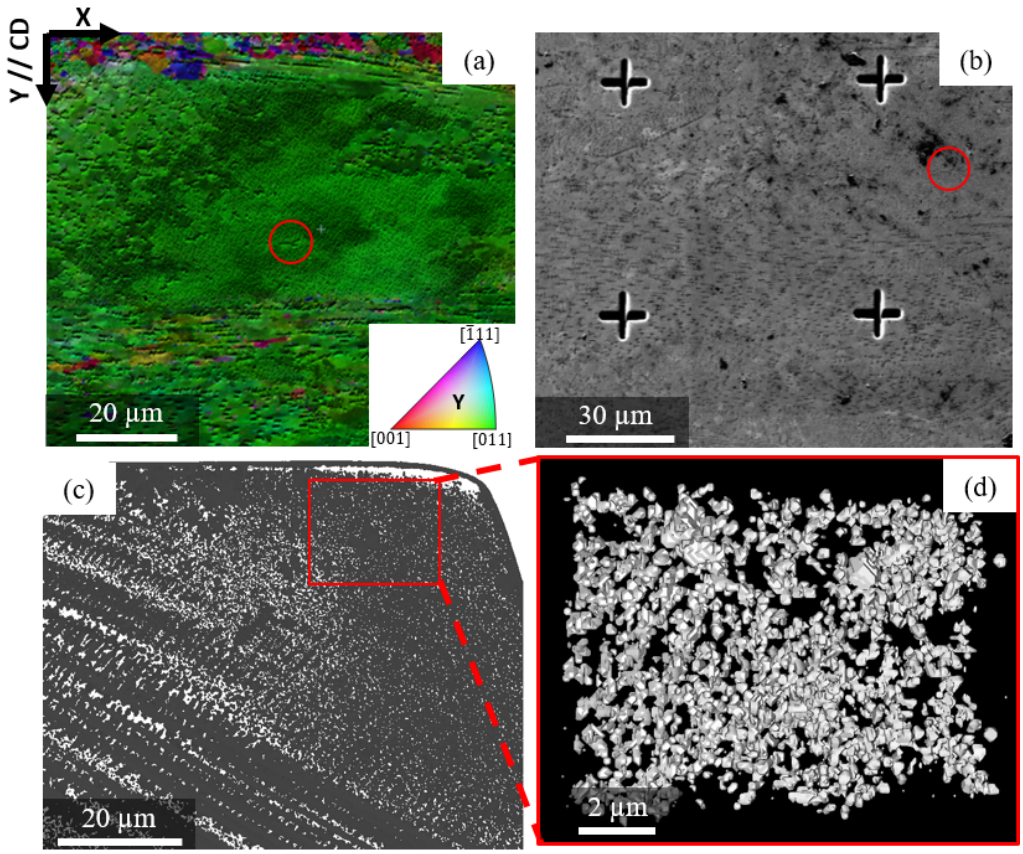


Figure 6.7: A 3D view of the fine and dense precipitates found after forging, obtained using FIB-SEM tomography. (a) BSE image of a region containing fine precipitates with overlaid IPF map showing they are within a single grain, also containing octodendrites and discontinuous precipitation, (b) SE image showing the markers used to delimit the region of interest, (c) 3D view of a segmented sub-volume, and (d) enlarged view of the dynamically formed precipitates in (c). The red circles in (a) and (b) indicate a particular octodendritic precipitate.

This leaves the third possibility open, that these precipitates formed dynamically. The phenomena of dynamic precipitation has been observed previously in different alloy systems, including MnS precipitates in steels [100] and Nb(C,N) in steels [101]. In DSC experiments, deformation at 800 °C was shown to lower the temperature of the exothermic peak associated with precipitation of γ'' in IN718 from 804 °C to 742 °C [102]. Dynamic precipitation has also been recorded in Rene-65 [103], and it was shown that low strain rates, deformation temperatures and high strain levels promote more dynamic recrystallisation. It is worth noting that in these cases, dynamic precipitation seems to have occurred uniformly throughout the microstruc-

ture, whereas these fine and dense spherical precipitates were only found in certain regions of some unrecrystallised grains.

Dynamic precipitation is explained as follows. During deformation, dislocation density increases, and the dislocations become entangled with one another. Precipitation along the dislocation line is energetically favourable, due to the interaction between the strain field of the dislocation and that of the precipitate. Such interactions are complex, and for the purposes of modelling dynamic precipitation they can be simplified to the assumption that precipitation along the dislocation releases the dislocation core energy over the precipitate radius, as done by Dutta *et al.*[101, 104].

Due to recrystallisation, and dislocation trapping by precipitates, sample D in this study is not expected to have a uniform distribution of dislocations, and certain high dislocation density regions with a higher density of dislocation nodes are the favoured sites for dynamic precipitation. Dutta *et al.* have shown that a non-uniform distribution of dislocations in the matrix of metal-matrix composites leads to different precipitation kinetics than in the pure matrix material [105]. In the present case, higher dislocation densities in the unrecrystallised grains may favour dynamic precipitation there, rather than in the recrystallised grains.

However, there are also some observations that count against the possibility that these precipitates form dynamically:

Firstly, to attempt to confirm that these precipitates have formed dynamically, experiment 1D (as shown in Fig. 6.1) was repeated, with the sample being subjected to a 45 minute hold at 1080 °C after forging, then being quenched in water. This was not found to dissolve all such small spherical precipitates, as highlighted in Fig. 6.8. The precipitates shown in Fig. 6.8 have sizes similar to the fine and dense precipitates found after forging, much smaller than those found in sample 1C, prior to forging.

Secondly, the regions with the fine and dense precipitates show very low intergranular misorientation levels (i.e., low KAM values), suggesting low, rather than high, dislocation densities.

As such, the formation mechanism of these spherical precipitates which are found after deformation is not clear, as there are points against each of the three possible origins listed.

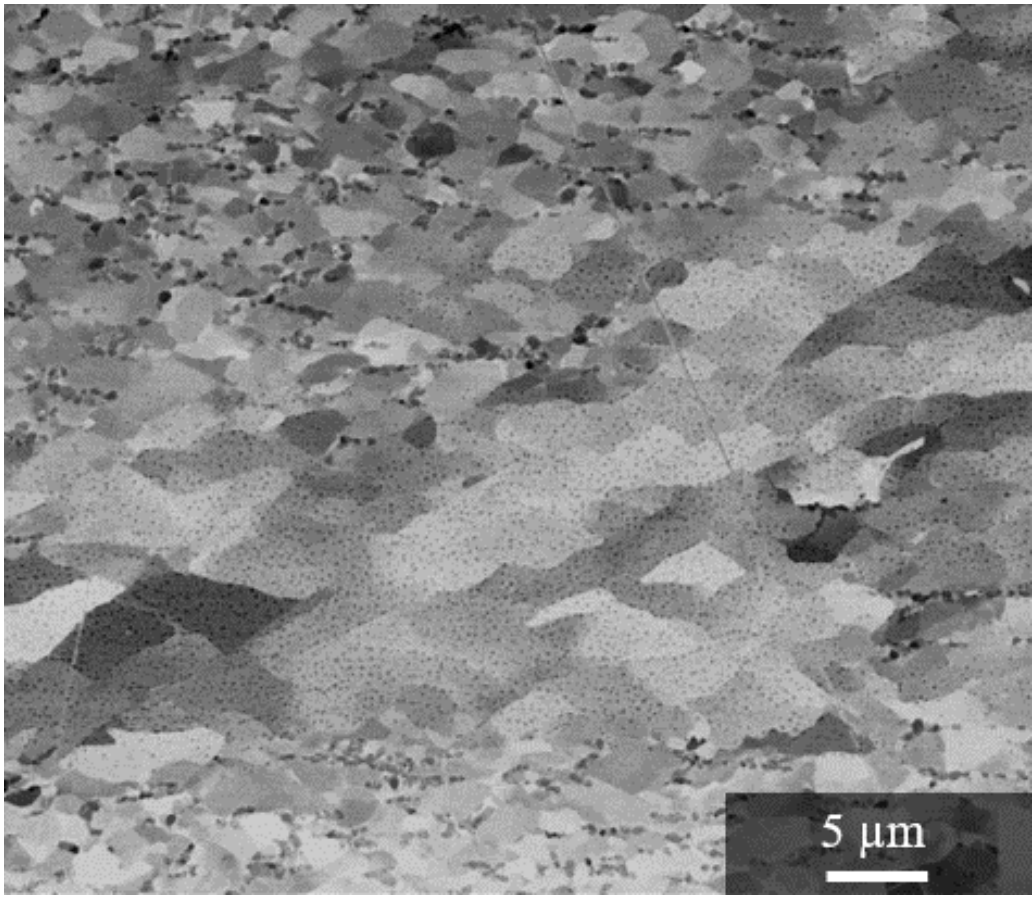


Figure 6.8: Example of the fine and dense spherical precipitates found after a post dynamic hold of 45 minutes at 1080 °C.

6.2.3 Effect of fine spherical precipitates on recrystallisation

Regions which contain this fine and dense spherical precipitation can be identified from EBSD data as regions having low levels of *local* misorientation, i.e. lower than elsewhere in the grain which contains them, as highlighted in Fig. 6.6. This is shown in the second column of Fig. 6.9. The KAM maps here show the first order KAM values, and these are very low in areas with the fine and dense spherical precipitation. Note that in Fig. 6.9 the KAM scale has been limited to 1 °, which is a low limitation considering that noise in EBSD data is typically on the order of 0.5 °. As such, most of the map shows red pixels (values $\geq$ 1 °), but some regions with very low KAM values can still be identified. These regions contain the fine and dense spherical precipitates - highlighted by the FSE images in the third column of Fig. 6.9. The low values of local misorientation can be explained either due to

a lack of long-range orientation gradients, or due to precipitates limiting sub-grain size, and hence sub-grain boundary misorientation angle.

The first possibility can be tested directly from the EBSD data, by using the KAM values in a 10$^{\text{th}}$ order KAM values (KAM_{10*}), calculated as described in Chapter 3. The data investigated here were collected using a step size of 1 µm, so the 10$^{\text{th}}$ order KAM kernel has a radius of 10 µm.

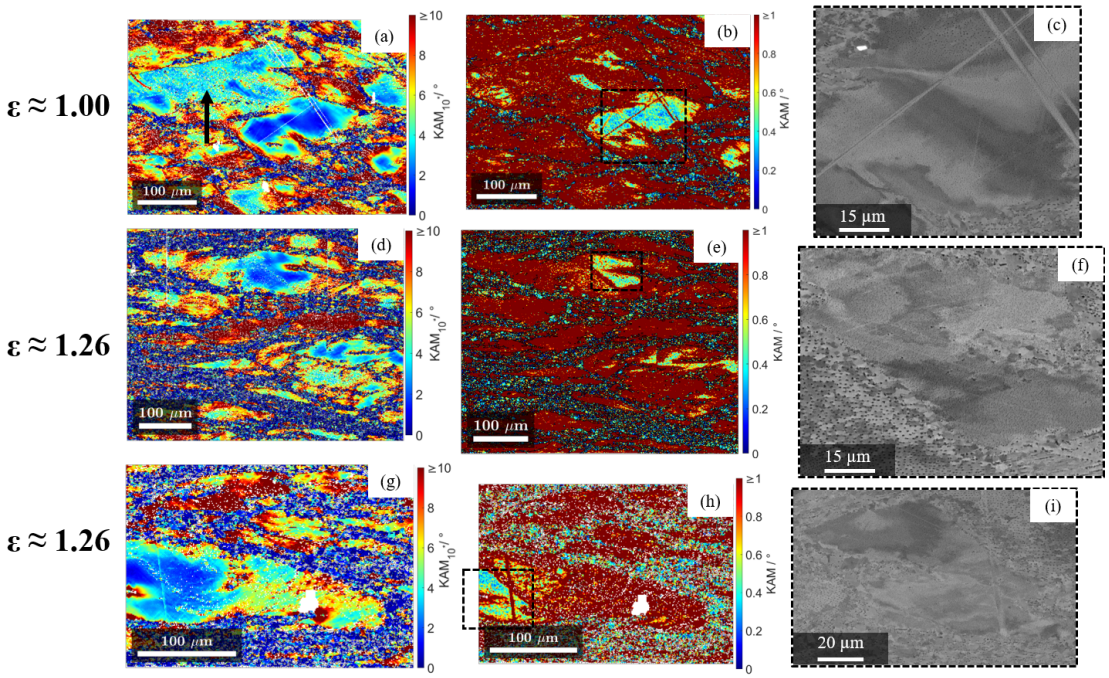


Figure 6.9: Examples of the long-range orientation gradients and local misorientations in regions containing fine and dense spherical precipitation. KAM maps showing only the 10$^{\text{th}}$ order nearest neighbours (first column, (a),(d) and (g)) give a measure of overall orientation gradients. Corresponding first order KAM maps show the local misorientations (second column, (d),(e) and (h)) in areas around spherical precipitates. The spherical precipitates are in regions indicated by the black boxes, and BSE images from these regions are shown in the third column ((c),(f) and (i)).

The 10$^{\text{th}}$ order KAM map so produced is shown in the 1$^{\text{st}}$ column of Fig. 6.9, and this gives a measure of the long-range orientation gradients about each point. Here we can see that the regions with the fine and dense spherical precipitates show very low long-range orientation gradients, as well as very low local misorientations (shown in the second column). Three examples of regions with the fine and dense spherical precipitation are shown, and in all three these regions have both very low long-range and local orientation gradients.

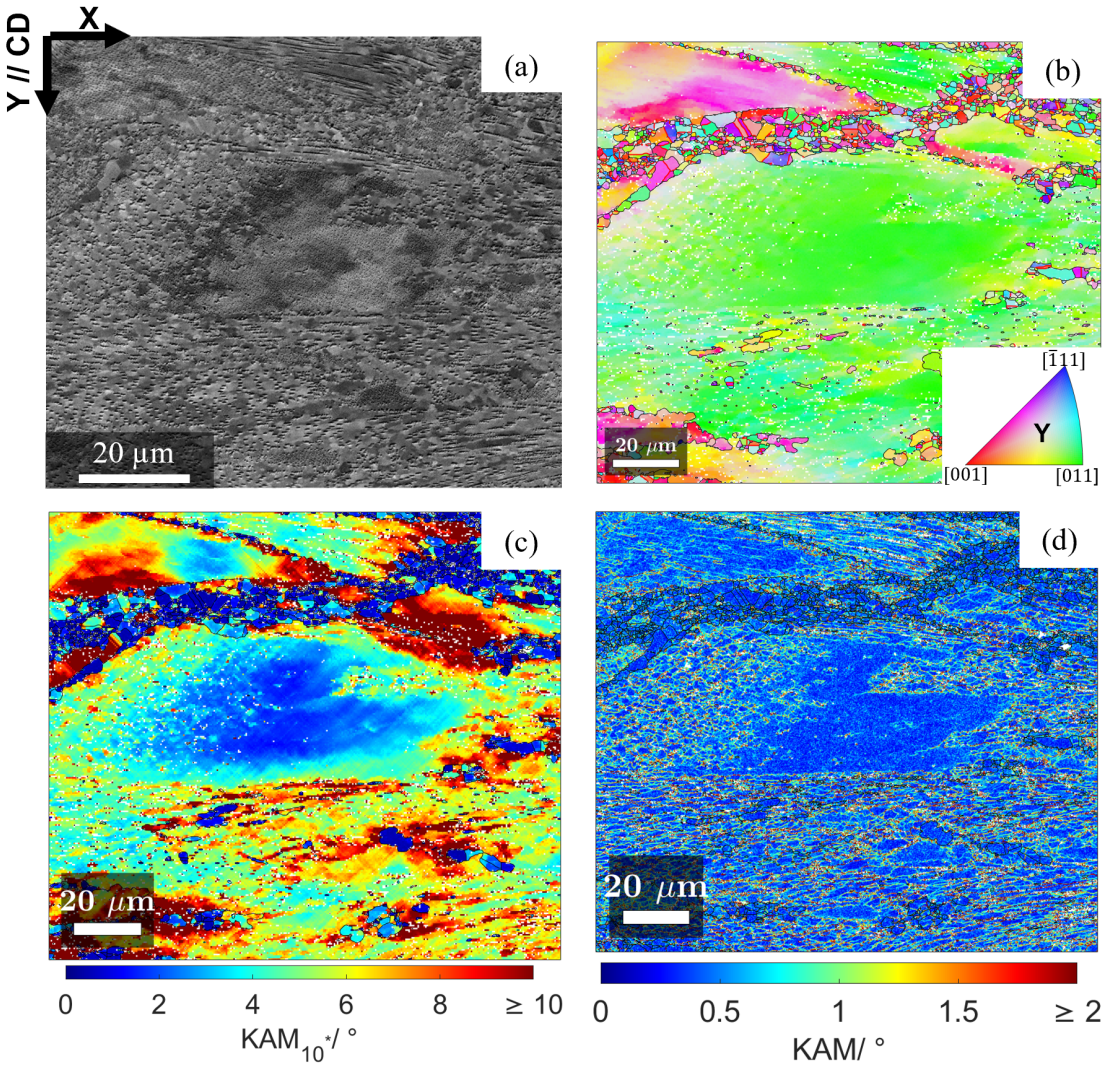


Figure 6.10: Comparison of the effect of fine and dense spherical precipitation and discontinuous precipitation on long-range and local orientation gradients. (a) shows a FSE image of a region in which a single grain contains both types of precipitate, (b) the corresponding IPF map. (c) Shows the long-range orientations gradients in a 9.9 µm radius kernel, and (d) the local orientation gradients.

The first row of Fig.6.9 shows a grain which has both discontinuous precipitation (in the region indicated by the black arrow) and fine and dense spherical precipitation. The region with discontinuous precipitation has both higher long and short-range orientation gradients. Implying that regions with the fine and dense spherical precipitation develop low long- and short-range orientation gradients.

This point is highlighted very clearly in Fig. 6.10 which shows a single grain that

contains both discontinuous precipitation and the fine and dense spherical precipitation. The fine spherical precipitates are at the centre of the FSE image in Fig. 6.10(a). Fig. 6.10(c) shows the long-range orientation gradient, using a kernel with a radius of 9.9 µm. Fig. 6.10 (d) shows the local orientation gradients in a KAM map (this map used a step size of 0.15 µm). The scale in (c) has been limited to clearly show the difference between the region with discontinuous precipitates and the one with the spherical precipitates.

Therefore, of the two options mentioned above to explain the low local misorientations in regions with the spherical precipitation, there is evidence of the fine and dense spherical precipitation limiting the sub-grain size *and* such precipitation also hindering the formation of long-range orientation gradients.

6.2.4 Influence of precipitation on recrystallisation

The effects of precipitation on dislocation substructures and recrystallisation is related to the inter-precipitate spacing, and can be understood using a model from Humphrey's textbook [63]. This model considers recrystallised sub-grains growing between precipitates, in a grain which has an orientation gradient Ω °/µm. The sub-grains are considered to be pinned by the precipitates, so that sub-grain size D_{sg} µm is limited to the inter-particle spacing. Under these conditions the misorientation angle of the sub-grain boundary θ is given by:

$$\theta = \Omega \cdot D_{sg} \tag{6.1}$$

The larger the inter-particle spacing, the higher angle boundary can be formed in a given orientation gradient. The precipitate limited sub-grain size can be *estimated* analytically, as a function of the precipitate volume fraction f, their size, and a geometric factor. For example, for a cubic arrangement of spherical precipitates with radii r, the particle spacing is given by:

$$D = \left(\frac{4\pi}{3}\right)^3 \cdot \left(\frac{r^3}{f}\right)^{1/3} \tag{6.2}$$

The reason why grains with continuous precipitation, rather than octodendritic precipitation, tend not to recrystallise can be justified based on a consideration of the inter-particle spacing; and by assuming that recrystallisation nucleation proceeds by

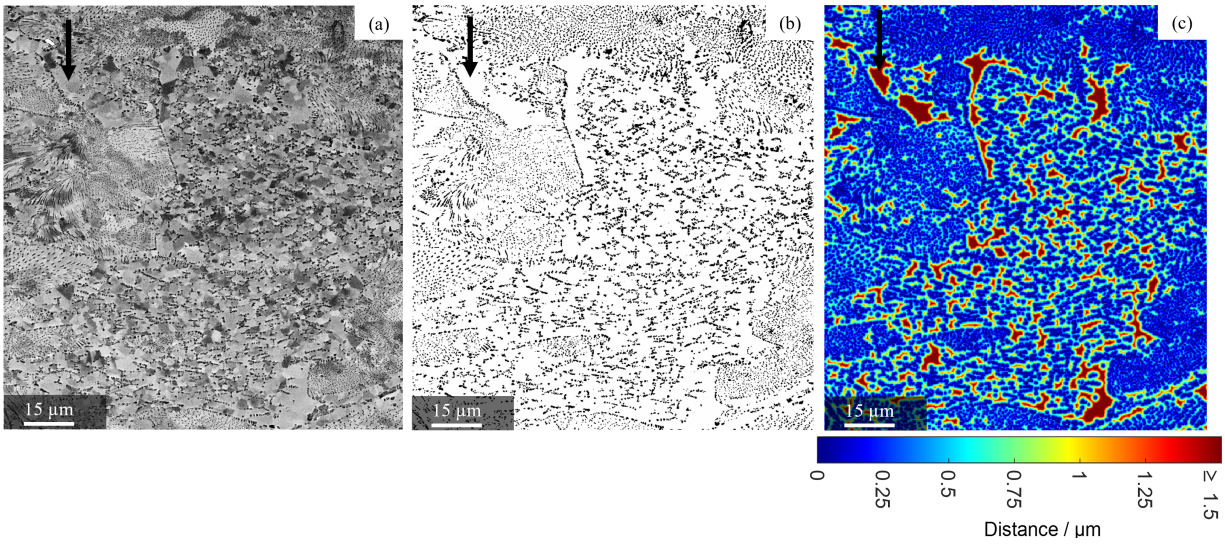


Figure 6.11: (a) A BSE image from a region with a local strain of 0.95 where both octodendritic and discontinuous precipitates are present. (b) A segmented binary version of (a), where the γ' precipitates are shown as black pixels. (c) The distance transform applied to (b). The arrows indicate positions near the centre of recrystallised grains, where the transform has a maximum value.

LAGB formation and migration. The regions with octodendritic precipitates have larger inter-particle spacings than other regions. This is shown in Fig. 6.11. Here a BSE image of region with a local strain level $\epsilon \approx 1.00$ is shown in (a). This region contains two grains with octodendritic precipitation near its centre, and around these are unrecrystallised grains with discontinuous precipitation. From the BSE image of such an area, it is possible to have a proxy measure of the inter-particle spacing, by using the distance transform. First, the BSE image in (a) is segmented to separate out the γ and γ' phases, this was done using ilastik and the result is shown in (b). The distance transform is then applied to this binary image. This transform gives a value to each pixel, which is the distance from that pixel to the nearest dark pixel, i.e. to the nearest γ' surface. Inside the precipitates this gives values of zero, and the largest values are in the centres of recrystallised grains. This is shown in (c) where the scale has been limited to show better contrast, and the arrows indicate a region near the centre of a recrystallised grain with high value of the distance transform. This shows clearly that the distance transform has higher values in the regions with octodendritic precipitation. As such, these regions will also have higher inter-particle spacings, corresponding with the easier recrystallisation there.

The low values of local misorientation (i.e. relatively low first order KAM values)

around the fine and dense spherical precipitates, which was observed in the previous section also agrees with this model. The fine precipitates limit the sub-boundaries to small sizes, so the sub-grain boundaries have low misorientation angles. The highest values of local misorientation, measured at these sub-boundaries, are then also low.

6.3 Formation of recrystallised grains

6.3.1 Overview

The precipitation found in the recrystallised grains formed during forging, is highlighted in Fig. 6.12. The larger recrystallised grains (about 10 µm) in size, such as the one highlighted in Figs. 6.12 (a) and (b), have little to no intragranular precipitation. The same is true for the smaller recrystallised grains (a few µm in size), shown in Figs. 6.12 (c) and (d), one of which is highlighted by an arrow. The precipitates in the recrystallised region in Figs. 6.12 (c) and (d) are concentrated at the grain boundaries, and based on their size, shape and distribution they can't be identified with any of the precipitate types present before forging. As such, the precipitates at their boundaries could either be fragments of whatever precipitation was here originally, or they could be the result of dissolution and reprecipitation during recrystallisation.

6.3.2 Recrystallisation around octodendrites

Inspection of a moderate strain location on sample 1D allows the distinct stages involved in the formation of recrystallised grains in a region with octodendritic precipitation to be identified.

Figs. 6.13 (a), (c) and (d) show that the regions enclosed by the red and black boxes in (b) both contain similar octodendritic γ' precipitation. Despite this similarity, recrystallisation is more advanced in the region enclosed by the black box, likely due to there being more dislocation activity in this region. This can be explained by the different textures of the grains in the two regions, and different plastic incompatibilities with their neighbouring grains.

Figs.6.13 (c) and (d) allow the progression of recrystallisation in regions with octodendritic γ' precipitates to be inspected. In the early stages of recrystallisation

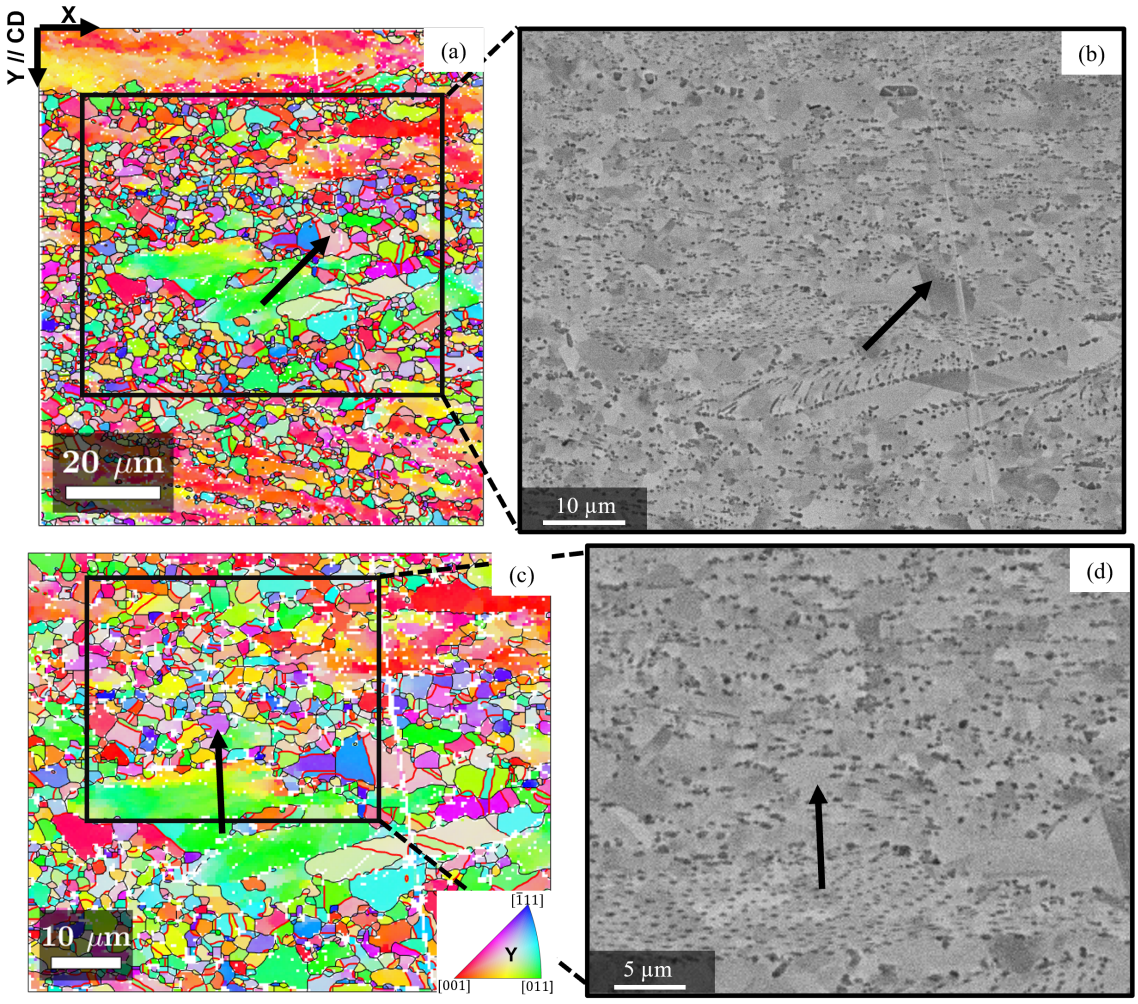


Figure 6.12: Recrystallised grains in a region where $\epsilon \approx 1.26$. An IPF Y map (a) with corresponding BSE image (b), where a relatively large recrystallised grain is highlighted with an arrow; higher magnification views of the same region are shown in (c) and (d), where a smaller recrystallised grain is highlighted.

dislocations pile up at the γ/γ' interfaces. This is evidenced by the medium angle grain boundaries (MAGBs) being concentrated at these interfaces in Fig. 6.13 (c). MAGBs are here defined as boundaries with misorientation angles between 5 ° and 10 °; they correspond to dislocation arrays and are plotted blue. Towards the top left of Fig. 6.13 (d) enclosed sub-grains (enclosed by MAGBs) have formed; these have no internal γ' precipitates, and their boundaries are decorated by γ' precipitates. The blue arrows indicate two such sub-grains. Towards the bottom right of Fig. 6.13 (d) two fully formed recrystallised grains (enclosed by HAGBs) are indicated

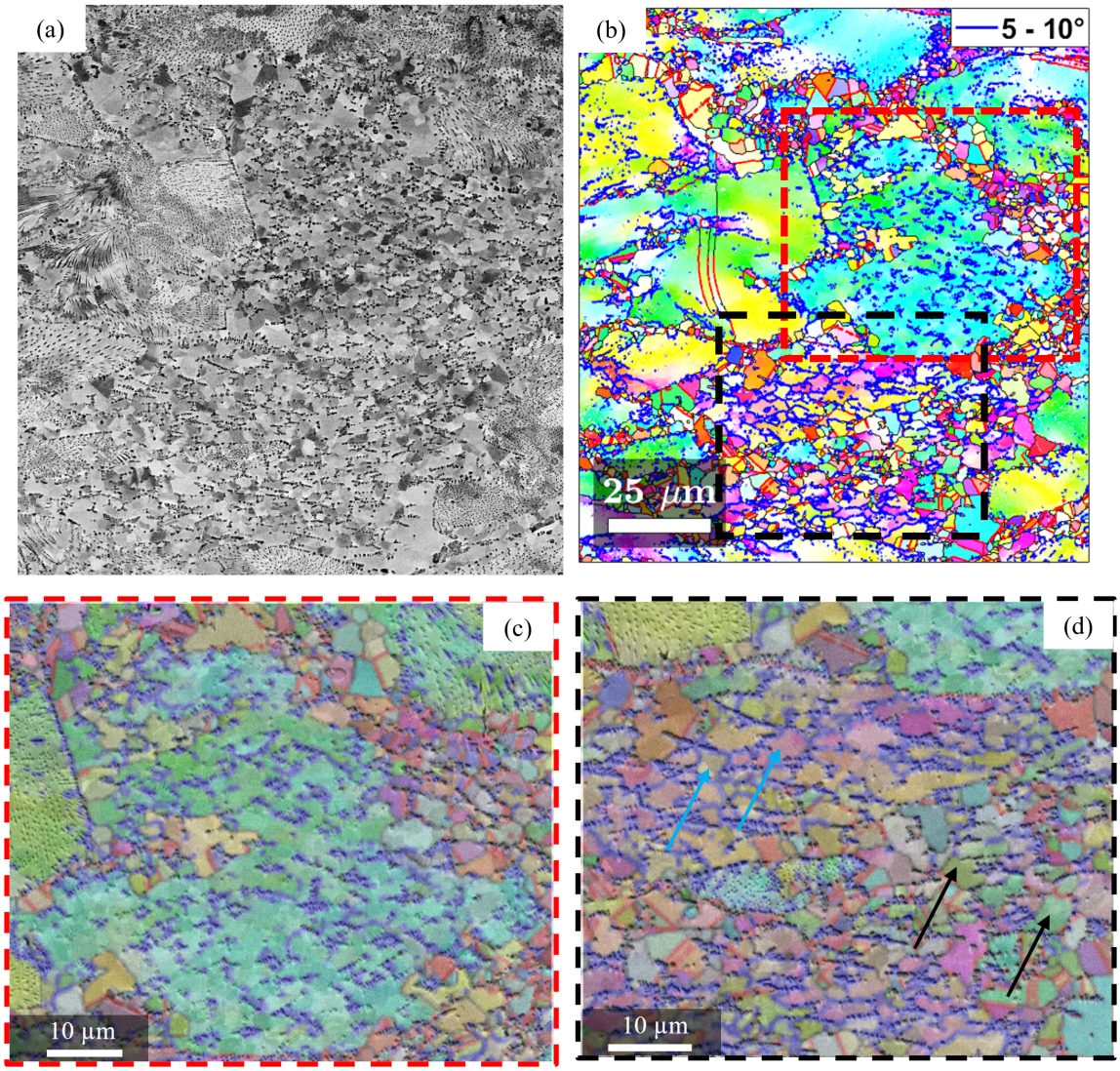


Figure 6.13: Recrystallisation around octodendritic γ' precipitates in sample 1D, under a local strain of $\epsilon \approx 0.95$ (a), BSE image and corresponding IPF Y map with overlaid MAGBs (5-10 ° misorientation angles, plotted blue), respectively. (c) And (d) higher magnification FSE images of the areas outlined in (b) containing octodendrites, with overlaid transparent IPF Y map and MAGBs.

by the black arrows. From Figs. 6.13 (c) and (d) the stages of recrystallisation in regions with octodendritic γ' precipitation can be suggested as follows:

Initially, dislocations pile up at the γ /γ' interfaces, indicated by the MAGBs in Fig. 6.13 (c). With further deformation, dislocation structures branch out from the γ /γ' interfaces and form enclosed sub-grains (enclosed by MAGBs) between the precipitates and may partially dissolve the γ' precipitates they encounter (Fig. 6.13

(d), blue arrows). As more dislocations are accumulated into these sub-boundaries they increase their misorientation angle and develop into high angle boundaries, enclosing recrystallised grains with no internal γ' precipitation (Fig. 6.13 (d), black arrows).

This recrystallisation mechanism, which occurs in regions with octodendritic precipitation could be described as continuous, since it involves a progressive increase in misorientation angle as sub-grains become recrystallised grains (temporally continuous), and because it appears to happen quite uniformly in regions with octodendritic precipitation (spatially continuous). This mechanism is shown schematically in Fig. 6.14. Here, (a) shows the formation of MAGBs at the γ /γ' interfaces, (b) shows the formation of enclosed sub-grains by the branching out of the MAGBs. (c) And (d) show the growth of these grains, which is accompanied by dissolution of surrounding precipitates and an increase in the misorientation angle they have to their surrounding unrecrystallised grain.

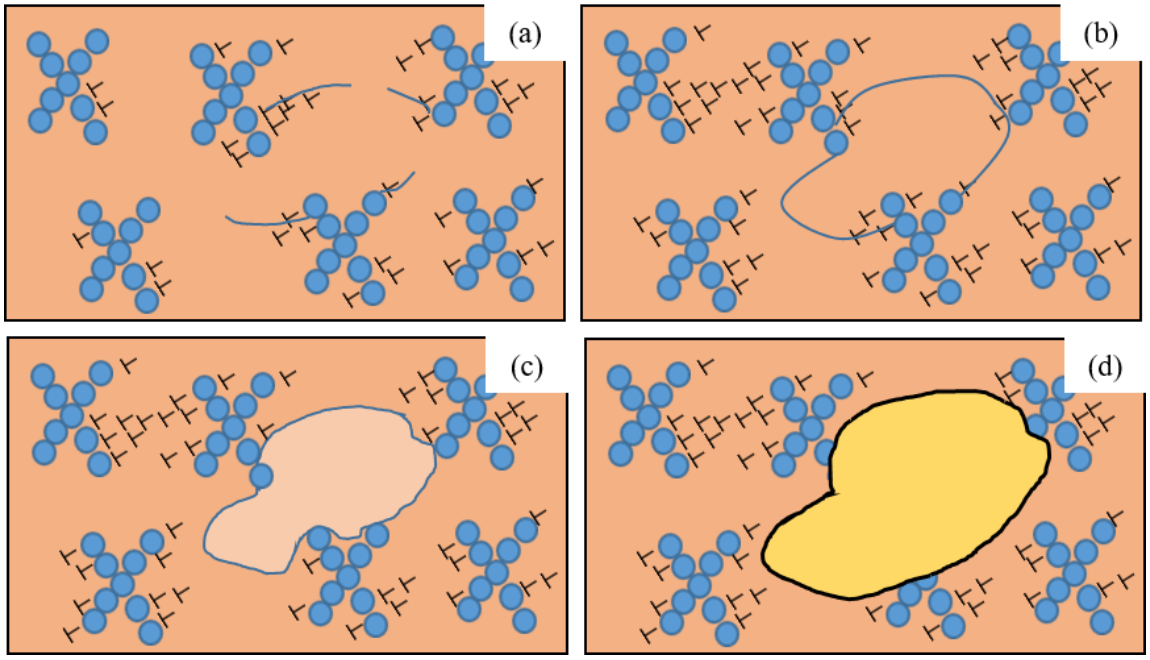


Figure 6.14: A schematic illustration of the stages involved in the formation of recrystallised grains in regions with octodendritic precipitation. (a) Branching out of (blue) MAGBs from γ /γ' interfaces (b) formation of enclosed sub grains (c) increase in misorientation angle of sub-grain boundaries (turning black), and (d) further increase in misorientation angle of sub-grains, sub-grain growth and partial precipitate dissolution.

6.3.3 The role of twinning in recrystallisation

One way for a MAGB to become a HAGB, is by twinning. In the case of recrystallisation this is rather useful, as it is a means by which a sub-grain can quickly become a recrystallised grain and its boundary can become much more mobile. Fig. 6.15 (a) shows a higher magnification view of the region seen in Fig. 6.13 with a local strain level of $\epsilon \approx 0.95$. Here we can see three examples (highlighted by black arrows) where it appears that a twin has formed along the boundary, and produced a more mobile higher angle boundary ahead of it. For two of these (the one in the middle and to the right), the involved boundary is a MAGB (having a misorientation angle between 5° and 10°) separating a recrystallised grain and the surrounding unrecrystallised grain.

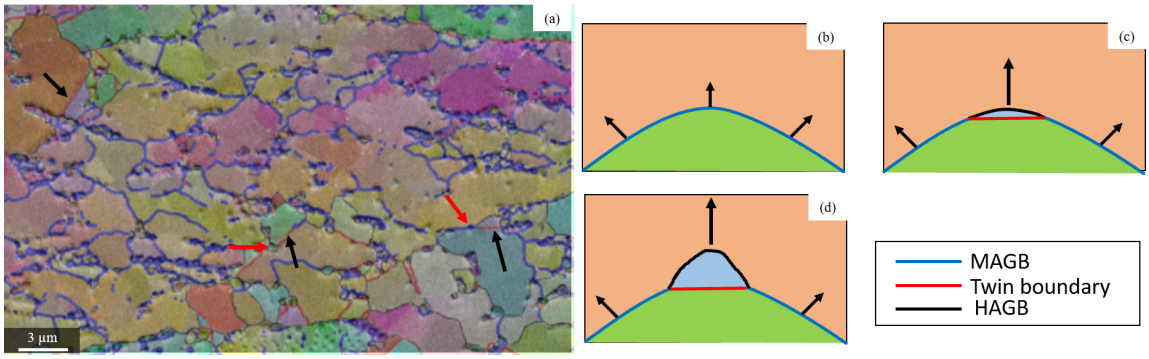


Figure 6.15: Examples of MAGBs being converted to HAGBs by twinning (a). A FSE image with overlaid IPF map and MAGBS, from a region in Fig. 6.13 (d) is shown. (b) A corresponding schematic of the stages involved in sub-grains (green) twinning as they consume a neighbouring (orange) unrecrystallised grain (c) producing a more mobile recrystallisation front segment which can protrude from the MAGB (d).

Schematically, this process is illustrated in Figs. 6.15(b-d). A sub-grain forms in an unrecrystallised grain, and can only grow relatively slowly because of its low mobility boundary. If twinning happens, this twinned grain will have some high angle boundary with the deformed grain, with higher misorientation angle and mobility than the original MAGB, resulting in a protrusion forming ahead of the twin, which is seen in the microstructure in Fig. 6.15 (a). This twinning will also contribute to texture randomisation in the recrystallised grains. Although this observation has been made in a region with octodendritic precipitation, it applies to other precipitate environments.

As such, twinning is shown to contribute to the formation of recrystallised grains

(by forming recrystallised grains from sub-grains, which are potential nuclei) and to their growth, by producing random high angle boundaries with high mobility. We can also notice in Fig. 6.15 (a) that the two twins which have occurred along MAGBs intersect γ' precipitates (red arrows). Using a statistical analysis of the locations of twin boundaries in a 3D EBSD dataset combined with *in situ* EBSD Charpagne *et al.* have shown that primary precipitates are correlated with twin boundaries, and so it is possible that these can induce growth accidents and promote twinning [106]. As such, γ' precipitates can in some cases *promote* the formation and growth of recrystallised grains, by assisting twining. Zouari *et al.* suggested this mechanism may operate to aid recrystallisation, and showed an example of twinning assisted nucleation [107, 72]. The possibility of twining participating in recrystallisation mechanisms was also noted by Bozzolo and Bernacki [108]. Fig. 6.15 provides a very clear example of how twinning promotes the formation and growth of recrystallised grains in the studied AD730 alloy, and how γ' precipitates can assist this process by generating twins as MAGBs cross them.

6.4 Summary

In this chapter the interaction between the precipitate distribution formed during slow cooling through the γ' solvus temperature (presented in chapter 5) and recrystallisation during forging has been investigated. This represents the first sub-solvus forging stage of an industrial forging process. The evolution of precipitates during recrystallisation has been examined, alongside the relative ease of recrystallisation around different precipitate distributions, and some mechanisms of recrystallisation have been shown. The influence of texture on recrystallisation was also discussed. The main conclusions are:

1. Unrecrystallised grains develop a $\langle 110 \rangle$ //CD fibre texture during compression which is typical of FCC metals. It was shown that such a texture can be attributed to two causes; firstly, the rotation of a $\langle 110 \rangle$ axis towards the compression direction during forging. Secondly, the fact that grains which are closer to this "stable" orientation at the start of forging develop lower orientation gradients than grains which are further from it, and so are less likely to be consumed by recrystallisation.

2. Regions with continuous precipitation which has grown to be octodendritic present less of a barrier to recrystallisation than regions with discontinuous precipitation, and this difference can be rationalised based on the inter-precipitate spacing. Neither type of precipitate was found in dynamically recrystallised areas after sub-solvus compression, where the recrystallised grains had little to no intra-granular precipitation, implying that both precipitates were dissolved by the recrystallisation front during recrystallisation.

3. A fine and dense distribution of spherical precipitates was found in some areas after forging, which was not present prior to forging. Their formation mechanism is not clear; their size and 3D morphology show that they are neither small continuous precipitates formed during slow cooling nor an end on view of discontinuous precipitates, however they also persist following a 45 minute hold at high temperature after forging, suggesting they are also not dynamic precipitates. These precipitates limit the formation of both long and short-range orientation gradients, and hinder recrystallisation. Although few areas containing such precipitates were found, they persist at high strain locations alongside discontinuous precipitation in the unrecrystallised grains.

4. Recrystallisation around octodenritic precipitates occurs via a three stage process, which has been shown and schematised. During recrystallisation the octodendritic precipitates are dissolved, and can no longer be identified in recrystallised regions.

5. Twinning can assist in the formation and growth of recrystallised grains from sub-grains, by converting low mobility MAGBs into higher mobility random HAGBs. γ' precipitates can promote the formation of such twins.

6. Texture and precipitation concomitantly affect recrystallisation during forging. Texture has been shown to affect the magnitude of long-range orientation gradients in grains deformed during compression, while precipitation influences the size of the sub-grains forming within those gradients.

7 Impact of forging parameters on microstructural evolution

In this chapter the impact of forging parameters on microstructural evolution, mainly the level of recrystallisation, are investigated. This includes the number of strokes used during an upsetting and the total level of strain applied. A methodology is set out to estimate recrystallisation level and an associated uncertainty based on EBSD data. The data in this chapter was collected from experiments 1 and 2, which are described in detail in Chapter 3, and a schematic of each is shown in Fig. 7.1 for reference.

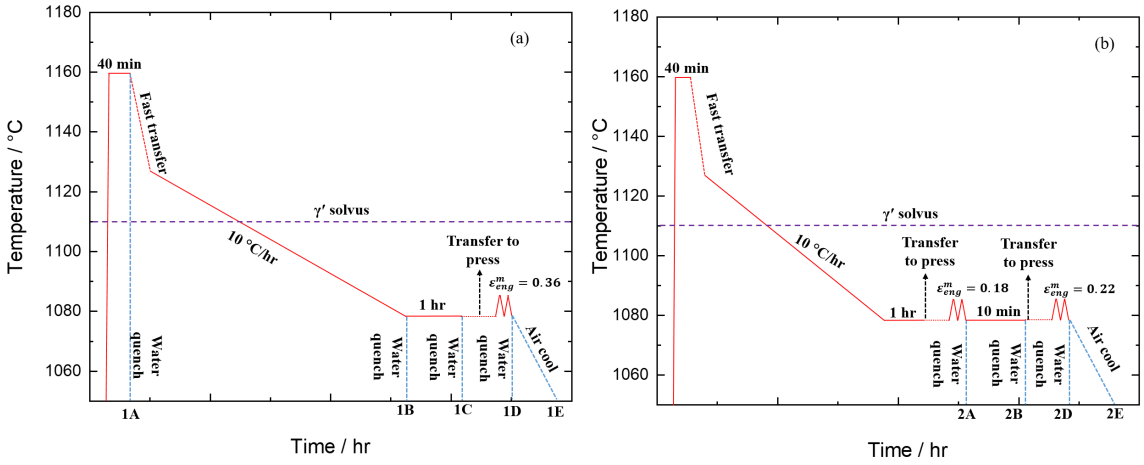


Figure 7.1: Schematic plot of the thermo-mechanical path applied in experiment 1 (a) and experiment 2 (b).

7.1 Comparison of strain distribution in experiments 1 and 2

Despite samples 2D and 2E being deformed to the same *macroscopic* level as samples 1D and 1E in experiment 1, the different applied heat treatments cause slightly

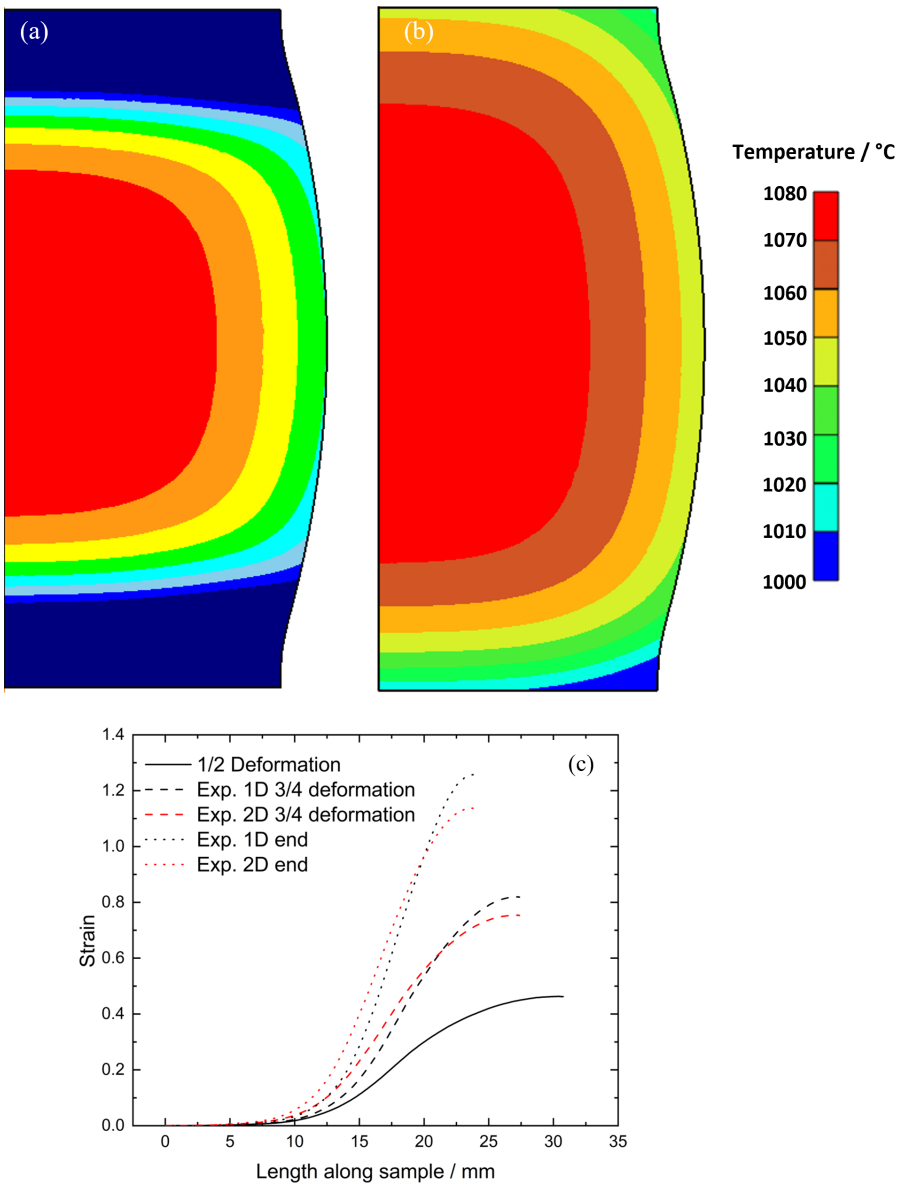


Figure 7.2: Temperature distribution in samples 1D and 1E halfway through forging (a), and in samples 2D and 2E halfway through forging (b). A comparison of the strain distributions along the centre lines of samples from experiment 1 and 2 at different stages of deformation resulting from the different temperature distributions (c).

different strain distributions. The temperature distribution at the mid point of experiment 1 (i.e. when the sample has been compressed from 75 mm to 61.5 mm, on the way to 48 mm) is shown in Fig. 7.2 (a). The temperature distribution at the mid point of experiment 2 (i.e. after the sample has been compressed from 75 mm

to 61.5 mm, returned to the furnace for 10 minutes, then placed back on the lower die of the press, and the upper die has just made contact with the top face of the sample) is shown in Fig. 7.2 (b). The samples in experiment 2 have broader strain distribution with a lower peak value. This is shown in Fig. 7.2 (c). Here the black lines show data for samples 1D and 1E from experiment 1, and the red lines show data for samples 2D and 2E from experiment 2. At the midpoint of deformation (i.e. when half of the total height reduction has been applied), the two types of sample have identical strain distributions. Beyond this point, the two differ, since the temperature distributions become different as samples from experiment 2 are returned to the furnace for 10 minutes whereas those from experiment 1 continue to be compressed.

The difference between these two predicted strain distributions can be explained due to the different temperature distribution during the second stroke of forging in samples 2 D and 1D as follows: In experiment 1, the extremities of the sample cool faster than the centre since they are in contact with the dies (heated only to 450 °C), so become harder to deform than the centre, and strain becomes concentrated at the centre of the sample. In experiment 2, this cooling is interrupted at the end of the first stroke, and the sample temperature becomes homogeneous after 10 minutes in the furnace. During the second stroke of forging in experiment 2, there is less of a temperature difference between the extremities of the sample and the centre, and strain is more uniformly distributed through the sample. Fig. 7.2 (c) shows the strain distribution along the sample mid-line for experiments 2 D and 1D at different stages during deformation, and highlights the differences described.

7.2 A method for estimating strain and recrystallisation level

As described in Chapter 3, section 3.4.2, four large area EBSD maps were taken from each of samples 1,D 1E, 2D and 2E, allowing recrystallisation level as a function of strain to be plotted. In samples 1D and 1E these four regions had local strain levels of $\epsilon \approx 0.69$, $\epsilon \approx 1.00$, $\epsilon \approx 1.19$, and $\epsilon \approx 1.26$. In samples 2D and 2E these four regions had local strain levels of $\epsilon \approx 0.76$, $\epsilon \approx 0.99$, $\epsilon \approx 1.10$, and $\epsilon \approx 1.13$.

7.2.1 Uncertainty in local strain level

Due to both the potential for slight errors in the EDM cutting of the plates and the accuracy of the FE simulation results, there is an uncertainty in the exact location of each EBSD map with respect to the sample centre, and in the strain level associated with each map. Of the four investigated regions, the strain gradient is shallowest towards the centre of the sample (region number 4), so this uncertainty is lowest there and highest where the slope of the strain vs length along sample graph is highest i.e. region 1. An estimate for this uncertainty was obtained by assuming a $\pm$ 0.5 mm uncertainty in the position on the sample being imaged, and this was converted into a strain uncertainty using the strain distribution calculated by FEM. This error is not the same in both directions, but the difference between the two errors was small, so the larger of the two was taken.

7.2.2 Estimating recrystallisation level and uncertainty

The IPF maps obtained from the four selected locations in sample 1D are shown in Fig. 7.3. These were collected using a step size of 1 µm, and allow the large unrecrystallised grains to be investigated, though the images Fig. 7.3 don't show any clear detail in the recrystallised grains.

To estimate the recrystallisation level from these maps, three different criteria were considered: GAM, equivalent grain radius and GOS. For each of these a relative area histogram was plotted and a suitable cut-off value was chosen based on these histograms. A comparison of the three different methods is shown in Fig 7.4, using data from sample 1E, from a region with a local strain level of $\epsilon \approx 1.00$. Fig. 7.4 (b) shows that GAM wasn't a suitable parameter to use, since large unrecrystallised grains with shallow orientation gradients have low GAM values, and end up being classed among the recrystallised grains. Examples of this are shown by the white arrows in Fig. 7.4 (b). Grain size and GOS provide reasonable separations between the two grain populations, as shown in Figs. 7.4 (c) and (d), with grain size producing higher estimates of the recrystallised fraction. The different values predicted by these different methods is one source of uncertainty.

Another source of potential uncertainty in the recrystallisation level is related to the scanned area potentially not being statically representative of the overall microstructure. An estimate of this uncertainty was obtained by comparing the

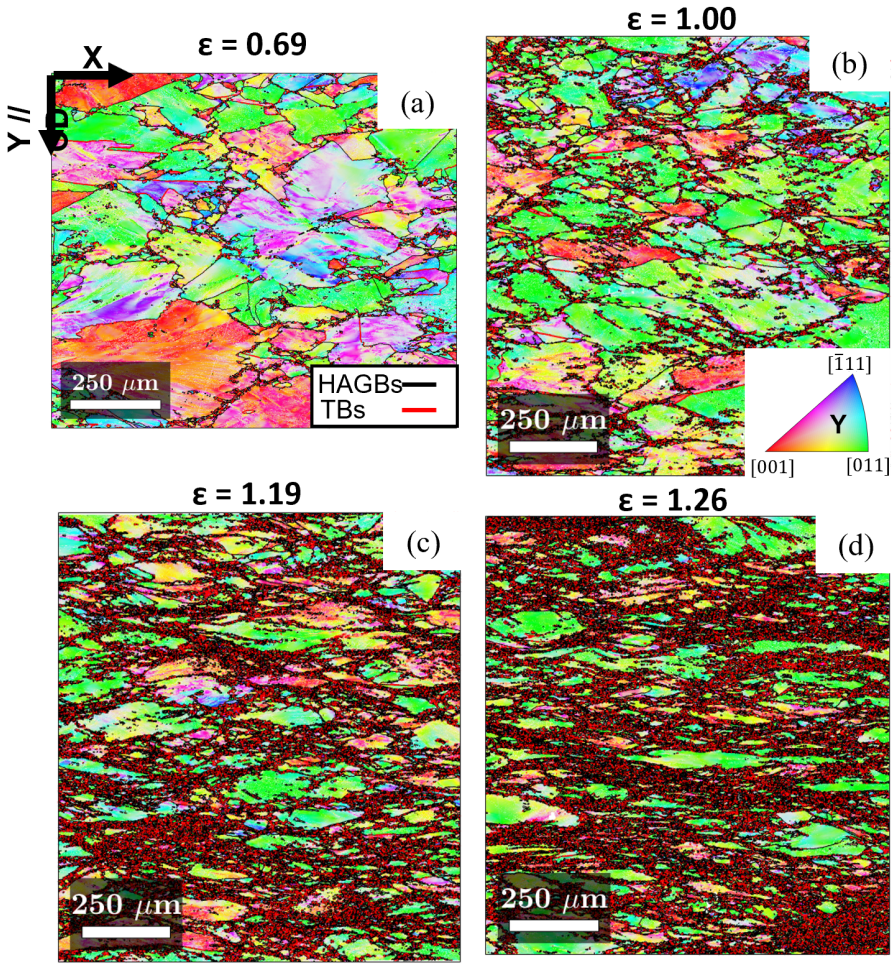


Figure 7.3: Large area IPF maps showing microstructure evolution as a function of strain in sample 1D (a) - (d). In (a-d) the recrystallised grains cannot be well seen due to their small size, and their boundaries (coloured red or black) obscure them.

estimated recrystallisation levels of the left and right sides of each map (according to the GOS threshold). This uncertainty can be compared with the uncertainty arising from the choice of metric to distinguish recrystallised and unrecrystallised grains (GOS or grain size) to give an estimate of the overall uncertainty. An example of this procedure is shown in Fig. 7.5 for sample 2E at a region with a local strain level of $\epsilon \approx 0.99$. The GOS and grain size thresholds were determined based on the map of the full area. Comparing Fig. 7.5 (b) and (c), or (e) and (f) shows that the difference in estimated recrystallisation level due to the different recrystallisation criteria is around 6.5 % in this case. Comparing Fig. 7.5 (b) and (e), or (c) and (f) shows that the difference between the left and right hand sides of the map is

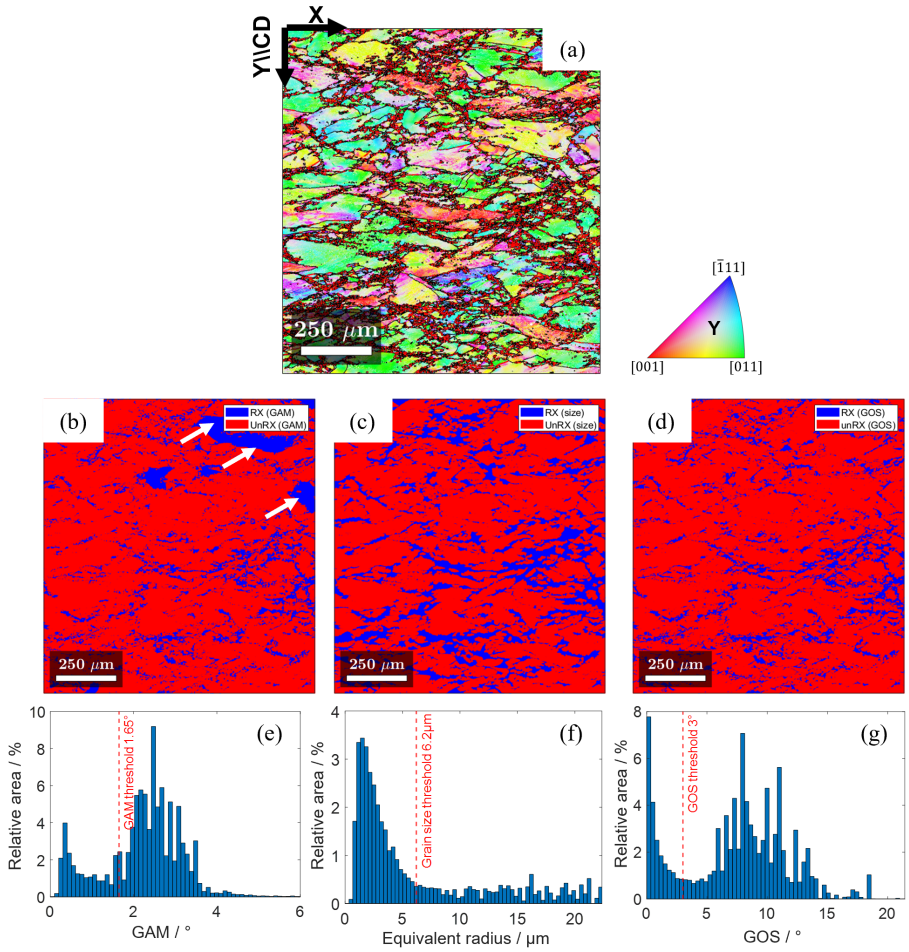


Figure 7.4: Different possible metrics to measure recrystallisation level. (a) An IPF map from sample 1E, from a region with a local strain of 1.00. (b-d) The same area, with grains classed as recrystallised plotted in blue, and unrecrystallised in red, according to the GAM, grain size and GOS thresholds, respectively. The threshold values chosen are based on the distributions of these parameters, shown in (e-g), where the red lines show the cut off values used to segregate the two populations. The white arrows in (b) indicate large unrecrystallised grains which are measured as recrystallised by the GAM metric.

around 3.1 %. In all cases, it was found that the uncertainty due to the choice of metric was greater than the uncertainty due to the map area potentially not being representative, and this was taken as an estimate of the uncertainty in the estimated recrystallisation level.

The recrystallisation level estimated using a GOS threshold was used to provide the estimate of the recrystallisation level.

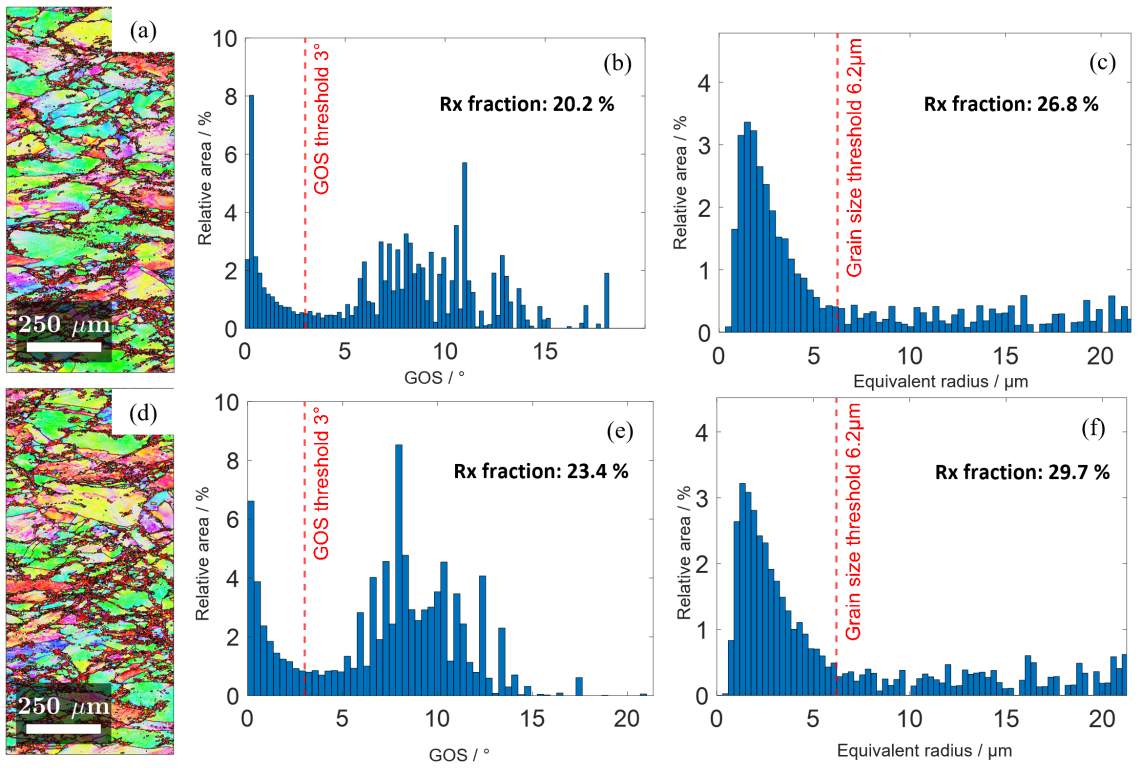


Figure 7.5: Illustration of uncertainty in recrystallisation levels due to spatial variations, data from sample 1E. The top row ((a) - (c)) shows the LHS of the IPF map from Fig. 7.4 (a), the relative area distribution of GOS (b) and the relative area distribution of grain equivalent radius (c); for the latter two the red dashed line indicates the cut-off value used to separate the recrystallised and unrecrystallised grains. The bottom row ((d) - (f)) shows similar information for the RHS of the IPF map.

7.3 Influence of forging parameters on recrystallisation level and microstructural evolution

7.3.1 Influence of strain level and cooling rate

With this method for estimating recrystallisation level and local strain level, the effect of strain level on recrystallisation can be investigated.

Fig. 7.6 (a) shows a plot of recrystallised fraction vs strain level for samples 1D and 1E. The values and error bars were calculated according to the method described previously. These show that recrystallisation level is increasing with applied strain

(as expected), and that there is no significant difference in the recrystallisation level measured for the two samples.

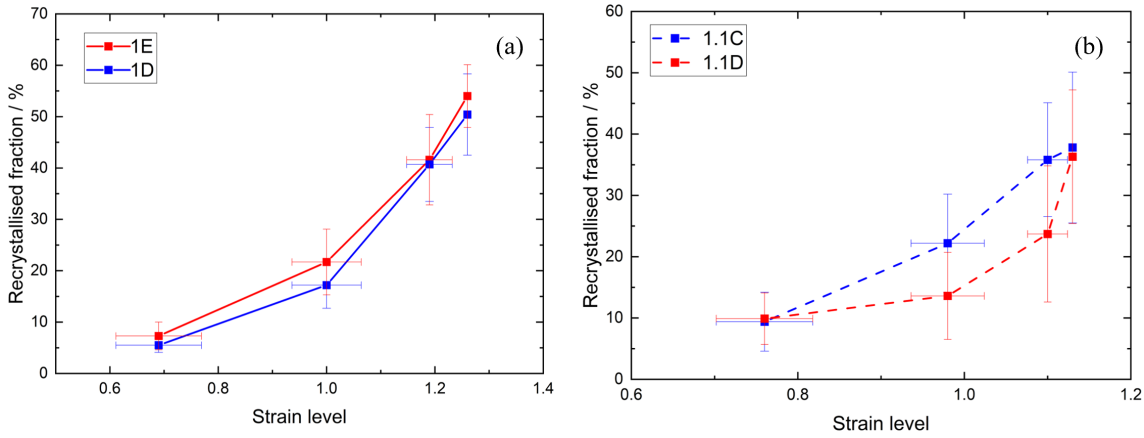


Figure 7.6: Recrystallised fraction as a function of strain for samples forged in one stroke (a) and in two strokes (b), followed by water or air quenching.

A similar dependence of recrystallisation level on strain is seen in samples 2D and 2E (water quenched and air cooled after single stroke forging, respectively) from the two stroke forging experiment in Fig.7.6 (b). Again, allowing for the uncertainty in the values of recrystallisation and strain level, there is no significant difference between samples 2D and 2E, i.e. there is no significant difference between samples which were water quenched and air cooled.

7.3.2 Influence of number of forging strokes

Overall recrystallisation level

Comparing the recrystallisation levels of samples from experiment 1 and 2 allows the effect of forging to a given strain in either 1 or 2 strokes to be investigated. On a practical level, upsetting to a given strain in a single stroke during an industrial forging operation can be more challenging than doing so in multiple strokes, as larger forces are required due to work hardening of the billet. Additionally, billets will spend longer out of the furnace in a single forging operation, cooling down more, requiring additional force to forge them.

Fig. 7.7 shows that there was no significant difference in the recrystallisation levels obtained under single or double stroke forging. In the case of the air cooled

samples (1E and 2E) the single stroke forging has produced a slightly higher recrystallisation level, but in the case of the water quenched samples (1D and 2D) the two stroke forging has produced a slightly higher recrystallisation level. In both cases the differences are not significant, considering the uncertainties in the measured recrystallisation level.

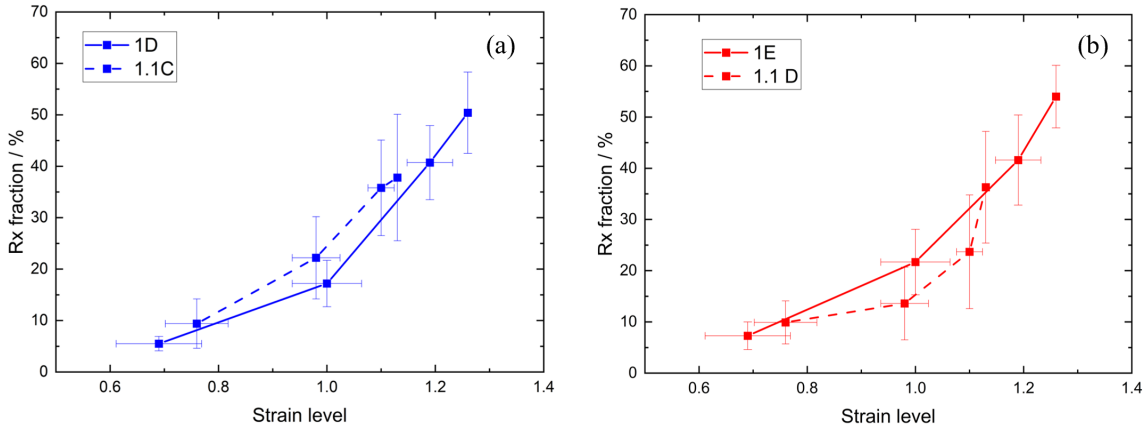


Figure 7.7: Recrystallisation level as a function of strain in the water quenched (a) and air cooled (b) samples from 1 and 2 stroke forging.

Evolution during heating between strokes

From Fig. 7.7 it may be noted that the *uncertainties* in recrystallisation level for samples 2D and 2E are larger than for samples 1D and 1E. This is caused by a larger difference in the recrystallisation level predicted by the two different metrics used (equivalent grain radius and GOS). This difference is due to the microstructural evolution occurring between samples 2A and 2B, i.e. the evolution during the 10 minutes reheating between strokes.

Samples 2A and 2B have relatively low strain gradients, so there is little difference in strain level between the four regions investigated in each sample (indicated in Figs. 3.7 (a) and (b)), so the evolution between the samples can be explained by comparing just one location between the two samples. The location chosen was the maximum strain location at the sample centre, with a local strain level of $\epsilon \approx 0.46$. Sample 2A has a recrystallisation level of 8.7 %, and sample 2B a recrystallisation level of 14.3 % at this location. IPF maps for these two samples are shown in Fig. 7.8.

The difference in recrystallisation level (an increase by a factor of 1.64) *could* be

due to a combination of static recrystallisation and post-dynamic growth of recrystallised grains, however, investigating the density and size of recrystallised grains suggests that the latter is primarily responsible. The average area of recrystallised grains increases by a factor of 1.93 from 12.3 μm^2 in sample 2A to 23.7 μm^2 in 2B. The number of recrystallised grains per unit area has fallen by a factor of 1.18; it is higher in sample 2A than 2B (7119 mm^{-2} in sample A and 6013 mm^{-2} in sample B).

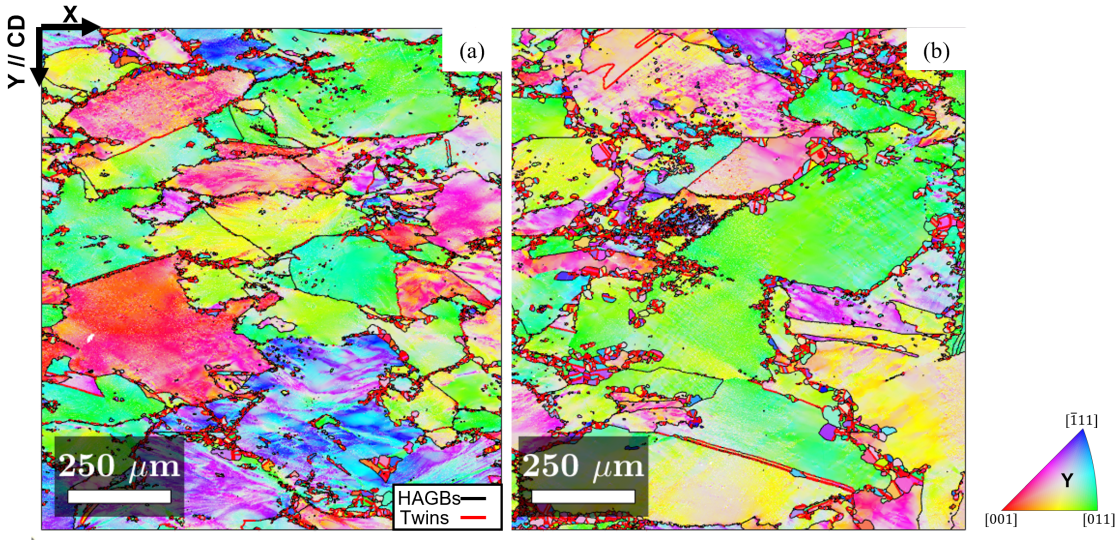


Figure 7.8: IPF maps from sample 2A (water quenched after a single stroke of forging) (a) 2B (water quenched after a single stroke of forging and 10 minutes reheating at 1080 °C in a furnace) (b). Maps taken from the centres of the compressed samples, with a local strain level of $\epsilon \approx 0.46$.

The fact that the higher recrystallisation level in sample 2B is primarily due to the growth of recrystallised grains post-dynamically is further highlighted by the grain size distribution in Fig. 7.9. This shows the grain size (as an equivalent radius) distribution for recrystallised grains in samples 2A and 2B (i.e grains with GOS values under 3.5 °, which is a reasonable cut off value for both samples). Sample 2B has a higher area fraction of larger recrystallised grains, due to the grain growth which has occurred during the 10 minutes annealing following compression.

These larger recrystallised grains mean that the threshold grain size for grains to be classed as recrystallised is higher in samples 2D and 2E than in 1D and 1E. This can be highlighted numerically by comparing region 4 from sample 2D (local strain level of $\epsilon \approx 1.13$) with region 3 from sample 1D (local strain level of $\epsilon \approx 1.19$). In region 4 of sample 2D, 12.6 % of the investigated area is covered by grains which

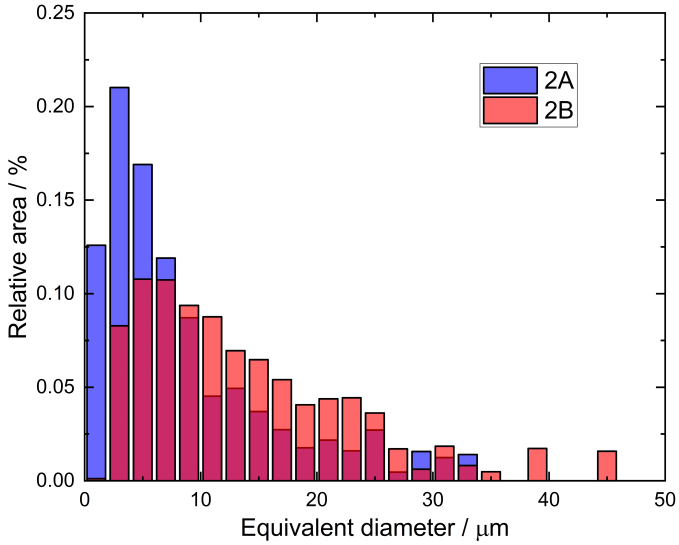


Figure 7.9: Grain size distribution for recrystallised grains in samples 2A and 2B, i.e. for grains with GOS values under 3.5 °, which was a reasonable cut-off value for both samples.

meet the grain size condition for being recrystallised but not the GOS condition. In region 3 of sample 1D, only 7.6 % of the investigated area is made up of grains which meet the grain size condition for being recrystallised but not the GOS condition, i.e. the uncertainty in region 4 of sample 2D is roughly 65 % higher than in region 3 of sample 1D.

7.3.3 Evolution of γ' precipitates

Effect of single stroke forging to low and high strains

Similarly to sample 1C (quenched after slow cooling from the super-solvus and a 1 hr hold at 1080 °C) discussed in Chapter 5, samples 2A and 2B show very inhomogeneous precipitate distributions. An example of this is shown in Fig. 7.10. Here, a vertical band (parallel to the macroscopic compression direction) which is free from precipitates can be found. On either side of this, within the same grain, regions containing octodendritic precipitation are present.

In Fig. 7.10 the variations in precipitate density are shown through an IPF map and a corresponding FSE image (note that the precipitate free region shows a wavy contrast in the FSE, similar to the regions with a fine and dense distribution of

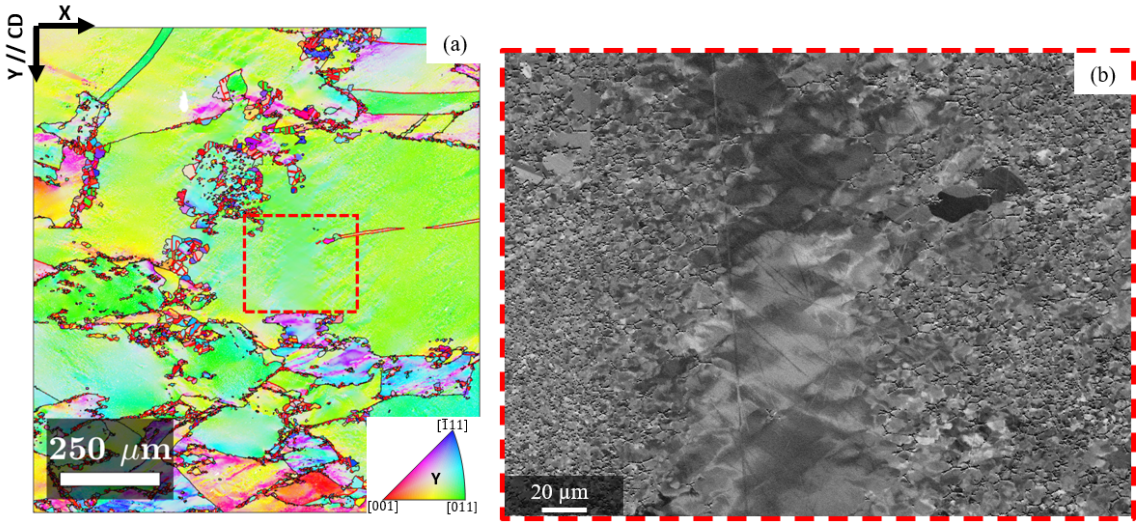


Figure 7.10: IPF Y map from a region in sample 2 A (which underwent one forging stroke before quenching in water) where $\epsilon \approx 0.44$ (a). An FSE image from the indicated region in (a) shows that within a single grain there is a very non-uniform precipitate distribution (b).

potentially dynamically forming precipitates in sample 1D, shown in Fig. 6.8). In samples 2A and 2B (quenched after the first forging stroke, and following a 10 minute reheating at 1080 °C, respectively), these variations can be observed via KAM maps. Since dislocations build up at the γ/γ' interfaces, these interfaces become high KAM areas, and regions without precipitation show lower KAM values.

Such KAM maps are shown for four regions from sample 2A in Fig. 7.11, and for four regions from sample 2B in Fig. 7.12. Fig. 7.11 (b) can be compared with Fig. 7.10 (a), as they correspond to the same area. The region with a low precipitate density highlighted by the red box in Fig. 7.10 (a) corresponds to a low KAM region in Fig. 7.11 (b). On either side of this low KAM region, within the same grain, are higher KAM regions, where dislocations have been able to build up at the γ/γ' interfaces. Such precipitate free bands can be found in samples 2A and 2B, and the largest ones are indicated by white arrows in Figs. 7.11 and 7.12.

A similar banding effect has been noted in AD730 by Vernier [32]. The different precipitate distributions in the different bands were hypothesised to lead to bands of differently sized recrystallised grains. The different precipitate distributions were hypothesised to be due to remnant chemical segregation; areas with higher concentrations of the γ' forming elements would correspond to inter-dendritic regions, and regions with lower concentrations would correspond to dendritic regions [97]. At a

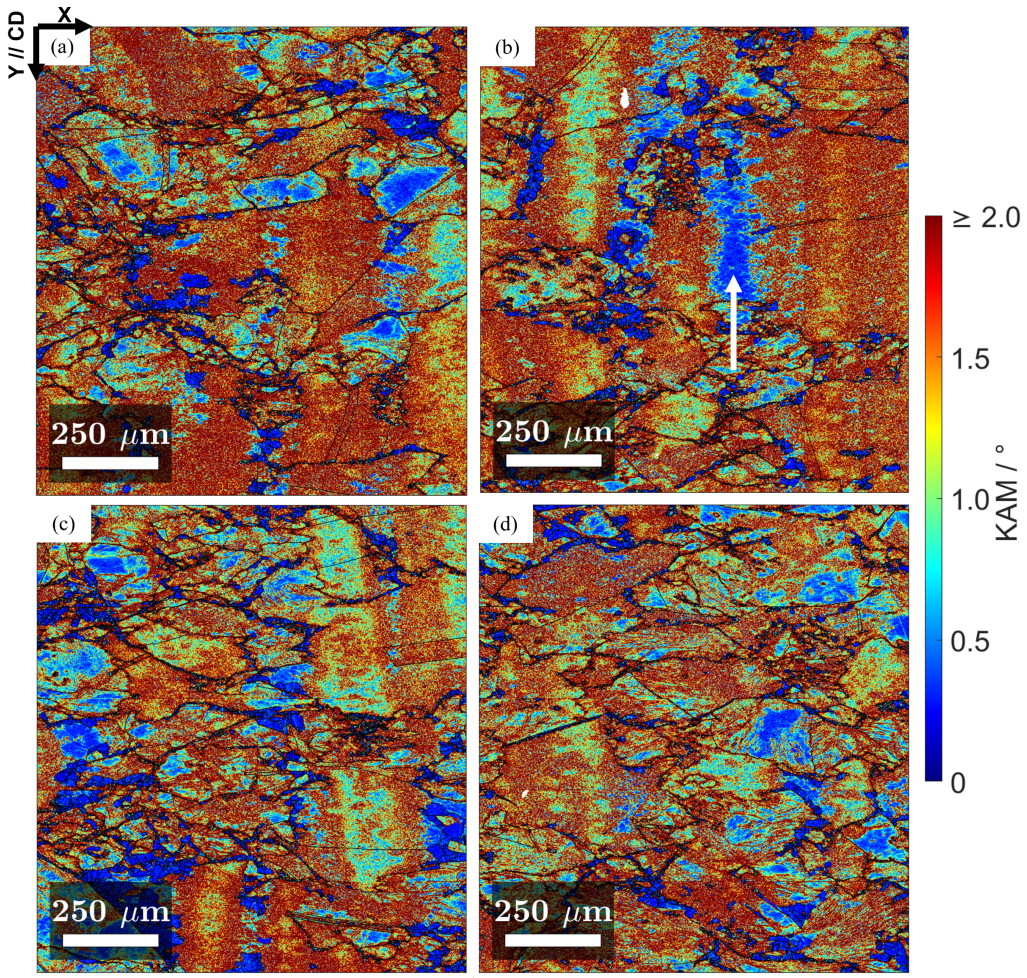


Figure 7.11: Four KAM maps from sample 2 A. The approximate local strain levels in regions (a) - (d) are 0.39, 0.42, 0.44 and 0.46, respectively. The white arrow indicates the precipitate free area shown in Fig. 7.10.

given forging temperature, the interdendritic regions would have a higher density of γ' precipitates, limiting the size to which the recrystallised grains there can grow [32].

The inhomogeneous distributions of precipitates seen in sample 1C and in samples 2A and 2B (with local strain levels $\epsilon \approx 0.44$), where there are large bands free from any precipitates, are found in neither samples 1D and 1E, nor samples 2D and 2E, which have been investigated in regions with strain levels $\epsilon \geq 0.69$. KAM maps for samples 1D and 1E are shown in Figs. 7.13, and 7.14, respectively. In these samples there are some low KAM regions, but they are not precipitate free, as in samples 1C and 2A and 2B. Instead, these regions either contain the fine and densely

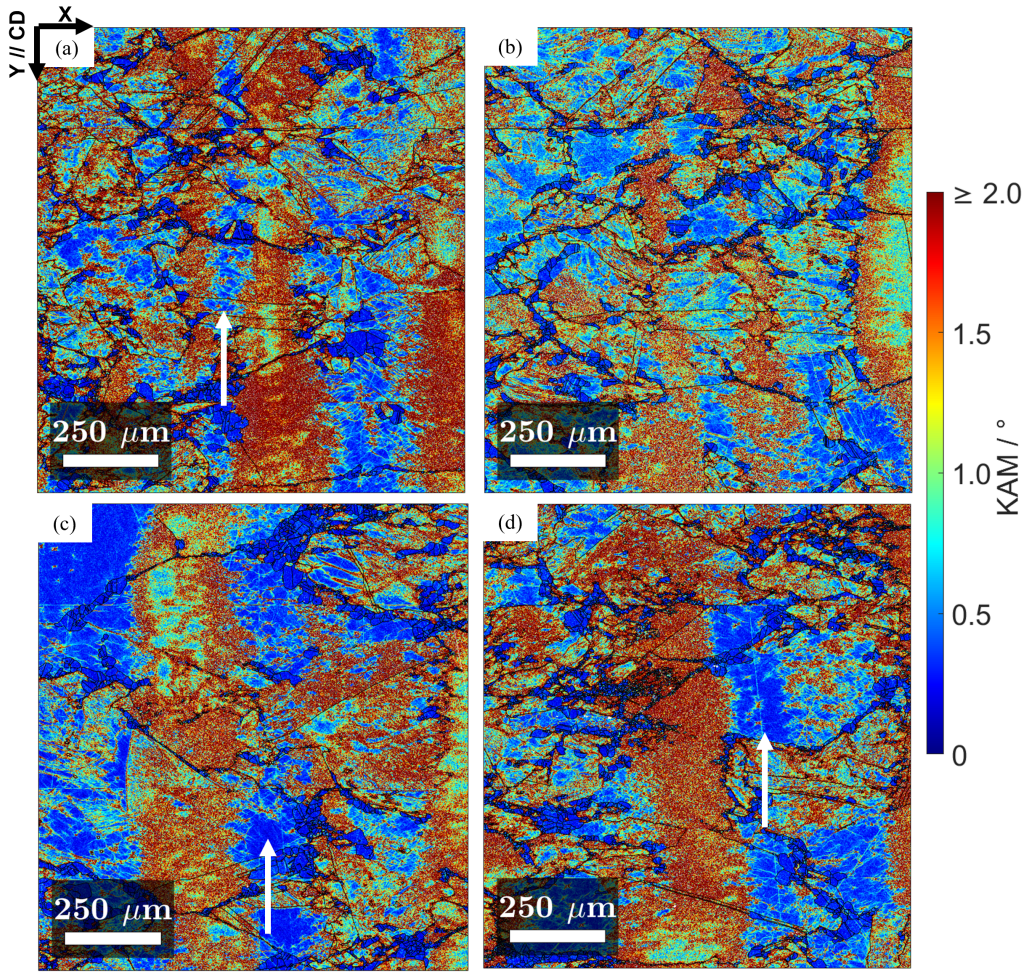


Figure 7.12: Four KAM maps from sample 2 B. The approximate local strain levels in regions (a) - (d) are 0.39, 0.42, 0.44 and 0.46, respectively. The white arrows indicate precipitate free areas, which show low KAM values, as discussed in the text.

distributed precipitates, or discontinuous precipitation, as discussed in Chapter 6. This is highlighted in Figs. 7.13 and 7.14 (e) and (f). As such, the precipitate free bands are lost during forging beyond a certain strain level; they have been found in regions where $\epsilon \approx 0.44$ (i.e. in Figs. 7.11 and 7.12), but not in regions where $\epsilon \approx 0.69$ (i.e. in Figs. 7.13 and 7.14).

One explanation that can be suggested for this is that dynamic precipitation occurs to a significant extent in the precipitate free bands at a sufficient strain level. The small spherical precipitates which have been found in unrecrystallised grains after single stroke forging to high strains may have formed dynamically, and these spherical precipitates are located in grains with a "wavy" BSE contrast, which is

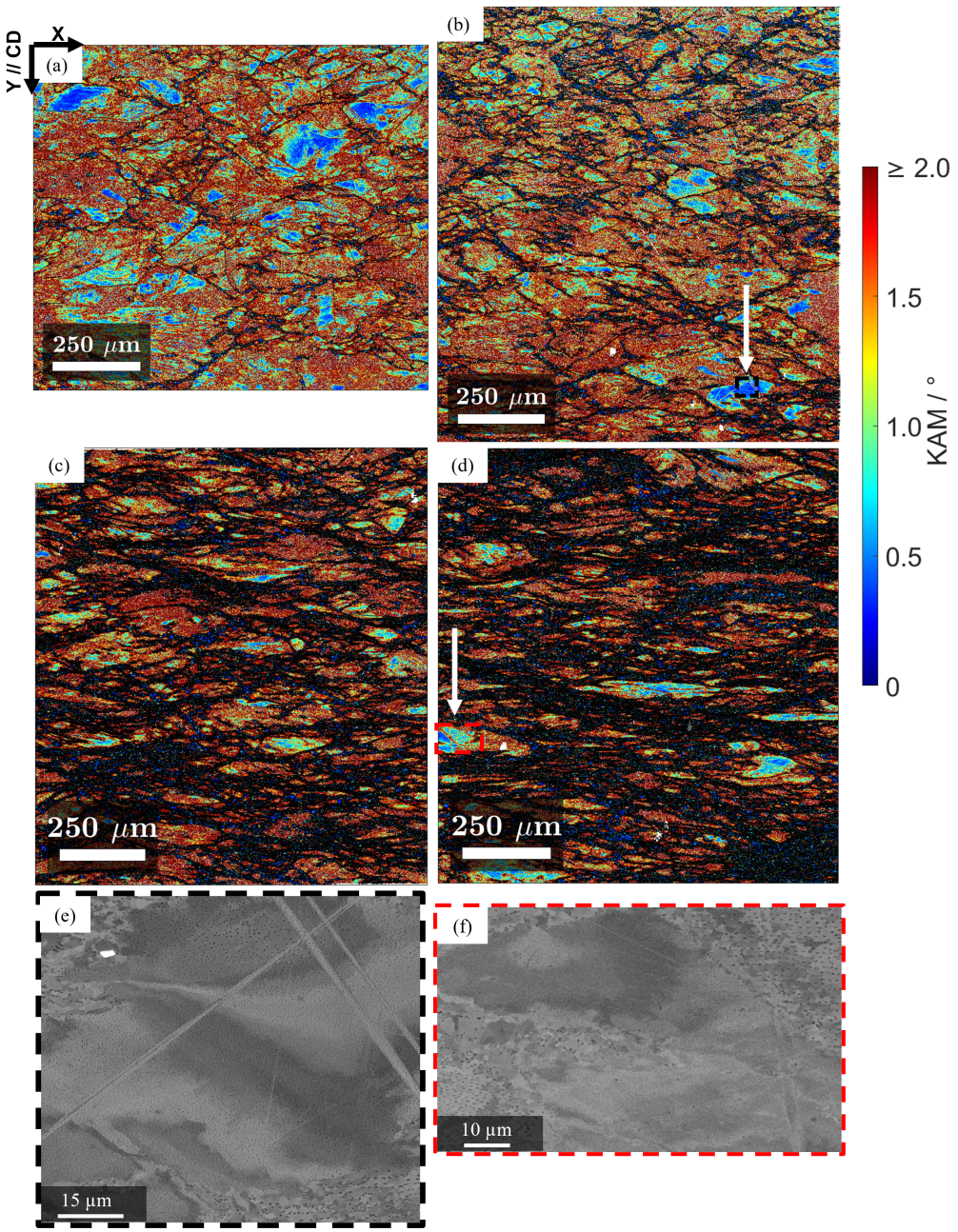


Figure 7.13: Four KAM maps from sample 1D which was water quenched after single stroke forging. The approximate local strain levels in regions (a) - (d) are 0.69, 1.00, 1.15 and 1.26, respectively. (e) and (f) show FSE images from the areas indicated by the black and red rectangles in (b) and (d) respectively.

also seen in the precipitate free band (e.g. in Figs. 7.10 (b) and 7.15 (a)). Such precipitate free bands were also not found after the second stroke of forging in the two stroke forging trials, suggesting that above a certain strain level, these bands are

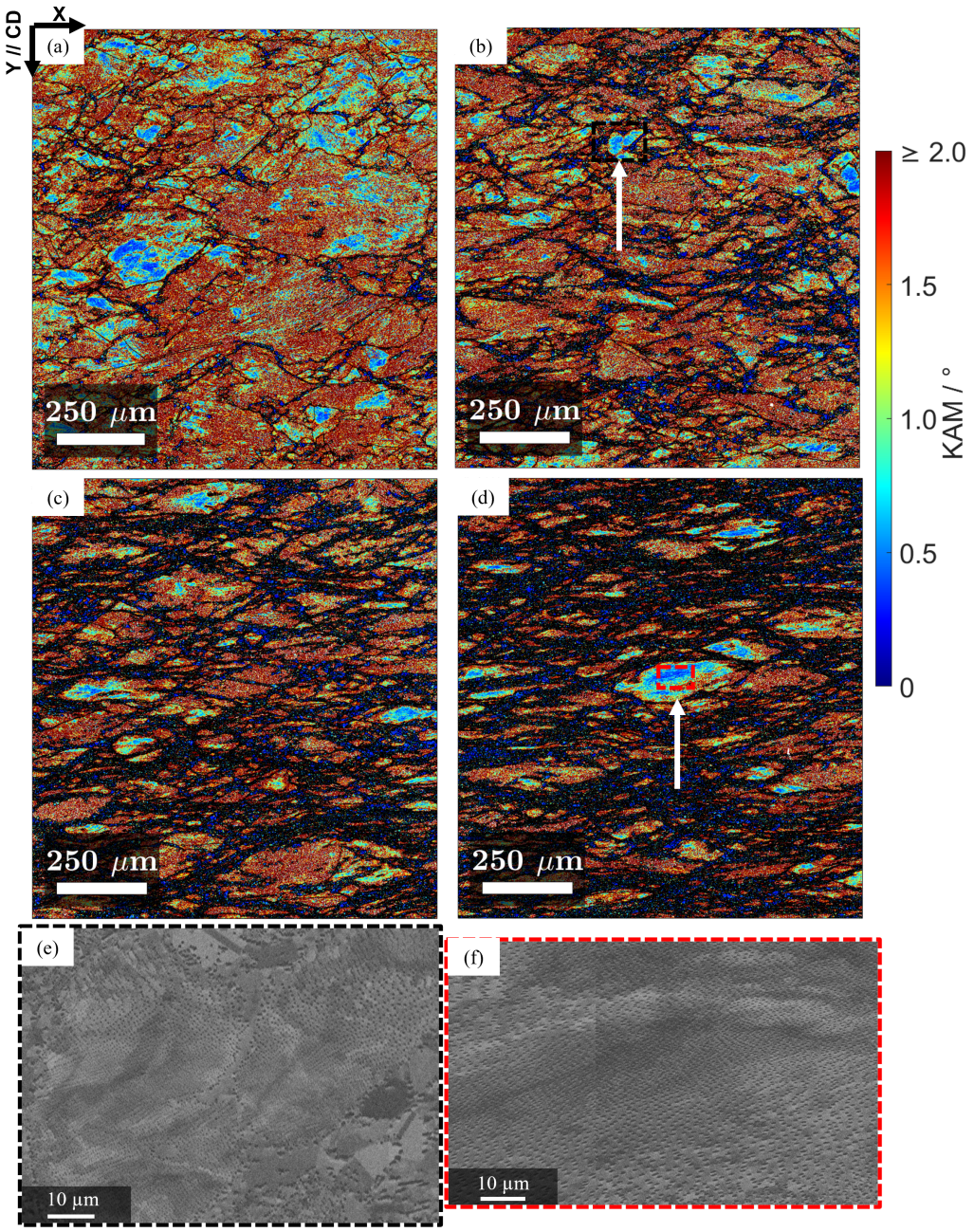


Figure 7.14: KAM maps from sample 1E, which was air cooled after single stroke forging. The approximate local strain levels in regions (a) - (d) are 0.69, 1.00, 1.15 and 1.26. FSE images from the regions indicated by the arrows in (b) and (d) are shown in (e) and (f), respectively.

either recrystallised, or dynamic precipitation occurs in them. The relation between the formation of precipitates and recrystallisation is that recrystallisation introduces

grain boundaries at which precipitation is kinetically and thermodynamically favored.

Comparing Figs. 7.11 and 7.12 shows that these bands are larger and more prevalent in sample 2B than in sample 2A, which could be consistent with the occurrence of dynamic precipitation in these bands: during the 10 minute hold at 1080 °C some of the precipitates which have formed dynamically in these bands are re-dissolved, giving the larger bands seen in sample 2B.

Role of remnant chemical segregation

To investigate the possible effect of remnant chemical segregation on the inhomogeneous precipitate distributions seen at low strains, regions with inhomogeneous precipitate distributions (such as the one shown in Fig. 7.10 (b)) from samples 2 A and 2 B were investigated using first EDS in the SEM, then WDS in an EPMA.

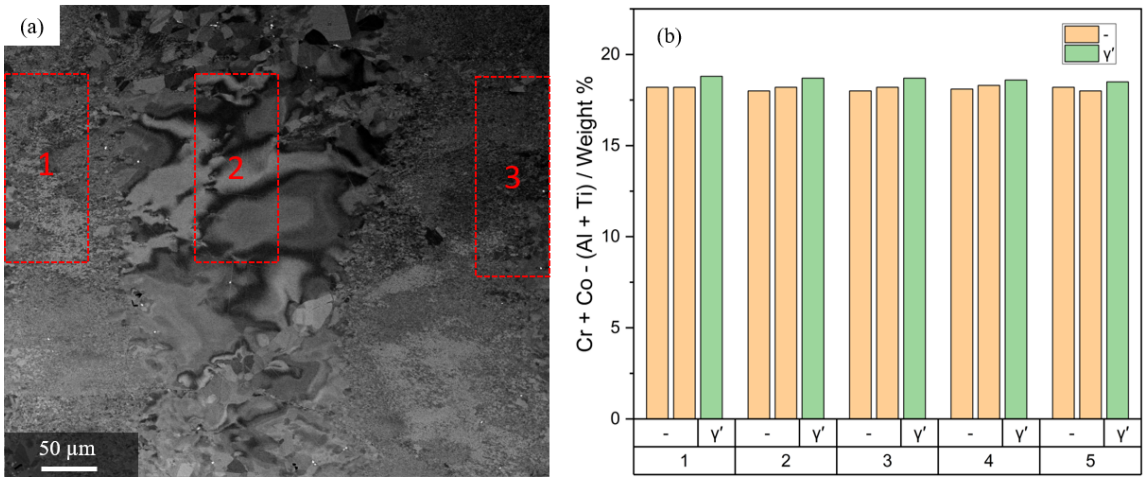
EDS data was collected from five regions in sample 2B. An example region is shown in Fig. 7.15 (a). For each region, three rectangular areas were investigated and their average compositions measured. Each area either contained precipitates (as in regions 1 and 3 of Fig. 7.15 (a)) or no precipitates (as in region 2 of Fig. 7.15 (a)). The result of the EDS analysis from the areas in Fig. 7.15 (a) are shown in the table in Fig. 7.15, with carbon and boron excluded. These tables shows that the concentration of chromium, for example, varies by ≈ 0.2 Wt. %, which is equivalent to ≈ 0.4 At. % between the areas.

These indicate that there is a *slight* segregation of the strong γ' forming elements (Ti and Al) to the areas with precipitates and a *slight* segregation of the strong γ forming elements (Cr and Co) to the areas without precipitation.

A similar *slight* segregation was seen in the other four regions investigated using EDS. This is shown in Fig. 7.15 (b), where the difference between the strong γ forming elements (Cr and Co) and the amount of strong γ' forming elements (Ti and Al) in Wt. % is shown for the five investigated regions.

As in the data collected by Vernier [32], the difference in composition between the different areas is small, so WDS data was collected using an EPMA to verify these differences, and increase confidence that there is a real difference in composition.

WDS data was collected from six regions, three from sample 2A (shown in Fig. 7.16) and three from 2B (shown in Fig. 7.17). Data was collected along a line of defocused spots (with diameters of 6 µm). These lines passed through areas



Composition in Wt. %											
Area	Ni	Fe	Cr	Co	Mo	W	Al	Ti	Nb	Zr	Segregation coefficient
1	56.1	4.1	15.8	8.4	2.8	3.2	2.3	3.7	1.1	0.2	18.2
2	55.7	4.2	16.0	8.5	2.8	3.3	2.2	3.5	1.0	0.1	18.8
3	55.8	4.1	15.8	8.4	2.9	3.1	2.3	3.7	1.1	0.2	18.2
Composition in At. %											
Area	Ni	Fe	Cr	Co	Mo	W	Al	Ti	Nb	Zr	Segregation coefficient
1	56.3	4.3	17.8	8.4	1.7	1.0	5.0	4.6	0.7	0.1	16.7
2	56.2	4.5	18.2	8.5	1.7	1.1	4.8	4.3	0.6	0.1	17.6
3	56.1	4.3	17.9	8.4	1.8	1.0	5.0	4.6	0.7	0.1	16.8

Figure 7.15: Three areas from sample 2B used to compare the chemical composition of the bands with and without γ' precipitation using EDS (a). Bands (1) and (3) show precipitates, while band 2 does not. Five such regions, each comprising three areas (two without and one with γ' precipitation) were measured using EDS. Remnant chemical segregation between the bands in the five regions is illustrated as Wt. % (Cr + Co) - (Al + Ti) (b). The orange bars and "-" symbol in (b) refer to bands without γ' precipitation. Tables give compositions of three regions in both provide weight and atomic percentages for three regions.

such as those indicated by the white arrows in Figs. 7.11 and 7.12 which show alternate high and low densities of precipitates. Given the relatively small size of the spots, quite significant variations in composition can be found between neighbouring spots, depending on whether or not the spot happens to intersect a precipitate. Nevertheless, a clear comparison can be made by grouping the spots into two groups: those in the areas with high precipitate densities, and those in the areas with low

precipitate densities.

As with the EDS data, the WDS data shows that there is *slight* remnant segregation. Typical compositions for the regions with and without precipitation (based on the WDS data in Fig. 7.16 (e)), and the differences between them, are shown in Table 7.1, in both Wt.% and At.%. The regions without precipitation have higher concentrations of the γ forming elements (Cr and Co) and lower concentrations of the γ' forming elements (Ti and Al). These tables shows that the concentration of chromium, for example, varies by ≈ 0.5 Wt. %, which is equivalent to ≈ 0.6 At. % between the areas.

In the WDS data, the measured Co concentrations are lower, and the measured Ni concentrations higher, than measured with EDS. However, the trends in terms of the strong γ and γ' forming forming elements are the same.

Table 7.1: Typical compositions of the bands with and without precipitation, based on WDS measurements from sample 2 A. The bands and WDS measurement spots are illustrated in Figs. 7.16 (e).

Composition in Wt. %											
Band	Ni	Fe	Cr	Co	Mo	W	Al	Ti	Nb	Zr	Segregation coefficient
γ'	61.4	2.4	16.8	4.8	2.5	2.6	3.6	4.2	1.0	0.1	13.8
-	60.7	2.5	17.3	4.9	2.6	2.7	3.4	3.9	1.0	0.1	14.9
γ'	60.90	2.4	16.9	4.8	2.6	2.6	3.4	4.0	1.0	0.1	14.3
Composition in At. %											
Band	Ni	Fe	Cr	Co	Mo	W	Al	Ti	Nb	Zr	Segregation coefficient
γ'	59.3	2.4	18.3	4.6	1.5	0.8	7.5	5.0	0.6	0.1	10.4
-	59.1	2.5	18.9	4.7	1.6	0.8	7.2	4.6	0.6	0.1	11.9
γ'	59.3	2.5	18.6	4.6	1.5	0.8	7.3	4.8	0.6	0.1	11.2

These data confirm the suggestion of Vernier that there is some remnant chemical segregation associated with the different bands of precipitation. From the EDS and WDS data collected, the concentration of Cr varies by an amount on the order of 0.5 At. %.

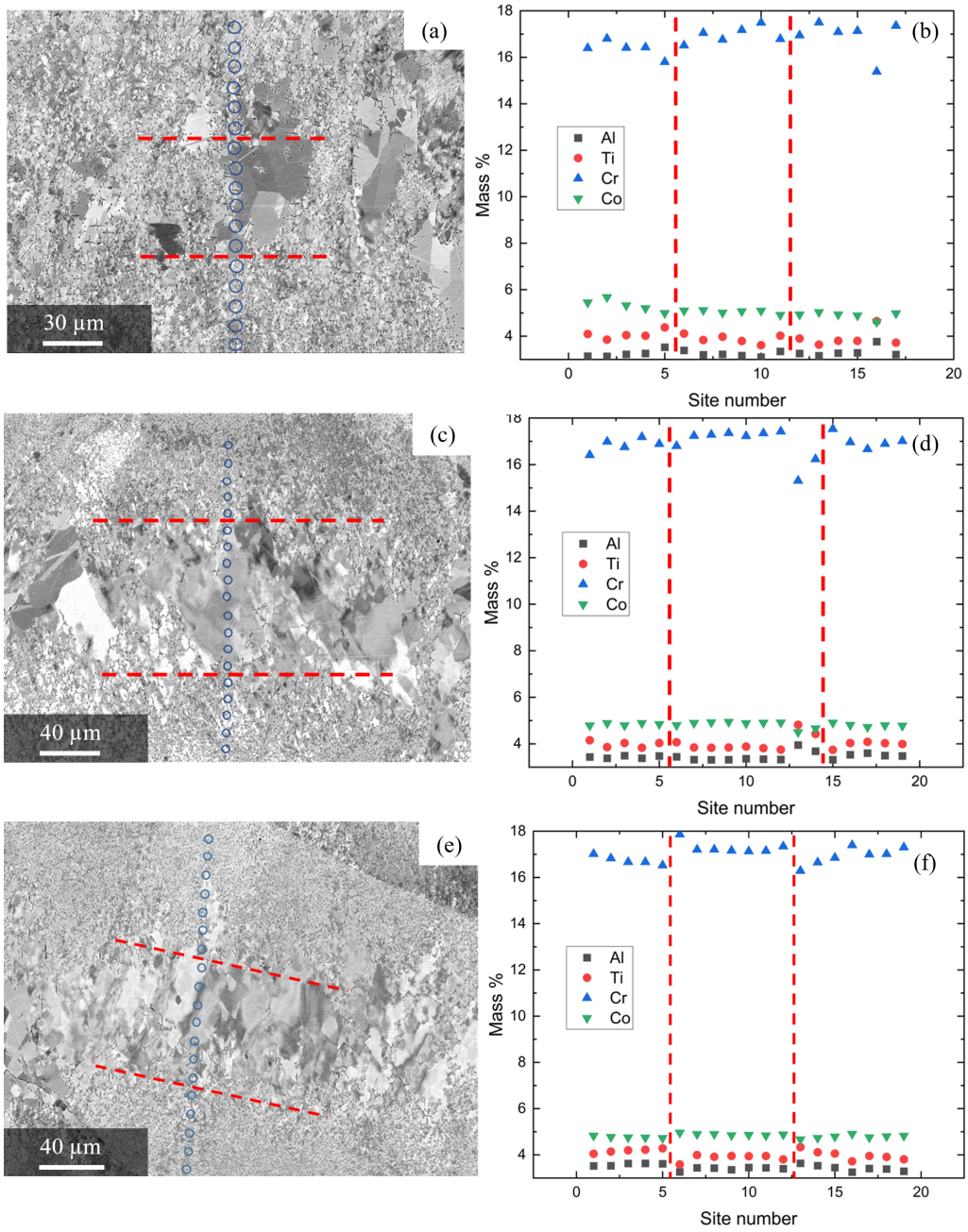


Figure 7.16: BSE images from sample 2A showing the defocused spots from which WDS data were collected (first column, (a), (c), (e)) and the corresponding local chemical compositions measured with WDS (second column, (b),(d), (f)). The red lines separate regions with and without precipitates.

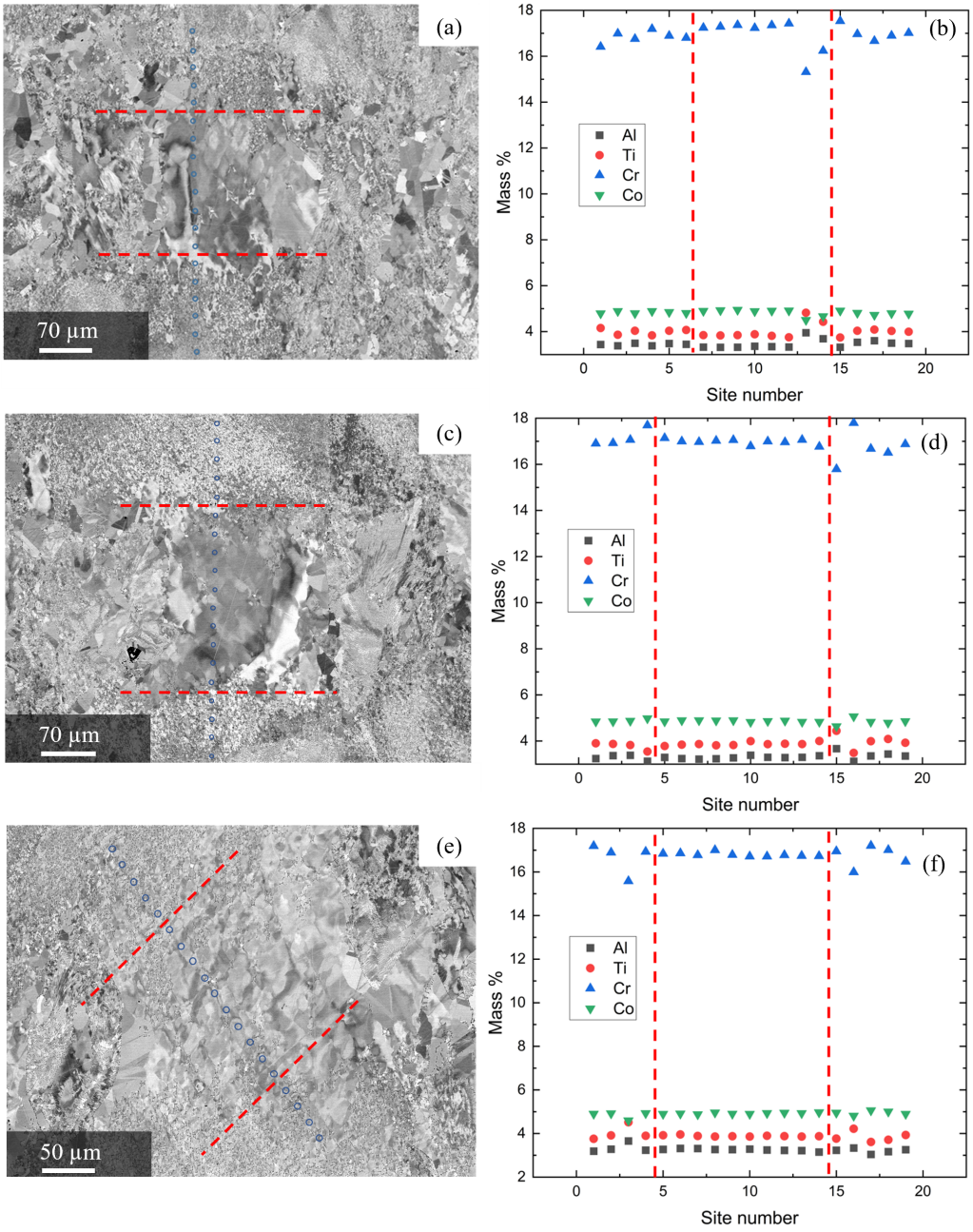


Figure 7.17: BSE images from sample 2B (which underwent a single forging stroke, 10 minutes reheating at 1080 °C, followed by water quenching) showing the defocused spots from which WDS data were collected (first column, (a), (c), (e)) and the corresponding local chemical compositions measured with WDS (second column, (b),(d), (f)). The red lines separate regions with and without precipitates.

7.4 Summary

In this chapter the effects of forging parameters (number of forging strokes, cooling rates after forging, reheating between forging strokes) on the level of recrystallisation have been investigated. The inhomogeneous precipitation distribution after forging to low strains, and the associated remnant chemical segregation were investigated. The main conclusions are:

1. Forging to a given strain level in either one or two strokes was not found to have a significant effect on the overall recrystallisation level achieved.

2. The increase in recrystallisation level with 10 minutes holding after a single forging stroke is primarily due to the growth of existing recrystallised grains, and not the static formation of new recrystallised grains.

3. The inhomogeneous precipitate distribution seen prior to forging, with precipitate free bands, is still present after forging to a strain of 0.44 (in samples 2A and 2B, which underwent a single forging stroke). However, these precipitate free bands are not seen after forging to a strain of 0.69 in a single stroke (the lowest strain region investigated in sample 1D, which was water quenched after forging in a single stroke). This potentially supports the interpretation that dynamic precipitation is onset at a particular strain level. Additionally, the precipitate free bands in samples 2A and 2B show a similar contrast in FSE images to the regions containing the potential dynamic precipitates identified in sample 1D, suggesting the dynamic precipitates have formed from the initially precipitate free bands during forging.

4. There is evidence of slight chemical segregation between areas with and without precipitation in samples 2A and 2B. The $\gamma\prime$ forming elements (Ti and Al) are concentrated in regions with precipitation and the γ forming elements (Cr and Co) are concentrated in regions without precipitation. The width of the precipitate free areas (i.e. the length scale of the segregation) is on the order of 150 µm.

   However, the magnitude of this segregation is small, and the effect on precipitate volume fraction is considerable.

8 Recrystallisation in an inhomogeneous microstructure from an intermediate stage of billet conversion

A main aim of industrial billet conversion is to produce a billet with uniform microstructure, comprising equiaxed recrystallised grains with an appropriate size and a suitable distribution of primary γ' precipitates. Macroscopically, this process involves repeated heating and deforming of the ingot; the finished billet is typically four times as long as the starting ingot with half the diameter. Microscopically, it involves as-cast grains with equivalent diameters on the order of 1 mm being refined through recrystallisation to equiaxed grains with equivalent diameters on the order of 20 µm (a 50-fold reduction). At the intermediate stages of this conversion, very inhomogeneous microstructures arise, with a wide spread of grain sizes, stored energy levels and different precipitate distributions. This chapter investigates the dynamic recrystallisation processes occurring in such a microstructure. This is relevant academically, as a vast majority of recrystallisation studies consider homogeneous starting microstructures, very few consider inhomogeneous starting microstructures, particularly microstructures containing grains as large as those observed at the intermediate stages of billet conversion (e.g. [66, 109]). This is also relevant industrially, as the microstructure investigated comes directly from an intermediate stage of industrial forging (from which material is rarely available), allowing its evolution through to the final billet material to be tracked. Fig. 8.1 gives a graphical overview of the thermomechanical experiment on which this chapter is based.

8.1 Starting microstructure

In this section, the starting microstructure comes from the end of a static recrystallisation heat treatment. The position of this forging stage in the overall forging process was shown in Fig. 3.1. Specifically, a cylindrical sample from the edge of

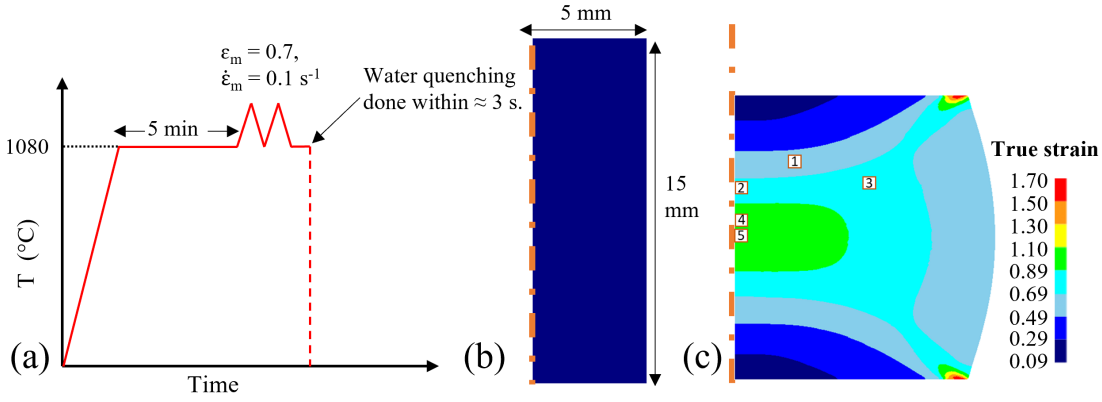


Figure 8.1: Schematic illustration of the hot compression test done to analyse microstructural evolution at an intermediate stage of the billet conversion process (a). Strain distributions predicted by DEFORM before (b) and after (c) compression.

the head end of a semi-finished billet was used. The axis of this cylinder was parallel to a radial axis of the billet. As is typical at this stage of the billet conversion process, this sample shows a very inhomogeneous starting microstructure, which is highlighted in Fig. 8.2.

Three distinct populations of grains, containing three distinct populations of precipitate can be identified:

1. Firstly, relatively large grains (equivalent diameters ≈ 28.4 µm) with low KAM values can be identified (indicated by the number 1). These are grains which have grown during static recrystallisation by consuming a neighbouring unrecrystallised grain with which they share a $\langle 111 \rangle$ axis [23]. These will be referred to as large initially statically recrystallised grains.

2. Secondly, larger grains (equivalent diameters ≈ 200 µm) with a large number of points with KAM values $\geq 1.5°$ are identified as initially unrecrystallised grains (indicated by the number 2). These will be referred to as initially unrecrystallised grains. The microstructure is mostly unrecrystallised, containing many of these large grains with high KAM values.

3. Thirdly, smaller grains with low KAM values can be identified at the boundaries of the initially unrecrystallised grains. Some of these are highlighted by the red arrows, and will be referred to as small initially recrystallised grains.

A higher magnification BSE image and corresponding IPF Y map are shown

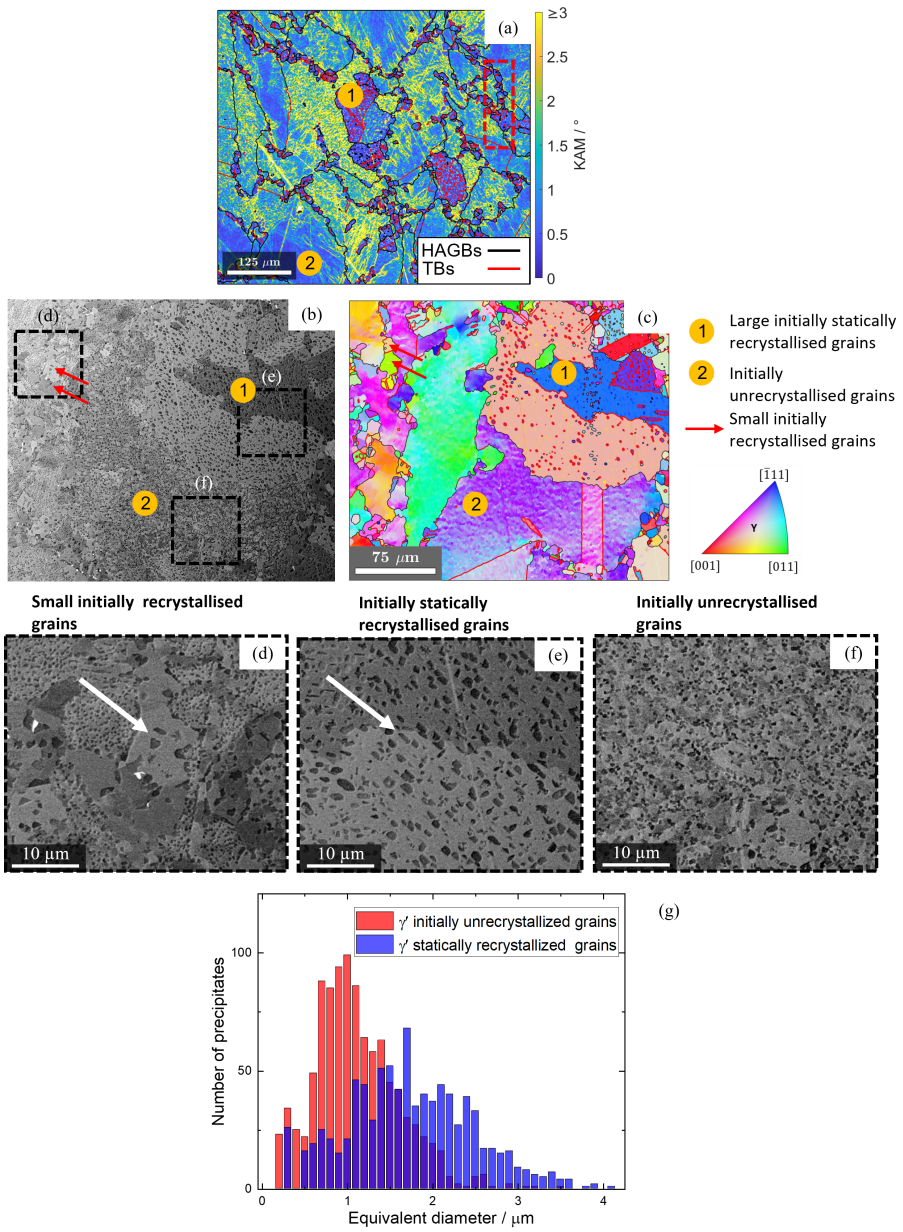


Figure 8.2: Microstructure of the as-received AD730 material, from after the static recrystallisation stage of the billet conversion process. (a) A KAM map (values limited to 3°) with three distinct populations of grain highlighted, (b) a higher magnification BSE micrograph, and (c) its corresponding IPF map. (d), (e), (f) Magnified micrographs of three selected areas highlighted in (b) showing the three distinct precipitation states in recrystallised, large initially statically recrystallised and initially unrecrystallised grains, respectively. (g) Histograms of precipitate size distribution in the large initially statically recrystallised and the initially unrecrystallised grains.

in (b-c), and these three categories of grain can again be identified. The higher magnification BSE images in (d-f) show the different precipitate states in the three grain populations.

In the large initially statically recrystallised grains, precipitates display a rectangular morphology in the 2D cross-sections revealed in the micrographs and have either a close to twin or close to coherent orientation relationship with their host γ grains (i.e. these are C/T type precipitates, as discussed in Chapters 2 and 4). Here, close to coherent means the precipitates have orientations sufficiently close to their host grains that they cannot be distinguished based on EBSD data, implying a misorientation angle below the orientation measurement accuracy, i.e. a misorientation angle ≤ 0.5 °. Note this is somewhat different from the strict crystallographic definition of the term coherent, which implies atomic correspondence at the interphase boundary. Vernier *et al.* have described the formation of such grains during the static recrystallisation of AD730, René65 and PER72 [24].

The initially unrecrystallised grains have a relatively high density of fine, spherical precipitates which are coherent, or at least sufficiently coherent that they cannot be distinguished from their host grains using EBSD data, implying a misorientation $\leq$ 0.5°. Note this is somewhat different from the strict crystallographic definition of the term coherent.

The small initially recrystallised grains show a mixture of rather large intragranular precipitates which are coherent with their host grain, and intergranular precipitates at their boundaries with the initially unrecrystallised grains.

Since the small initially recrystallised grains do not contain easily identifiable precipitates, it is not possible, after deformation, to identify such grains which have persisted through recrystallisation. Therefore, only the evolution of the initially unrecrystallised and large initially statically recrystallised grains will be examined in the following. A summary of the characteristics of the precipitate distribution in the three different grain populations is given in Table 8.1.

The T/C type precipitates in the large initially statically recrystallised grains were imaged in 3D using FIB-SEM nanotomography. The results of this are shown in Fig. 8.3. This shows that, despite their rectangular appearance in 2D sections, in 3D these precipitates have the shape of short cylinders. The diameter of the precipitate shown in Fig. 8.3(d) is approximately 4.1 µm and the thickness is approximately 0.6 µm. Calculating an equivalent circle diameter based on the area of the rectangular 2D sections of these precipitates is thus likely to produce an underes-

Table 8.1: Summary of precipitate characteristics in the three different grain types in the starting microstructure.

Grain type	Equivalent diameter (µm)	Area density (μm^{-2})	Precipitates counted	Precipitate area fraction (%)	Maximum Feret diameter (µm)
Large initially statically recrystallised	1.8 ± 0.7	0.074	882	21.7 %	2.6 ± 1.2
Initially unrecrystallised	1.2 ± 0.5	0.167	1016	20.8 %	-
Small recrystallised	2.2 ± 0.6	-	100	-	-

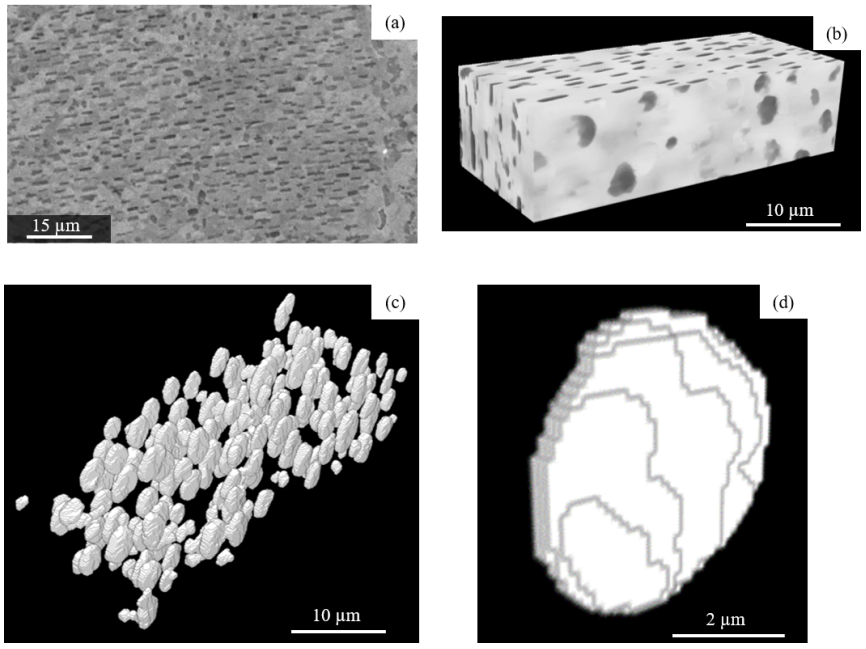


Figure 8.3: A 3D view of the T/C type precipitates found in the large initially statically recrystallised grains. (a) A region of interest which contains the "rectangular" precipitates in 2D, (b) a processed stack of 2D BSE images of a sub-volume extracted from (a) taken at 0.1 µm successive serial sectioning using FIB milling, (c) the same region as (b) after segmentation of the precipitates, and (d) a higher magnification view of a single precipitate.

timate of their actual diameter. The maximum Feret diameter of the "rectangular" precipitates is likely to be a more accurate estimate of the true diameter of these precipitates, hence its inclusion in Table 8.1. However, the maximum Feret diameter will also be influenced by sectioning effects, and will on average underestimate the

ture precipitate diameter; it can vary between the true diameter of the precipitate, and almost 0.

8.2 Overall microstructural evolution with strain

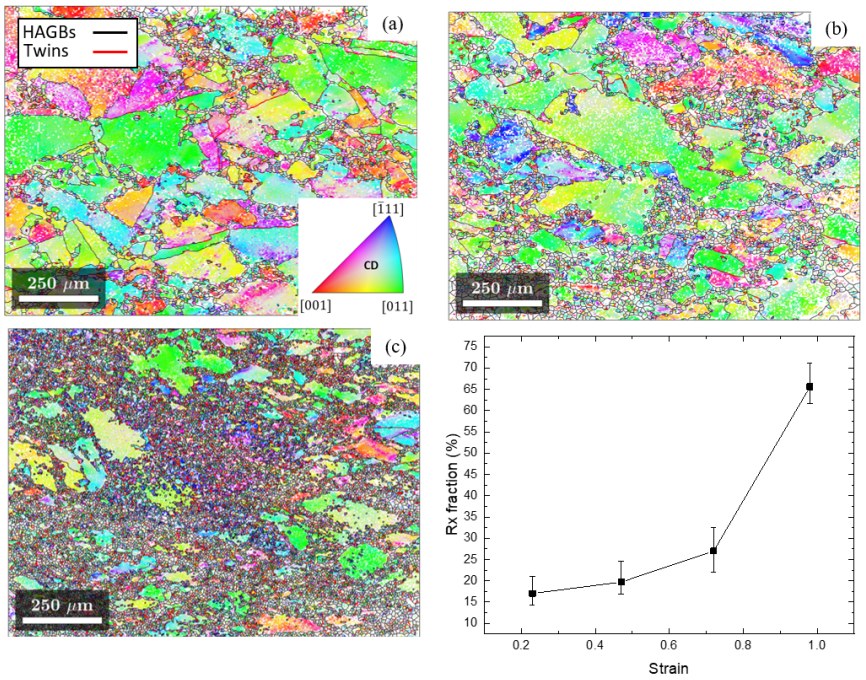


Figure 8.4: Effect of local strain on microstructure evolution. The approximate local strain levels in (a-c) are (a) $\epsilon \approx 0.23$, (b) $\epsilon \approx 0.72$, and (c) $\epsilon \approx 0.98$. The step size for the EBSD maps in (a) through to (c) were 4 µm, 4 µm and 2.5 µm, respectively. (d) A plot of the area fraction of recrystallised grains as a function of strain. The compression direction (CD) is vertical, as indicated.

To gain a representative large area overview of the starting microstructure's evolution with strain, four EBSD maps with an area of approximately 1.24 mm^2 were taken using a step size in the range 2.5 to 4 µm from four different regions along the compression axis of the sample. In these low magnification maps, at least 80 % of the points were indexed in all cases.

Fig. 8.4 shows these IPF maps coloured with respect to the compression direction. The relatively large step size (2.5 µm to 4 µm) means these maps do not show fine microstructural details (i.e., accurate shapes of the recrystallised grains) though they do provide an overall picture of the microstructure and the progression of re-

crystallisation. The size, shape and orientation of the large deformed grains, which have not undergone recrystallisation, can be inspected from these orientation maps.

Fig. 8.4 (d) shows a plot of recrystallised fraction as a function of strain. For this plot, recrystallised and unrecrystallised grains were separated based on grain size. Grains with an equivalent radius smaller than 10 µm were classed as recrystallised, and those above as unrecrystallised. This threshold was decreased to 8 µm and increased to 15 µm to produce the error bars in Fig. 8.4 (d). This approach is similar to the one used by Eriksson *et al.* [110].

The relatively high recrystallisation levels at low strains can be attributed to the fact that the starting microstructure was partially recrystallised, and it already contained stored energy (notably within the initially unrecrystallised grains). Fig. 8.4 (c) shows that even at the highest local strain level analysed, quite large unrecrystallised grains exist. This raises the question of whether these grains are remnants of the initially unrecrystallised grains of the as-received material, or deformed fragments of the large initially statically recrystallised grains, whose lower initial stored energy may have been a kinetic disadvantage for recrystallisation. The progress of recrystallisation in both of these grain populations, are analysed for different local strain levels in the following.

To do this, more detailed analyses were performed on five smaller EBSD maps acquired with smaller step sizes. The locations of these regions are indicated in Fig. 8.1 (c), and their respective step size and indexing rate are provided in Table 8.2.

Immediately before and after these EBSD scans, forward scattered electron (FSE) images were also captured from the same area using a forward-scattered electron detector (FSD) attached to the EBSD detector screen. Since these FSE images were captured under identical conditions to the EBSD scans, data from the two can be compared and overlaid (e.g., grain boundaries from the EBSD data overlaid onto the FSE image) to help identify the precipitates, which can't be separated from the matrix using EBSD data.

Table 8.2: Map properties for five regions at different local strain levels investigated with EBSD in this Chapter.

Region number	Local strain	Map area (µm^2)	Step size	Indexing rate (%)
1	0.53	231.6 x 202.4	0.20	91.0
2	0.72	148.2 x 111.1	0.20	98.5
3	0.76	122.3 x 107.0	0.15	94.0
4	1.00	98.6 x 74.0	0.20	98.5
5	1.04	86.5 x 45.5	0.50	96.2

8.3 Recrystallisation of the large initially statically recrystallised grains

Fig. 8.5 shows the area corresponding to region 3 in Table 8.2 with a local strain level of $\epsilon \approx 0.76$. This region must have contained a large initially statically recrystallised grain prior to deformation, as indicated by the "rectangular" precipitates seen in Fig. 8.5 (b). However, the IPF map in Fig. 8.5 (a) and the KAM map in Fig. 8.5 (e) show that this statically recrystallised grain has almost completely recrystallised, with only small fragments of the original grain remaining. One such fragment is indicated in Fig. 8.5 (c). Inspecting this small fragment of the large initially statically recrystallised grain reveals that LAGBs (here defined as intragranular boundaries with misorientation angles between 3° and 5°, plotted yellow) and MAGBs (here defined as intragranular boundaries with misorientation angles between 5° and 10°, plotted white) have formed intragranularly. The KAM map for this area (Fig. 8.5 (e)) shows that geometrically necessary dislocations within this fragment are strongly concentrated at these intragranular sub-boundaries. This suggests that the large initially statically recrystallised grains can recrystallise via a continuous process which involves intragranular dislocation polygonisation, forming regions which are initially walled off by LAGBs. As more dislocations accumulate, these LAGBs progressively become MAGBs and eventually HAGBs. In the large initially statically recrystallised grains these LAGBs and MAGBs can form around the existing precipitates, which persist through recrystallisation.

Fig.8.6 was taken from an area where the local strain was $\epsilon \approx 1.00$ (corresponding to region 4 in Table 8.2) and shows that the characteristic shapes and orientations of

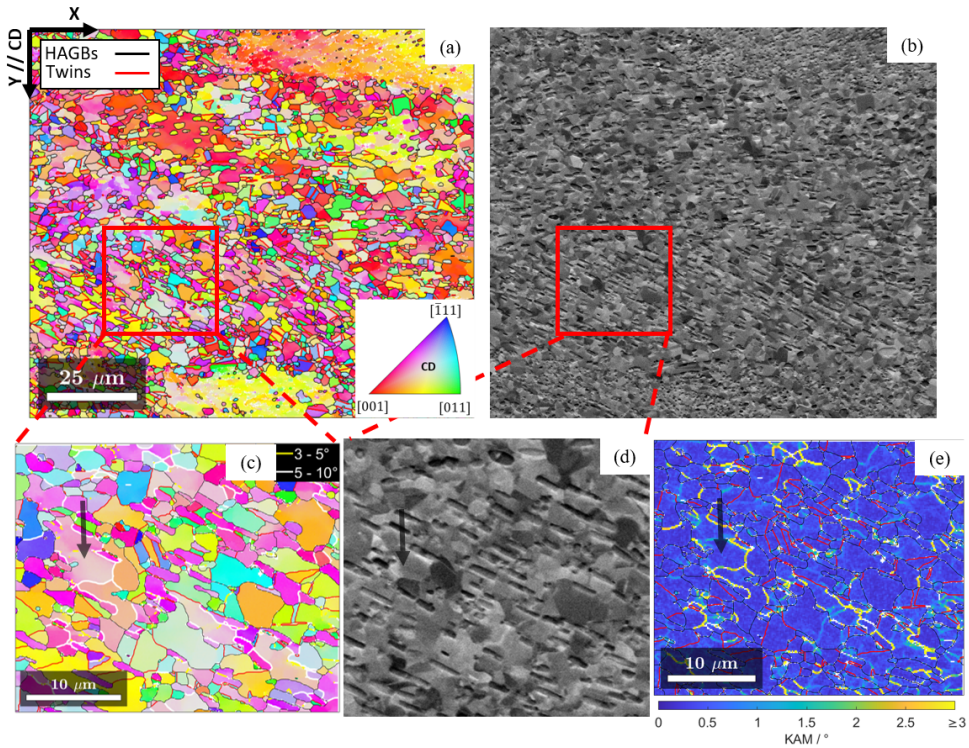


Figure 8.5: Intragranular recrystallisation in a large initially statically recrystallised grain from region 3 in Table 8.2, where the local strain is $\epsilon \approx 0.76$. (a) An IPF map of an area containing fragments of a large initially statically recrystallised grain, (b) FSE micrograph of the same area in (a). (c), (d) And (e) respectively show an IPF map, FSE micrograph and KAM map for the region enclosed by the red rectangle in (a) and (b). LAGBs (3-5 °) and MAGBs (5-10 °) are indicated by yellow and white lines in (c). The black arrow indicates a remaining fragment of the large initially statically recrystallised grain.

the "rectangular" precipitates in the large initially statically recrystallised grains are preserved throughout deformation and dynamic recrystallisation of their host large initially statically recrystallised grains. In Fig. 8.6(a), the "rectangular" precipitate indicated by the red arrow was taken as a reference orientation. All grains with orientations within 10° of this reference are highlighted with a blue outline in Fig. 8.6(c). This shows that many "rectangular" precipitates, or the small recrystallised grains which contain them, have an orientation close to that of the reference, indicating that their orientation has been preserved throughout deformation and recrystallisation. This reference orientation is shown by the red circles on the pole figure in Fig. 8.6(d). A selection of 10 grains containing "rectangular" precipitates which do not satisfy the 10° condition are indicated with black arrows in Fig. 8.6(c), labelled as "selected

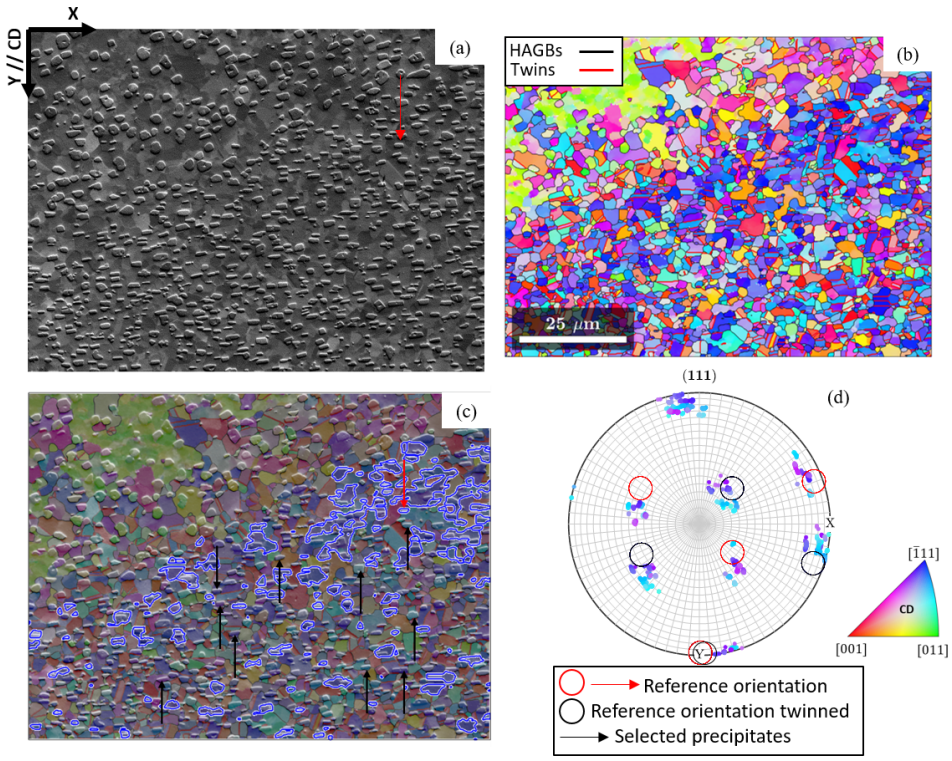


Figure 8.6: Crystallographic orientation of "rectangular" precipitates in region 4 from Table 8.2, where $\epsilon \approx 1.00$. (a) A FSE micrograph of a region which contained a large initially statically recrystallised grain prior to deformation, (b) the corresponding IPF map depicting that the large initially statically recrystallised grain has dynamically recrystallised during deformation. (c) The FSE micrograph in (a) with a partially transparent overlay of the IPF map and (d) a $\langle 111 \rangle$ polefigure of a selection of 10 grains indicated by black arrows in (c) containing "rectangular" precipitates with orientations outwith 10° of the reference precipitate highlighted by the red arrow in (c). Note that the reference orientation (red circles) and one of its twin orientations (black circles) are highlighted in (d). The blue lines in (c) outline grains with orientations within 10° of the reference orientation.

orientations". Their orientations are plotted on a pole figure in Fig. 8.6(d). These precipitates either have small misorientations to the reference orientation, which appear to be close to the red circles corresponding to the reference orientation, or have an approximately twin orientation relationship with the reference orientation and appear close to the black circles, which show an orientation that is twin related to the reference orientation. Since a given large initially statically recrystallised grain can contain both close to coherent and close to twin precipitates [23], the evidence in Fig. 8.6 is consistent with these precipitates retaining their initial orientations

through recrystallisation.

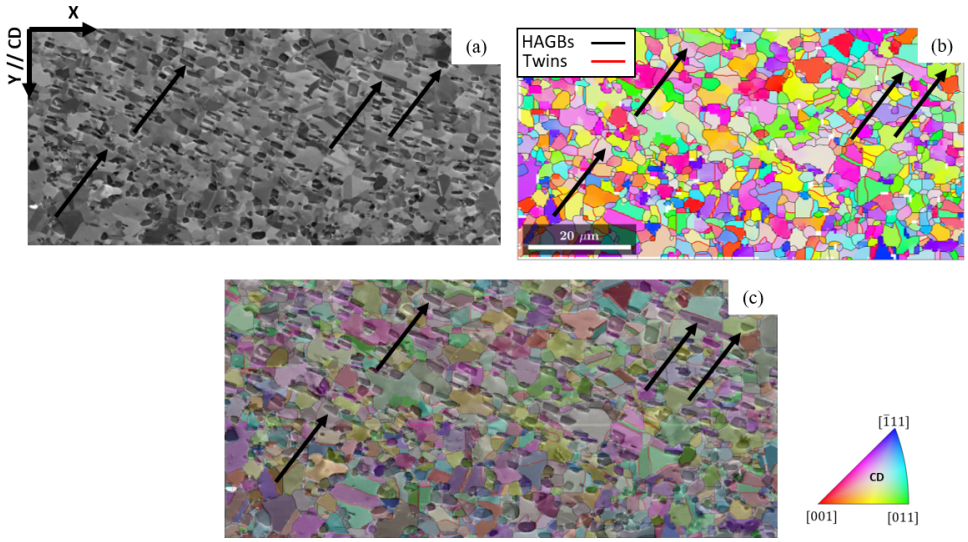


Figure 8.7: Examples of HERX within a large initially statically recrystallised grain, from region 5 in Table 8.2, where $\epsilon \approx 1.04$. (a) A BSE micrograph with four "rectangular" precipitates indicated by black arrows, (b) a corresponding IPF map confirming that these precipitates are the only ones within their grains, and (c) a transparent version of the IPF map overlaid onto the BSE micrograph to ease visualisation.

Additionally, recrystallisation can be seen to occur immediately around the relatively large "rectangular" γ' particles in the large initially statically recrystallised grains. Some examples of this are presented in Fig. 8.7. These were taken from an area where the calculated local strain was $\epsilon \approx 1.04$, corresponding to region 5 in Table 8.2. These examples show the indicative features of the hetero-epitaxial recrystallisation (HERX) mechanism. HERX is a recently characterised recrystallisation mechanism, in which a coherent shell (or piece of a shell) of γ phase precipitated around a γ' particle acts as recrystallisation nucleus. Recrystallised grains which have undergone this mechanism are expected to contain a single, close to coherent γ' precipitate [59, 60], as is indeed the case for the grains highlighted in Fig. 8.7.

8.4 Recrystallisation in and around the initially unrecrystallised grains

In total, four different recrystallisation processes were observed to occur in/around the initially unrecrystallised grains, giving rise to four distinguishable types of recrystallised grain. These different groups of grains are highlighted in Fig. 8.8, which comes from an area with a calculated local strain of $\epsilon \approx 0.72$, corresponding to region 2 in Table 8.2. The vast majority of the recrystallised grains are found at the boundaries of the initially unrecrystallised grains, are small, have low intergranular misorientations (indicated by their low KAM values) and display little to no intragranular precipitation. These grains form a typical necklace structure around the initially unrecrystallised grains. Such recrystallised grains will be referred to as "necklace recrystallised grains" hereafter.

In addition to these necklace recrystallised grains, a second population of recrystallised grains which are larger, contain rectangular precipitates and display higher internal KAM values can also be found within the necklace structure; examples of these are indicated by the yellow arrows in Figs. 8.8 (a) and (b). The average equivalent diameter of the recrystallised grains surrounding the initially unrecrystallised grain on the right hand side of Fig. 8.8(a) is 2.7 µm, and those of the large recrystallised grains highlighted by the yellow arrows are 13.8 µm and 11.0 µm. These will be referred to as "large recrystallised grains" or "large recrystallised grains containing rectangular precipitates" hereafter.

Thirdly, intragranular "channels" can be identified, indicated by the red arrows in Figs. 8.8 (a) and (b). These regions have a slight misorientation to their surrounding initially unrecrystallised grain (as is shown by the KAM maps), a lower density of precipitation than the surrounding initially unrecrystallised grain and slightly lower internal KAM values, though not as low as seen in the recrystallised regions. Finally, a grain which is likely to have undergone HERX can be identified (black arrow).

Fig. 8.8(e) shows an IPF Z map (as opposed to the IPF Y map in Fig. 8.8(a)), which confirms that the initially unrecrystallised grains at the centre and to the right of the region in Fig. 8.8 have very similar orientations (with a misorientation angle of 7.7° between their mean orientations), whereas the grain towards the top left has a different orientation. As such, the first two may have previously been a single

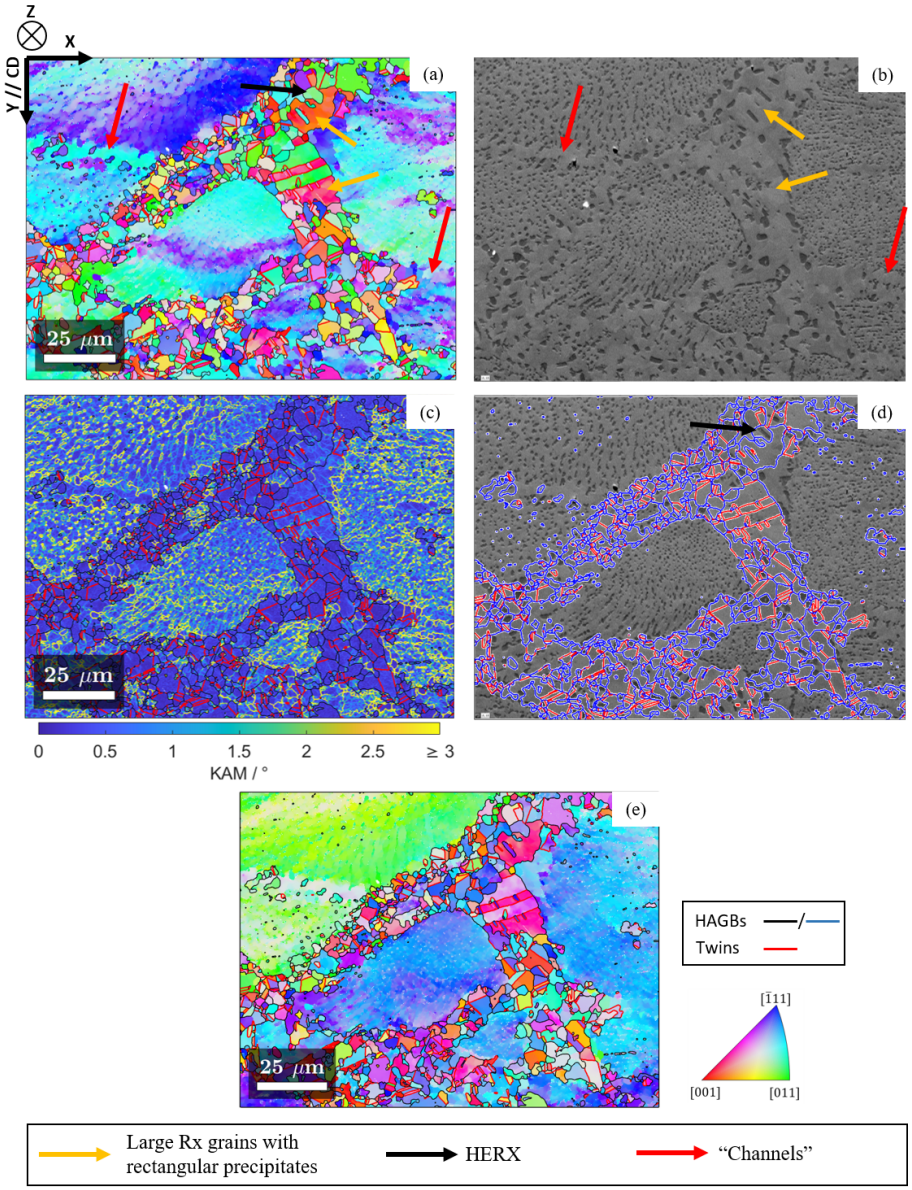


Figure 8.8: Overview of the different recrystallisation mechanisms occurring around and within an initially unrecrystallised grain (from region 2 in Table 8.2, where $\epsilon \approx 0.72$). (a) An IPF Y map, (b) corresponding FSE micrograph, (c) KAM map, (d) the FSE image with the grain boundaries overlaid, and (e) an IPF Z map. Yellow arrows indicate large recrystallised grains containing rectangular precipitates, black arrows grains likely to have formed through HERX and red arrows recrystallised "channels".

grain, which has now been split into two parts due to intragranular recrystallisation, i.e. via one of the "channels". Inside the recrystallised region separating these two

grains a recrystallised grain containing rectangular precipitates can also be identified (highlighted by the orange arrow).

8.4.1 Necklace recrystallised grains

Fig. 8.9 highlights the formation of the necklace recrystallised grains, by showing sub-grains forming at the periphery of an initially unrecrystallised grain. LAGBs are indicated by yellow lines in Fig. 8.9 and MAGBs are indicated by white lines. The sub-grains are separated from the neighbouring initially unrecrystallised grains by MAGBs, shown in Figs. 8.9 (b) and (f). The FSE micrographs shown in Figs. 8.9 (a) and (d) reveal that the sub-grains are free from intragranular precipitation. The KAM maps in Figs. 8.9 (c) and (g) show that the sub-grains have low internal misorientations. They progressively develop into necklace recrystallised grains when the misorientation of the boundary between them and the neighbouring initially unrecrystallised grain increases beyond 10°. This misorientation angle progressively increases as more and more dislocations are incorporated into the boundary during deformation. Bearing in mind the defining features of these necklace recrystallised grains, the following can be hypothesised as their formation mechanism:

During deformation, sub-grains form close to the existing boundaries of initially unrecrystallised grains due to the higher local dislocation densities near the grain boundaries, which are a consequence of plastic incompatibility between neighbouring grains. Further deformation leads to the migration of mobile sub-grain boundaries, which absorb additional dislocations as they migrate, increasing their misorientation angle to their parent grains. These moving sub-grains may dissolve the precipitates they encounter [63]. Once a sufficiently high misorientation angle is achieved the sub-grain becomes a recrystallised grain with a HAGB between it and the initially unrecrystallised parent grain.

Eventually, the boundaries of the newly recrystallised grain would become saturated with γ' forming elements, and its growth would be halted due to a combination of solute drag and pinning from further precipitates encountered in the initially unrecrystallised parent grain.

This process accounts for the observed differences in precipitation between initially unrecrystallised and necklace recrystallised grains, although the concentration of γ' forming elements at the grain boundaries remains to be proved. During the formation of necklace recrystallised grains, precipitates are dissolved into the mi-

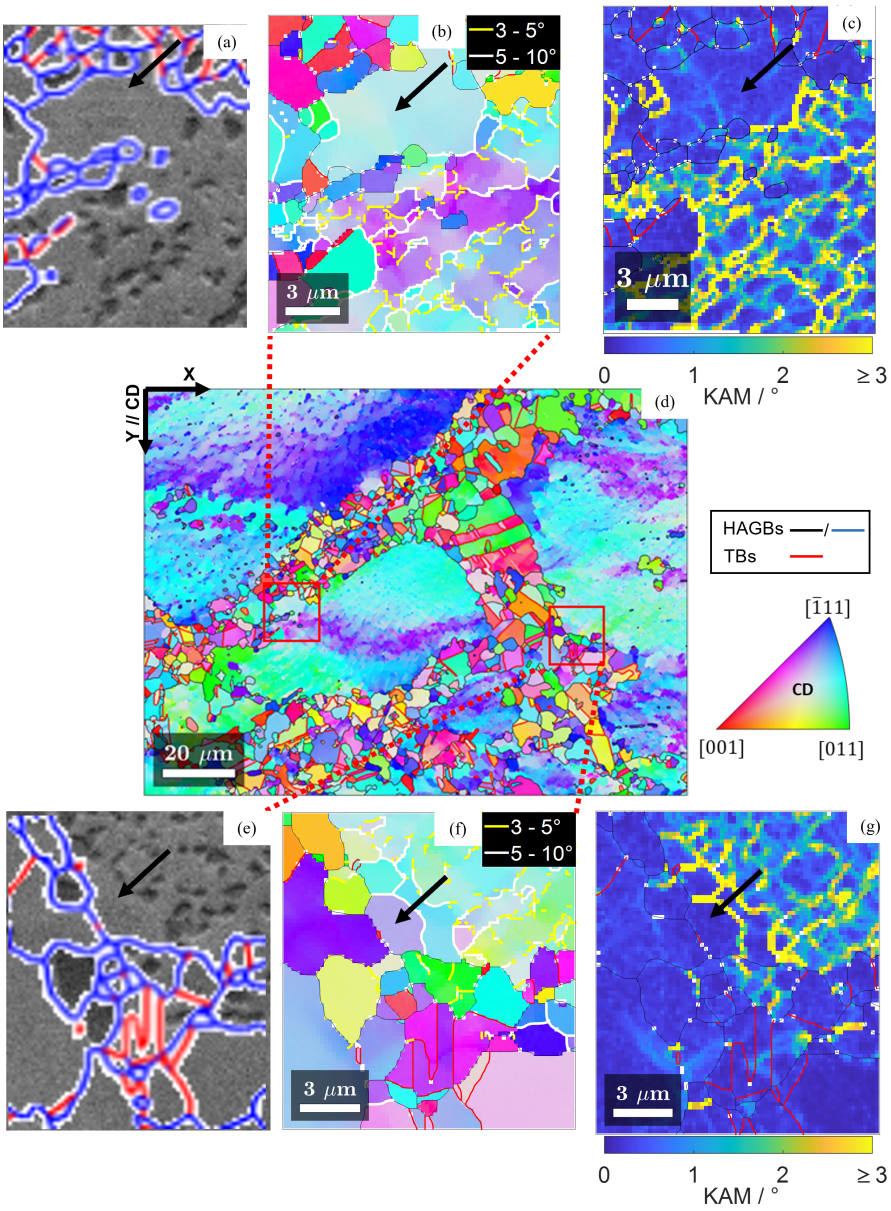


Figure 8.9: The formation of sub-grains near the boundaries of the initially unrecrystallised grains (from region 2 in Table 2, where $\epsilon \approx 0.76$). (a), (b) And (c) respectively show a FSE micrograph with overlaid grain boundaries, an IPF map, and a KAM map of an area highlighted in (d), which is an IPF map of an area containing several initially unrecrystallised grains. (e),(f) and (g) show similar information to (a), (b) and (c), respectively, but for a separate area in (d).

grating sub-grain boundaries. When the grain is fully developed, it will likely be surrounded by other recrystallised grains which have formed by a similar mechanism at the boundary of the initially unrecrystallised grain, and precipitation can occur at

their shared boundaries. Fast diffusion through the saturated boundaries allows for these precipitates to coarsen, giving rise to the relatively large precipitates (i.e., with equivalent diameters of 2.1 - 3.1 µm based on the recrystallised regions in Fig. 8.8 (b)) seen at the boundaries of the necklace recrystallised grains. The intergranular precipitates between the necklace recrystallised grains show no special orientation relationship to their surrounding grains.

The role of grain boundary bulging in the formation of these grains is not clear, although it is one of the most commonly invoked mechanisms to explain the formation of recrystallised grains near grain boundaries. The most common explanation of grain boundary bulging is that of Belyakov [111], where plastic incompatibility between neighbouring grains gives rise to boundary serration. This leads to boundaries interlocking and eventually preventing further boundary sliding or shearing, so dislocations build up near the boundary. This high dislocation density leads to the formation of sub-grains and eventually recrystallised grains near the boundary [112]. Here, the new recrystallised grain will have an orientation similar to the host initially unrecrystallised grain.

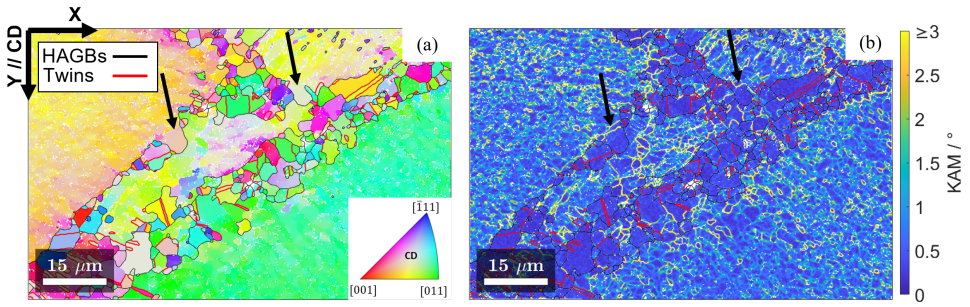


Figure 8.10: The formation of sub-grains at bulged grain boundaries. (a) Two bulged grain boundaries indicated by the black arrows, and (b) the corresponding KAM map showing that the regions within the bulges have low internal misorientations. Data from region 1 in Table 8.2 with a local strain of $\epsilon \approx 0.53$.

Grain boundary bulging is not necessarily involved in the formation of the necklace recrystallised grains. There are instances of sub-grains forming adjacent to entirely flat boundary sections (at least as visible in a 2D section), such as Figs. 8.9(e) – (g), and instances of sub-grains which are adjacent to bulged boundaries, shown in Fig. 8.10. The formation of recrystallised grains and sub-grains next to flat boundary sections has also been observed during recrystallisation of Haynes 282 above its γ' solvus temperature [110].

A different pathway to grain boundary bulging also exists, namely strain induced boundary migration (SIBM). This was first reported by Beck and Sperry [113], then studied in more detail by Bailey and Hirsch [114]. This mechanism argues that local differences in stored energies across a boundary (due to differing dislocation densities) are the driving force for grain boundary bulging. Bulging occurs when this driving force exceeds the increase in energy due to the curvature induced by bulging – which will depend on the sub-grain size (larger sub-grains mean lower curvature), and the difference in stored energies across the boundary.

These two pathways to grain boundary bulging differ in measurable ways – for example, the first makes no reference to stored energy, and a bulge could advance in either direction at a boundary (as has been observed in [110]). On the other hand, SIBM requires that a bulge progress from a sub-grain with low stored energy in to a region of a grain with higher stored energy. Additionally, the first mechanism requires serrated boundaries to form before the occurrence of bulging, but SIBM may begin from a flat, un-serrated boundary.

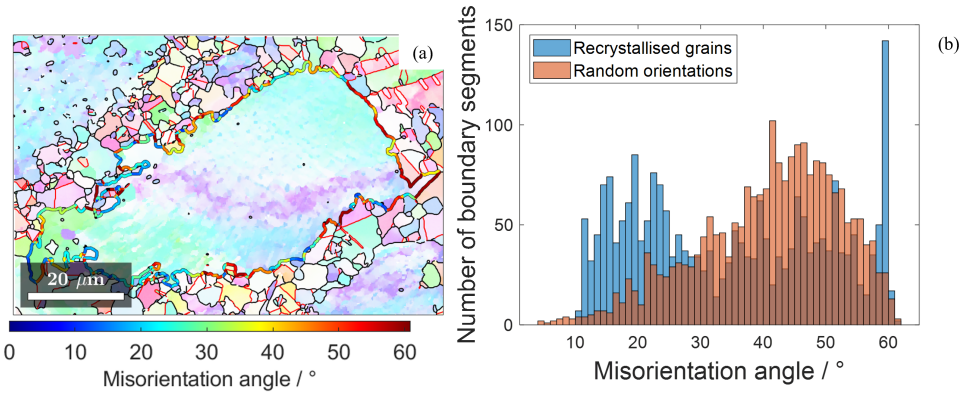


Figure 8.11: Misorientation angle distribution around the initially unrecrystallised grains. (a) EBSD grain boundary map of an initially unrecrystallised grain colourised according to the local misorientation angle, (b) the distribution of misorientation angles between this grain and the surrounding recrystallised grains, shown by the blue bars. The red bars in (b) show misorientation angle distributions between the initially unrecrystallised grain and a set of random orientations in the map. Data from region 2 in Table 8.2 with a local strain of $\epsilon \approx 0.72$.

The abundance of the grain boundary recrystallisation mechanism leading to necklace recrystallised grains is indicated in Fig. 8.11, which shows the misorientation angle distributions around the boundary of an initially unrecrystallised grain. The disproportionately high fraction of lower angle boundaries around the initially

unrecrystallised grain suggests that the majority of recrystallised grains surrounding the initially unrecrystallised grain form as necklace recrystallised grains, which is also consistent with the precipitation state found in the recrystallised regions surrounding the initially unrecrystallised grains. This is evidence that this grain boundary recrystallisation mechanism, which may occur with or without bulging, is the most abundant mechanism in the initially unrecrystallised grains during subsolvus forging. The misorientation angle distribution also shows a sharp peak around 60°, suggesting that the necklace recrystallised grains often undergo twining during their formation. Twin assisted nucleation of dynamically recrystallised grains has been observed in IN718 [72]. Twining may further assist the growth of recrystallised grains by forming mobile high misorientation angle grain boundaries as discussed in Chapter 6 and elsewhere [107, 108].

8.4.2 Large recrystallised grains

Microstructures of large recrystallised grains containing rectangular precipitates are shown in Fig. 8.12, which highlights the misorientation angles between these grains and their neighbouring initially unrecrystallised grains. For all cases, the misorientation angles were high ($> 50°$), with one exception highlighted with a red arrow. The grain with the lower misorientation contains precipitates which are approximately coherent with it (i.e., misorientation angle $< 1°$), while those with the higher misorientations (indicated by the black arrows) contain precipitates which have approximately twin orientation relationships with their host grains (corresponding to red boundaries in (a) and (b)).

To inspect the orientation relationships between the large recrystallised grains, their rectangular precipitates, and their neighbouring initially unrecrystallised grains further, pole figures for all three are plotted in Fig. 8.13. Figs. 8.13(b) and (d) show that there is a shared $\langle 111 \rangle$ axis between the large recrystallised grains, their rectangular precipitates, and the neighbouring initially unrecrystallised grain. This axis is outlined by the red circle in Figs. 8.13(b) and (d).

As the large recrystallised grains with rectangular precipitates have a number of distinguishing features which separate them from the necklace recrystallised grains, a different mechanism may have resulted in their formation. Similar grains, i.e., large recrystallised grains containing close to twin or close to coherent precipitates displaying a rectangular shape in 2D sections, have been observed to form statically

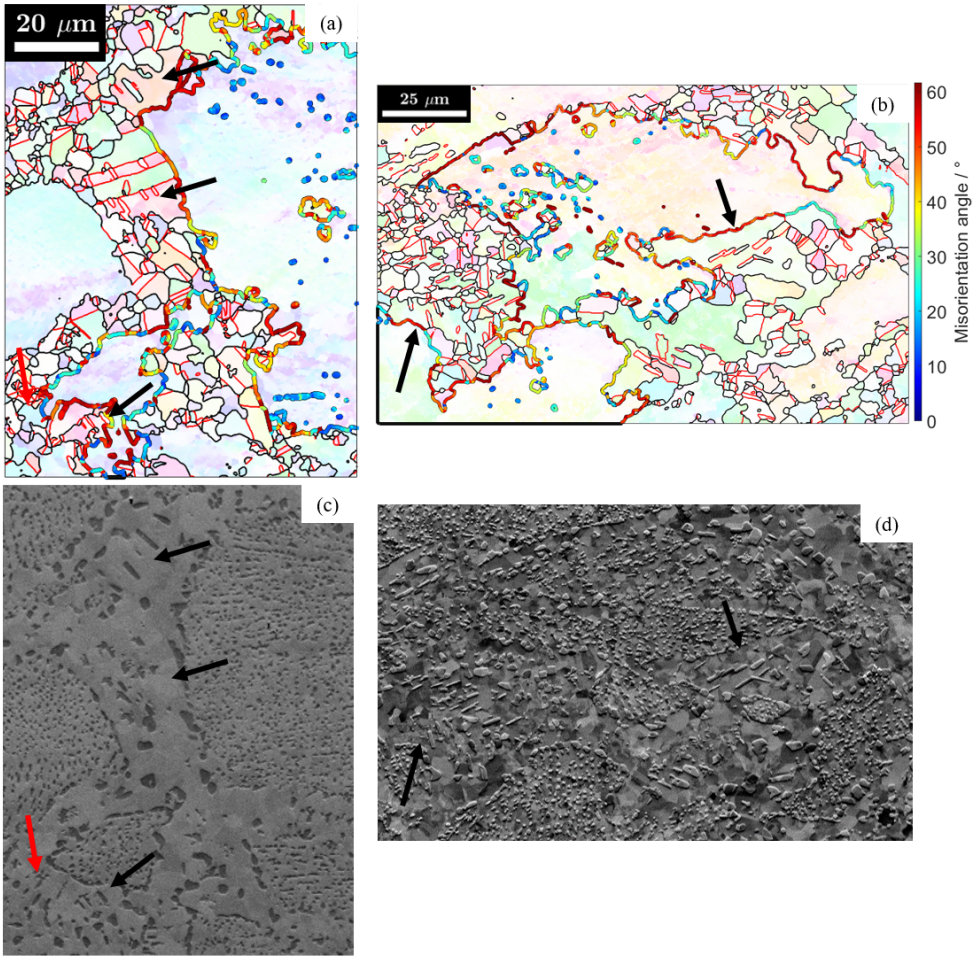


Figure 8.12: Misorientation angles between the large recrystallised grains and their neighbouring initially unrecrystallised grains. (a) And (b) EBSD grain boundary maps of two initially unrecrystallised grains, colourised according to their local boundary misorientation angle. The positions of selected large recrystallised grains containing rectangular precipitates are indicated by the black arrows. These recrystallised grains tend to show high misorientations with the initially unrecrystallised grain ($> 50°$), although the grain indicated by the red arrow shows a lower misorientation. (c) And (d) FSE micrographs of the same regions as those of (a) and (b), respectively, where the rectangular precipitates are evident. (b) And (d) are from region 1 in Table 8.2 with a local strain of $\epsilon \approx 0.53$, (a) and (c) are from region 2 in Table 8.2 with a local strain of $\epsilon \approx 0.72$.

in AD730 and other alloys by Vernier *et al.* [24] (leading to grains such as the "large initially statically recrystallised grains" in the as-received material shown in Fig. 8.2), but here they appear to form dynamically. Vernier *et al.* showed that in order to overcome the relatively fine and dense precipitation in initially unrecrystallised

grains, it is advantageous for the growing recrystallised grain to approximately share a ⟨111⟩ axis with the initially unrecrystallised grain, as was described in Chapter 2 (section 2.5.1).

In the present case, with the recrystallised grains forming dynamically, the common ⟨111⟩ axis has been demonstrated in Fig. 8.13. Additionally, consistent with previous observations, the tendency for twin related precipitates to form in the case of higher misorientation angles, and coherent ones in the case of lower misorientation angles has been demonstrated in Fig. 8.12.

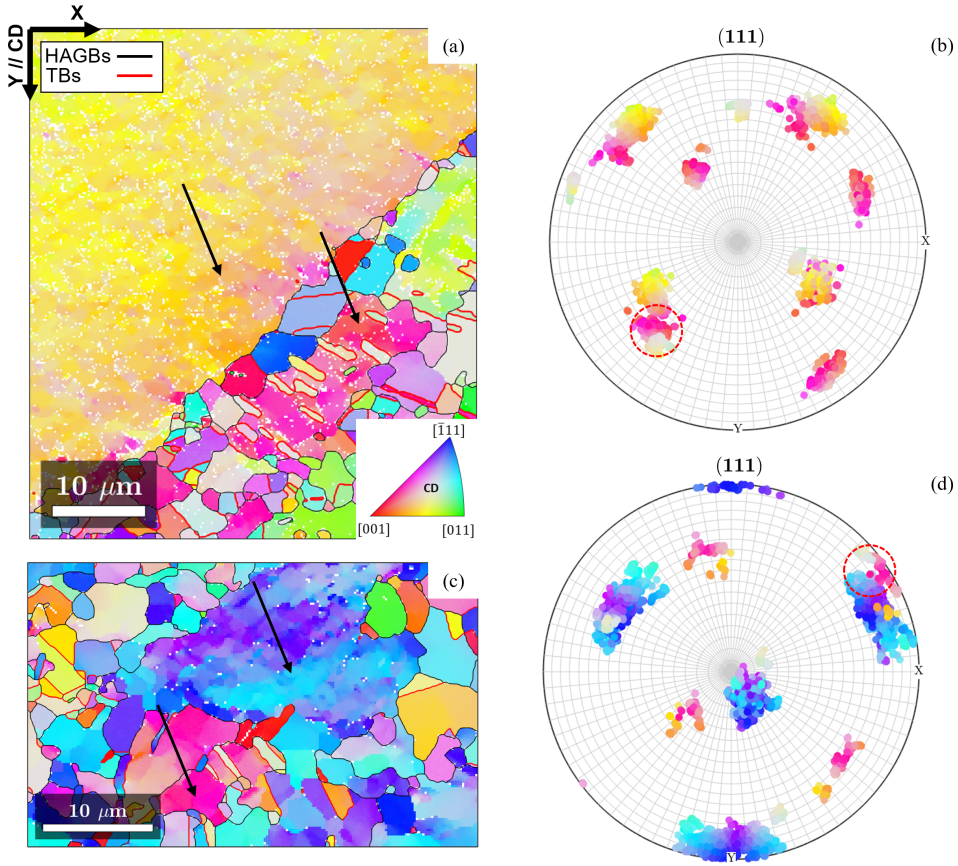
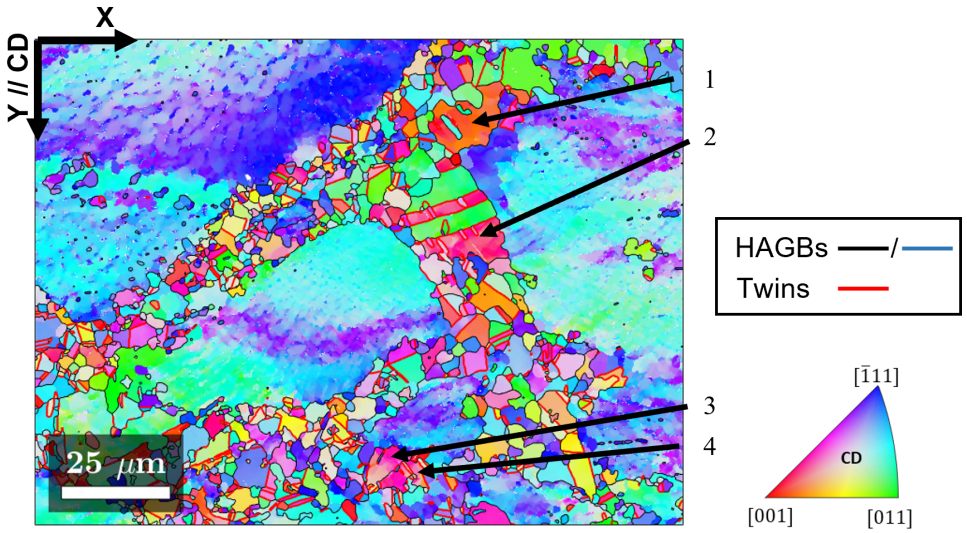


Figure 8.13: Orientation relationships between two large recrystallised grains, their rectangular precipitates and their neighbouring initially unrecrystallised grain. (a) And (c) IPF maps containing a large recrystallised grain and neighbouring initially unrecrystallised grain indicated by black arrows, (b) and (d) corresponding {111} pole figures for the large recrystallised grain, its precipitates and the initially unrecrystallised grains. The red dashed circles in (b) and (d) enclose the {111} pole which is common to all three. (a) And (b) from region 1 in Table 8.2 with a local strain $\epsilon \approx 0.53$, (a) and (c) from region 2 in Table 8.2 with a local strain $\epsilon \approx 0.72$.

The dynamic formation of the large recrystallised grains containing rectangular precipitates is thus thought to be rather similar to their formation in static recrystallisation. When a recrystallised grain approximately shares $\langle 111 \rangle$ axis with a neighbouring initially unrecrystallised grain, it can grow by consuming the initially unrecrystallised grain and its precipitation. Reprecipitation occurs in the form of rectangular precipitates with a close to twin or close to coherent orientation relationships to the recrystallised grain. Reprecipitation was observed to occur at the interface between the recrystallised and initially unrecrystallised grains in [24], and it is likely that this is also the case in this study.

An additional comment can be made regarding the orientation of the precipitates forming in these larger recrystallised grains. As discussed previously, they have a $\langle 111 \rangle$ axis in common with their host grain a neighbouring deformed grain. They are also observed to have their long axis parallel to a $\langle 110 \rangle$ axis of their host grain. Since these precipitates are all observed to be parallel to each other within a given grain, this particular $\langle 110 \rangle$ axis seems to be chosen in preference of any other $\langle 110 \rangle$ axis. The chosen $\langle 110 \rangle$ axis is not found to lie in the $\{111\}$ plane shared by the recrystallised grain, neighbouring deformed grain and precipitate. This is highlighted for the four chosen grains in Fig. 8.14.

Instead, a correlation has been observed between the long axis of the "rectangular" precipitates and the $\langle 110 \rangle$ axis belonging to the highest Schmid factor slip system of the recrystallised grain housing these precipitates. This correlation is illustrated in Fig. 8.15 for five of the large recrystallised grains. This could nevertheless be coincidental, as no logical explanation has been made.



Grain number	Common ⟨111⟩ axis	Precipitate long axis (hkl of deformed grain)
1	[1 -1 1]	17.7,15.3,-5.9
2	[1 -1 1]	6.6,-6.6,-0.13
3	[-1 1 1]	-8.14,-10.1,4.8
4	[1 1 -1]	8.5,-8.6,-0.9

Figure 8.14: Four of the larger grains with rectangular precipitates. The shared ⟨111⟩ axis for these four grains and their neighbouring deformed grain, and the crystallographic direction parallel to the long axis of these precipitates is shown in the table. Data from region 2 in Table 8.2 with a local strain of $\epsilon \approx 0.72$.

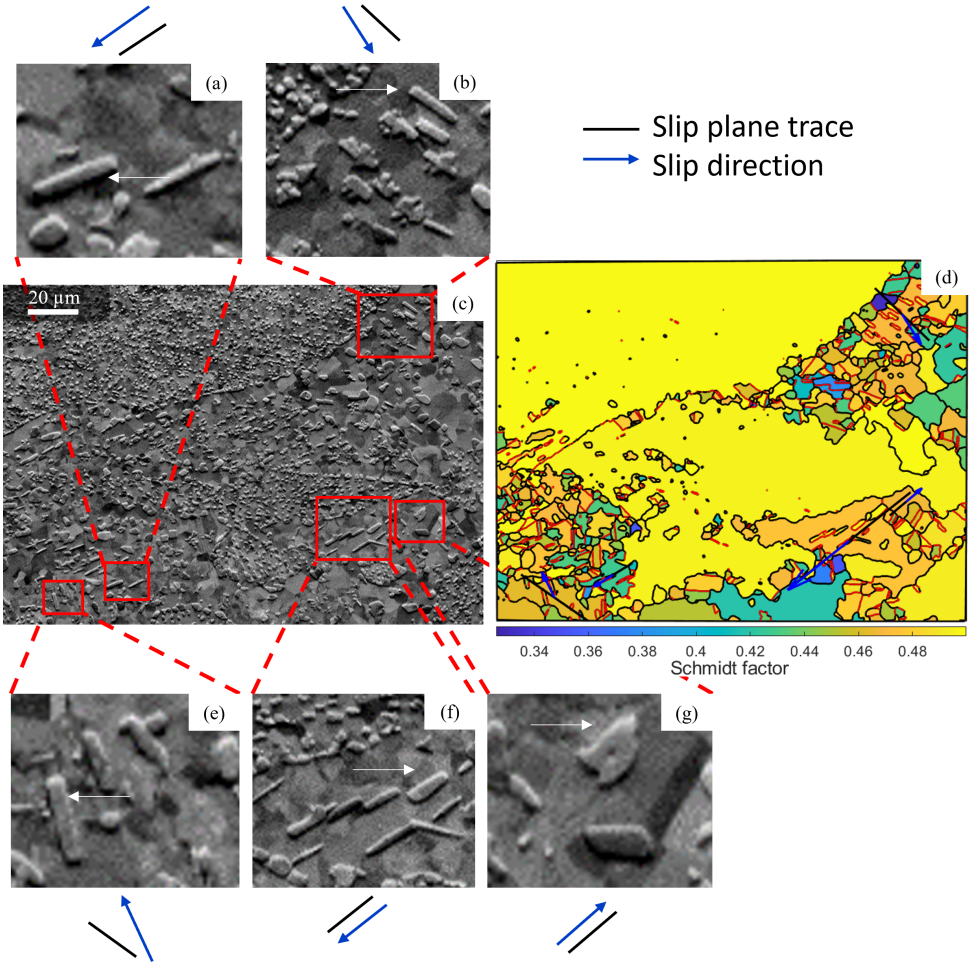


Figure 8.15: The orientation of rectangular precipitates within the large recrystallised grains. A FSD image from region 1 in Table 8.2 in which the local strain was $\epsilon \approx 0.53$ (c) with a map showing grains colourised according to their Schmid factor for the same area (d). The slip plane trace and slip direction for the highest Schmid factor slip system of five of the large recrystallised grains are shown by the black lines and blue arrows, respectively, in (d). These five grains containing rectangular precipitates are shown enlarged in the inserts (a),(b),(e),(f),(g). For each of these the slip plane trace and slip direction of the highest Schmid factor slip system are shown, and one of the precipitates within the grain is indicated by a white arrow.

8.4.3 Recrystallised channels

Alongside the two types of recrystallisation observed along the former grain boundaries, a form of intragranular recrystallisation was also seen inside the initially unrecrystallised grains (see Fig. 8.16). Figs. 8.16(a) – (d) show long "channels" within the initially unrecrystallised grains, which exhibit a very low density of precipitates, and lower KAM values on their interior than the surrounding initially unrecrystallised grain. The precipitates at the edges of such a channel are slightly coarser than elsewhere in the grain (shown in Figs. 8.16(c) and (d)), suggesting that the precipitates previously present within the channel could have been dissolved and re-precipitated at their edge. In Fig. 8.16(f) a band of recrystallised grains within an initially unrecrystallised grain, adjacent to one of the channels, is highlighted by a black arrow.

Looking at the misorientation profiles within such channels in Figs. 8.16(e) - (h), it is evident that sub-grain boundaries have formed within the channels, generating point to point orientation changes of larger than 2°. These sub-grain boundaries could progressively increase their misorientation to become MAGBs and then HAGBs, and create a band of intragranular recrystallised grains, such as the one shown by the black arrow in Fig. 8.16(g). The interiors of the recrystallised grains indicated in Fig. 8.16(g) are free from precipitation, showing that the formation of the recrystallised channels is accompanied by local precipitate dissolution.

Plastic flow inhomogeneity within the initially unrecrystallised grains could play a role in the formation of such channels. Here, dislocations within certain regions of the initially unrecrystallised grains would be more active, and could move to arrange themselves into LAGBs. Whilst doing so, the dislocations could assist in the dissolution of the precipitates they encounter (and growth of precipitates at the borders of the channels), giving rise to precipitate free channels bordered by LAGBs and coarser precipitates within the initially unrecrystallised grains. Dislocation assisted dissolution of γ' and subsequent recrystallisation in a Ni-based superalloy has recently been demonstrated [115]. In Fig. 8.17, two regions within initially unrecrystallised grains, where local precipitate dissolution has occurred, are highlighted. Such regions could go on to form the recrystallised channels. This would imply that precipitate dissolution precedes the formation of LAGBs during the formation of such "channels".

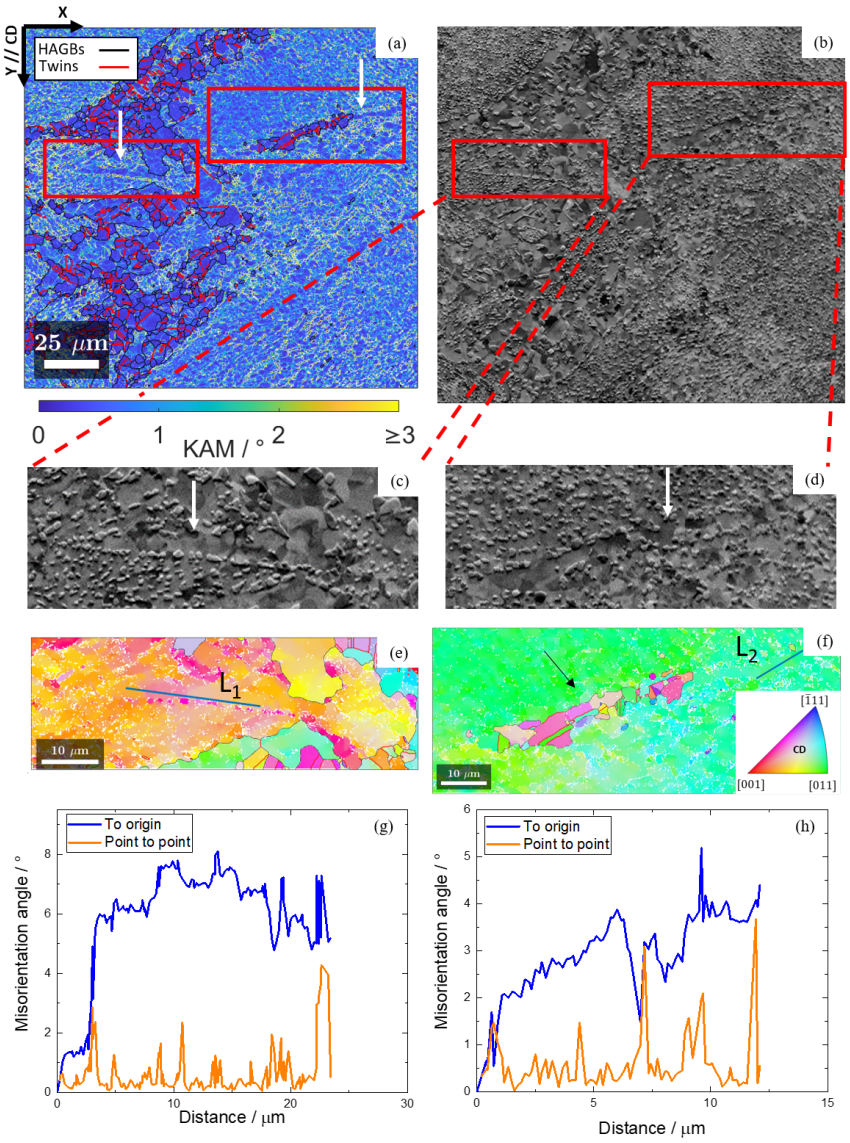


Figure 8.16: Intragranular recrystallisation in the initially unrecrystallised grains. (a) A KAM map depicting two low KAM "channels" within initially unrecrystallised grains highlighted by white arrows in the red rectangles. (b) Corresponding FSE micrograph, (c) and (d) are higher magnification FSE micrographs of the low KAM channels where the white arrows indicate the "channels". (e) And (f) are IPF maps of the areas shown in (c) and (d), the black arrow in (f) highlights a band of recrystallised grains within the initially unrecrystallised grain. (g) And (h) are misorientation profiles taken along the blue lines L1 and L2, respectively, showing both "point to point" and "point to origin" misorientations. Data from region 1 in Table 8.2 with a local strain of $\epsilon \approx 0.53$.

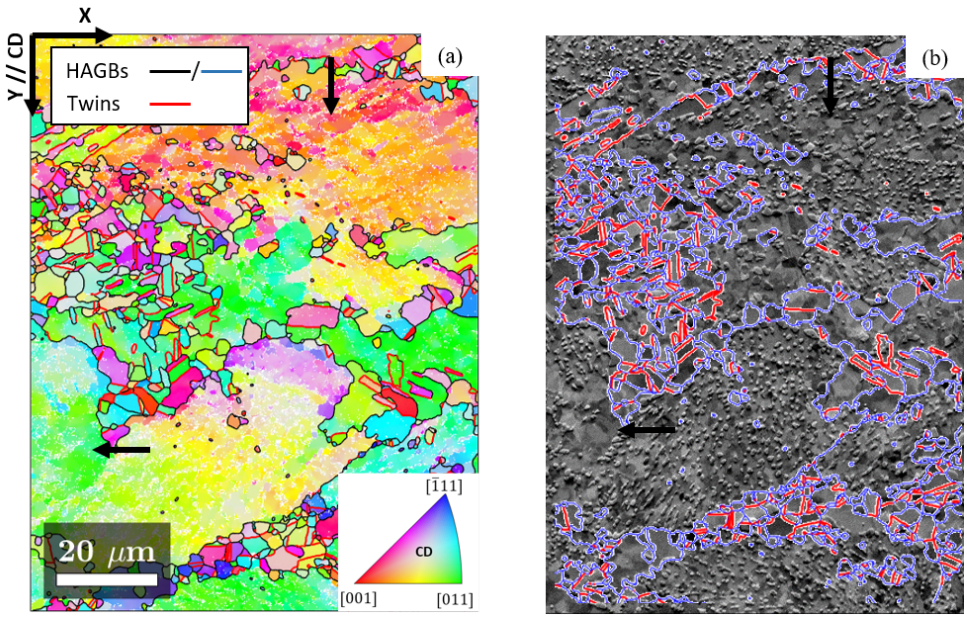


Figure 8.17: Examples of inhomogeneous precipitation within the initially unrecrystallised grains. (a) IPF map and (b) the corresponding FSE micrograph of an area containing two regions within initially unrecrystallised grains where there has been a local dissolution of precipitates, these regions are indicated by the black arrows. The grain and twin boundaries from (a) have been overlaid onto (b). Data from region 1 in Table 8.2 with a local strain of $\epsilon \approx 0.53$.

The formation of these "channels" presents an important recrystallisation effect, in the sense that they can span considerable lengths within a grain, and dramatically reduce the size of the initially unrecrystallised grains. One such channel could effectively split an initially unrecrystallised grain in half. In Fig. 8.16(b), the total length of the band of intragranular recrystallised grains and the adjacent channel is approximately 75 µm. The recrystallised region separating the two similarly orientated initially unrecrystallised grains in Fig. 8.8 could have originated from such a channel.

8.5 The effects of microstructural heterogeneity on recrystallisation

Different recrystallisation mechanisms are operative in the initially unrecrystallised and the large initially statically recrystallised grains. These different mechanisms

are a consequence of the different precipitation states in the two types of grain, i.e. they are a consequence of microstructural heterogeneity.

The fine and dense distribution of precipitates in the initially unrecrystallised grains restrict dislocation motion, and the nucleation of new recrystallised grains is restricted predominately to the grain boundaries, where dislocation densities are highest. By way of contrast, in the large initially statically recrystallised grains recrystallisation occurs predominately intragranularly as dislocations can progressively accumulate into low/medium angle boundaries, less impeded by the more coarse and sparse distribution of precipitates. These different recrystallisation mechanisms, which operate in different grain populations as a result of microstructural heterogeneity, have two important effects.

Firstly, the different mechanisms affect the overall kinetics of recrystallisation. Figs. 8.6 and 8.7 show that at strains of 1.00 – 1.04, the large initially statically recrystallised grains are almost fully recrystallised. However, from Fig. 8.4, the overall recrystallisation level at this strain is approximately 65 %. Therefore, at high strains only parts of the initially unrecrystallised grains remain unrecrystallised. The large initially statically recrystallised grains recrystallise more easily (i.e. at lower strains) than the initially unrecrystallised grains, due to their different recrystallisation mechanisms. These different mechanisms are due to the different local precipitate distributions in the large initially statically recrystallised and initially unrecrystallised grains.

Secondly, the different mechanisms affect the evolution of precipitates. Fig. 8.6 shows that the orientation and morphology of the special type of precipitates found in the large initially statically recrystallised grains was unchanged during deformation and DRX. This indicates that DRX can occur in these grains without the dissolution/reprecipitation of precipitates, the opposite of what has been observed in the initially unrecrystallised grains. Regarding the size of these precipitates, counting 470 of the "rectangular" precipitates from Fig. 8.6 (a) gives an equivalent circle diameter of 1.3 ± 0.5 µm and an area fraction of 18.5 %. This diameter and area fraction are smaller than those measured in the as-received microstructure (1.8 ± 0.7 µm and 21.7 %). It is not clear from these measurements alone whether the size of these precipitates has actually decreased (perhaps due to partial dissolution by the grain boundaries forming around and between them), as this could be an artefact due to the particular 2D section of the precipitates being imaged.

While the "rectangular" precipitates in the large initially statically recrystallised

grains are still present after recrystallisation, the more fine and dense precipitates in the initially unrecrystallised grains are removed during recrystallisation. In the initially unrecrystallised grains, recrystallised sub-grains nucleate predominately at the grain boundaries. These can only grow through their boundary moving and dissolving the fine and dense precipitation encountered, leading to the removal of the fine and dense precipitation in the deformed grains as a consequence of recrystallisation. In the statically recrystallised grains, (sub)-grain boundaries can form around and between the rectangular precipitates. The rectangular precipitates may be partially dissolved by these boundaries, but are clearly still present after recrystallisation of their host grain (as shown in Figs. 8.5, 8.6 and 8.7). Again, the evolution of precipitates differs due to the different recrystallisation mechanisms, which are themselves a consequence of microstructural heterogeneity.

8.6 The origin of primary γ'

The process of precipitate dissolution and reprecipitation during recrystallisation calls into question the origin of primary γ' precipitates. Primary γ' precipitates are often thought to form at grain boundaries either during cooling from above the solvus temperature, or during solutioning which dissolves the other populations of γ' [116]. The data here suggest that all precipitates in recrystallised regions of billet material are subject to dissolution and reprecipitation processes. Even the precipitates in the large initially statically recrystallised grains of the as-received material, which have been shown to persist through dynamic recrystallisation of their hosting grain, themselves form through dissolution and reprecipitation at the boundary between grains with a particular orientation relationship [23]. This implies that the so-called primary γ' phase seen in billet material (at the end of forging) is not primitive, i.e., it does not form from the first solvus crossing and persist throughout the entire forging sequence.

The primary γ' which is undissolved during sub-solvus partial solutioning could either result from coarsening of precipitates at boundaries of the necklace recrystallised grains, or coarsening and globularisation of the "rectangular" (actually cylindrical in 3D) precipitates. In this latter case, it should be possible to find clusters of primary γ' which share similar orientations to each other. This would require discriminating EBSD data from the γ and γ' phases, e.g., by using coupled EBSD-EDS or the

iCHORD-SI technique [117, 118]. The globularisation of the "rectangular" precipitates can be expected following the recrystallisation of their host grain, as they will no longer share a special orientation relationship with the grains surrounding them and will thus have more isotropic interface energies, promoting globularisation during coarsening.

8.7 Summary

In this chapter, the recrystallisation mechanisms occurring in an inhomogeneous microstructure, representative of the latter stages of industrial billet conversion, were studied. The main conclusions are:

- Within a single sample, under a single set of external TMP parameters, different local microstructures, particularly different precipitation states, lead to a range of different recrystallisation mechanisms operating.

- The initially unrecrystallised grains recrystallised predominantly intergranularly, leading to relatively small recrystallised grains with little intragranular precipitation. The misorientation angle distribution of these grains with respect to their neighbouring initially unrecrystallised grain revealed a disproportionately high fraction of relatively low misorientation angles ($\leq 25°$) and of twin orientation relationships, implying that twinning plays an important role in the formation of dynamically recrystallised grains. This recrystallisation mechanism was observed at both bulged grain boundaries, and boundaries which appeared flat (in 2D).

- Large recrystallised grains containing precipitates with an approximately twin or coherent orientation relationship, which have previously been observed to form statically, were observed to form dynamically. In 3D these precipitates have the shape of a flat cylinder.

- An intragranular recrystallisation process produced precipitate free recrystallised "channels" up to 75 µm long. This process can produce significant grain refinement, with a "channel" of recrystallised grains splitting an initially unrecrystallised grain into two similarly orientated parts. The mechanism by

which these channels forms has not been explained, but is hypothesised to involve the dissolution of fine precipitates as γ' forming elements diffuse along dislocations concentrated in intragranular bands. The coarser precipitates at the edges of the channel are thought to have been fed by the dissolution of the fine precipitates within the channels.

- Precipitates interact in at least four different ways with dynamic recrystallisation:

    1. In the necklace recrystallised grains, precipitates were dissolved into moving (sub)boundaries which they slow via solute drag, and were then reprecipitated on the recrystallised side at the boundaries of recrystallised grains, generating small recrystallised grains with little intragranular precipitation.
    2. If a recrystallised and initially unrecrystallised grain share a $\langle 111 \rangle$ axis, precipitates can be dissolved by the recrystallisation front and reprecipitated at the moving interface, with a specific orientation relationship to growing recrystallised grain.
    3. Precipitates can stimulate recrystallisation, via the HERX mechanism.
    4. Large precipitates presenting a low number per unit volume may be unaffected (or only partially dissolved) by recrystallisation, allowing continuous recrystallisation processes to occur around them.

- On billet material, precipitates in recrystallised regions are the result of dissolution and reprecipitation processes associated with recrystallisation. The "primary" precipitates in billet material and later in forgings are not "primitive", i.e., they do not persist through the entire forging process from the first solvus crossing.

9 Summary and conclusions

In this thesis, the microstructural evolutions happening during the open die forging of the Ni-based superalloy AD730 have been investigated. Chapters 1 and 2 provided a background and context, introducing the academic and industrial challenges, and describing some relevant literature, respectively. In Chapter 3, an experimental methodology allowing different stages of the billet conversion process to be investigated was set out. Chapter 4 described the microstructures typical of the latter stages of the industrial forging route, and showed that even at the end of the industrial forging process, the microstructure remains inhomogeneous, containing large unrecrystallised grains with a relatively fine and dense distribution of γ' precipitates. In Chapter 5, it was shown that this inhomogeneous microstructure could be traced back to at least the solvus transition stage of the industrial forging route, during which a very inhomogeneous precipitate distribution develops on slow cooling. In Chapter 6, the interaction of this distribution with recrystallisation during forging was investigated, simulating the first sub-solvus forging operation. It was found that the different precipitate states interact differently with recrystallisation, and have a strong influence on the kinetics of recrystallisation. In Chapter 7, the influence of different sub-solvus forging parameters was investigated, as well as the microstructural evolution during reheating between forging strokes. The level of remnant chemical segregation was measured. Finally, in Chapter 8, the microstructural evolutions during the final sub-solvus forging evolution were simulated with a lab scale trial. Here, the large variety of different recrystallisation mechanisms operating simultaneously within a single sample were characterised and related to different local precipitate distributions.

In this chapter, the main conclusions will be emphasised, and suggestions are made for future work based on open questions from this thesis.

Figure 9.1: Summary of the three main experiments carried out in this thesis, including their goals, sample naming, and the key results.

9.1 Conclusions

9.1.1 Precipitation during slow cooling

Lab scale studies on the precipitation developing when cooling through the γ' solvus temperature generally do not consider the very slow cooling rates which are rel-

evant to industrial forging processes. The work of Atrazhev [80] has shown that discontinuous fan-type precipitates are more likely to form at slower cooling rates. In the present work, it was shown that when cooling at slow rates, relevant to industrial forging conditions, a very inhomogeneous precipitate distribution develops. This comprises a mixture of continuous and discontinuous precipitates, as well as "bands" completely free from any precipitation visible the SEM. Notably, during slow cooling from the super-solvus, precipitation was not observed upon quenching from 1090 °C, an under-cooling of 20 °C below the solvus.

The 3D shape of the discontinuous precipitates has been characterised, and it was shown that they can present very different apparent morphologies and sizes in 2D micrographs, and so cannot be well described based just on 2D data. Both type 1 discontinuous precipitation, in which precipitation occurs behind a grain boundary passing through a super-saturated matrix containing no precipitates, and type 2 discontinuous precipitation, where the boundary encounters precipitates, dissolves them, and reprecipitates them discontinuously in its wake, were observed. The grain boundary motion associated with discontinuous precipitation had a significant effect on grain size. Both area and number weighted average grain size decreased on cooling from the super-solvus domain. This was a surprising result, as there is no stored energy available to onset static recrystallisation in the experiments performed. These results actually show that that discontinuous precipitation during slow cooling leads to grain refinement. Additionally, a change in grain boundary shape was seen, with the ratio of grain area to grain perimeter (for a given grain size) decreasing on cooling through the solvus. This is caused partially by continuous precipitation at grain boundaries, and partially by the serrations due to the moving grain boundaries, behind which discontinuous precipitation is occurring, being locally pinned by the precipitates they encounter.

The discontinuous precipitation reaction front does not always coincide with a grain boundary; examples of which were shown in Chapter 5. In this case, it appeared that the grain boundary had moved on, while the discontinuous precipitation reaction had stopped. To the author's knowledge, this has not been observed previously.

The distribution of twin boundary length is changed as a result of γ' precipitation during slow cooling from the super-solvus domain. Below the solvus temperature, there are a higher number of shorter twin boundaries than above. The total length of grain boundary per unit area increases, due to the grain boundary motion and grain refinement caused by discontinuous precipitation.

The continuous precipitates had undergone the well documented growth sequence from spheres to octodendrites. The distribution of all precipitates (i.e. continuous and discontinuous) was very inhomogeneous. In Chapter 5 a "banding" effect was seen, where adjacent channels showed high or low precipitate densities following slow cooling from the super-solvus domain. This banding effect could be related to chemical segregation measured using EDS and WDS in Chapters 5 and 7. The levels of segregation were up to ≈ 0.5 At.% for Cr, and the trends observed (γ' forming elements concentrated in bands with precipitates, γ forming elements in bands without) were consistent.

Based on EDS data, in Chapter 6, this inhomogeneous precipitate distribution could be related to a segregation coefficient (Wt.% (Cr+ Co) - Wt.%(Ti+Al)). The bands with precipitates having slightly higher contents of γ' forming elements, and the bands without having slightly lower contents of γ' forming elements. In Chapter 7, the banding effect was also seen in samples 2A and 2B from experiment 2, in regions with strain levels $\epsilon \approx 0.44$. EDS and WDS data collected in Chapter 7 again showed that the "banding" was associated with remnant chemical segregation; "bands" which were free from any precipitation contained lower concentrations of the γ' forming elements.

9.1.2 Interaction between recrystallisation and precipitation

An inhomogeneous distribution of precipitates has a very significant effect on recrystallisation during sub-solvus forging. This was shown to be the case in Chapter 6, which looked at the early stages of industrial subsolvus forging, and in Chapter 8, which looked at the final sub-solvus forging operation. In both cases it was seen that the kinetics of recrystallisation (i.e. the recrystallisation level as a function of applied strain) are affected by precipitation, and in Chapter 8 it was shown that the mechanisms of recrystallisation are also affected.

Regarding the difficulty of recrystallising areas with particular (fine and dense) precipitate distributions, a model from Humphrey's textbook was able to explain the observed behaviors. The key parameters are the inter-particle spacing, which limits the size to which sub-grains can grow, and the orientation gradient which controls the increase in misorientation as the sub-boundary is moving. The closer spaced the precipitates are, the smaller the sub-grains, and the lower angle boundary they are able to form in a given long-range orientation gradient. This accounted for

the relative ease of recrystallisation around relatively large octodendrites and the C/T type precipitates in statically recrystallised grains, and the relatively difficult recrystallisation around discontinuous precipitates and in areas with fine and dense spherical precipitates.

With only one exception, recrystallisation involved the dissolution of the surrounding γ' precipitates. This was observed for continuous and discontinuous precipitates in Chapter 6, and for the relatively fine precipitates in unrecrystallised grains in Chapter 8. The only exception to this was the case of C/T type precipitates in the statically recrystallised grains, which preserved their shape and orientation after dynamic recrystallisation. However, there was partial evidence that they had become slightly smaller, possibly due to partial dissolution during recrystallisation. However, this evidence is only partial, since the non-equiaxed shape of these precipitates (flat cylinders in 3D) makes their apparent size vary with section plane. Additionally, the industrial microstructures investigated in Chapter 4 showed that, in the industrial process, these C/T precipitates are not found after the final sub-solvus forging, at least not with their initial shape. This could be due to precipitate growth following deformation and recrystallisation of the matrix, with these precipitates globularising. In this case they should retain orientations similar to their neighbours, and this could be investigated in future work.

In all recrystallised areas on billet material, the γ' precipitates present are the result of dissolution and re-precipitation processes while the γ matrix recrystallises. As such, in all recrystallised regions in the final billet material, there are no pristine γ' precipitates, which have formed during cooling through the solvus and persisted.

9.1.3 Recrystallisation mechanisms

In Chapter 8, it was shown that many recrystallisation mechanisms operate simultaneously in the inhomogeneous microstructure present at the start of the final sub-solvus forging operation. Precipitation was seen to affect the operative mechanism. Around the relatively fine and dense precipitates in the initially unrecrystallised grains, recrystallisation was limited primarily to the grain boundaries, where subgrains formed and dissolved the precipitates they encountered, giving rise to a high number of small recrystallised grains in a necklace microstructure with little to no intragranular precipitation. Inspecting the misorientation angles between these necklace recrystallised grains and their parent unrecrystallised grain showed that a dis-

proportionately high fraction have orientations close to that of their parent unrecrystallised grain, or close to twin related to it. This mechanism sometimes involved bulging of the grain boundary, but sometimes sub-grain boundaries and recrystallised grains were found next to flat boundary sections. Around the relatively coarse and widely spaced C/T type precipitates, recrystallisation was more continuous, and less restricted to the grain boundaries. The mechanism which was identified around these precipitates is similar to the one which was identified around the octodendritic precipitates in Chapter 6, with the difference that octodendrities were not found in recrystallised areas, i.e. they were dissolved during recrystallisation, but the C/T type precipitates were not (or not fully).

It was shown in Chapter 6 that twinning can assist in the formation and growth of recrystallised grains by creating high angle grain boundaries from medium angle grain boundaries.

The increase in recrystallisation level during re-heating between two forging strokes was shown to be predominately due to the growth of recrystallised grains into the deformed matrix, rather than the nucleation of new recrystallised grains.

9.2 Outlook and future work

9.2.1 Discontinuous precipitation and its effect on grain structure

Chapter 5 showed the precipitate distribution which forms during slow cooling through the γ' solvus, and will be present at the start of sub-solvus forging. This comprised a mixture of continuous and discontinuous precipitation. Additionally, it was noted that grain boundaries became serrated and grain sizes **decreased** as a result of this precipitation. The change in grain size is related to the grain boundary movement associated with discontinuous precipitation. The mechanisms of discontinuous precipitation seem to be much less understood than for continuous precipitation. The thermodynamic driving force for type 2 discontinuous precipitation (in which the advancing boundary dissolves precipitates and reprecipitates them discontinuously in its wake) is not clear, as it does not lead to a change in the volume fraction of precipitates, just their morphology. Additionally, to the author's knowledge, the

observation of the discontinuous reaction front stopping whilst the associated grain boundary continues to move has not been made previously; although it is somewhat similar to Ferguson's observation of precipitation ahead of the moving grain boundary in discontinuous precipitation, where there is also a separation between the discontinuous precipitation reaction and a moving grain boundary [88].

In Chapter 5, a reduction in grain size from $\approx$ 500 µm to $\approx$ 90 µm was achieved just by slow cooling from the super-solvus. Future work could aim to exploit such a change in grain size as a means of achieving grain refinement without forging. This is similar to thermal cycling approaches which have been used to achieve microstructural refinement in titanium alloys [119] and in steels [120], where repeated cycling through a phase transition drives a change in grain size. Future work could carry out a cyclic heat treatment on the lab scale, with repeated slow cooling through the γ' solvus. If the change in grain size observed here during the first solvus crossing is repeated in subsequent cooling cycles, this could be a means to reduce grain size at the start of the sub-solvus forging. This will likely increase the recrystallisation level which can be achieved with sub-solvus forging, and lead to a more homogeneous microstructure at the end of sub-solvus forging, with a higher level of recrystallisation and smaller unrecrystallised grains in the final billet material.

As well as grain refinement, this thermal cycling could be investigated as a mechanism of grain boundary engineering, as the total boundary length increases during discontinuous precipitation, and the length fraction of twin boundaries decreases.

9.2.2 The effect of minor differences in composition on precipitation and recrystallisation

Chapters 5 and 6 showed that the inhomogeneous precipitate distribution forming during slow cooling through the solvus affects subsequent recrystallisation behavior. There were large areas found which were completely precipitate free, adjacent to areas with high densities of precipitates.

The inhomogeneous precipitation is suggested to be due to remnant chemical segregation inherited from the early solidification stage and not fully removed by the homogenization treatments. The level of segregation is quite small (the segregation coefficient (Wt.% (Cr+ Co) - Wt.%(Ti+Al)) varies by at most 0.8 Wt. %), however at temperatures close to the γ' solvus, these small differences may lead to significant

differences in the volume fraction of precipitates present, and their size.

9.2.3 Exploiting the easy recrystallisation of the large initially statically recrystallised grains

Chapter 8 showed that the large statically recrystallised grains formed during the static recrystallisation portion of the industrial forging route are relatively easy to recrystallise again in sub-solvus forging, owing to their relatively coarse C/T precipitation state. As such, introducing additional static recrystallisation treatments could be a means of making the final sub-solvus forging more efficient. For instance, the final sub-solvus forging could be split into two steps, with a static recrystallisation treatment between them. A schematic example of this is shown in Fig. 9.2.

An associated piece of future work could involve tracking the post-dynamic evolution of the T/C type precipitates. In Chapter 4 it was shown that their distinctive shape cannot be identified anymore after the final sub-solvus forging in the industrial forging process, but on a lab scale trial they were still clearly present in recrystallised areas after dynamic recrystallisation.

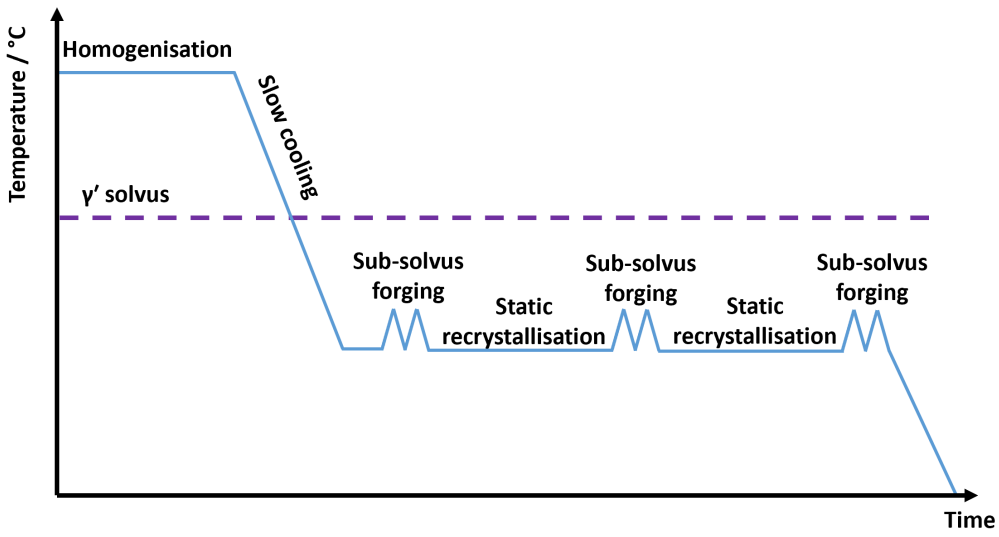


Figure 9.2: A schematic of an amended industrial forging route which involves two static recrystallisation treatments.

9.2.4 Precipitate free bands and the origin of fine and dense spherical precipitates

In Chapter 6 it was observed that a population of very fine and densely distributed precipitates are found after forging, which were not found prior. It was confirmed that these are not discontinuous precipitates (based on their 3D morphology), nor were they small continuous precipitates, based on their size compared with the smallest continuous precipitates present prior to forging. However, they were seen to persist with a 45 minute post-dynamic hold at 1080 °C, which seems to not be consistent with them being dynamically forming precipitates. As such, the origin of these is unclear. Their formation appears to be strain dependent, since they are not found in the low strain samples 2A and 2B investigated in Chapter 7 ($\epsilon \approx 0.45$), which retain the precipitate free bands. However, they appear to have formed in areas with local strain levels $\epsilon \geq 0.69$ during forging, in the areas which were free from precipitation after slow cooling through the γ' solvus temperature.

Bibliography

[1] A. Devaux, B. Picque, M. F. Gervais, E. Georges, T. Poulain, and P. Heritier, "AD730^{TM} - a new nickel-based superalloy for high temperature engine rotative parts," *Superalloys 2012*, pp. 911–919, 2012.

[2] R. C. Reed, *The Superalloys*. 1st ed., 2006.

[3] R. S. Minisandram, L. A. Jackman, J. L. Russell, M. L. Lasonde, J. A. Heaney, and A. M. Powell, *Recrystallization Response during Thermo-Mechanical Processing of Alloy René 65 Billet*, pp. 95–105. John Wiley & Sons, Ltd, 2014.

[4] P. Merica, "Nickel alloy and method of making the same," U.S. Patent 1 572 744A, Feb. 1926.

[5] D. Locq and P. Caron, "On some advanced nickel-based superalloys for disk applications," *J. Aerosp. Lab, Onera, Iss.*, vol. 3, 11 2011.

[6] T. M. Pollock and S. Tin, "Nickel-based superalloys for advanced turbine engines: Chemistry, microstructure, and properties," *Journal of Propulsion and Power*, vol. 22, no. 2, pp. 361–374, 2006.

[7] Z. C. Wang, H. Wang, G. Q. Liu, H. L. Huang, H. F. Zhang, Y. L. Shao, and B. F. Hu, "Effect of ta on the microstructure of high performance ni-based powder metallurgy superalloys," *Science China-Technological Sciences*, vol. 62, no. 11, pp. 1961–1967, 2019.

[8] J. A. Heaney, M. L. Lasonde, A. M. Powell, B. J. Bond, and C. M. O'Brien, "Development of a new cast and wrought alloy (rene 65) for high temperature disk applications," *8th International Symposium on Superalloy 718 and Derivatives*, pp. 67–77, 2014.

[9] J. H. Chen, P. M. Rogers, and J. A. Little, "Oxidation behavior of several chromia-forming commercial nickel-base superalloys," *Oxidation of Metals*, vol. 47, no. 5-6, pp. 381–410, 1997.

[10] Y. Yuan, Y. Gu, C. Cui, T. Osada, Z. Zhong, T. Tetsui, T. Yokokawa, and H. Harada, "Influence of co content on stacking fault energy in ni–co base disk superalloys," *Journal of Materials Research*, vol. 26, no. 22, p. 2833–2837, 2011.

[11] C. G. Tian, G. M. Han, C. Y. Cui, and X. F. Sun, "Effects of co content on tensile properties and deformation behaviors of ni-based disk superalloys at different temperatures," *Materials & Design*, vol. 88, pp. 123–131, 2015.

[12] F. Masoumi, M. Jahazi, D. Shahriari, and J. Cormier, "Coarsening and dissolution of γ' precipitates during solution treatment of AD730^{TM} Ni-based superalloy: Mechanisms and kinetics models," *Journal of Alloys and Compounds*, vol. 658, pp. 981–995, 2016.

[13] P. Kontis, E. Alabort, D. Barba, D. M. Collins, A. J. Wilkinson, and R. C. Reed, "On the role of boron on improving ductility in a new polycrystalline superalloy," *Acta Materialia*, vol. 124, pp. 489–500, 2017.

[14] H. E. Huang and C. H. Koo, "Effect of zirconium on microstructure and mechanical properties of cast fine-grain cm 247 lc superalloy," *Materials Transactions*, vol. 45, no. 2, pp. 554–561, 2004.

[15] F. Masoumi, M. Jahazi, J. Cormier, and D. Shahriari, "Dissolution kinetics and morphological changes of γ' in AD730^{TM} superalloy," in *2nd European Symposium on Superalloys and their Applications*, vol. 14 of *MATEC Web of Conferences*, (CEDEX A), E D P Sciences, 2014.

[16] F. Masoumi, D. Shahriari, M. Jahazi, J. Cormier, and A. Devaux, "Kinetics and mechanisms of γ' reprecipitation in a Ni-based superalloy," *Scientific Reports*, vol. 6, p. 16, 2016.

[17] L. Thebaud, P. Villechaise, J. Cormier, C. Crozet, A. Devaux, D. Bechet, J. M. Franchet, A. Organista, and F. Hamon, "Relationships between microstructural parameters and time-dependent mechanical properties of a new nickel-based superalloy AD730^{TM}," *Metals*, vol. 5, no. 4, pp. 2236–2251, 2015.

[18] S. Tabaie, D. Shahriari, C. Plouze, A. Devaux, J. Cormier, and M. Jahazi, "Hot ductility behavior of AD730^{TM} nickel-base superalloy," *Materials Science and*

Engineering a-Structural Materials Properties Microstructure and Processing, vol. 766, p. 13, 2019.

[19] L. Thebaud, P. Villechaise, C. Crozet, A. Devaux, D. Bechet, J. M. Franchet, A. L. Rouffie, M. Mills, and J. Cormier, "Is there an optimal grain size for creep resistance in ni-based disk superalloys?," *Materials Science and Engineering a-Structural Materials Properties Microstructure and Processing*, vol. 716, pp. 274–283, 2018.

[20] A. Devaux, A. Helstroffer, J. Cormier, P. Villechaise, J. Douin, M. Hantcherli, and F. Pettinari-Sturmel, "Effect of aging heat-treatment on mechanical properties of AD730^{TM} superalloy," *8th International Symposium on Superalloy 718 and Derivatives*, pp. 521–535, 2014.

[21] F. Pettinari-Sturmel, W. Vultos, M. Hantcherli, B. Warot-Fonrose, C. Marcelot, J. Douin, J. Cormier, P. Villechaise, and A. Devaux, "Creep behavior in the new AD730^{TM} nickel-based disk superalloy - influence of aging heat treatment and local chemical fluctuations," *Materials Science and Engineering a-Structural Materials Properties Microstructure and Processing*, vol. 754, pp. 9–17, 2019.

[22] A. Seret, C. Moussa, M. Bernacki, and N. Bozzolo, "On the coupling between recrystallization and precipitation following hot deformation in a γ-γ' nickel-based superalloy," *Metallurgical and Materials Transactions a-Physical Metallurgy and Materials Science*, vol. 49A, no. 9, pp. 4199–4213, 2018.

[23] S. Vernier, J. M. Franchet, C. Dumont, P. Vennegues, and N. Bozzolo, "γ' precipitates with a twin orientation relationship to their hosting grain in a γ/γ' nickel-based superalloy," *Scripta Materialia*, vol. 153, pp. 10–13, 2018.

[24] S. Vernier, J. M. Franchet, C. Dumont, and N. Bozzolo, "A mechanism leading to γ' precipitates with 111 facets and unusual orientation relationships to the matrix in γ/γ' nickel-based superalloys," *Metallurgical and Materials Transactions a-Physical Metallurgy and Materials Science*, vol. 49A, no. 9, pp. 4308–4323, 2018.

[25] T. Konkova, S. Rahimi, S. Mironov, and T. N. Baker, "Effect of strain level on the evolution of microstructure in a recently developed AD730 nickel based

superalloy during hot forging," *Materials Characterization*, vol. 139, pp. 437–445, 2018.

[26] M. Perez, C. Dumont, O. Nodin, and S. Nouveau, "Impact of forging direction on the recrystallization behaviour of nickel base superalloy AD730 billet material at subsolvus temperatures," *Materials Characterization*, vol. 146, pp. 169–181, 2018.

[27] F. Masoumi, D. Shahriari, M. Jahazi, J. Cormier, and B. C. D. Flipo, "On the occurrence of liquation during linear friction welding of Ni-Based superalloys," *Metallurgical and Materials Transactions a-Physical Metallurgy and Materials Science*, vol. 48A, no. 6, pp. 2886–2899, 2017.

[28] F. Masoumi, D. Shahriari, H. Monajati, J. Cormier, B. C. D. Flipo, A. Devaux, and M. Jahazi, "Linear friction welding of AD730$^{\mathrm{TM}}$ ni-base superalloy: Process-microstructure-property interactions," *Materials & Design*, vol. 183, p. 19, 2019.

[29] F. Masoumi, L. Thelaud, D. Shahriari, M. Jahazi, J. Cormier, A. Devaux, and B. C. D. Flipo, "High temperature creep properties of a linear friction welded newly developed wrought Ni-based superalloy," *Materials Science and Engineering a-Structural Materials Properties Microstructure and Processing*, vol. 710, pp. 214–226, 2018.

[30] B. J. Bond, C. M. O'Brien, J. L. Russell, J. A. Heaney, and M. L. Lasonde, *René 65 Billet Material for Forged Turbine Components*, pp. 107–118. John Wiley & Sons, Ltd, 2014.

[31] J. Gayda, T. Gabb, and P. Kantzos, "The effect of dual microstructure heat treatment on an advanced nickel-base disk alloy," *Proceedings of the International Symposium on Superalloys*, 01 2004.

[32] S. Vernier, *evolution de la microstructure du superalliage base nickel AD730^{TM} au cours des operations de forgeage industrielles*. PhD thesis, PSL Research University, 2018.

[33] F. Pyczak, B. Devrient, F. C. Neuner, and H. Mughrabi, "The influence of different alloying elements on the development of the $\gamma/\ \gamma'$ microstructure of

nickel-base superalloys during high-temperature annealing and deformation," *Acta Materialia*, vol. 53, no. 14, pp. 3879–3891, 2005.

[34] P. A. J. Bagot, O. B. W. Silk, J. O. Douglas, S. Pedrazzini, D. Crudden, T. L. Martin, M. C. Hardy, M. P. Moody, and R. C. Reed, "An atom probe tomography study of site preference and partitioning in a nickel-based superalloy," *Acta Materialia*, vol. 125, pp. 156–165, 2017.

[35] N. Saunders, "Phase diagram calculations for ni-based superalloys," *Superalloys 1996*, pp. 101–110, 1996.

[36] K. Alvarado, I. Janeiro, S. Florez, B. Flipon, J.-M. Franchet, D. Locq, C. Dumont, N. Bozzolo, and M. Bernacki, "Dissolution of the primary γ' precipitates and grain growth during solution treatment of three nickel base superalloys," *Metals*, vol. 11, no. 12, 2021.

[37] J. L. Qu, X. F. Xie, Z. N. Bi, J. H. Du, and M. C. Zhang, "Hot deformation characteristics and dynamic recrystallization mechanism of GH4730 Ni-based superalloy," *Journal of Alloys and Compounds*, vol. 785, pp. 918–924, 2019.

[38] U. Krupp, K. Wackermann, H. J. Christ, M. H. Colliander, and K. Stiller, "Intergranular oxidation effects during dwell-time fatigue of high-strength superalloys," *Oxidation of Metals*, vol. 88, no. 1, pp. 3–14, 2017.

[39] W. Hermann, M. Fahrmann, and H. G. Sockel, "Determination of the γ' solvus temperature of two commercial wrought ni-base superalloys by thermal expansion measurements," *Superalloys 2004*, pp. 517–522, 2004.

[40] R. Radis, M. Schaffer, M. Albu, G. Kothleitner, P. Polt, and E. Kozeschnik, "Evolution of size and morphology of γ' precipitates in udimet 720 li during continuous cooling," *Superalloys 2008*, pp. 829–836, 2008.

[41] L. Connor, *The development of a dual microstructure heat treated Ni-base superalloy for turbine disc applications*. PhD thesis, University of Cambridge, 2009.

[42] J. W. Christian, *The theory of transformations in metals and alloys : an advanced textbook in physical metallurgy, part 1 : equilibrium and general kinetic theory*. 2nd ed., 1975.

[43] W. W. Mullins and R. F. Sekerka, "Morphological stability of a particle growing by diffusion or heat flow," *Journal of Applied Physics*, vol. 34, no. 2, pp. 323–329, 1963.

[44] T. Grosdidier, A. Hazotte, and A. Simon, "Precipitation and dissolution processes in γ/γ' single crystal nickel-based superalloys," *Materials Science and Engineering: A*, vol. 256, no. 1, pp. 183–196, 1998.

[45] R. A. Ricks, A. J. Porter, and R. C. Ecob, "The growth of γ'-precipitates in nickel-base super-alloys," *Acta Metallurgica*, vol. 31, no. 1, pp. 43–53, 1983.

[46] P.-R. Cha, D.-H. Yeon, and S.-H. Chung, "Phase-field study for the splitting mechanism of coherent misfitting precipitates in anisotropic elastic media," *Scripta Materialia*, vol. 52, no. 12, pp. 1241–1245, 2005.

[47] R. Ricks, A. Porter, and R. Ecob, "The growth of γ' precipitates in nickel-base superalloys," *Acta Metallurgica*, vol. 31, no. 1, pp. 43–53, 1983.

[48] R. D. Doherty, "Role of interfaces in kinetics of internal shape changes," *Metal science*, vol. 16, pp. 1–14, 1982.

[49] M. Durand, J. Cormier, P. Villechaise, J.-M. Franchet, C. Dumont, and N. Bozzolo, *Metallurgical Mechanisms upon Stress Relaxation Annealing of the AD730TM Superalloy*. 08 2020.

[50] C.-M. Katsari, S. Katnagallu, and S. Yue, "Microstructural characterization of three different size of gamma prime precipitates in Rene 65," *Materials Characterization*, p. 110542, 2020.

[51] S. Lalam, S.Yoshitake, H. Harada, and H. Bhadeshia, "MAP_NICKEL_LATTICE." https://www.phase-trans.msm.cam.ac.uk/map/nickel/programs/lattice.html, 1999.

[52] P. W. Voorhees, "The theory of ostwald ripening," *Journal of Statistical Physics*, vol. 38, no. 1-2, pp. 231–252, 1985.

[53] S. L. Semiatin, N. C. Levkulich, A. E. Saurber, D. W. Mahaffey, E. J. Payton, and O. N. Senkov, "The kinetics of precipitate dissolution in a nickel-base superalloy," *Metallurgical and Materials Transactions a-Physical Metallurgy and Materials Science*, vol. 48A, no. 11, pp. 5567–5578, 2017.

[54] P. Kontis, Z. M. Li, D. M. Collins, J. Cormier, D. Raabe, and B. Gault, "The effect of chromium and cobalt segregation at dislocations on nickel-based superalloys," *Scripta Materialia*, vol. 145, pp. 76–80, 2018.

[55] M. Doi, D. Miki, T. Moritani, and T. Kozakai, "Gamma/gamma-prime microstructure formed by phase separation of gamma-prime precipitates in a Ni-Al-Ti alloy," *Superalloys 2004*, pp. 109–114, 2004.

[56] S. Meher, L. K. Aagesen, M. C. Carroll, T. M. Pollock, and L. J. Carroll, "The origin and stability of nanostructural hierarchy in crystalline solids," *Science Advances*, vol. 4, no. 11, p. 10, 2018.

[57] A. S. Taha, K. E. Mohamed, F. H. Hammad, and M. E. El Mossalamy, "The effect of microstructure on the ultrasonic attenuation and hardness of zircaloy-2," *physica status solidi (a)*, vol. 136, pp. 25–30, 1993.

[58] B. Porter, A. Ralph, "The recrystallization of nickel-base superalloys," *J Mater Sci*, vol. 16, pp. 707–713, 1981.

[59] M. A. Charpagne, T. Billot, J. M. Franchet, and N. Bozzolo, "Heteroepitaxial recrystallization: A new mechanism discovered in a polycrystalline gamma-gamma ' nickel based superalloy," *Journal of Alloys and Compounds*, vol. 688, pp. 685–694, 2016.

[60] M. Charpagne, T. Billot, J. Franchet, and N. Bozzolo, "Heteroepitaxial recrystallization, a new recrystallization mechanism in sub-solvus forged γ - γ' nickel-based superalloys with low lattice mismatch," in *Proceedings of the 6th International Conference on Recrystallization and Grain Growth (ReX&GG 2016)* (E. Holm, S. Farjami, P. Priyadarshan Manohar, G. Rohrer, A. Rollett, D. Srolovitz, and H. Weiland, eds.), pp. 259–264, TMS, July 2016.

[61] A. M. Wusatowska-Sarnek, H. Miura, and T. Sakai, "Nucleation and microtexture development under dynamic recrystallization of copper," *Materials Science and Engineering a-Structural Materials Properties Microstructure and Processing*, vol. 323, no. 1-2, pp. 177–186, 2002.

[62] R. D. Doherty, D. A. Hughes, F. J. Humphreys, J. J. Jonas, D. J. Jensen, M. E. Kassner, W. E. King, T. R. McNelley, H. J. McQueen, and A. D. Rollett, "Current issues in recrystallization: a review," *Materials Science and*

Engineering a-Structural Materials Properties Microstructure and Processing, vol. 238, no. 2, pp. 219–274, 1997.

[63] J. Humphreys, G. S. Rohrer, and A. Rollett, *Recrystallization and Related Annealing Phenomena, 3rd Edition*, pp. 1–704. Amsterdam: Elsevier Science Bv, 2017.

[64] A. Seret, *Influence de la mise en forme sur les cinétiques de précipitation durcissante dans les superalliages base nickel Inconel 625 et AD730^{TM}*. PhD thesis, PSL Research University, 2019.

[65] Y. C. Lin, X. Y. Wu, X. M. Chen, J. Chen, D. X. Wen, J. L. Zhang, and L. T. Li, "Ebsd study of a hot deformed nickel-based superalloy," *Journal of Alloys and Compounds*, vol. 640, pp. 101–113, 2015.

[66] B. C. Xie, B. Y. Zhang, H. Yu, H. Yang, Q. Liu, and Y. Q. Ning, "Microstructure evolution and underlying mechanisms during the hot deformation of 718plus superalloy," *Materials Science and Engineering a-Structural Materials Properties Microstructure and Processing*, vol. 784, p. 11, 2020.

[67] A. Nicolay, G. Fiorucci, J. M. Franchet, J. Cormier, and N. Bozzolo, "Influence of strain rate on subsolvus dynamic and post-dynamic recrystallization kinetics of inconel 718," *Acta Materialia*, vol. 174, pp. 406–417, 2019.

[68] A. Nicolay, J. M. Franchet, J. Cormier, H. Mansour, M. De Graef, A. Seret, and N. Bozzolo, "Discrimination of dynamically and post-dynamically recrystallized grains based on ebsd data: application to inconel 718," *Journal of Microscopy*, vol. 273, no. 2, pp. 135–147, 2019.

[69] S. S. S. Kumar, T. Raghu, P. P. Bhattacharjee, G. A. Rao, and U. Borah, "Strain rate dependent microstructural evolution during hot deformation of a hot isostatically processed nickel base superalloy," *Journal of Alloys and Compounds*, vol. 681, pp. 28–42, 2016.

[70] H. B. Zhang, K. F. Zhang, H. P. Zhou, Z. Lu, C. H. Zhao, and X. L. Yang, "Effect of strain rate on microstructure evolution of a nickel-based superalloy during hot deformation," *Materials & Design*, vol. 80, pp. 51–62, 2015.

[71] L. Hui-zhong, L. Yang, . Y. Wang, G. Tan, S. Qiao, Z. Huang, and M. Liu, "Thermal deformation and dynamic recrystallization of a novel hexed p/m nickel-based superalloy," *Materials Characterization*, vol. 163, pp. 707–713, 2020.

[72] M. Zouari, N. Bozzolo, and R. E. Loge, "Mean field modelling of dynamic and post-dynamic recrystallization during hot deformation of inconel 718 in the absence of δ phase particles," *Materials Science and Engineering: A*, vol. 655, pp. 408–424, 2016.

[73] M. Perez, "Microstructural evolution of nimonic 80a during hot forging under non-isothermal conditions of screw press," *Journal of Materials Processing Technology*, vol. 252, pp. 45–57, 2018.

[74] J. Schindelin, I. Arganda-Carreras, E. Frise, V. Kaynig, M. Longair, T. Pietzsch, S. Preibisch, C. Rueden, S. Saalfeld, B. Schmid, J.-Y. Tinevez, D. J. White, V. Hartenstein, K. Eliceiri, P. Tomancak, and A. Cardona, "Fiji: an open-source platform for biological-image analysis," *NATURE METHODS*, vol. 9, pp. 676–682, JUL 2012.

[75] S. Berg, D. Kutra, T. Kroeger, C. N. Straehle, B. X. Kausler, C. Haubold, M. Schiegg, J. Ales, T. Beier, M. Rudy, K. Eren, J. I. Cervantes, B. Xu, F. Beuttenmueller, A. Wolny, C. Zhang, U. Koethe, F. A. Hamprecht, and A. Kreshuk, "ilastik: interactive machine learning for (bio)image analysis," *Nature Methods*, Sept. 2019.

[76] B. El-Dasher and A. Deal, *Application of Electron Backscatter Diffraction to Phase Identification*, pp. 81–95. Boston, MA: Springer US, 2009.

[77] R. Hielscher and H. Schaeben, "A novel pole figure inversion method: specification of the *MTEX* algorithm," *Journal of Applied Crystallography*, vol. 41, pp. 1024–1037, Dec 2008.

[78] M. Kulakov, S. Rahimi, and S. Semiatin, "Effect of deformation heating on microstructure evolution during hot forging of ti-6al-4v," *Metallurgical and Materials Transactions A*, vol. 53, pp. 407–419, Nov. 2021.

[79] R. Mitchell, H. Li, and Z. Huang, "On the formation of serrated grain boundaries and fan type structures in an advanced polycrystalline nickel-base superalloy," *Journal of Materials Processing Technology*, vol. 209, no. 2, pp. 1011–1017, 2009.

[80] V. Atrazhev, S. Burlatsky, D. Dmitriev, D. Furrer, N. Kuzminykh, I. Lomaev, D. Novikov, S. Stolz, and P. Reynolds, "The mechanism of grain boundary serration and fan-type structure formation in ni-based superalloys," *Metallurgical and Materials Transactions A*, vol. 51, 05 2020.

[81] A. J. Wilkinson and P. B. Hirsch, "Electron diffraction based techniques in scanning electron microscopy of bulk materials," *Micron*, vol. 28, no. 4, pp. 279–308, 1997.

[82] A. NICOLAŸ, J. Franchet, J. Cormier, H. Mansour, M. De Graef, A. Seret, and N. Bozzolo, "Discrimination of dynamically and post-dynamically recrystallized grains based on ebsd data: application to inconel 718," *Journal of Microscopy*, vol. 273, no. 2, pp. 135–147, 2019.

[83] D. B. Williams and E. P. Butler, "Grain boundary discontinuous precipitation reactions," *International Metals Reviews*, vol. 26, no. 1, pp. 153–183, 1981.

[84] H. B. Zhang, S. X. Qin, H. P. Li, J. Liu, Y. T. Lv, Y. Wang, P. Zhang, H. P. Zhou, and T. Wu, "Ebsd study of strain dependent microstructure evolution during hot deformation of a typical nickel-based superalloy," *Journal of Materials Research*, vol. 34, no. 2, pp. 321–334, 2019.

[85] F. Findik, "Discontinuous (cellular) precipitation," *Journal of Materials Science Letters*, vol. 17, pp. 79–83, 01 1998.

[86] K. Tu and D. Turnbull, "Morphology of cellular precipitation of tin from lead-tin bicrystals," *Acta Metallurgica*, vol. 15, no. 2, pp. 369–376, 1967.

[87] R. A. Fournelle and J. B. Clark, "The genesis of the cellular precipitation reaction," *Metallurgical Transactions*, vol. 3, pp. 2757–2767, Nov. 1972.

[88] C. G. Ferguson, K. A. Christofidou, E. M. Hildyard, A. S. Wilson, N. G. Jones, and H. J. Stone, "On the continuous and discontinuous precipitation of the l12 phase in cu-ni-al alloys," *Materialia*, vol. 13, p. 100855, 2020.

[89] H. Danflou, M. Macia, T. Sanders, and T. Khan, "Mechanisms of formation of serrated grain boundaries in nickel base superalloys," *Superalloys 1996*, pp. 119–127, 01 1996.

[90] M. F. Henry, Y. S. Yoo, D. Y. Yoon, and J. Choi, "The Dendritic Growth of γ' Precipitates and Grain Boundary Serration in a Model Nickel-Base Superalloy," *Metallurgical and Materials Transactions A*, vol. 24, pp. 1733–1743, Aug. 1993.

[91] D. Furrer and H.-J. Fecht, "γ' formation in superalloy u720li," *Scripta Materialia*, vol. 40, 05 1999.

[92] H. Benfu, L. Guoquan, W. Kai, and H. Penghui, "Morphological changes behavior of fan-type structures of γ' precipitates in nickel-based powder metallurgy superalloys," *Acta Metall Sin*, vol. 48, no. 7, p. 830, 2012.

[93] L. Wu, T. Osada, I. Watanabe, T. Yokokawa, T. Kobayashi, and K. Kawagishi, "A new approach to strength prediction of ni-base disk superalloys with dual-phase γ/γ'," in *Superalloys 2020* (S. Tin, M. Hardy, J. Clews, J. Cormier, Q. Feng, J. Marcin, C. O'Brien, and A. Suzuki, eds.), (Cham), pp. 651–658, Springer International Publishing, 2020.

[94] J. Cahn, "The kinetics of cellular segregation reactions," *Acta Metallurgica*, vol. 7, no. 1, pp. 18–28, 1959.

[95] F. Den Broeder, "Interface reaction and a special form of grain boundary diffusion in the cr-w system," *Acta Metallurgica*, vol. 20, no. 3, pp. 319–332, 1972.

[96] N. Kaur, C. Deng, and O. Ojo, "The physical origin of diffusion induced grain boundary migration explored by atomistic simulations," *SSRN Electronic Journal*, 01 2019.

[97] M. Ganesan, D. Dye, and P. Lee, "A technique for characterizing microsegregation in multicomponent alloys and its application to single-crystal superalloy castings," *Metallurgical and Materials Transactions A*, vol. 36, pp. 2191–2204, 01 2005.

[98] F. Kocks, C. Tomé, and H.-R. Wenk, *Texture and Anisotropy. Preferred Orientations in Polycrystals and Their Effect on Material Properties*. 2000.

[99] M. Maric, *Influence of Metallurgical State on Hydride Precipitation and Reorientation in Zircaloy-4*. PhD thesis, University of Manchester, 2022.

[100] F.-H. An, D.-Q. Zhang, and P. Feng, "Effect of strain on strain-induced precipitation behavior of mns in 3% si steel," *steel research international*, vol. 92, no. 1, p. 2000224, 2021.

[101] B. Dutta, E. Valdes, and C. Sellars, "Mechanism and kinetics of strain induced precipitation of nb(c,n) in austenite," *Acta Metallurgica et Materialia*, vol. 40, no. 4, pp. 653–662, 1992.

[102] H. Zhang, C. Li, Y. Liu, Q. Guo, Y. Huang, H. Li, and J. Yu, "Effect of hot deformation on γ'' and δ phase precipitation of inconel 718 alloy during deformation and isothermal treatment," *Journal of Alloys and Compounds*, vol. 716, pp. 65–72, 2017.

[103] J. Cormier, I. Janeiro, N. Bozzolo, and J.-M. Franchet, "Dynamic precipitation during forging of a γ - γ' nickel-based superalloy," *Metallurgical and Materials Transactions A*, 02 2023.

[104] B. Dutta, E. Palmiere, and C. Sellars, "Modelling the kinetics of strain induced precipitation in nb microalloyed steels," *Acta Materialia*, vol. 49, pp. 785–794, 01 2006.

[105] I. Dutta and D. Bourell, "Influence of dislocation density and distribution on the aging behavior of 6061 alsicw composites," *Acta Metallurgica et Materialia*, vol. 38, no. 11, pp. 2041–2049, 1990.

[106] M. Charpagne, A. Polonsky, M. Echlin, S. Jacomet, J. de Jaeger, M. De Graef, N. Bozzolo, and T. Pollock, "Growth accidents induced by primary γ' precipitates in a polycrystalline nickel-based superalloy," *Scripta Materialia*, vol. 186, pp. 109–113, 2020.

[107] N. Bozzolo, M. Zouari, and R. Logé, "In situ characterization of inconel 718 post-dynamic recrystallization within a scanning electron microscope," *Metals*, vol. 7, p. 476, 11 2017.

[108] N. Bozzolo and M. Bernacki, "Viewpoint on the Formation and Evolution of Annealing Twins During Thermomechanical Processing of FCC Metals and Alloys," *Metallurgical and Materials Transactions A*, vol. 51, pp. 2665–2684, May 2020.

[109] B. Zhang, Z. Wang, H. Yu, and Y. Ning, "Microstructural origin and control mechanism of the mixed grain structure in ni-based superalloys," *Journal of Alloys and Compounds*, vol. 900, p. 163515, 2022.

[110] E. Eriksson and M. Hörnqvist Colliander, "Dynamic and post-dynamic recrystallization of haynes 282 below the secondary carbide solvus," *Metals*, vol. 11, no. 1, 2021.

[111] A. Belyakov, H. Miura, and T. Sakai, "Dynamic recrystallization under warm deformation of a 304 type austenitic stainless steel," *Materials Science and Engineering: A*, vol. 255, no. 1, pp. 139–147, 1998.

[112] K. Huang and R. Logé, "A review of dynamic recrystallization phenomena in metallic materials," *Materials & Design*, vol. 111, pp. 548–574, 2016.

[113] P. A. Beck and P. R. Sperry, "Strain induced grain boundary migration in high purity aluminum," *Journal of Applied Physics*, vol. 21, no. 2, pp. 150–152, 1950.

[114] J. Bailey and P. Hirsch, "The recrystallization process in some polycrystalline metals," *Proceedings of the royal society A*, vol. 267, pp. 11–30, 1962.

[115] L. Lilensten, P. Kürnsteiner, J. R. Mianroodi, A. Cervellon, J. Moverare, M. Segersäll, S. Antonov, and P. Kontis, "Segregation of solutes at dislocations: A new alloy design parameter for advanced superalloys," in *Superalloys 2020* (S. Tin, M. Hardy, J. Clews, J. Cormier, Q. Feng, J. Marcin, C. O'Brien, and A. Suzuki, eds.), (Cham), pp. 41–51, Springer International Publishing, 2020.

[116] M. Jackson and R. Reed, "Heat treatment of udimet 720li: the effect of microstructure on properties," *Materials Science and Engineering: A*, vol. 259, no. 1, pp. 85–97, 1999.

[117] S. Vernier, J.-M. Franchet, M. Lesne, T. Douillard, J. Silvent, C. Langlois, and N. Bozzolo, "ichord-si combination as an alternative to eds-ebsd coupling for the characterization of γ - γ' nickel-based superalloy microstructures," *Materials Characterization*, vol. 142, pp. 492–503, 2018.

[118] M.-A. Charpagne, P. Vennégués, T. Billot, J. M. Franchet, and N. Bozzolo, "Evidence of multimicrometric coherent γ' precipitates in a hot-forged γ–γ' nickel-based superalloy," *Journal of Microscopy*, vol. 263, 2016.

[119] H. Clemens, A. Bartels, S. Bystrzanowski, H. Chladil, H. Leitner, G. Dehm, R. Gerling, and F. Schimansky, "Grain refinement in γ-tial-based alloys by solid state phase transformations," *Intermetallics*, vol. 14, no. 12, pp. 1380–1385, 2006.

[120] Z. Nasiri, S. Ghaemifar, M. Naghizadeh, and H. Mirzadeh, "Thermal mechanisms of grain refinement in steels: A review," *Metals and Materials International*, vol. 27, p. 2078–2094, 07 2021.